DISSERTATION

submitted to the
Combined Faculties for the Natural Sciences and Mathematics
of the Ruperto-Carola-University of Heidelberg, Germany
for the degree of

Doctor of Natural Sciences

Put forward by

Francesca Dordei

born in Cagliari, Italy.

Oral examination: May 19$^{\text{th}}$, 2015

Lifetime measurements of beauty hadrons at the LHCb experiment

Referees: Prof. Dr. Stephanie Hansmann-Menzemer
             Prof. Dr. Johanna Stachel

Acknowledgments

Knowledge is in the end based on acknowledgement.

— Ludwig Wittgenstein

I have always found difficulties in writing aknowledgments, always thinking about them at 4 a.m. in the night, right before the deadline to print the bachelor or master thesis, rushing and trying hard to not forget anyone. This time I took my time and I hope that these aknowledgments do justice to all the people that have accompanied me in the last four years of my life.

I would like to thank Prof. Stephanie Hansmann-Menzemer for her guidance, all the physics she taught me during this period and for giving valuable comments to this thesis. It is a tradition that supervisors are quoted first in the aknowledgments, however I feel that in this case the position is really deserved. It was a pleasure to work with you, I felt supported and encouraged all the time and you gave me countless opportunities without having to ask for them. Thanks because you succeeded in the delicate task to help me finding my way. A special thank goes to Prof. Johanna Stachel for agreeing to be the second referee for my thesis and for having supported me in a difficult period. Moreover, I am grateful to Prof. Timo Weigand and Prof. Ulrich Glasmacher for taking part in my exam and I would like to thank Prof. Ulrich Uwer for his suggestions and constructive critcism.

I would like to thank all of my colleagues in Heidelberg. George and Katharina for being my first officemates and having supported me in the first period of my german experience. Christian F. for introducing me quickly in his life and letting me know all his friends. Sebastian W. for being an incredible friend, for understanding my mmm mmm, for the wonderful travel in Japan, for all the laughs, for your support. If I didn't miss Sardinia too much was thanks to people like you that made me feel at home. Luci, for bringing a lot of *italianità* in the Heidelberg group, we shared together all our achievements and problems, all the misunderstandings with the German culture and many awkwards moments. And well, also for the cutest nickname ever! Paul,

because you are Paul, the only person capable of learning italian in Germany (and I didn't learn german, shame on me!), for the endless chats about everything and for being the only person I know still sending postcards (I love it!). Hanni and Nanni, for all the time we spent together. In particular, Alex for always having a smile, for the sincronised swimming and all the other incredibly funny stories and Marco for always being available to resurrect my car, for the german doctors advices or for gossip chats, in few words, for being a nice friend. Thomas, for the pain au chocolat at Cern, yours nussecken and for the skiing adventure (and for not laughing for my absurd suit!). Christian L. for all the moments (and bottles of wine) we shared together and for don't being mad at me when Italy won against Germany at football (you see? Now you are World champion!!). Andreas, for your extreme courteousness and helpfulness, you are one of the rare people that are always available to help someone else. Saschi, for being a perfect officemate, for your wonderful pizza and for believing in me, so much so to keep a free desk in your new office. Blake, for becoming silently part of my life and for always making me feel part of your life, too. Svende, you came late but you managed to occupy an important role in my life. Thanks for your cheerfulness, for choosing me when something was going wrong and you wanted to talk, for your constant gossip updates and together with Snow, for motivating me to go to zumba!! Alessio, thanks for sharing the office in the last period, I discovered a very nice person. Now, the responsability for tiramisù is yours! And thanks to all my other colleagues, thanks to your advices, your funny stories and your constant availability my stay in Heidelberg was very nice.

During my PhD, I had the privilege to work with many people within the LHCb collaboration. In particular, I would like to thank the members of the B2CC working group and especially Greig and Yasmine, for their irreplaceable contributions to my work and their support that certainly made me a better physicist. I would like to thank also Frederic, that shared this work with me and was a great companion during this adventure.

A person that is impossible to forget in these aknowledgments is Marianna. We have been together since the very first day of University, sharing notes, anxiety and the lode after the exams, bayles and dinners together. We went through this incredible adventure together, trying to bring a little of Sardinia in Heidelberg (our mirto was a success) and I always knew that for anything you were there. And thanks to Dorothea, that made the last year in Heidelberg even more lovely. Thanks for all the support and for sharing together our hypochondria, difficult moments but also for the eel sushi and for uncountable feasts together.

Thanks to Fra e Andre, you started years ago as tutors and now, besides being bright and smart physicists, you are special friends.

I would like to say a huge thank to all my friends because, in spite of the distance, I never felt forgotten and it has been a pleasure to come back to Sardinia especially to see all of you again: Silvi, Paoletta, Fra Loi & Fabri, Charli & Giuli, RickyMu, Matte, QQ & Ale, Sara, Rob, Albe, Sonj, Riky & Pinci, Stefy & Mosi.

Grazie a mamma e papà, senza voi che da piccola mi avete instillato la curiosità verso tutte le cose che succedono nel mondo, che mi avete sempre incoraggiato a credere in me stessa e che mi avete aiutato a rialzarmi ogni volta che qualcosa non andava per il verso giusto, non sarei qui a scrivere questi ringraziamenti.

Last, as usual, but clearly the most important, comes Matte. Without you, your unconditional love, your support, your patience, none of the things I have done would have been possible. Wherever I am, I always feel that someone is waiting for me at home and this reminds me what is the most important thing in life. Ti amo.

Francesca

Abstract

This thesis presents several lifetime measurements of b-flavoured hadrons at the LHCb experiment. They represent an important test of the theoretical approach to b-hadron observables known as Heavy Quark Expansion (HQE). This analysis uses data corresponding to an integrated luminosity of 1 fb^{-1} collected in proton–proton collisions at a centre-of-mass energy of $\sqrt{s} = 7$ TeV. For the decays $B^+ \to J/\psi\, K^+$, $B^0 \to J/\psi\, K^{*0}$, $B^0 \to J/\psi\, K^0_S$, $\Lambda_b^0 \to J/\psi\, \Lambda$ and $B_s^0 \to J/\psi\, \phi$, the lifetimes are measured to be

$$
\begin{aligned}
\tau_{B^+ \to J/\psi\, K^+} &= 1.637 \pm 0.004 \pm 0.003 \,\text{ps}, \\
\tau_{B^0 \to J/\psi\, K^{*0}} &= 1.524 \pm 0.006 \pm 0.004 \,\text{ps}, \\
\tau_{B^0 \to J/\psi\, K^0_S} &= 1.499 \pm 0.013 \pm 0.005 \,\text{ps}, \\
\tau_{\Lambda_b^0 \to J/\psi\, \Lambda} &= 1.415 \pm 0.027 \pm 0.006 \,\text{ps}, \\
\tau_{B_s^0 \to J/\psi\, \phi} &= 1.480 \pm 0.011 \pm 0.005 \,\text{ps},
\end{aligned}
$$

where the first uncertainty is statistical and the second is systematic. These are the most precise lifetime measurements in these decay modes to date. Ratios of these lifetimes also are reported in this thesis, as they are well-defined quantities where many theoretical or experimental uncertainties cancel.

The ratio of the decay width difference, $\Delta\Gamma_d$, to the average width, Γ_d, in the B^0 system is found to be $\Delta\Gamma_d/\Gamma_d = -0.044 \pm 0.025 \pm 0.011$.

Using data corresponding to an integrated luminosity of 3 fb^{-1} collected at centre-of-mass energies of 7 TeV and 8 TeV, the measurements of the decay width difference, $\Delta\Gamma_s$, and the average width, Γ_s, in the B_s^0 system are performed. Using the decay $B_s^0 \to J/\psi\, \phi$, they are measured to be

$$
\begin{aligned}
\Delta\Gamma_s &= 0.0805 \pm 0.0091 \pm 0.0033 \,\text{ps}^{-1}, \\
\Gamma_s &= 0.6603 \pm 0.0027 \pm 0.0015 \,\text{ps}^{-1}.
\end{aligned}
$$

These are the most precise determinations of these observables to date. All measurements are consistent with HQE predictions.

Kurzfassung

In dieser Arbeit wird die Messung der Lebensdauern von b-Hadronen mit dem LHCb-Experiment vorgestellt. Diese Messung ist ein wichtiger Test der theoretischen Beschreibung der b-Hadronen durch den sogenannten Heavy-Quark-Expansion (HQE) Ansatz. Die verwendeten Daten entsprechen einer integrierten Luminosität von 1 fb^{-1}, und wurden in Proton-Proton Kollisionen mit einer Schwerpunktsenergie von $\sqrt{s} = 7$ TeV aufgezeichnet. In den Zerfallsmoden $B^+ \to J/\psi\, K^+$, $B^0 \to J/\psi\, K^{*0}$, $B^0 \to J/\psi\, K_S^0$, $\Lambda_b^0 \to J/\psi\, \Lambda$ und $B_s^0 \to J/\psi\, \phi$ wurden die Lebensdauern zu

$$
\begin{aligned}
\tau_{B^+ \to J/\psi\, K^+} &= 1.637 \pm 0.004 \pm 0.003 \,\text{ps}, \\
\tau_{B^0 \to J/\psi\, K^{*0}} &= 1.524 \pm 0.006 \pm 0.004 \,\text{ps}, \\
\tau_{B^0 \to J/\psi\, K_S^0} &= 1.499 \pm 0.013 \pm 0.005 \,\text{ps}, \\
\tau_{\Lambda_b^0 \to J/\psi\, \Lambda} &= 1.415 \pm 0.027 \pm 0.006 \,\text{ps}, \\
\tau_{B_s^0 \to J/\psi\, \phi} &= 1.480 \pm 0.011 \pm 0.005 \,\text{ps},
\end{aligned}
$$

bestimmt, wobei zuerst die statistischen und anschließend die systematischen Unsicherheiten angegeben sind. Dies sind die präzisesten b-Lebensdauermessungen in diesen Zerfallskanälen. Die Verhältnisse der Lebensdauern werden ebenfalls angegeben, worin sich viele theoretische und experimentelle Unsicherheiten aufheben.

Das Verhältnis der Zerfallsbreitendifferenz $\Delta\Gamma_d$ zur mittleren Zerfallsbreite Γ_d im B^0-System, $\Delta\Gamma_d/\Gamma_d = -0.044 \pm 0.025 \pm 0.011$, wurden bestimmt.

Zusätzlich wurden Messungen der Zerfallsbreitendifferenz $\Delta\Gamma_s$ und der mittleren Zerfallsbreite Γ_s im B_s^0-System mit einem Datensatz von 3 fb^{-1} bei Schwerpunktsenergien von 7 TeV und 8 TeV durchgeführt. In der Analyse des Zerfalls $B_s^0 \to J/\psi\, \phi$ wurden diese Parameter zu

$$
\begin{aligned}
\Delta\Gamma_s &= 0.0805 \pm 0.0091 \pm 0.0033 \,\text{ps}^{-1}, \\
\Gamma_s &= 0.6603 \pm 0.0027 \pm 0.0015 \,\text{ps}^{-1},
\end{aligned}
$$

bestimmt. Das ist die bisher präziseste Messung dieser Größen. Alle in dieser Arbeit vorgestellten Messungen stimmen mit den HQE-Vorhersagen überein.

Contents

Preface

> *Considerate la vostra semenza: (Consider well the seed that gave you birth:)*
> *fatti non foste a viver come bruti, (you were not made to live as brutes,)*
> *ma per seguir virtute e canoscenza. (but to follow virtue and knowledge.)*
>
> — Dante Alighieri

The move towards a rational understanding of nature began more than 2500 years ago when different philosophers in the Ancient Greece refused to accept various supernatural, religious or mythological explanations for natural phenomena and started to search for a natural cause for every event. Since then, significant progress has been made. In the last two centuries, more and more complex experiments have revealed that the atoms, which were thought to be indivisible and the smallest constituents of matter, are instead made out of electrons, protons and neutrons. For quite some time, these were thought to be all elementary particles. The current understanding is that protons and neutrons have a complex structure and are constituted by smaller objects, called *quarks*. Moreover, heavier replicas of the electrons have been observed. These, together with some very elusive particles, called neutrinos, are collectively called *leptons*. Everything in the universe is found to be made from six quarks and six leptons, which are related in pairs, called *generations*. The lightest particles make up the first generation, whereas the heavier particles belong to the second and third generation. From several observations it has been established that the known stable matter in the universe is made from particles that belong to the first generation. Indeed, all heavy particles decay in the end to the lighter particles of the first generation.

The Standard Model (SM) of particle physics is the theory that describes, to the best of today's knowledge, the fundamental particles and the forces through which particles interact, namely the electromagnetic, the strong and the weak interactions. Over the last decades, the SM has been extensively tested. Its predictions have been confirmed by innumerable experimental results and it has precisely predicted a wide variety of phenomena. Despite the many successes, some big questions are still unanswered and the most familiar force in our everyday lives, gravity, is not included. Furthermore, the fact that there is a large number of free parameters leads physicists to believe that

the SM is not the final theory of particle physics. In particular, a large number of undetermined parameters is associated with the so-called *flavour sector* of the SM. These parameters are the masses of quarks and leptons, as well as the four free parameters of the Cabibbo-Kobayashi-Maskawa (CKM) matrix, which describe the transitions between different quarks by means of the weak interaction.

Weak decays offer the most direct way to determine the CKM parameters and to test the flavour sector of the SM. In particular, decays from hadrons that are composed by a beauty (b) quark, referred to as b hadrons, are extensively used. The b quarks can decay into all other quark species, but the top (t) quark which is much heavier. Since these decays are quite suppressed, b hadrons have a relatively long lifetime compared to the other quarks and provide access to a large variety of decay channels that can be independently used to measure the CKM parameters.

However, weak decays are also ideally suited to study that part of strong interaction physics which is least understood: the nonperturbative long-distance forces, which are responsible for the confinement of quarks and gluons (the carriers of the strong force) inside hadrons. These low energy phenomena that are involved in particle production and decay are far from being well described by the SM. Only a few phenomenological models exist, but have no direct connection to the underlying theory of strong interactions, the quantum chromodynamics. The understanding of the connection between quark and hadron properties is a prerequisite for a precise determination of many parameters of the SM. Moreover, the extraction from experimental data of fundamental parameters, such as CKM matrix elements, often relies on theoretical inputs coming from these models.

One of the most useful is the so-called *heavy quark expansion* (HQE) model. Among other quantities, it allows for rather precise predictions about lifetimes of different b hadrons. Thus, measurements of b-hadron lifetimes are extremely helpful to validate this model. Namely, the b hadrons of interest are the B^+, the B^0 and the B_s^0 mesons and the Λ_b^0 baryon. Historically, there have been several discrepancies between experimental results and theory predictions that questioned the validity of HQE. For this reason precise measurements are extremely important to confirm or to contradict its predictions. A good agreement between theory and experimental lifetime results would enforce the reliability on the other HQE predictions which are used to test the validity of the SM.

Neutral mesons, like the B^0 and the B_s^0, exhibit the phenomenon of mixing between particles and antiparticles. This results in a decay-time distribution characterised by the sum of two exponential decays with different lifetimes. The difference between the inverse of the two lifetimes is defined as $\Delta\Gamma_s$ and $\Delta\Gamma_d$ for B_s^0 and B^0 mesons, respectively. These observables are very interesting since they are sensitive to possible effects that are not included in the SM and that could modify their values. In particular, $\Delta\Gamma_d$ has a very small SM value and is only weakly constrained by measurements

$$\left|\frac{\Delta\Gamma_d}{\Gamma_d}\right|^{\mathrm{HQE}} = (4.2 \pm 0.8) \cdot 10^{-3} \, [1], \qquad \left|\frac{\Delta\Gamma_d}{\Gamma_d}\right|^{\mathrm{EXP}} = (15 \pm 18) \cdot 10^{-3} \, [2],$$

where Γ_d is the average lifetime of the B^0 meson. Thus, a measurement of these observables is also of great importance.

The LHCb experiment at the Large Hadron Collider (LHC) in Geneva is designed to study heavy-flavour physics. The large $b\bar{b}$ production cross-section from proton-proton collisions at the TeV scale provide unprecedented statistical power to investigate decays in the b-hadron sector. It is the perfect laboratory to make precise lifetime measurements. From an experimental point of view, there are several effects which have to be controlled when performing these measurements at the LHCb experiment. In particular, acceptance effects that depend on the b-hadron decay time can be introduced at any stage of the analysis. One example, which was revealed in the course of this work, is that the efficiency to reconstruct the particle trajectories inside the LHCb detector slightly decreases at long decay-times of the b hadrons. If such effects are not properly taken into account, the corresponding lifetime measurements are biased. The understanding and the correction of these effects is the main challenge of precision lifetime measurements. Given the statistical precision of a few femtoseconds that is expected for the different lifetime measurements, they must be controlled to a very accurate level. Therefore, data-driven techniques must be developed in order to reduce the size of the systematic uncertainties related to the correction procedure. A successful correction for all these effects is essential to demonstrate a good understanding of the LHCb detector and it is of crucial importance for other lifetime related analyses.

This thesis presents several lifetime measurements of b-flavoured hadrons and lifetime ratios. Moreover the measurements of $\Delta\Gamma_s$ and $\Delta\Gamma_d$ are also illustrated. The thesis is organised in four parts. The first part familiarises the reader to all the necessary knowledge to understand the analysis presented. The first chapter of this thesis gives an introduction to the Standard Model of particle physics and the aspects of flavour physics relevant to this work. It focuses particularly on the heavy quark expansion formalism. The LHC accelerator complex and the LHCb experiment are presented in the second chapter. A particular focus is given to the vertex detector which plays a central role in the determination of the particles decay time. The third chapter is devoted to a short review of the software used at LHCb for the reconstruction of the trajectories of the particles, since it is the source of an acceptance effect that depends on the b-hadron decay time. The last section of each chapter recapitulates the fundamental information. In the second part the measurement of the B^+, the B^0 and the B_s^0 mesons and the Λ_b^0 baryon lifetimes is presented. Additionally, starting from these lifetime measurements the value of $\Delta\Gamma_d/\Gamma_d$ is determined. The analysis strategy is detailed in the fourth chapter as well as the remaining structure of the document. In the third part, the measurements of $\Delta\Gamma_s$ and Γ_s are reported. The last section of each chapter summarises its important results. Finally, in the last part of this thesis, the results obtained are summarised and commented upon.

The author of this thesis was one of the main proponents of the publication [3] which covers the same analysis presented in the second part of this thesis. The author also significantly contributed to other publications. They are the measurement of the Λ_c cross-section in proton-proton collisions at $\sqrt{s} = 7$ TeV [4]; and the measurement of the CP violating phase ϕ_s in the decay $B_s^0 \to J/\psi\,\phi$ using a sample corresponding to an integrated luminosity of 1 fb^{-1} [5] and 3 fb^{-1} [6]. The latter is presented in the third part of this thesis.

Part I

Introduction

<div style="text-align: right; font-size: 3em;">*1*</div>

Theoretical overview of b hadrons and their lifetime

Somewhere in Steinbeck country two tired men sit down at the side of the road. Lenny combs his beard with his fingers and says, "Tell me about the laws of physics, George." George looks down for a moment, then peers at Lenny over the tops of his glasses. "Okay, Lenny, but just the minimum."

— Leonard Susskind, George Hrabovsky

This chapter introduces the theoretical basis upon which the work presented in this thesis is based and the motivation to study b-hadron lifetimes. First, a brief introduction to the Standard Model of particle physics is presented, followed by an overview of the weak interaction and of the properties of b hadrons relevant for this thesis.[1] Second, the concept of particle lifetimes is introduced. The focus is put in particular on the lifetime of b hadrons. The last section is devoted to the Heavy Quark Expansion model and its predictions for the ratio of lifetimes. Comparisons between these predictions and the experimental status of lifetime measurements, before the inclusion of the results shown in this thesis, are finally reviewed.

1.1 Brief introduction to the Standard Model of particle physics

The Standard Model (SM) of particle physics [7–9] is a theoretical framework which describes the current knowledge of the fundamental particles and the forces through which particles interact. It was formulated throughout the second half of the 20th century, based on a compilation of laws, theories, and empirical observations. During the last decades, it has been scrutinized by hundreds of experiments, the overwhelming majority of which has been able to verify its accuracy and predictive power to remarkable precision. More recent discoveries such as that of the Higgs boson in 2012 [10, 11], or the Z and W bosons in 1983 [12, 13], both of which were predicted based on fundamental concepts in the theory, have further reinforced our current

---

[1]Throughout the document b hadron stands for mesons and baryons containing a b quark, like B^+, B^0 and B_s^0 mesons and Λ_b^0 baryons. The inclusion of charge-conjugate processes is implied throughout the work unless explicitly stated otherwise.

Table 1.1: The classification of fermions in the SM.

	1st **generation**	2nd **generation**	3rd **generation**
quarks	u (up)	c (charm)	t (top)
	d (down)	s (strange)	b (beauty)
leptons	ν_e (electron neutrino)	ν_μ (muon neutrino)	ν_τ (tau neutrino)
	e^- (electron)	μ^- (muon)	τ^- (tau)

picture of particle physics.

The SM of particle physics describes the strong, electromagnetic, and weak interactions of elementary particles in the framework of a renormalisable quantum field theory. All observed microscopic phenomena can be attributed to one or the other of these interactions. For example, the forces that hold together the protons and the neutrons in the atomic nuclei are due to strong interactions, the binding of electrons to nuclei in atoms or of atoms in molecules is caused by electromagnetism and the energy production in stars occurs through nuclear reactions induced by weak interactions. Only the gravitational force is not included in the SM. Nevertheless, compared to the others, the gravitational force is so weak that it can be safely neglected when dealing with elementary particles.

The elementary particles

Within the SM description, all visible matter in the Universe is made up of elementary particles, fermions, with intrinsic angular momentum, the spin, equal to $1/2$. These known elementary fermions are described in terms of fields and are divided into two categories, *quarks* and *leptons*. They are distinguished by the fact that quarks participate in all interactions, whereas leptons do not participate in the strong interaction.

Quarks and leptons come in three generations or families with identical quantum numbers, apart from the flavour, and with increasing masses, according to the scheme in Table 1.1. Each generation includes one lepton, namely the electron, the muon and the tau (e^-, μ^-, τ^-), which carries one unit of elementary electric charge, and one uncharged lepton, called a neutrino (ν_e, ν_μ, ν_τ). Each quark generation consists of an up-type quark and a down-type quark. The up-type quarks are the up, the charm and the top quark (u, c, t), with electric charge $Q_u = +2/3\,e$, where e is the elementary electric charge. The down-type quarks are the down, the strange and the beauty quark (d, s, b), with electric charge $Q_d = -1/3\,e$.

The masses and electric charges of quarks and leptons are given in Table 1.2. The corresponding antiparticles have the same mass but opposite quantum numbers.

Table 1.2: *Measured mass [14] and electric charge of fermions. The electric charge is given in units of the elementary charge e.*

Fermions (Spin ¹/₂)

		Quarks			Leptons	
Generation	Type	Mass	El. Charge	Type	Mass	El. Charge
1st	u	$2.3\,\mathrm{MeV}/c^2$	2/3	ν_e	$< 2\,\mathrm{eV}/c^2$	0
	d	$4.8\,\mathrm{MeV}/c^2$	-1/3	e^-	$511.0\,\mathrm{keV}/c^2$	-1
2nd	c	$1.275\,\mathrm{GeV}/c^2$	2/3	ν_μ	$< 190\,\mathrm{keV}/c^2$	0
	s	$95\,\mathrm{MeV}/c^2$	-1/3	μ^-	$105.7\,\mathrm{MeV}/c^2$	-1
3rd	t	$173.5\,\mathrm{GeV}/c^2$	2/3	ν_τ	$< 18.2\,\mathrm{MeV}/c^2$	0
	b	$4.18\,\mathrm{GeV}/c^2$	-1/3	τ^-	$1.78\,\mathrm{GeV}/c^2$	-1

The fundamental interactions

The SM has the structure of a gauge theory, with the SM Lagrangian being invariant under local transformations of the symmetry group

$$SU(3)_C \otimes SU(2)_L \otimes U(1)_Y \ ,$$

where the subscripts C, L and Y denote colour, left-handed chirality and weak hypercharge, respectively. The gauge group uniquely determines the interactions and the number of vector gauge bosons, which correspond to the generators of the group (see Table 1.3). All the gauge bosons have spin 1.

Quantum Chromodynamics The $SU(3)_C$ is the symmetry group of *quantum chromodynamics (QCD)*, the theory that describes strong interactions. The QCD charge is the so-called colour charge. It can take the quantum numbers red, green and blue, as well as the corresponding anti-colours. There are eight massless coloured gluons, g, which correspond to the eight generators of $SU(3)_C$. Gluons couple to quarks and to themselves via their colour charges. Due to the self-interaction of gluons the strong force has a very short range, even though gluons are massless.

The most remarkable properties of QCD are *confinement* and *asymptotic freedom*. Both features describe the fact that the effective coupling constant of QCD, α_s, which defines the strength of the interaction, is a function of the transferred four-momentum squared, Q^2, among the participants in the interaction. In particular, $\alpha_s(Q^2)$ decreases for increasing Q^2 and vanishes asymptotically. As a consequence, the QCD interactions become very weak in processes with large Q^2 and quarks are quasi-free. This property is the so-called asymptotic freedom. On the contrary, at large distances or small transferred momenta, the coupling becomes strong, leading to non–perturbative phenomena. The impossibility of separating colour charges, like individual quarks and gluons, is called confinement. Only neutral colour objects can be observed, so-called hadrons, where quark and gluons are confined on a length scale $R_{\mathrm{had}} \sim \hbar c/\Lambda_{\mathrm{QCD}} \sim 1\,\mathrm{fm}$.

Table 1.3: *Fundamental interactions of the SM and their mediator particles [14].*

Exchange bosons (spin 1)

Interaction	Mediator type	Mediator mass	Relative Strength
Strong	g (8)	0	1
Electromagnetic	γ	0	10^{-2}
Weak	Z^0	$91.2\,\mathrm{GeV}/c^2$	10^{-7}
	$W^\pm$	$80.4\,\mathrm{GeV}/c^2$	

Traditionally, hadrons can be subdivided into two groups: *mesons*, consisting of a quark-antiquark pair and *baryons*, containing three quarks. However, the existence of the $Z(4430)$ resonance, which has a minimal content of four quarks (two quarks and two antiquarks), has been confirmed [15] by the LHCb collaboration in 2014. This exotic state, called tetraquark, represents the first particle that unambiguously cannot be classified within the traditional quark model of mesons and baryons.

The value of $\Lambda_{\mathrm{QCD}} \sim 0.2$ GeV is the energy scale that separates the regions of large and small coupling constant, i.e. it is the scale where perturbative phenomena appear. If the mass of a quark is much larger than this scale, $m_q \gg \Lambda_{\mathrm{QCD}}$, the quark is considered *heavy*. The quarks of the SM fall naturally into two classes: up, down and strange are light quarks, whereas charm, beauty and top are heavy quarks. For heavy quarks, the effective coupling constant $\alpha_s(m_q)$ is small, implying that on length scales comparable to the Compton wavelength $\lambda_q \sim 1/m_q$ the strong interactions can be treated using perturbative methods. Different techniques used in order to make predictions for QCD processes are discussed in more detail in Section 1.6.3, with special emphasis on the theory used to make predictions about the lifetime of b hadrons.

Electroweak Theory   The $SU(2)_L \times U(1)_Y$ is the gauge group of the weak and electromagnetic interactions, which in the SM are unified into the *electroweak* (EW) interaction. The EW gauge boson fields corresponding to the three bosons of weak isospin from $SU(2)$ and the boson of weak hypercharge from $U(1)$ are W_i^μ ($i = 1, 2, 3$) and B^μ, respectively. These bosons are all massless. The charges to which the EW gauge bosons couple are the weak isospin, T, with third component, T_3, and the hypercharge, $Y = 2(Q - T_3)$, with the electric charge Q.

The fermionic fields are divided into doublets of one up-type and the corresponding down-type quark, which carry weak isospin (left-handed)

$$\begin{pmatrix} u \\ d \end{pmatrix}, \; \begin{pmatrix} c \\ s \end{pmatrix}, \; \begin{pmatrix} t \\ b \end{pmatrix} \, .$$

Similar doublets exist for charged leptons and the corresponding neutrinos

$$\begin{pmatrix} \nu_e \\ e^- \end{pmatrix}, \; \begin{pmatrix} \nu_\mu \\ \mu^- \end{pmatrix}, \; \begin{pmatrix} \nu_\tau \\ \tau^- \end{pmatrix} \, .$$

Singlets, which have weak isospin T = 0, exist as well (right-handed) for all particles except neutrinos. For antiparticles the right-handed fields are weak isospin doublets and the left-handed fields are the singlets.

The W_i^μ boson fields only couple to the left-handed particle and right-handed antiparticle doublets of the weak isospin. The B^μ boson field couples to particles carrying hypercharge independently of the weak isospin.

In the SM, for energies below the electroweak scale, the electroweak $SU(2)_L \times U(1)_Y$ symmetry group is spontaneously broken to the electromagnetic $U(1)_Q$ symmetry group. This spontaneous symmetry breaking of the electroweak gauge symmetry is induced by the so-called *Higgs mechanism*. One result of this mechanism is that the fields corresponding to the physical mediators of the weak and electromagnetic force are not the W_i^μ and the B^μ boson fields, but linear combinations of them. The *electromagnetic interaction* is mediated via the photon, γ, whose field is a linear combination of the W_3^μ and the B^μ boson fields. The photon is massless and it is characterized by equal couplings to the left- and right-handed fermions, with a strength equal to the electric charge. The *weak interaction* is divided into the so-called charged and neutral currents. The *neutral current* of the weak interaction is mediated by the Z^0 boson. Its field is, like the photon, a linear combination of the W_3^μ and the B^μ boson fields. The Z^0 boson can couple to any SM particle, except gluons and photons. The *charged current* of the weak interaction is mediated by the $W^\pm$ bosons, whose fields are linear combinations of the W_1^μ and W_2^μ boson fields. Charged currents allow transitions between up- and down-type quarks as well as transitions between charged and neutral leptons. Since the mediators of the weak interaction are quite massive (see Table 1.3), they are responsible for rather short ranged interactions.

A priory, particles in the SM are massless. However, the bosons of the weak interaction, the $W^\pm$ and the Z^0 bosons, are massive, as a consequence of the Higgs mechanism. The mechanism predicts a massive spin-0 particle, the so-called Higgs boson, H, finally discovered in 2012 by the ATLAS [10] and CMS [11] experiments. The Higgs mechanism also generates fermion masses via the Yukawa terms in the Lagrangian. Yukawa interactions are responsible for a complex phenomenology. They underpin not only a spectrum of elementary matter particles spanning many orders of magnitude in mass (see Table 1.2), but also the quark mixing, which is discussed in more detail in Section 1.3. Another important phenomenon is the breakdown of the *CP* symmetry, which is introduced in next section, together with other important discrete symmetries in the SM.

1.2 Symmetries in particle physics

One of the most fundamental principle in physics is that of symmetry. A symmetry operation leaves (at least conceptually) a system invariant.

In particle physics, the discrete symmetries with a significant relevance are

- **Charge conjugation**, C: It changes the sign of all internal quantum charges, like the sign of the electric charge of a particle.

- **Parity**, P: It is a reflection operator that changes the sign of all three spatial coordinates. For example, under this operation the momentum, $\overrightarrow{p}$, of a particle changes its sign, $-\overrightarrow{p}$.

- **Time reversal**, T: It reverses the time coordinate $(t \mapsto -t)$.

Each of these three discrete symmetries is broken in weak interactions. These broken symmetries are found to be important, as the search for reasons and consequences of a violated symmetry opens the way to physics beyond the generally accepted theories, usually referred to as new physics.

Although these symmetries are broken, the CPT theorem states that in relativistic quantum field theories, all interactions are invariant under the combined transformations of C, P and T. The theorem is based on very general assumptions and it is not easy to circumvent. However, in view of the fact that many symmetries which were thought to be good turned out experimentally not to be conserved (such as the combination of C and P operators, known as CP symmetry, see Section 1.4.3), it is desirable to determine experimentally whether the CPT theorem is violated. For this one needs to focus the attention on the consequences of the CPT theorem and see to what extend they hold. For example, particles and antiparticles, according to the CPT theorem, must have the same mass and lifetime. The magnetic moments, μ, have to be the same in magnitude but have opposite sign. These equalities are well established experimentally [14]

$$[m_{e^+} - m_{e^-}]/m_e^{\text{average}} < 8 \cdot 10^{-9}, CL = 90\% \,, \tag{1.1}$$

$$\left[\tau_{\mu^+} - \tau_{\mu^-}\right]/\tau_\mu^{\text{average}} = (2 \pm 8) \cdot 10^{-5} \,, \tag{1.2}$$

$$[|\mu_{e^+}| - |\mu_{e^-}|]/|\mu_e|^{\text{average}} = (-0.5 \pm 2.1) \cdot 10^{-12} \,. \tag{1.3}$$

Nevertheless, it is important to continue to question the validity of this fundamental theorem performing different measurements.

1.3 Quark flavour physics

In the following section charged and neutral weak currents, introduced in Section 1.1, are described in detail. In particular, beauty decays and the process of mixing of neutral B mesons are discussed, since they are relevant for the analysis presented in this thesis.

1.3.1 Charged currents and CKM matrix

In the SM quarks and leptons acquire mass through the so-called Yukawa terms in the Lagrangian. For the quark fields this can be written as[2]

$$\mathcal{L}^{\text{quarks}} = -\frac{v}{\sqrt{2}} \left(\bar{d}'_L Y_d d'_R + \bar{u}'_L Y_u u'_R \right) + \text{h.c.} \,, \tag{1.4}$$

where left-handed quarks, q'_L, are coupled to right-handed ones, q'_R, (q' here stands for the weak eigenstates of an up-type, u', or a down-type, d', quark), together with the

---

[2]The leptonic part of the Lagrangian will be neglected in the following since it is not relevant for all processes discussed in this analysis
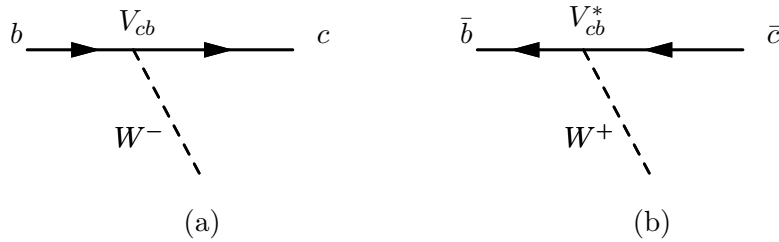
Figure 1.1: Feynman diagram of (a) $b \to c$ transition and (b) $\bar{b} \to \bar{c}$ transition.

Higgs boson in a gauge invariant way. Here the Higgs field is represented by the vacuum expectation value of the Higgs potential, v. The Yukawa matrices, Y_d and Y_u, are 3×3 complex matrices, with non-zero diagonal elements. This results in the weak eigenstates not being identical to the physical mass eigenstates, u and d. The latter are obtained from the previously mentioned weak eigenstates, u' and d', by a unitary transformation, $q'_A = V_{A,q}\, q_A$ for $q = u', d'$ and $A = L, R$. The unitary matrices $V_{A,q}$ are determined by requiring that they diagonalise the Yukawa matrices as follows

$$M_u = \frac{v}{\sqrt{2}}\, V_{L,u}\, Y_u\, V^\dagger_{R,u} \quad \text{and} \quad M_d = \frac{v}{\sqrt{2}}\, V_{L,d}\, Y_d\, V^\dagger_{R,d}\,. \tag{1.5}$$

The quark masses, M_q, appear then in the SM Lagrangian as Dirac mass terms

$$\mathcal{L}^{\text{quarks}} = -\,\bar{d}_L\, M_d\, d_R - \bar{u}_L\, M_u\, u_R + \text{h.c.}\,. \tag{1.6}$$

These transformations leave all parts of the SM Lagrangian unchanged except for the term describing the charged current of the weak interaction, since it is the only interaction combining up-type with down-type quarks

$$\mathcal{L}_{cc} = -\frac{g_2}{\sqrt{2}} \left(\bar{u}'_L\, \gamma^\mu\, W^+_\mu\, (1 - \gamma^5)\, d'_L \;+\; \bar{d}'_L\, \gamma^\mu\, W^-_\mu\, (1 - \gamma^5)\, u'_L \right), \tag{1.7}$$

where g_2 is the $SU(2)_L$ coupling constant. As the up-type and down-type Yukawa matrices cannot be diagonalised simultaneously, that is, by the same unitary transformation, $V_{A,d} \neq V_{A,u}$, the transformation from the weak eigenstates to the mass eigenstates leaves one net effect in Equation 1.7. This is the Cabibbo-Kobayashi-Maskawa (CKM) quark mixing matrix, $V_{\text{CKM}} = V_{L,u} V^\dagger_{L,d}$, which appears in the charged current Lagrangian

$$\mathcal{L}_{cc} = -\frac{g_2}{\sqrt{2}} \left(\bar{u}_L\, \gamma^\mu\, W^+_\mu\, (1 - \gamma^5)\, V_{\text{CKM}}\, d_L \;+\; \bar{d}_L\, \gamma^\mu\, W^-_\mu\, (1 - \gamma^5)\, V^\dagger_{\text{CKM}}\, u_L \right). \tag{1.8}$$

Writing explicitly the CKM matrix, it reads

$$V_{\text{CKM}} = \begin{pmatrix} V_{ud} & V_{us} & V_{ub} \\ V_{cd} & V_{cs} & V_{cb} \\ V_{td} & V_{ts} & V_{tb} \end{pmatrix}. \tag{1.9}$$

For a non-trivial CKM matrix, as realised in nature, the weak interaction allows for transitions between different generations of quarks through charged current interactions. As an example, the Feynman diagram for a $b \to c$ transition is shown in Figure 1.1. Feynman diagrams are pictorial representations of the calculation rules to obtain the transition matrix element of fundamental processes. The transition matrix element of

a $b \rightarrow c$ transition is proportional to the corresponding matrix element V_{cb}, while the matrix element of a $\overline{b} \rightarrow \overline{c}$ quark transition is proportional to its complex conjugate, V_{cb}^*.

The CKM matrix has four free parameters, three amplitudes and one phase. The presence of a phase in the CKM matrix breaks the CP symmetry. Phenomenologically, the CKM matrix is hierarchical, $V_{ud} < V_{cs} < V_{tb} \sim 1$, with smaller contributions outside the diagonal. A useful parameterisation emphasizing the hierarchy is given by Wolfenstein [16]

$$
V_{\text{CKM}} = \begin{pmatrix} 1 - \frac{1}{2}\lambda^2 & \lambda & A\lambda^3(\rho - i\eta) \\ -\lambda & 1 - \frac{1}{2}\lambda^2 & A\lambda^2 \\ A\lambda^3(1 - \rho - i\eta) & -A\lambda^2 & 1 \end{pmatrix} + \mathcal{O}(\lambda^4) \, . \tag{1.10}
$$

The expansion parameter λ is roughly 0.23. The other parameters of the Wolfenstein parameterisation are between 0.1 and 1, they do not change the order of magnitude of the elements. The observed structure of the CKM matrix shows that quark transitions within the same generation (diagonal elements) are preferred, since they are of $\mathcal{O} \sim 1$, and the further one goes away from the diagonal, the stronger is the suppression. The matrix elements describing transitions between the first two generations are suppressed by a factor λ, between the second and third generation by λ^2 and between the first and third generation by λ^3. Up to λ^3 terms, the only elements with a complex component, which is responsible for CP violation in the SM, are V_{ub} and V_{td}.

1.3.2   Flavour changing neutral currents

In the SM, neutral current interactions conserve flavour. However through quantum loops, charged currents can induce flavour-changing neutral current (FCNC) processes, which involve different flavours with the same electric charge.

Relevant for this thesis is the phenomenon of neutral B meson mixing. The neutral K^0, D^0, B_d and B_s^0 mesons are the only ones that oscillate into their antiparticles. These meson states are flavour eigenstates and the corresponding $\overline{K}^0$, $\overline{D}^0$, $\overline{B}_d^0$ and $\overline{B}_s^0$ have opposite flavour quantum numbers

$$
\begin{aligned}
K^0 &= \overline{s}d, & D^0 &= c\overline{u}, & B_d^0 &= \overline{b}d, & B_s^0 &= \overline{b}s \, , \\
\overline{K}^0 &= s\overline{d}, & \overline{D}^0 &= \overline{c}u, & \overline{B}_d^0 &= b\overline{d}, & \overline{B}_s^0 &= b\overline{s} \, .
\end{aligned}
$$

As an example, the Feynman diagrams of the SM contributions to $B^0 - \overline{B}^0$ and $B_s^0 - \overline{B}_s^0$ mixing are shown in Figure 1.2 (a) and (b), respectively. The internal quark contribution is dominated by the top quark, so the only difference among $B^0 - \overline{B}^0$ and $B_s^0 - \overline{B}_s^0$ mixing is the difference in CKM suppression: The amplitude of the latter is proportional to V_{ts}^2 instead of V_{td}^2 (a factor of λ less, see Equation 1.10). Due to less suppression, the mixing is much faster for B_s^0 mesons, as is quantitatively shown in Section 1.4.2.

1.4   Production and decay of b hadrons

In the following the production, hadronisation and decay of b hadrons is discussed from a phenomenological point of view. First, particle production in proton-proton
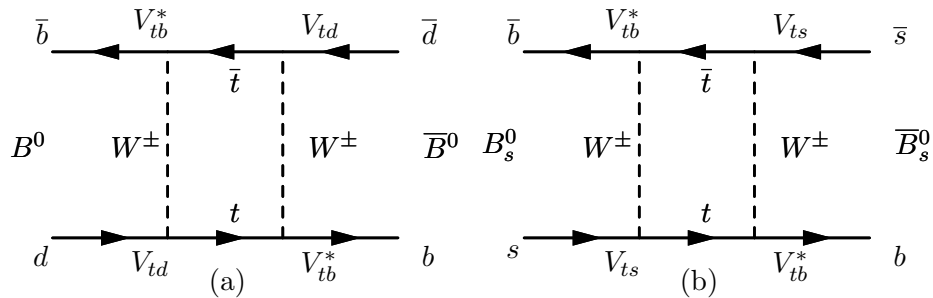
Figure 1.2: The lowest order SM contribution to (a) $B^0 - \overline{B}^0$ and (b) $B_s^0 - \overline{B}_s^0$ mixing. Diagrams with internal quarks swapped with the W are also possible.

Table 1.4: The measured b hadron production fractions at the LHC at $\sqrt{s} = 7$ TeV [2].

b hadron fraction	value
B^+ or B^0, $f_u = f_d$	0.402 ± 0.007
B_s^0, f_s	0.105 ± 0.006
b baryons, f_{baryon}	0.092 ± 0.015

collisions is addressed. In particular, differences in the production rate of mesons and the corresponding anti-mesons are examined. Second, the phenomenology of mixing, introduced in Section 1.3.2, is revisited with the focus on neutral B mesons. Third, the decays of b hadrons are analysed, with particular emphasis on the decay channels relevant for this work.[3]

1.4.1 Production of b hadrons at the Large Hadron Collider

The Large Hadron Collider, LHC, will be explained in more detail in Section 2.1. It collides two beams of protons, with a centre-of-mass energy, $\sqrt{s}$, of 7 TeV in 2011. A proton is a composite object built out of three valence quarks, two up quarks and one down quark, sea quarks and gluons. All its constituents interact via strong interaction. In the proton-proton, pp, collisions at the LHC, heavy quarks are produced as $q\bar{q}$ pairs, as a consequence of the flavour conservation of strong interaction. The leading order processes for the production of a heavy quark, like the b quark, are flavour creation, i.e., quark-antiquark annihilation, $q\bar{q} \to b\bar{b}$, and gluon-gluon fusion, $gg \to b\bar{b}$. A $b\bar{b}$ pair has an invariant mass of about $10\,\text{GeV}/c^2$, so the $b\bar{b}$ production threshold is small compared to the centre-of-mass energy, which has a typical value of $Q^2 = 10^4$ GeV^2 for hadron colliders like the LHC. Looking at the parton distribution function of the proton at the corresponding scale of $Q^2 = 10^4$ GeV^2 in Figure 1.3, it is clear that for low values of the Bjørken x the gluons are the dominant component inside the proton. Thus, the $b\bar{b}$ pair is mainly produced by gluon-gluon fusion processes. When two protons collide, it is very likely that the two gluons carry different momenta. This results in the $b\bar{b}$ pair being highly boosted in the forward or backward direction along the beam line. Figure 1.4 shows the polar angle distribution for the b and $\bar{b}$ quarks produced in proton-proton interactions at the LHC. It can be seen that they are mostly produced in the same direction close to the beam line.

---

[3]The presented summary is based on Ref. [9, 17].
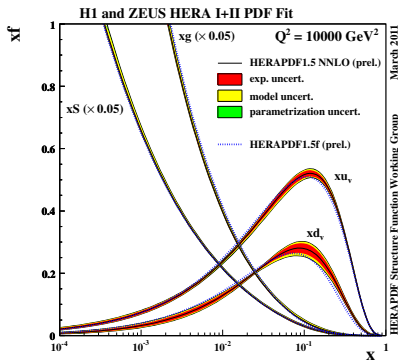
Figure 1.3: The proton parton distribution functions for valence u and d quarks, gluons and sea quarks from HERAPDF1.5 [18] at $Q^2 = 10^4\,\text{GeV}^2$, a region relevant for the LHC. The gluon and sea distributions are scaled down by a factor of 20.
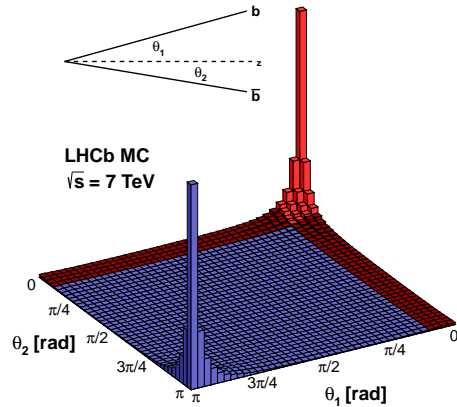
Figure 1.4: Polar angle distribution of b and $\bar{b}$ quarks in pp collisions at $\sqrt{s} = 7\,\text{TeV}$. The beam line is the z-axis, the red region indicates the LHCb acceptance. Figure taken from Ref. [19].

The b quarks then hadronise to form a bound state, the hadron. During the hadronisation the b quark combines with one or two lighter (anti)quarks (u, d, s or c) to create a meson or a baryon, respectively. The lighter quarks come from the proton remnants or the fragmentation process of the initial interaction. The measured fractions of hadronisations of a b quark to B^+ ($\bar{b}u$), B^0, B_s^0 mesons and b baryons are shown in Table 1.4, where the contribution from the B_c^+ ($\bar{b}c$) meson production is neglected. It is usually assumed that the same amount of B^+ and B^0 mesons is produced due to the so-called isospin symmetry among the u and the d quark.

The $b\bar{b}$ cross-section for inelastic pp collisions at a centre-of-mass energy of 7 TeV has been measured by LHCb to be [20]

$$\sigma_{b\bar{b}} = \sigma(pp \to b\bar{b}X) = (288 \pm 4 \pm 48)\mu\text{b}\,, \qquad (1.11)$$

using J/ψ mesons from b-hadron decays.

Production asymmetries of B mesons

In the previous section it was explained that heavy quarks are predominantly produced in quark-antiquark pairs. So, one does not expect a different number of B mesons with respect to the number of anti-B mesons. On the other hand, the LHC is colliding two proton beams. We expect an overall excess in the production of baryons to anti-baryons and an overall charge asymmetry, as QCD is baryon-number conserving. Moreover, since in the initial state there is an excess of u and d quarks with respect to their antipartners, one would expect produced particles with these constituents to be asymmetric. Such a mechanism is responsible for an excess of B^0 ($\bar{b}d$) or B^+ ($\bar{b}u$) with respect to $\bar{B}^0$ ($b\bar{d}$) or B^- ($b\bar{u}$) mesons. One expects the ratios $N(B^+)/N(B^-)$ and $N(B^0)/N(\bar{B}^0)$ to be greater than one, with N the number of produced mesons.

As these mechanisms effect the availability of certain quark species they even produce an asymmetry in species which are unable to directly accept a beam remnant. Since $\bar{b}$ quarks can produce B^+ or B^0 with the remnants from the protons, there are more b quarks that can hadronise with an $\bar{s}$ quark from the vacuum than $\bar{b}$ quarks that can hadronise with an s quark. For this reason one expects the ratio $N(B_s^0)/N(\bar{B}_s^0)$ to be smaller than one.

However, even if the leading mechanisms responsible for asymmetries in the production of B mesons have been identified, it is not straightforward to translate these effects into numerical predictions of production asymmetries of heavy mesons. The production asymmetry of B mesons is defined as

$$A_P(\bar{B}) \equiv \frac{\mathcal{P}(\bar{B}) - \mathcal{P}(B)}{\mathcal{P}(\bar{B}) + \mathcal{P}(B)} \; , \tag{1.12}$$

where $\mathcal{P}(\bar{B})$ and $\mathcal{P}(B)$ are the probabilities to produce a $\bar{B}$ and B meson[4], respectively. Production asymmetries with an absolute value of the order $\mathcal{O}(0.1\% - 1\%)$ are expected within the LHCb detector acceptance. The measured values are $A_P(B^+) = (-0.3 \pm 0.9)\%$ [21], $A_P(B_s^0) = (4 \pm 8)\%$ [22] and $A_P(B^0) = (0.1 \pm 1.0)\%$ [22].

1.4.2 Neutral meson mixing phenomenology

In the SM, the $B_q^0 - \bar{B}_q^0$ mixing, with $q = (d, s)$, is caused by flavour changing weak processes described at the lowest order by the box diagrams in Figure 1.2. An initial B_q^0 evolves in time into a superposition of B_q^0 and $\bar{B}_q^0$. The time evolution, $B_q^0(t)\,(\bar{B}_q^0(t))$, of an initially produced $B_q^0\,(\bar{B}_q^0)$ can be described by an effective Schrödinger equation[5]

$$i\frac{\mathrm{d}}{\mathrm{d}t}\left(\begin{vmatrix}B_q^0(t)\rangle \\ \bar{B}_q^0(t)\rangle\end{vmatrix}\right) = \mathcal{H}\left(\begin{vmatrix}B_q^0(t)\rangle \\ \bar{B}_q^0(t)\rangle\end{vmatrix}\right) , \tag{1.13}$$

$$\text{where} \quad \mathcal{H} = \left(\boldsymbol{M} - \frac{i}{2}\boldsymbol{\Gamma}\right) = \left(\begin{pmatrix}M_{11} & M_{12} \\ M_{12}^* & M_{22}\end{pmatrix} - \frac{i}{2}\begin{pmatrix}\Gamma_{11} & \Gamma_{12} \\ \Gamma_{12}^* & \Gamma_{22}\end{pmatrix}\right) ,$$

and $\boldsymbol{M} = \boldsymbol{M}^\dagger$ and $\boldsymbol{\Gamma} = \boldsymbol{\Gamma}^\dagger$. The matrix $\boldsymbol{M}$ is called the mass matrix and $\boldsymbol{\Gamma}$ the decay matrix. The diagonal elements M_{11} and M_{22} are the meson-antimeson masses, m_q and $\overline{m}_q$, that are generated from the quark mass terms in the Lagrangian in Equation 1.4 and from the binding energy of the strong interaction. The diagonal elements Γ_{11} and Γ_{22} are the meson-antimeson decay widths (the inverse of the lifetimes), Γ_q and $\bar{\Gamma}_q$, coming from the weak interaction. CPT symmetry requires that the diagonal elements are equal: $m_q = M_{11} = M_{22}$ and $\Gamma_q = \Gamma_{11} = \Gamma_{22}$. In case of mixing, the off-diagonal elements M_{12} and Γ_{12} are non-zero. The off-diagonal elements of the mass matrix $\boldsymbol{M}$ are related to the box diagrams shown in Figure 1.2. The off-diagonal elements of the decay matrix $\boldsymbol{\Gamma}$ originate from weak decays common to the states B_q^0 and $\bar{B}_q^0$. As a consequence of these off-diagonal elements, the flavour states, $\left|B_q^0\right\rangle$ and $\left|\bar{B}_q^0\right\rangle$, in which the neutral B mesons are produced are not mass eigenstates.

---

[4]Here B ($\bar{B}$) refers to B^0, B_s^0 and B^+ ($\bar{B}^0$, $\bar{B}_s^0$ and B^-).
[5]The convention $\hbar = c = 1$ is used here to simplify the formulae.

The mass eigenstates, $\left|B_{H/L}\right\rangle$, are defined as the eigenvectors of the Hamiltonian in Equation 1.13. They are obtained diagonalising the $\mathcal{H}$ matrix and can be expressed as a linear combination of the flavour states

$$
\begin{aligned}
\left|B_H\right\rangle &\propto p\left|B_q^0\right\rangle + q\left|\overline{B}_q^0\right\rangle \quad , \\
\left|B_L\right\rangle &\propto p\left|B_q^0\right\rangle - q\left|\overline{B}_q^0\right\rangle \quad ,
\end{aligned}
\tag{1.14}
$$

where p and q are complex parameters with the normalisation requirement $|p|^2+|q|^2= 1$. The time evolution of the mass states is given by

$$
\left|B_{H/L}(t)\right\rangle \;=\; e^{-iM_{H/L}\,t}\,e^{-\Gamma_{H/L}\,t/2}\left|B_{H/L}\right\rangle \quad ,
\tag{1.15}
$$

where $M_{H/L}$ denotes the mass and $\Gamma_{H/L}$ the width (the inverse of the lifetime, τ) of the heavy and light mass eigenstates, respectively. They follow the relations:

$$
\begin{aligned}
m_q &= \frac{M_H + M_L}{2}, & \Gamma_q &= \frac{\Gamma_L + \Gamma_H}{2} \equiv \frac{1}{\tau}, \\
\Delta m_q &= M_H - M_L, & \Delta\Gamma_q &= \Gamma_L - \Gamma_H.
\end{aligned}
\tag{1.16}
$$

The mass difference Δm_q is always chosen to be positive, while $\Delta\Gamma_q$ can have both signs. The mass eigenstates obey a simple exponential decay time distribution, with a lifetime $\tau_{L/H} = 1/\Gamma_{L,H}$.

The time evolution of a B meson produced in a pure flavour state

$$
\begin{aligned}
\left|B_q^0(t)\right\rangle &\propto \frac{1}{2p}\left(\left|B_L(t)\right\rangle + \left|B_H(t)\right\rangle\right) \quad , \\
\left|\overline{B}_q^0(t)\right\rangle &\propto \frac{1}{2q}\left(\left|B_L(t)\right\rangle - \left|B_H(t)\right\rangle\right) \quad ,
\end{aligned}
\tag{1.17}
$$

can be obtained by combining Equations 1.14 and 1.15:

$$
\left|B_q^0(t)\right\rangle = \quad g_+(t)\left|B_q^0\right\rangle + \frac{q}{p}\,g_-(t)\left|\overline{B}_q^0\right\rangle \quad ,
\tag{1.18}
$$

$$
\left|\overline{B}_q^0(t)\right\rangle = \frac{p}{q}\,g_-(t)\left|B_q^0\right\rangle + \quad g_+(t)\left|\overline{B}_q^0\right\rangle \quad ,
\tag{1.19}
$$

where the functions $g_+(t)$ and $g_-(t)$ are given by

$$
g_+(t) = e^{-im_q t}\,e^{-\Gamma_q t/2}\left[\quad \cosh\frac{\Delta\Gamma_q\,t}{4}\cos\frac{\Delta m_q\,t}{2} - i\sinh\frac{\Delta\Gamma_q\,t}{4}\sin\frac{\Delta m_q\,t}{2}\right] , \tag{1.20}
$$

$$
g_-(t) = e^{-im_q t}\,e^{-\Gamma_q t/2}\left[-\sinh\frac{\Delta\Gamma_q\,t}{4}\cos\frac{\Delta m_q\,t}{2} + i\cosh\frac{\Delta\Gamma_q\,t}{4}\sin\frac{\Delta m_q\,t}{2}\right] . \tag{1.21}
$$

Table 1.5 summarises the mixing parameters of B^0 and B_s^0 mesons. The oscillation frequency of B^0 mesons is comparable to their lifetime, $\Delta m_d/\Gamma_d \approx 0.77$, while B_s^0 mesons oscillate many times before they decay, $\Delta m_s/\Gamma_s \approx 27$. The width difference $\Delta\Gamma_d$ is basically zero for B^0 mesons. Consequently the lifetime corresponding to the heavy and light mass eigenstate in the B_d system are the same ($y_d \equiv \Delta\Gamma_d/2\Gamma_d \approx 0$). On the contrary, due to the sizeable magnitude of $\Delta\Gamma_s$, the difference between the lifetime of the two mass eigenstates in the B_s^0 system is almost 200 fs, which is around 15% of the lifetime itself ($y_s \equiv \Delta\Gamma_s/2\Gamma_s \approx 0.07$).

Table 1.5: The mixing parameters of B^0 and B^0_s mesons [2].

Meson	Mass	Lifetime
B^0	$m = (5279.58 \pm 0.17)\,\mathrm{MeV}/c^2$ $\Delta m_d = (0.510 \pm 0.004) \times 10^{12}\hbar\,\mathrm{s}^{-1}$	$\tau = (1.519 \pm 0.007) \times 10^{-12}\,\mathrm{s}$ $\Delta\Gamma_d \approx 0$
B^0_s	$m = (5366.77 \pm 0.24)\,\mathrm{MeV}/c^2$ $\Delta m_s = (17.69 \pm 0.08) \times 10^{12}\hbar\,\mathrm{s}^{-1}$	$\tau = (1.516 \pm 0.011) \times 10^{-12}\,\mathrm{s}$ $\Delta\Gamma_s = (0.081 \pm 0.011) \times 10^{12}\,\mathrm{s}^{-1}$

1.4.3 CP violation

In Section 1.3.1 the mechanism of CP violation has been introduced. There are three categories of CP violation which are introduced in the following in order to better understand the formulae derived in the next section. They are described for B mesons, but are generally valid.

1. **CP violation in decay**, also known as direct CP violation. It can occur both in charged and neutral meson decays when the amplitude for a decay and its CP conjugate decay have different magnitudes. If A_f and $\overline{A}_{\overline{f}}$ are the amplitudes for the process $B \to f$ and $\overline{B} \to \overline{f}$, respectively, where f and $\overline{f}$ are CP-conjugate multi-particle final states, direct CP violation occurs if

$$\left| \frac{A_f}{\overline{A}_{\overline{f}}} \right| \neq 1 \,.$$

2. **CP violation in mixing**. It is possible only for neutral mesons which exhibit the phenomenon of mixing. It is defined as

$$|q/p| \neq 1 \,. \tag{1.22}$$

It occurs if the amplitude of the process, $B^0_{d,s} \to \overline{B}^0_{d,s}$ is different with respect to the opposite process $\overline{B}^0_{d,s} \to B^0_{d,s}$. It does not depend on the final state.

3. **CP violation in the interference between mixing and decay**. If there is a final state, f, common to $B^0_{d,s}$ and $\overline{B}^0_{d,s}$ the neutral meson can either decay to the final state directly or first oscillate and then decay. This gives rise to CP violation in the interference between mixing and decay. It occurs if

$$\mathcal{I}m(\lambda_f) \;=\; \mathcal{I}m\left(\frac{q}{p} \frac{\overline{A}_f}{A_f} \right) \neq 0 \,, \tag{1.23}$$

where λ_f is a parameter that quantifies this kind of CP violation. The requirement that the final state is common to $B^0_{d,s}$ and $\overline{B}^0_{d,s}$ is automatically fulfilled if the final state is a CP eigenstate, $|f_{CP}\rangle$

$$CP\,|f_{CP}\rangle = \eta^{CP}_f\,|f_{CP}\rangle \ \text{with}\ \eta_{CP} = \pm 1 \ \,. \tag{1.24}$$

1.4.4   Weak decay of b hadrons

In this section the weak decay of b hadrons will be summarised. According to the structure of the charged-current interaction, weak decays of hadrons can be divided into three classes: leptonic decays, in which the quarks of the decaying hadron annihilate each other and only leptons appear in the final state; semileptonic decays, in which both leptons and hadrons appear in the final state; and hadronic decays, in which the final state consists of hadrons only. In this thesis, only hadronic decays of b hadrons are analysed. The majority of b decays have a c hadron in the final state because transitions between the third and the first generation are suppressed by an additional factor of λ. In this thesis the decays of interest are decays with a J/ψ meson, composed of a $c\bar{c}$, in the final state. Namely, the relevant decays are: $B^+ \to J/\psi K^+$, $B^0 \to J/\psi K^*(892)^0$, $B^0 \to J/\psi K_S^0$, $B_s^0 \to J/\psi \phi$ and $\Lambda_b^0 \to J/\psi \Lambda$. Collectively, these are referred to as $H_b \to J/\psi X$ decays.

The decay amplitude of a b hadron, H_b or $\overline{H}_b$, to a final state f and its CP conjugate $\bar{f}$ can be written as

$$A_f = \langle f | \mathcal{H}_w | H_b \rangle \qquad \text{and} \qquad \overline{A}_f = \langle f | \mathcal{H}_w | \overline{H}_b \rangle , \qquad (1.25)$$

$$A_{\bar{f}} = \langle \bar{f} | \mathcal{H}_w | H_b \rangle \qquad \text{and} \qquad \overline{A}_{\bar{f}} = \langle \bar{f} | \mathcal{H}_w | \overline{H}_b \rangle . \qquad (1.26)$$

Here, $\mathcal{H}_w$ denotes the Hamiltonian operator of the weak interaction.

The time-dependent decay rate $\Gamma(H_b(t) \to f)$ of a b hadron into some final state f is defined as [23]

$$\Gamma(H_b(t) \to f) \quad = \quad \frac{1}{N_{H_b}} \frac{dN(H_b(t) \to f)}{dt} , \qquad (1.27)$$

where N_{H_b} is the total number of H_b's produced at time $t = 0$. An analogous definition holds for $\Gamma(\overline{H}_b(t) \to f)$ and substituting f with $\bar{f}$.

Since charged B mesons do not oscillate, only transitions as $B^+ \to f$ and $B^- \to \bar{f}$ are allowed (similarly for the Λ_b^0 baryons). The time-dependent decay rate becomes

$$\Gamma(B^+(t) \to f) \quad = \quad \mathcal{N}_f |A_f|^2 e^{-\Gamma_{B^+} t}, \qquad (1.28)$$

$$\Gamma(B^-(t) \to \bar{f}) \quad = \quad \mathcal{N}_f |\overline{A}_{\bar{f}}|^2 e^{-\Gamma_{B^-} t}, \qquad (1.29)$$

where $\mathcal{N}_f$ is a time-independent normalisation factor. Similar formulae apply for Λ_b^0.

For neutral mesons the formulae become more complicated due to oscillations. By

making use of Equation 1.18 - 1.21, one finds the general expression for the decay rates:

$$\Gamma(B_q(t) \to f) = \mathcal{N}_f |A_f|^2 e^{-\Gamma_{B_q} t} \tag{1.30}$$
$$\times \left[\cosh \frac{\Delta\Gamma_q t}{2} + \mathcal{A}_{\text{CP}}^{\text{dir}} \cos(\Delta m_q t) + \mathcal{A}_{\Delta\Gamma} \sinh \frac{\Delta\Gamma_q t}{2} + \mathcal{A}_{\text{CP}}^{\text{mix}} \sin(\Delta m_q t) \right],$$

$$\Gamma(\overline{B}_q(t) \to f) = \mathcal{N}_f |A_f|^2 e^{-\Gamma_{B_q} t} \tag{1.31}$$
$$\times \left[\cosh \frac{\Delta\Gamma_q t}{2} - \mathcal{A}_{\text{CP}}^{\text{dir}} \cos(\Delta m_q t) + \mathcal{A}_{\Delta\Gamma} \sinh \frac{\Delta\Gamma_q t}{2} - \mathcal{A}_{\text{CP}}^{\text{mix}} \sin(\Delta m_q t) \right],$$

$$\Gamma(B_q(t) \to \overline{f}) = \mathcal{N}_f |A_{\overline{f}}|^2 e^{-\Gamma_{B_q} t} \tag{1.32}$$
$$\times \left[\cosh \frac{\Delta\Gamma_q t}{2} - \mathcal{A}_{\text{CP}}^{\text{dir}} \cos(\Delta m_q t) + \mathcal{A}_{\Delta\Gamma} \sinh \frac{\Delta\Gamma_q t}{2} - \mathcal{A}_{\text{CP}}^{\text{mix}} \sin(\Delta m_q t) \right],$$

$$\Gamma(\overline{B}_q(t) \to \overline{f}) = \mathcal{N}_f |\overline{A}_{\overline{f}}|^2 e^{-\Gamma_{B_q} t} \tag{1.33}$$
$$\times \left[\cosh \frac{\Delta\Gamma_q t}{2} + \mathcal{A}_{\text{CP}}^{\text{dir}} \cos(\Delta m_q t) + \mathcal{A}_{\Delta\Gamma} \sinh \frac{\Delta\Gamma_q t}{2} + \mathcal{A}_{\text{CP}}^{\text{mix}} \sin(\Delta m_q t) \right],$$

where

$$\mathcal{A}_{\text{CP}}^{\text{dir}} = \frac{1 - |\lambda_f|^2}{1 + |\lambda_f|^2}, \qquad \mathcal{A}_{\text{CP}}^{\text{mix}} = -\frac{2\, \text{Im}\, \lambda_f}{1 + |\lambda_f|^2} \quad \text{and} \quad \mathcal{A}_{\Delta\Gamma} = -\frac{2\, \text{Re}\, \lambda_f}{1 + |\lambda_f|^2}. \tag{1.34}$$

If f is a CP eigenstate (see Equation 1.24) then $\mathcal{A}_{\text{CP}}^{\text{dir}} \neq 0$ or $\mathcal{A}_{\text{CP}}^{\text{mix}} \neq 0$ signals CP violation: a non-vanishing $\mathcal{A}_{\text{CP}}^{\text{dir}}$ implies $|A_f| \neq |\overline{A}_f|$, meaning direct CP violation; $\mathcal{A}_{\text{CP}}^{\text{mix}}$ measures mixing-induced CP violation in the interference of $B_q \to f$ and $\overline{B}_q \to f$. The third quantity, $\mathcal{A}_{\Delta\Gamma}$, plays a role if $\Delta\Gamma_q$ is sizeable. The three quantities obey the relation

$$|\mathcal{A}_{\text{CP}}^{\text{dir}}|^2 + |\mathcal{A}_{\text{CP}}^{\text{mix}}|^2 + |\mathcal{A}_{\Delta\Gamma}|^2 = 1.$$

1.5 Lifetimes of b hadrons

The rich phenomenology of weak decays has always been a source of information about the nature of elementary particle interactions and properties. Lifetimes, in particular, are among the most fundamental properties of particles.

In this thesis measurements of the lifetime of three different mesons containing a b quark, namely the B^-, the B^0 and the B_s^0, as well as the lifetime of the Λ_b^0 baryon are presented.

In order to determine the lifetime, the time-dependent decay rate has to be determined from data. On average, b hadrons live longer time than other heavy particles. As the top quark has a mass of about 170 GeV/c^2, B mesons with a mass of about 5.3 GeV/c^2 cannot decay into a top quark. The transition with the largest amplitude is $b \to cW^-$, which is already suppressed by two orders of λ. This gives b hadrons a substantial lifetime. For example, the lifetime of a B^0 meson is (1.519 ± 0.007) ps [14].

The decay time of a particle can be found by locating the particle's decay vertex, DV, and measuring the spatial separation, L, from its production point in the laboratory
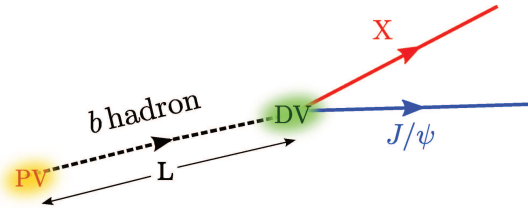
Figure 1.5: Sketch of the decay of a b hadron $H_b \to J/\psi X$. The b hadron is produced at the primary vertex PV and it decays at the decay vertex DV. The length L is the spatial separation between the two vertices.

frame as illustrated in Figure 1.5. Using the reconstructed three-momentum, $\vec{p}$, of the b-hadron, the decay time t is given by

$$t = L\,\frac{m}{|\vec{p}|} = \frac{Lc}{\beta\,\gamma}\,, \tag{1.35}$$

where m is its reconstructed invariant mass. It can also be expressed as a function of $\beta = v/c$ and $\gamma = 1/\sqrt{1-\beta^2}$, the usual relativistic quantities describing the Lorentz boost.

Note that the determination of the b-hadron momentum requires the reconstruction of all decay particles. Semileptonic H_b decays of b hadrons are advantageous because, due to their large branching fractions, the available number of decays is larger than using hadronic decays. However, the unmeasured neutrino is missing in the reconstruction of the H_b kinematics. While it is possible to correct for the missing momentum on average, the momentum resolution of a single event is significantly degraded. So, for precise lifetime measurements, hadronic decays are more suitable.

1.5.1 Effective lifetime

Whereas the decay width difference $\Delta\Gamma$ is negligibly small in the B^0 system, it is sizeable for B_s^0 mesons. Hence, the untagged[6] B_s^0 data sample contains both mass eigenstates, B_H and B_L, which have different lifetimes. When B_s^0 and $\overline{B}_s^0$ are produced in equal numbers, the untagged decay rate for the decay $B_s^0(\overline{B}_s^0) \to f$ is obtained by adding Equation 1.30 and Equation 1.31

$$
\begin{aligned}
\Gamma[f,t] &= \Gamma(B_s^0(t) \to f) + \Gamma(\overline{B}_s^0(t) \to f) \\
&= \mathcal{N}_f\left[e^{-\Gamma_L t}\,|\langle f\,|B_L\rangle|^2 + e^{-\Gamma_H t}\,|\langle f\,|B_H\rangle|^2\right] \tag{1.36} \\
&= \mathcal{N}_f\,|A_f|^2\,e^{-\Gamma_s t}\left\{\cosh\frac{\Delta\Gamma_s t}{2} + \mathcal{A}_{\Delta\Gamma}\,\sinh\frac{\Delta\Gamma_s t}{2}\right\}. \tag{1.37}
\end{aligned}
$$

In Equation 1.36 it is clearly illustrated that the decay is governed by two exponentials. It is possible to see that the untagged decay rate is not sensitive anymore to the terms $\mathcal{A}_{\mathrm{CP}}^{\mathrm{dir}}$ and $\mathcal{A}_{\mathrm{CP}}^{\mathrm{mix}}$ since they have opposite signs in the decay rates of B_q and $\overline{B}_q$ mesons (comparing Equation 1.30 and Equation 1.31).

---

[6]With the term untagged indicating a sample composed of B_s^0 and $\overline{B}_s^0$, where from the final state it is not possible to distinguish the initial state.

The *effective lifetime* for the decay $B_s^0(\overline{B}_s^0) \to f$, where f is accessible to both B_s^0 mesons, is defined as the time expectation value of the untagged rate

$$\tau_f^{\text{eff}} \equiv \frac{\int_0^\infty t\,\Gamma[f,t]\,dt}{\int_0^\infty \Gamma[f,t]\,dt}, \tag{1.38}$$

which is equivalent to the lifetime that results from combining the two exponentials in Equation 1.36 to a single exponential. The effective lifetime is expressed as [24]

$$\frac{\tau_f^{\text{eff}}}{\tau_{B_s^0}} = \frac{1}{1-y_s^2}\left(\frac{1+2\,\mathcal{A}_{\Delta\Gamma}\,ys+y_s^2}{1+\mathcal{A}_{\Delta\Gamma}\,ys}\right) \tag{1.39}$$

$$= 1 + \mathcal{A}_{\Delta\Gamma}\,ys + \left[2-(\mathcal{A}_{\Delta\Gamma})^2\right]y_s^2 + \mathcal{O}(y_s^3). \tag{1.40}$$

Different final states f have different combinations of the two mass eigenstates ($\mathcal{A}_{\Delta\Gamma}$ depends on the final state), and hence, the effective lifetime varies with the final state that is considered.

An analogous definition of the effective lifetime holds for B^0 mesons. However, since $\Delta\Gamma_d$ is negligibly small, the heavy and light mass eigenstates cannot be resolved experimentally.

Decays to flavour specific final states The decay $B^0 \to J/\psi K^*(892)^0$, with $K^*(892)^0 \to K^+\pi^-$, is a B^0 decay to a flavour-specific final states. The term flavour-specific means that the final state is only reachable by the decay of the B^0 meson, and consequently possible for a meson originally produced as a $\overline{B}^0$ only through oscillation ($A_{\overline{f}} = \overline{A}_f = 0$). Flavour specific final states have $\mathcal{A}_{\Delta\Gamma}^{B^0 \to J/\psi K^*(892)^0} = 0$, so the effective lifetime can be expressed as

$$\tau_{B^0 \to J/\psi K^*(892)^0}^{\text{eff}} = \frac{1}{\Gamma_d}\cdot\frac{1}{1-y_d^2}\left(1+y_d^2\right). \tag{1.41}$$

Since $\Delta\Gamma_d$ is small, $y_d^2 \approx 0$, a measurement of an effective lifetime in the $B^0 \to J/\psi K^*(892)^0$ channel is basically a measurement of $1/\Gamma_d$ up to a second order correction $\mathcal{O}(\Delta\Gamma_d^2/\Gamma_d^2)$

$$\tau_{B^0 \to J/\psi K^*(892)^0}^{\text{eff}} \approx \frac{1}{\Gamma_d}\cdot\left[1+\left(\frac{\Delta\Gamma_d}{\Gamma_d}\right)^2\right]. \tag{1.42}$$

Decays to *CP* eigenstates The decay $B^0 \to J/\psi K_S^0$, with $K_s^0 \to \pi^+\pi^-$, is a B^0 decay to a *CP* eigenstates (see Equation 1.24). For this decay, to a very good approximation in the SM, one has

$$\mathcal{A}_{\Delta\Gamma}^{B^0 \to J/\psi K_S^0} = \cos(2\beta), \qquad \text{where} \quad \beta \equiv \arg\left[-(V_{cd}V_{cb}^*)/(V_{td}V_{tb}^*)\right]. \tag{1.43}$$

The effective lifetime can be expressed as

$$\tau_{B^0 \to J/\psi K_S^0}^{\text{eff}} = \frac{1}{\Gamma_d}\cdot\frac{1}{1-y_d^2}\left(\frac{1+2\cos(2\beta)\,y_d+y_d^2}{1+\cos(2\beta)\,y_d}\right). \tag{1.44}$$

1.5.2 Decay width difference $\Delta\Gamma_d$

It is interesting to note that it is possible to perform a measurement of the decay width difference in the B^0 system, $\Delta\Gamma_d$, by using the effective B^0 lifetime measurements in a flavour specific decay and in a decay to a CP eigenstate. The ratio, R, of the effective lifetimes in Equation 1.41 and Equation 1.44 is

$$R = \frac{\tau^{\text{eff}}_{B^0 \to J/\psi K^0_{\text{S}}}}{\tau^{\text{eff}}_{B^0 \to J/\psi K^*(892)^0}} = \frac{1 + 2\cos(2\beta)\,y_d + y_d^2}{(1 + y_d^2)(1 + \cos(2\beta)\,y_d)}. \tag{1.45}$$

From this ratio it is possible to derive an expression for y_d in term of the two B^0 effective lifetimes, as proposed in [25]

$$y_d = \frac{\Delta\Gamma_d}{2\Gamma_d} = \frac{1}{\cos(2\beta)}(R-1) + \frac{1}{\cos(2\beta)^2}(R-1)^2 + \mathcal{O}(R-1)^3. \tag{1.46}$$

These two channels, $B^0 \to J/\psi K^0_{\text{S}}$ and $B^0 \to J/\psi K^*(892)^0$, are also advantageous from an experimental point of view. The branching fractions are large, the decay $J/\psi \to \mu^+\mu^-$ in the final state makes these two channels easy to reconstruct while suppressing most of the background. Moreover, they are topologically similar, so many systematic uncertainties related to the reconstruction of the particles and of the vertex of the decay are the same. One systematic effect in the determination of $\Delta\Gamma_d$ is an asymmetry, $A_{\text{P}}(\overline{B}^0)$, between the production rates of B^0 and $\overline{B}^0$. If non zero, the cancellation of terms proportional to $\mathcal{A}^{\text{dir}}_{\text{CP}}$ and $\mathcal{A}^{\text{mix}}_{\text{CP}}$ in Equation 1.31 would not be exact, so that the untagged rate of Equation 1.37 would include an additional factor proportional to

$$A_{\text{P}}(\overline{B}^0)\left(\mathcal{A}^{\text{mix}}_{\text{CP}}\sin(\Delta m_d t) - \mathcal{A}^{\text{dir}}_{\text{CP}}\cos(\Delta m_d t)\right). \tag{1.47}$$

1.5.3 Decay width difference $\Delta\Gamma_s$

The decay width difference in the B^0_s system, $\Delta\Gamma_s$, is measured in the decay $B^0_s \to J/\psi\phi$. The B^0_s meson is a pseudoscalar meson, which means that the total spin is zero. The J/ψ and the ϕ are two vector mesons, meaning that the total spin for each of them is one. Due to the total angular momentum conservation, the final state in this decay channel is a superposition of three possible states with relative orbital momentum $l = 0, 1, 2$. Thus, the final state is a mixture of CP-even ($l = 0, 2$) and CP-odd ($l = 1$) eigenstates. The different CP-eigenstates are predominantly the result of either B_H or B_L decays, and hence allow to measure Γ_H and Γ_L. In order to disentangle statistically the three components of the final state, an angular analysis is needed where the angular distributions of the decay products $B^0_s \to J/\psi(\to \mu^+\mu^-)\phi(\to K^+K^-)$ are used [26]. Three angles are needed to describe this final state. The differential decay rate becomes a quite complicated function of the angular distributions and of the decay time of the B^0_s meson.

For illustrative purposes, it is very instructive to see the differential decay rate in the projection on one single angle θ, which means that one integrates over the other

two angles. The form of the differential decay rate is, in this case, simple enough to be written as a single expression

$$
\begin{aligned}
\frac{d\Gamma}{dt\,d\cos\theta} \quad \propto \quad & \frac{1}{2}(1+\cos^2\theta)\,(1-R_\perp)\times \\
\times \quad & \left[(1+\cos\phi_s)\,e^{-\Gamma_L t}+(1-\cos\phi_s)\,e^{-\Gamma_H t}+\sin\phi_s\sin\left(\Delta m_s t\right)\right] \\
+ \quad & \sin^2\theta\,R_\perp\times\left[(1-\cos\phi_s)\,e^{-\Gamma_L t}+(1+\cos\phi_s)\,e^{-\Gamma_H t}-\sin\phi_s\sin\left(\Delta m_s t\right)\right]\,.
\end{aligned}
\tag{1.48}
$$

In this expressions $R_\perp$ is the fraction of the CP-odd final state which has to be determined from the data. The quantity ϕ_s is the CP-violating phase that arises in this decay due to the interference between B_s^0 decays to $J/\psi\phi$ directly or via $B_s^0 - \overline{B}_s^0$ oscillation first. In the SM, it is predicted to be $\phi_s = (-0.0360^{+0.0020}_{-0.0016})$ rad [27], so it is a good approximation to set ϕ_s to zero in the previous equation, obtaining

$$
\frac{d\Gamma}{dt\,d\cos\theta}\propto(1+\cos^2\theta)\,(1-R_\perp)\,e^{-\Gamma_L t}+2\sin^2\theta\,R_\perp\,e^{-\Gamma_H t}\,.
\tag{1.49}
$$

In this way it is clear that the decay rate is the sum of two exponentials with different coefficients. The two exponentials can be separated by using the angular information. Then, each of Γ_L and Γ_H are determined and hence $\Delta\Gamma_s$. In particular, Γ_L is mainly determined by the CP-even component and Γ_H by the CP-odd component.

The analogous expressions when all three decay angles are used are significantly more complicated [5, 28]. In this case the separation of the different CP-final states is naturally better as there is more information available and therefore, the measurements of Γ_H and Γ_L are less correlated.

1.6 Theoretical tools for computation of *b*-hadron lifetimes

A precise lifetime measurement of the various weakly decaying charm and beauty hadrons possesses great experimental value per se. Furthermore, there is also a strong theoretical interest in determining and interpreting those lifetimes. Hadronic weak decays and, in particular, the measurement of lifetimes, is a good probe of that part of strong-interaction phenomenology that is least understood: the confinement of quarks and gluons inside hadrons.

It is important to validate the theoretical models developed to describe these features of QCD by comparing the experimental value of several meson and baryon lifetimes with the theoretical predictions, since these models are used to make predictions of quantities that are used as a test of the SM itself. Unfortunately, this task is very demanding from both a theoretical and an experimental point of view. The experimental challenges of precise lifetime measurements will be discussed in Chapter 4. In this section, a brief overview of the theoretical framework used to determine hadron lifetimes will be given, together with the current status of lifetime ratio predictions in the *b*-flavoured hadron sector [1, 29–31].
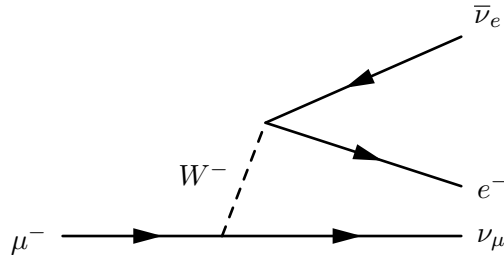
Figure 1.6: Feynman diagram of the muon decay $\mu^- \to \nu_\mu e^- \overline{\nu}_e$.

1.6.1   Spectator Model

From a theoretical point of view, working with hadronic decays is very complicated since many QCD effects have to be taken into account. In this section, the difficulties of having hadrons in the initial and in the final state will be analysed, starting from the simple muon decay, where no hadrons are involved, in order to gradually increase complexity.

The muon decay $\mu^- \to \nu_\mu e^- \overline{\nu}_e$, shown schematically in Figure 1.6, represents the most simple weak decay, because there are no QCD effects involved. The total decay rate of the muon reads

$$\Gamma_{\mu^- \to \nu_\mu e^- \overline{\nu}_e} = \frac{G_F^2 m_\mu^5}{192\pi^3} \, f\left(\frac{m_e}{m_\mu}\right), \tag{1.50}$$

where m_μ (m_e) is the mass of the muon (electron) and G_F is the Fermi coupling constant given by

$$G_F = \frac{\sqrt{2}}{8} \frac{g^2}{m_W^2}, \tag{1.51}$$

where g is the weak interaction coupling constant and m_W is the mass of the W boson. The function $f(m_e/m_\mu)$ denotes the phase-space factor for one massive particle in the final state[7]. The lifetime of the muon is obtained by taking the inverse of the total decay rate in Equation 1.50. Using the measured values of $G_F = 1.16637887(6) \cdot 10^{-5}$ GeV^{-2}, and $m_\mu = 0.1056583715(35)$ GeV/c^2 [14], the muon lifetime is estimated to be[8]

$$\tau_\mu^{\text{theo}} = \frac{1}{\Gamma_\mu} = 2.18776 \cdot 10^{-6} \text{ s}. \tag{1.52}$$

This value is in quite good agreement with the measured value [14]

$$\tau_\mu^{\text{exp}} = 2.1969811(22) \cdot 10^{-6} \text{ s}. \tag{1.53}$$

The remaining tiny difference (the prediction is about 0.4% smaller than the experimental value) is due to higher order electroweak corrections.

---

[7]Taking the function f into account leads to an almost negligible correction to the muon lifetime, about 0.02%, but it will turn out to be quite sizable for a decay of a beauty quark into a charm quark.

[8]This is just a pedagogical derivation of the muon lifetime since in reality the measured muon lifetime is used to extract the Fermi constant.
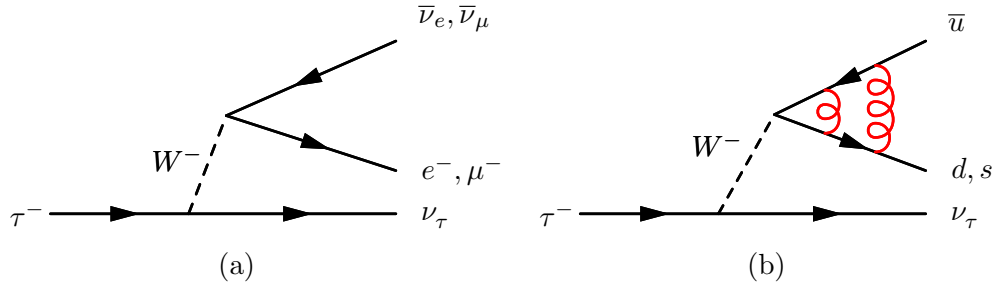
Figure 1.7: Feynman diagram of the tau lepton decay: (a) leptonic channels and (b) semi-leptonic channels.

Moving to the tau lepton, there are two leptonic decay channels as well as decays into quarks:

$$\tau \to \nu_\tau + \begin{cases} e^- + \overline{\nu}_e \\ \mu^- + \overline{\nu}_\mu \\ d + \overline{u} \\ s + \overline{u} \end{cases} \tag{1.54}$$

The corresponding Feynman diagrams are shown in Figure 1.7. Heavier quarks, like charm- or beauty-quark cannot be created, because the lightest meson containing such quarks, $D^0 = c\overline{u}$, is heavier ($m_{D^0} \approx 1.86\,\text{GeV}/c^2$) than the tau lepton ($m_\tau \approx 1.78$ GeV/c^2). Neglecting the correction due to the mass of the particles in the final state and using the approximation $|V_{ud}|^2 + |V_{us}|^2 \approx 1$, the overall correcting factor, c_τ, for this decay is found to be equal to five. Thus, the relation for the tau lepton lifetime is

$$\tau_\tau = \frac{\tau_\mu}{c_\tau} \left(\frac{m_\mu}{m_\tau} \right)^5 = \frac{\tau_\mu}{5} \left(\frac{m_\mu}{m_\tau} \right)^5 . \tag{1.55}$$

Substituting the experimental value of τ_μ, m_μ and m_τ, the lifetime of the tau lepton is found to be about 12% larger than the measured value. This large discrepancy with respect to the good agreement found for the simple muon lifetime is mostly due to sizable QCD corrections that arise when there are quarks in the final state that form light mesons and that can interact by means of gluons.

When moving to the meson sector, one of the main difficulties of making lifetime predictions is indeed the presence of quarks in the final and also in the initial state. On the one hand, quarks are the relevant weakly decaying entities for which it is possible to formulate fundamental theories. On the other hand, in the *real world*, quarks are confined inside hadrons, bound by the exchange of soft gluons. As an example, the Feynman diagram for the decay $B^+ \to \overline{D}^0 \pi^+$ is shown in Figure 1.8 (a). In Figure 1.8 (b) a more realistic picture is shown: the simplicity of the weak interactions is overshadowed by the complexity of strong interactions.
One quantitative measure for the additional effects introduced by the strong forces is provided by the lifetimes of weakly decaying hadrons carrying the same heavy flavour: if strong forces were negligible, the lifetime of every meson or baryon containing the same heavy quark would be the same. Focusing, for instance, on the decay of the b quark, shown in Figure 1.9, it is possible to see that, neglecting QCD effects among quarks
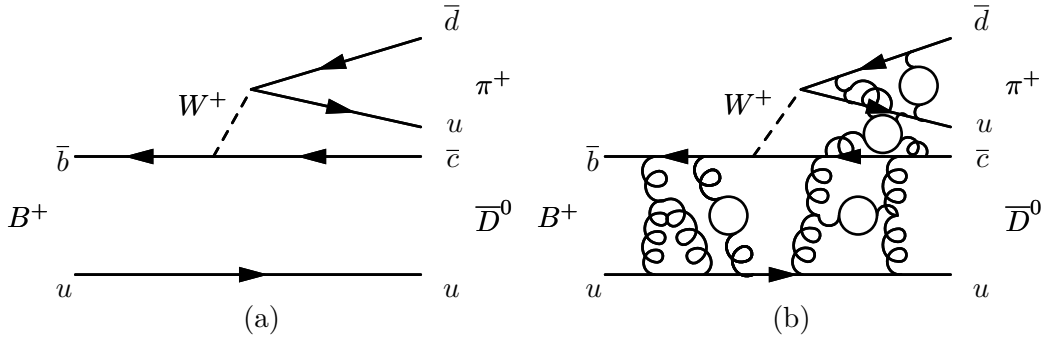
Figure 1.8: Feynman diagrams of the $B^+ \to \overline{D}^0 \pi^+$ decay: (a) a simplified diagram where only initial and final state quarks are drawn, (b) a more realistic representation of the decay.

in the final state, it is analogous to that of the muon, shown in Figure 1.6. This is the basic assumption behind the so-called *spectator model*: the lifetime of b-flavoured hadrons is fully dominated by the decay of the heavy b quark and the lighter quarks[9] (u, d or s) neither participate nor influence that decay: they are just a spectator of the b decay.

Calculating the total inclusive decay rate of a b-quark one gets

$$\Gamma_b = \frac{G_F^2 m_b^5}{192\pi^3} |V_{cb}|^2 c_b \,, \tag{1.56}$$

where the muon mass is replaced with that of the beauty-quark mass and a factor $|V_{cb}|^2$ arises due to the different coupling between the beauty and the charm quark and between muon and neutrino. The factor c_b takes into account the different phase space for the beauty quark decay. Neglecting all the masses of the final state particles and keeping only dominant CKM matrix element, the correcting factor for the beauty quark decay is found to be $c_b = 9$. Thus, it is possible to obtain the simple approximate relation for the b-quark lifetime

$$\tau_b = \tau_\mu \left(\frac{m_\mu}{m_b} \right)^5 \frac{1}{9|V_{cb}|^2} \,. \tag{1.57}$$

Substituting the experimental values of τ_μ, m_μ, m_b, and $|V_{cb}|$ the lifetime of the b quark is estimated to be between 1.3 and 1.6 ps[10].

The lifetime of the b quark that is predicted by this model is of the order of the observed B mesons lifetime. However this is only by accident, since in reality we cannot neglect the charm quark mass in the calculation. Taking it into account, the phase space factor c_b changes dramatically from 9 to $3 < c_b < 4.5$. The prediction for the b-quark lifetime becomes $\tau_b \sim 3$ ps, which is about 70% larger than the experimental number for

---

[9]The B_c^+ ($\overline{b}c$) meson is not included in this discussion since it is formed by two heavy quarks and thus, the spectator model does not apply.

[10]Predictions of the lifetimes have a huge parametric dependence on the definition of the quark mass ($\propto m_q^{-5}$). For confined quarks no, a priori natural, choice for the definition of the mass exists. Hence, a range of the lifetime prediction is reported, depending on the definition of the mass.
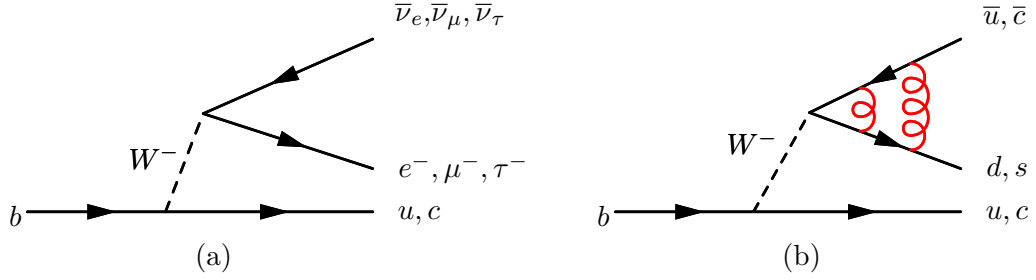
Figure 1.9: *Feynman diagram of the b quark decay: (a) leptonic channels and (b) non-leptonic channels.*
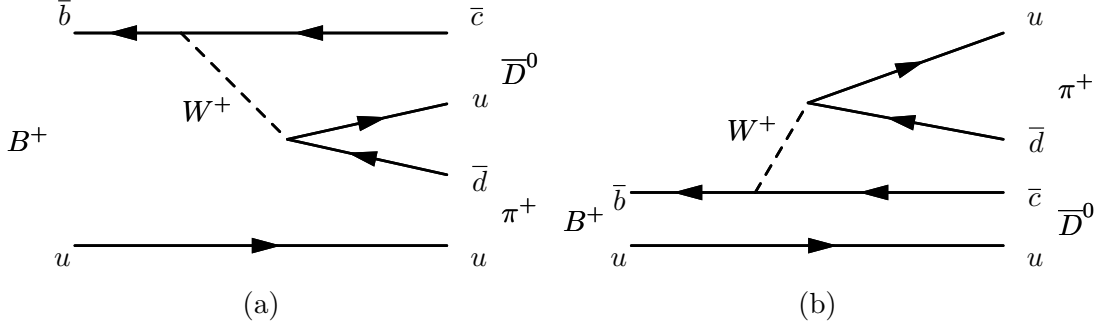
Figure 1.10: *Decay of a B^+ via an external (a) and an internal (b) emission of a W boson to the same final state. The two diagrams interfere destructively. As a result the total decay width of the B^+ is reduced and hence the B^+ lifetime is prolonged.*

the B mesons lifetime. There are in principle two sources for that discrepancy. Firstly, several CKM-suppressed decays have been neglected in this calculation. An inclusion of these decays would reduce the lifetime prediction by about 10%. Secondly, and most importantly, there are large QCD effects as spectator quarks cannot be neglected; including them moves the theory prediction very close to the experimental number.

1.6.2 Pauli interference and weak annihilation

From experimental results it is known that hadrons with the same heavy flavour (the s quark is, just for a moment, considered heavy) possess different lifetimes

$$
\begin{aligned}
\tau_{K^+(\bar{s}\,u)}/\tau_{K_S(\bar{s}\,d)} &\sim 140, \\
\tau_{D^+(c\,\bar{d})}/\tau_{D^0(c\,\bar{u})} &\sim 2.5, \text{ and} \\
\tau_{B^+(\bar{b}\,u)}/\tau_{B^0(\bar{b}\,d)} &\sim 1.08.
\end{aligned}
\tag{1.58}
$$

This means that the light quark component can no longer be considered as a spectator but is also involved in the decay. However, deviations of the lifetime ratios from unity evidently decrease for an increasing heavy-flavour mass ($m_b > m_c > m_s$). In the limit of the mass of the heavy-flavour quark, m_q, going to infinity, the "Spectator Ansatz" should hold and the lifetimes of all hadrons, H_q, containing the same heavy-flavour quark coincide. In Section 1.6.3 effects due to the spectator quark are shown to be suppressed by $1/m_q$; the bigger the quark mass is more these effects will be suppressed. So in case of B mesons, because of the large value of the b-quark mass, one expects a
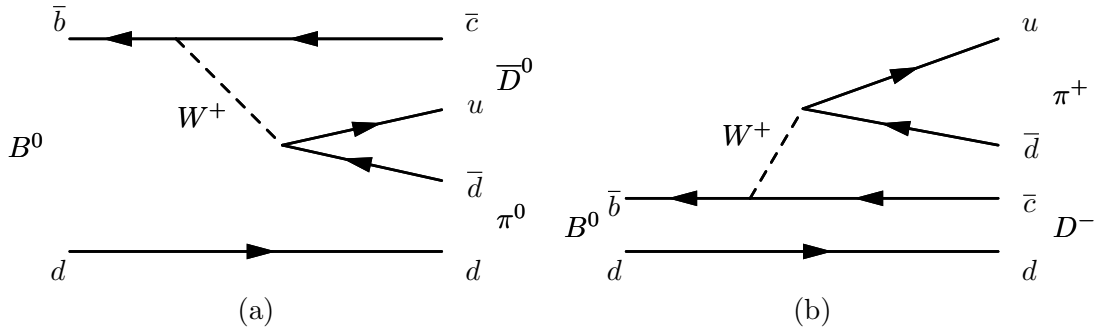
Figure 1.11: *Decay of a B^0 via an external (a) and an internal (b) emission of a W boson to different final states. There is no interference between the two diagrams.*
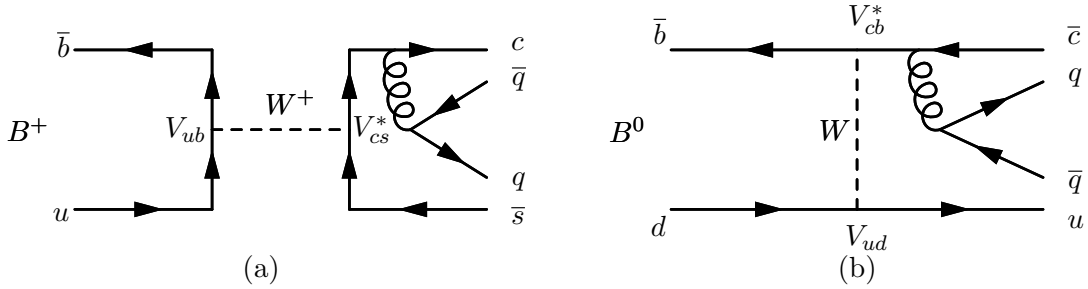
Figure 1.12: *Feynman diagrams of (a) B^+ decay through weak annihilation (b) B^0 decay through weak exchange.*

better description of the meson decay in terms of the simple b-quark decay. For m_q sufficiently large, the quark q decays before it can hadronise: this is the case for the top quark. Then, there is an universal lifetime for such a heavy flavour and the spectator ansatz applies trivially.

It is possible to get an indication of how light quarks contribute to the lifetime phenomenology via a comparison between the B^+ and the B^0 meson lifetimes. The light quarks serve to give the B^+ meson a longer lifetime in comparison to the B^0 meson: this effect is due to so-called *Pauli interference* between the possible final states of the decay. The B^+ has two decay paths to the same final state (there are two identical u quarks in the final state), as shown in Figure 1.10. The two diagrams interfere with each other destructively and this leads to a decrease of the decay width for the B^+ meson. Conversely, as can be seen in Figure 1.11, for the B^0 decay there are two different final states and hence, no interference occurs. This argument can also be used to expect the B_s^0 lifetime to be shorter than that of the B^+, as the B_s^0 system also decays to two different final states.

Another effect that contributes to the prolongation of the B^+ lifetime is the so-called *weak annihilation*. The B^+ decays through annihilation of the valence quarks, $\bar{b}u$, into a W boson, which then decays into the final state quarks (see Figure 1.12 (a)). The amplitude of this decay is proportional to the CKM matrix elements V_{ub} and V_{cs}^*. To the contrary, for the B^0 decay it is possible to have an exchange of a W boson among the two valence quarks, $\bar{b}d$ (see Figure 1.12 (b)). The amplitude of this decay is proportional to the CKM matrix elements V_{cb}^* and V_{ud}. Since $(V_{cb}^*V_{ud}) > (V_{ub}V_{cs}^*)$ it follows that $\tau_{B^+} > \tau_{B^0}$. Using similar arguments it is possible to show that $\tau_{B^+} > \tau_{B_s^0}$.

Both effects, namely Pauli interference and weak annihilation, work in the same direction, i.e. both enhance the lifetime of the B^+ over the lifetime of the B^0 and B_s^0 mesons. This logic gives the following hierarchy

$$\tau_{B^+} > \tau_{B^0}, \tau_{B_S^0}. \tag{1.59}$$

Nevertheless, using this phenomenological approach, no clear predictions can be made on the lifetime ratios among beauty hadrons, namely whether the lifetimes of B^+ and B^0 differ by a few percent only, or by $20 - 30\%$. Thus, there existed a need for a description based on a systematic theoretical framework rather than a set of phenomenological prescriptions.

1.6.3 Heavy Quark Expansion (HQE)

In order to make any numerically reliable estimate of meson decays, effects arising from the presence of spectator quarks have to be taken into account properly, as it was pointed out in the previous section. Non-perturbative corrections to heavy-flavour decays can be expressed through an expansion in inverse powers of m_q. To do so, weak decays of heavy quarks are described with the help of an effective Hamiltonian. The basis for any phenomenology of weak decays of hadrons is the *Operator Product Expansion* (OPE) [32], which allows to write the effective weak Hamiltonian simply as follows

$$\mathcal{H}_{eff} = \frac{G_F}{\sqrt{2}} \sum_i V_{\text{CKM}}^i C_i(\mu) Q_i(\mu) \ . \tag{1.60}$$

Here, G_F is the Fermi constant and Q_i are the relevant local operators which govern the decays in question. They are built out of quark and lepton fields. The Cabibbo-Kobayashi-Maskawa matrix elements V_{CKM}^i and the Wilson coefficients $C_i(\mu)$ describe the strength with which a given operator enters the Hamiltonian. The latter coefficients can be considered as scale dependent "couplings" related to "vertices" Q_i and can be calculated using perturbative methods as long as μ, the renormalisation scale, is not too small.

The amplitude for the decay of a given hadron in the initial state, I, into a final state, F, is then given by

$$\mathcal{A}(I \to F) = \langle F | \mathcal{H}_{eff} | I \rangle = \frac{G_F}{\sqrt{2}} \sum_i V_{CKM}^i C_i(\mu) \langle F | Q_i(\mu) | I \rangle, \tag{1.61}$$

where $\langle F | Q_i(\mu) | I \rangle$ are the matrix elements of Q_i between the initial and the final state, evaluated at the scale μ. In the simplest case of the β-decay, $\mathcal{H}_{eff}$ takes the familiar form

$$\mathcal{H}_{eff}^{(\beta)} = \frac{G_F}{\sqrt{2}} \cos \theta_c [\bar{u} \gamma_\mu (1 - \gamma_5) d \otimes \bar{e} \gamma^\mu (1 - \gamma_5) \nu_e] \ , \tag{1.62}$$

where V_{ud} has been expressed in terms of the Cabibbo angle. In this particular case the Wilson coefficient is equal to unity and the local operator, the object between the square brackets, is given by a product of two $V - A$ currents. Equation 1.62 represents the Fermi theory for β-decays as formulated by Feynman and Gell-Mann [33] more than forty years ago, except that in Equation 1.62 the quark language has been used and

the small deviation of V_{ud} from unity has been incorporated in terms of the so-called Cabibbo angle, θ_c. In this context Equation 1.61 can be regarded as a generalization of the Fermi Theory to include all known quarks and leptons as well as their strong and electroweak interactions as summarised by the SM. Due to the interplay of electroweak and strong interactions, the structure of the local operators for hadronic weak decays is much richer than in the case of the β-decay and other operators appear in Equation 1.61.

The main advantage of OPE is that it allows to separate the problem of calculating the amplitude $\mathcal{A}(I \to F)$ into two distinct parts. The *short distance* (perturbative) calculation of the coefficients $C_i(\mu)$ and the *long-distance* (generally non-perturbative) calculation of the matrix elements $\langle F|Q_i(\mu)|I\rangle$, separated by the scale μ. The value of μ can be chosen arbitrarily but the final result must be μ-independent. It is customary to choose μ to be of the order of the mass of the decaying hadron. This is $\mathcal{O}(m_b)$ and $\mathcal{O}(m_c)$ for b- and c-hadron decays, respectively.

In order to calculate the amplitude $\mathcal{A}(I \to F)$ the matrix elements $\langle F|Q_i(\mu)|I\rangle$ have to be evaluated. Since they involve long distance contributions, one is forced in this case to use non-perturbative methods such as lattice calculations, QCD sum rules and the Heavy Quark Effective Theory (HQET). At present, the technique of lattice simulations is the most used (for a recent review, see [34]): it is based on first principles and it has produced very valuable results on hadronic matrix elements, bound states, and so on. Needless to say, non-perturbative methods have many limitations. Consequently, usually the dominant theoretical uncertainties in the decay amplitudes reside in the matrix elements $\langle F|Q_i(\mu)|I\rangle$.

The decay rate of the transition of a b-flavoured hadron[11], H_b, to an inclusive final state X can be expressed as a phase space (PS) integral of the square of the matrix element, summed over all final states X with the same quark quantum numbers

$$\Gamma(H_b \to X) = \frac{1}{2m_{H_b}} \sum_X \int_{\text{PS}} (2\pi)^4 \delta^{(4)}(p_{H_b} - p_X)|{<}X|\mathcal{H}_{eff}|H_b{>}|^2 \ . \qquad (1.63)$$

Explicitly calculating the integral one arrives at the *Heavy Quark Expansion* [35–38] of decay rates of heavy hadrons:

$$\Gamma(H_b \to X) = \Gamma_0 + \frac{\Lambda^2}{m_b^2}\Gamma_2 + \frac{\Lambda^3}{m_b^3}\Gamma_3 + \frac{\Lambda^4}{m_b^4}\Gamma_4 + ... \ , \qquad (1.64)$$

where the expansion parameter is denoted by Λ/m_b. The actual value of Λ has to be determined for each order of the expansion separately, but it is of order $\Lambda \sim 1\,\text{GeV}$. The following comments can be made.

1. The leading contribution to the total decay width is given by the first term on the right-hand-side of Equation 1.64 that is common to all hadrons of a given heavy-flavour quantum number. It is Γ_0, the free b-quark decay width in case of b hadrons, as given in the spectator model. For $m_q \to \infty$ one has thus derived the spectator picture attributing equal lifetimes to all hadrons of a given heavy-flavour.

---

[11]In this definition any hadron containing a b quark and any of the light u, d and s (anti-)quarks as valence quarks is included.

2. The leading non-perturbative corrections are of order $1/m_b^2$ rather than $1/m_b$. This non-trivial result explains why the B meson lifetimes differ at most by almost 10%, while in case of D mesons, which contain a charm quark, the $1/m_c^2$ terms are not so suppressed and there is a large difference among the D meson lifetimes. The $1/m_b^2$ terms originate from the so-called chromo-magnetic and kinetic energy operators and give no difference in the lifetimes of B^+ and B^0 mesons (they are shifted by the same amount). They enhance the B_s^0 lifetime by about 3‰, compared to the B^0 lifetime, and they reduce the Λ_b^0 lifetime by about 1% compared to the B^0 lifetime. The origin of these contributions can be understood in the following way. The b quark is expected to possess a different kinetic energy inside a meson or a baryon. This difference in the heavy quark motion means that Lorentz time dilation prolongs the lifetime of the b quark by a different amount in baryons compared to mesons. Due to a small sensitivity of this correction to the spectator quark mass, the B_s^0 lifetime is slightly enhanced with respect to the B^+ and B^0 lifetimes. Moreover, the decay width is affected by spin-spin interactions of the b-quark with the light quark in mesons or with the light diquark system for baryons. While there exists a spin interaction between the b and the antiquark $\bar{q}$ in the meson system, there is no such coupling inside Λ_b^0 since the diquark system carries spin zero.

3. Differences in meson lifetimes are generated at order $1/m_b^3$ by operators describing Pauli interference as well as weak annihilation. The first one is the dominant effect: it receives a phase-space enhancement factor of $16\pi^2$, with respect to the leading terms in Equation 1.64. This term is sensitive to the flavour of the spectator quark because in principle, each different spectator quark gives a different contribution. The situation is much more complex for the Λ_b^0 and baryons in general: Pauli interference can now be constructive as well as destructive and weak annihilation plays an important role so it is not easy to make reliable predictions anymore.

4. If one includes in the calculation of the weak annihilation and Pauli interference diagrams also small momenta and masses of the spectator quark, one gets corrections that are suppressed by four powers of m_b compared to the free-quark decay. These terms have currently only been estimated.

One important assumption behind the heavy quark expansion is the so-called *quark-hadron duality*. It can be stated as follows: sufficiently inclusive transitions rates (i.e. taking all possible final states into account) between hadronic systems can be calculated in terms of quarks and gluons. This means that transition rates calculated on the quark-gluon level are equal to the observable ones involving the corresponding hadrons, provided one sums over a sufficient number of final states. There is a considerable amount of literature about theoretical attempts to prove or disprove this duality, but all these attempts have to rely on strong model assumptions. If quark-hadron duality does not hold it is possible that the series in Equation 1.64 does not converge well enough. One of the best ways of addressing this question is to confront precise HQE-based predictions with precise experimental data. An especially well suited candidate for this problem is the decay $b \to c\bar{c}s$ where violations of duality are expected to be more pronounced. A perfect observable for testing the HQE is the decay width difference

$\Delta\Gamma_s$ of the neutral B_s^0 mesons, which is measured in $b \to c\bar{c}s$ transition.

1.6.4   Overview of HQE predictions

Predictions of the lifetimes of b hadrons have a large parametric dependence on the definition of the quark mass ($\propto m_q^{-5}$). This is the reason why typically only lifetime ratios are determined theoretically, with $\tau(B^0)$ chosen as the common denominator. The dominant mass dependence as well as CKM matrix elements, like $|V_{cb}|^2$, and some sub-leading non perturbative corrections cancel. Here, recent predictions are reviewed, putting particular emphasis on possible future improvements.

Lifetimes of B mesons   The lifetimes of charged and neutral B mesons differ mainly because of the Pauli interference effect described in Section 1.6.2. The most recent prediction is [1]

$$\frac{\tau_{B^+}}{\tau_{B^0}}^{\text{HQE 2014}} = 1.04^{+0.05}_{-0.01} \pm 0.02 \pm 0.01 \ . \tag{1.65}$$

The main contribution to the uncertainty is due to the lack of precision in the knowledge of a so-called "bag parameter", which is useful in lattice calculations. Using different values for this parameter moves the central value of the lifetime ratio prediction from 1.03 to 1.09. This is indicated by the first asymmetric error and clearly shows the urgent need for more profound calculations of these non-perturbative parameters. The second uncertainty is due to varying the matrix elements $\langle F|Q_i(\mu)|I\rangle$ in their allowed range. The third uncertainty comes from the renormalisation scale dependence as well as the dependence on m_b. The total uncertainty on this ratio is about a factor of ten larger than previously quoted uncertainties [39, 40]. This is due to some recent developments in lattice calculations, especially a better understanding of the uncertainties, and also to the fact that in this prediction also other non-perturbative methods have been included and the difference with respect to the result given by lattice calculation is included in the uncertainty.

The lifetimes of the two neutral mesons B_s^0 and B^0 differ because of tiny differences in the $1/m_b^2$ corrections. The most recent prediction is [1]

$$\frac{\tau_{B_s^0}}{\tau_{B^0}}^{\text{HQE 2014}} = 1.001 \pm 0.002 \ . \tag{1.66}$$

Note that $\tau_{B_s^0}$ denotes the average lifetime of the two B_s^0 mass eigenstates, whose individual lifetimes are expected to differ by a sizeable amount. Since there is an almost perfect cancellation of all the effects in this ratio, it can be used to search for physics effects beyond the Standard Model which are not included in the HQE.

Lifetimes of b baryons   Although, as stated in Section 1.6.3, the lifetime differences between heavy mesons and baryons start at order $1/m_b^2$ in the heavy quark expansion, the main effects appear at order $1/m_b^3$. Theoretically reliable predictions are available only for the Λ_b^0 baryon and the current value is [1]

$$\frac{\tau_{\Lambda_b^0}}{\tau_{B^0}}^{\text{HQE 2014}} = 0.935 \pm 0.054 \ . \tag{1.67}$$

To reduce this large uncertainty, new lattice calculations are necessary.

Decay width difference, $\Delta\Gamma_d$ and $\Delta\Gamma_s$ The current status of mixing quantities, both in the B- and the D-system, has been recently reviewed in [41]. Here, only the decay rate differences $\Delta\Gamma_s$ and $\Delta\Gamma_d$ are discussed, since their measurement is part of this thesis.

The HQE predictions are [1, 42]

$$\Delta\Gamma_s^{\mathrm{HQE\,2014}} = (0.087 \pm 0.021) \text{ ps}^{-1} \text{ and} \tag{1.68}$$

$$|\Delta\Gamma_d/\Gamma_d|^{\mathrm{HQE\,2014}} = (0.42 \pm 0.08) \cdot 10^{-2} . \tag{1.69}$$

Concerning future developments, it is clear that the experimental uncertainty will be reduced in future, while the larger theory uncertainty is dominated from unknown matrix elements of dimension six operators, see [43]. The fact that in many cases the hadronic matrix elements cannot be reliably calculated at present, is very unfortunate since many theoretical predictions are already less precise than the experimental values, as it will be shown in the next section. It is obvious that improvements in lattice calculations or, even better, the development of an analytical solution are fundamental in order to perform precise and reliable theory predictions.

1.6.5 Experimental status and motivation of the analysis

A comparison of experimental results as given by the Heavy Flavour Averaging Group (HFAG) [2] and HQE predictions derived in [1] is shown in Figure 1.13. This reflects the status at the beginning of 2014, i.e. before the inclusion of the results which are the topic of this thesis. In Table 1.6 also different predictions are included and a range of possible values including all of them is shown. Here, $\tau_{B_s^0}$ indicates the average B_s^0 lifetime, $\tau_{B_s^0} \equiv 1/\Gamma_s$, while the effective B_s^0 lifetime measured in the $J/\psi\phi$ final state is explicitly referred to as $\tau_{B_s^0 \to J/\psi\phi}$. Since $\Delta\Gamma_d$ is beyond the current experimental sensitivity, this distinction is not necessary when referring to B^0 lifetime measurements. Thus, B^0 effective lifetime measurements will be referred in the following as τ_{B^0}, specifying the decay mode used when necessary. The same notation will be used in the rest of this document.

Concerning the ratio of B^+ and B^0 meson lifetimes it can be seen that the experimental uncertainty is almost a factor of ten smaller than the uncertainty of the theoretical predictions. More interesting is the ratio between the B_s^0 and B^0 meson lifetimes. Here, most of the poorly known terms in heavy quark expansion cancel and the theoretical prediction is very clean. Unfortunately, from an experimental point of view this ratio is the most challenging because of the B_s^0 mixing, which makes the determination of the average lifetime difficult. An angular analysis of the decay $B_s^0 \to J/\psi\phi$ is needed, as explained in Section 1.5.3.

In the early part of the past decade, measurements of the ratio of Λ_b^0 to $\overline{B}^0$ lifetimes gave results considerably smaller than the theoretical expectation. In 2003 one widely quoted average for this ratio coming from several experimental results was
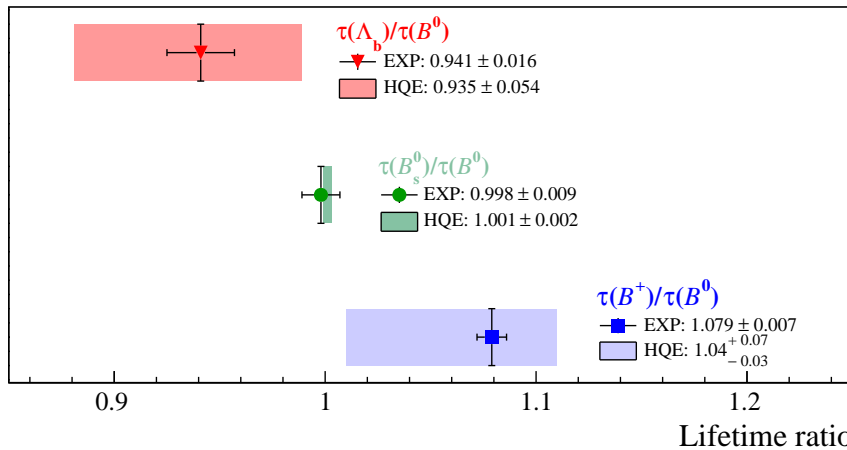
Figure 1.13: Current status of experimental [2] and HQE [1] ratios of b-hadron lifetimes.

0.796 ± 0.052 [40], while another was 0.786 ± 0.034 [44, 45]. Some authors sought to explain the small value of the ratio by including additional operators or other modifications [46–48], while some thought that the HQE could be pushed to provide a ratio of about 0.9 [49], but not so low as the measured value. Recent measurements have shown indications that a higher value is possible [50–52], in good agreement with the theoretical prediction as shown in Figure 1.13. This long standing puzzle indeed needs to be finally settled experimentally, so a confirmation of the measurement of the Λ_b^0 lifetime is desirable.

The decay width differences $\Delta\Gamma_s$ and $\Delta\Gamma_d$ in the B_s^0 and B^0 system, respectively, are sensitive to new physics effects [53]. The parameter $\Delta\Gamma_s$ was measured for the first time in 2012 by the LHCb Collaboration [54]. The average from HFAG [2] at the beginning of 2014 reads

$$\Delta\Gamma_s^{\mathrm{Exp}} = (0.081 \pm 0.011) \ \mathrm{ps}^{-1} \,. \tag{1.70}$$

It includes the measurements from LHCb [54], ATLAS [55], CDF [56] and DØ [57]. Experiment and theory agree perfectly for $\Delta\Gamma_s$, thus excluding huge violations of quark hadron duality or new physics effects.

Both the BaBar [58, 59] and Belle [60] collaborations have measured $|\Delta\Gamma_d/\Gamma_d|$ and the world average at beginning of 2014 was [2]

$$|\Delta\Gamma_d/\Gamma_d|^{\mathrm{Exp}} = 0.015 \pm 0.018 \,, \tag{1.71}$$

which is compatible with $\Delta\Gamma_d = 0$. A deviation in the value of $\Delta\Gamma_d$ from the SM prediction has recently been proposed [23, 53] as a potential explanation for the anomalous like-sign dimuon charge asymmetry measured by the DØ collaboration [61]. A measurement of a larger value would clearly reveal the presence of physics beyond the SM.

In this thesis all the techniques developed to perform precise measurements of the B^+, B^0, B_s^0 and Λ_b^0 lifetimes are described. The measurement of all these lifetimes using the same analysis is very advantageous since it allows to use the lifetimes that are well

Table 1.6: Theoretical predictions and current world-average values [2] for b-hadron lifetimes, lifetime ratios and decay width in the B_s^0 and in the B^0 system, $\Delta\Gamma_s$ and and $\Delta\Gamma_d/\Gamma_d$.

Observable	Prediction	World average
τ_{B^+} [ps]	-	1.641 ± 0.008
τ_{B^0} [ps]	-	1.519 ± 0.007
$\tau_{B_s^0}$ [ps]	-	1.516 ± 0.011
$\tau_{B_s^0 \to J/\psi\phi}$ [ps]	-	1.429 ± 0.088
$\tau_{\Lambda_b^0}$ [ps]	-	1.429 ± 0.024
τ_{B^+}/τ_{B^0}	1.01-1.11 [1, 40]	1.079 ± 0.007
$\tau_{B_s^0}/\tau_{B^0}$	0.99-1.01 [1, 39, 40]	0.998 ± 0.009
$\tau_{\Lambda_b^0}/\tau_{B^0}$	0.86 - 1.01 [1, 37, 44, 47, 48, 62–65]	0.941 ± 0.016
$\Delta\Gamma_s$ [ps^{-1}]	0.087 ± 0.021 [1]	0.081 ± 0.011
$|\Delta\Gamma_d/\Gamma_d|$	$(0.42 \pm 0.08) \cdot 10^{-2}$ [42]	0.015 ± 0.018

known experimentally, like the B^+ lifetime, as a benchmark to check if the procedure is working correctly. The determination of the B_s^0 effective lifetime in the $J/\psi\phi$ final state does not have a great value per se. However, it is important to control that the lifetime measurement is unbiased since the same procedure is used to determine the average decay width, Γ_s, and the decay width difference, $\Delta\Gamma_s$, between the light and the heavy B_s^0 mass eigenstates. Part of this analysis is also the derivation of the decay width difference in the B^0 system, $\Delta\Gamma_d$. Moreover, ratios among B^+, B^0, Λ_b^0 and the corresponding anti-particle lifetimes are measured, as they are an important test of the validity of the *CPT* theorem. One of the main achievements of this work is to develop the necessary tools which enable a precise determination of the lifetime acceptance. This makes these measurements a good test of the HQE predictions and beyond but also an important benchmark of the performance of the LHCb experiment. The first point is crucial, since the HQE is a tool that is used not only to make predictions about lifetimes, but also about many other important quantities that are used to experimentally search for physics beyond the SM. So it is of vital importance to validate its predictions.

1.7   Summary

The essential information of this chapter is briefly summarised here.

- The flavour-changing currents of the weak interaction induce neutral meson mixing. As a result of it, the decay time distribution of neutral B_q^0 ($q = d, s$) mesons is characterised by two parameters, namely the average decay width, Γ_q, and the decay width difference, $\Delta\Gamma_q$, between the light and the heavy B_q^0 mass eigenstates. The lifetime that is measured ignoring the non-zero $\Delta\Gamma_q$ is called effective lifetime.

- The value of $\Delta\Gamma_d$ can be extracted from the effective lifetimes of $B^0 \to J/\psi K^*(892)^0$ and $B^0 \to J/\psi K^0_S$ decays.

- Within the framework of heavy quark expansion theory (HQE), b-hadron lifetimes are calculated as a perturbative expansion in inverse powers of the b-quark mass.

- Precise lifetime measurements, and in particular lifetime ratios, can be used to constrain the predictions of the HQE theory within the Standard Model and the validity of the CPT theorem.

- The value of $\Delta\Gamma_s$ can be extracted from an angular analysis of the decay $B^0_s \to J/\psi\phi$ and it is important to confirm the convergence of the perturbative expansion above mentioned.

- The production cross section of $b\bar{b}$ is high in pp collisions at LHC energies, particularly in the forward region. This ensures a unprecedented sample of heavy flavour decays to perform precise measurements of the B^+, B^0, B^0_s and Λ^0_b lifetimes, lifetime ratios and of the decay width differences, $\Delta\Gamma_s$ and $\Delta\Gamma_d$.

- The theoretical predictions and current world-average values for all the aforementioned quantities are summarised in Table 1.6.

2

The LHCb experiment

A race of hyperintelligent pan-dimensional beings once built themselves a gigantic supercomputer called Deep Thought to calculate once and for all the Answer to the Ultimate Question of Life, the Universe, and Everything.

— Douglas Adams

The LHCb experiment is dedicated to flavour physics studies at the Large Hadron Collider (LHC) at CERN. In particular, it is designed for precision measurements of *CP* violation and rare decays of beauty (*b*) and charm (*c*) hadrons, in order to indirectly search for new physics effects beyond the Standard Model.

The LHCb detector has been designed to accomplish these delicate measurements. The detection of short lived particles and lifetime measurements require optimal vertex and momentum resolution. The latter ensures a good invariant mass resolution, which helps to reduce combinatorial background. Particle identification is a critical issue for the discrimination of final states. In addition to muons and electrons and neutral particles, also charged hadrons, like protons, kaons and pions have to be distinguished to separate the different final states. Last but not least, a high-bandwidth data acquisition and a flexible and robust trigger is needed to select many different final states in a hadronic environment.

In the following chapter the LHCb detector is described. After an overview of the LHC accelerator complex, in Section 2.1, the LHCb detector is introduced in Section 2.2, with particular emphasis on the vertex detector, the so-called Vertex Locator, see Section 2.2.1. This will provide the reader with sufficient details to subsequently follow the studies described in Chapter 3 and Chapter 6.

2.1 The Large Hadron Collider

The Large Hadron Collider at the European Council for Nuclear Research, CERN, located near Geneva is the most powerful particle accelerator ever built. The LHC
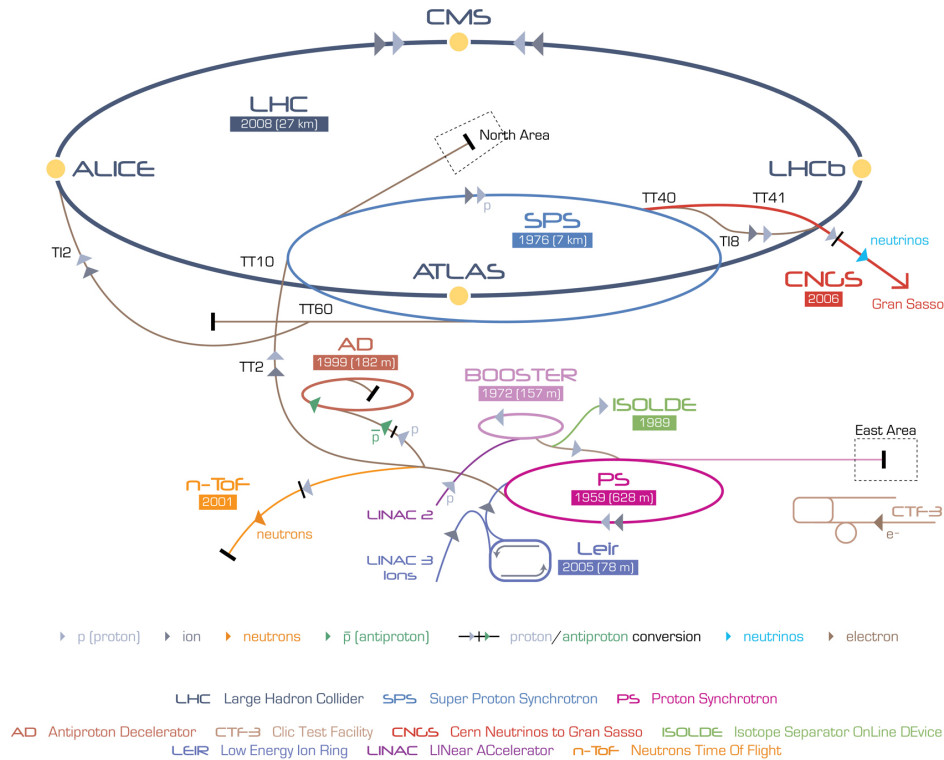
Figure 2.1: Layout of the CERN accelerator complex. Before reaching the LHC, protons are injected from the linear accelerator (LINAC2) into the PS Booster, the Proton Synchrotron (PS), and the Super Proton Synchrotron (SPS). Figure taken from [66].

is placed about 100 m underground in the 27 km tunnel previously occupied by the Large Electron-Positron, LEP, collider. It is capable of accelerating proton beams, injected from the Super Proton Synchrotron, SPS, by mean of two separate, parallel vacuum pipes in which the two proton beams are guided and accelerated in opposite directions. The performance of the accelerator is typically defined by its centre-of-mass energy, $\sqrt{s}$, which indicates the energy available for producing particles in collisions, and the luminosity, $\mathcal{L}$, which gives the rate for an interaction when multiplied by the interaction cross-section, σ. The LHC is designed to accelerate proton beams up to a centre-of-mass energy of 14 TeV with a design luminosity of $10^{34}\,\mathrm{cm^{-2}s^{-1}}$. At the design conditions, protons are packed into 2808 bunches, separated by 25 ns, with about 10^{11} particles each. In order to keep the rotating protons in orbit a high magnetic field of 8.3 T is required, provided by superconducting dipole magnets operating at a temperature of 1.9 K. However, following an accident in 2008 involving interconnections between the superconducting dipole magnets, the LHC has been operated at almost half of the designed energy, whilst the peak luminosity approached the design value in 2012. Since the pilot run in 2009, the LHC has been delivering proton-proton, pp, collision data at centre-of-mass energy of $\sqrt{s} = 7$ TeV in 2010 and 2011, and of $\sqrt{s} = 8$ TeV in 2012. Each dataset can be further divided into a number of so-called fills, with each representing one complete filling and subsequent circulation of protons within the LHC. Each fill itself contains a
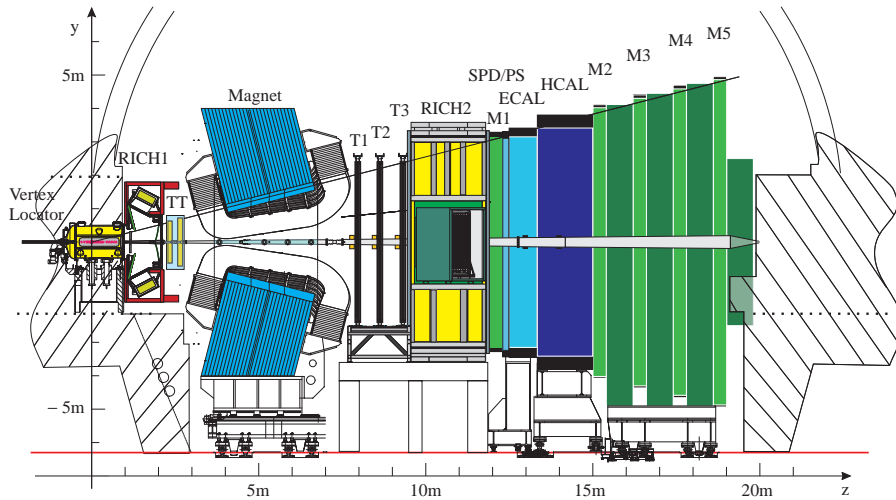
Figure 2.2: Schematic view of the LHCb detector in the y−z plane. The right-handed coordinate system used has the z axis along the beam direction pointing from the interaction point into the experiment, the y axis vertically upwards and the x axis pointing towards the outside of the LHC ring. Figure taken from [19].

number of runs which represent a single non-stop period of data taking by a particular LHC experiment. The number of bunches increased smoothly in 2010 and 2011, up to about 1300 colliding bunches and a bunch spacing of 50 ns. In 2012 the running conditions were more stable such that the delivered luminosity was about twice the one of 2011.

The beams cross at four locations that correspond to the main LHC experiments: A Large Ion Collider Experiment (ALICE), A Toroidal LHC Apparatus (ATLAS), Compact Muon Solenoid (CMS) and Large Hadron Collider Beauty (LHCb). The ALICE [67] experiment is specialised in studying the properties of QCD in heavy ion collisions. ATLAS [68] and CMS [69] are general purpose detectors which cover the full spectrum of high-energy physics. The LHCb [70] experiment is dedicated to measure the properties of b- and c-hadron decays. A schematic view of the CERN accelerator complex and main experiments is shown in Figure 2.1. ALICE and LHCb are operated at an average lower luminosity than CMS and ATLAS. This choice has the advantage that the number of collisions per bunch crossing is smaller and the particle flux within the detector is reduced. In the following the LHCb detector is described in detail.

2.2 The LHCb detector

The LHCb detector [70] is located in the cavern of the former LEP experiment Delphi. The detector layout, shown in Figure 2.2, was designed to cover the region from approximately 10 mrad to 300 (250) mrad in the $x−z$ ($y−z$) plane. This structure, which is that of a single-arm forward spectrometer, follows the forward production of the b- and c-quark pairs from pp collisions, as shown in Figure 1.4 for b quarks. Additionally,
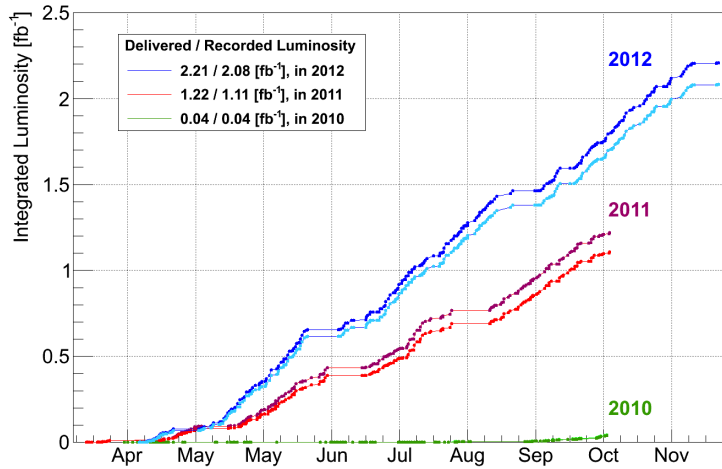
Figure 2.3: Integrated luminosity collected by the LHCb experiment during the data-taking years of 2010, 2011 and 2012. The figure shows the curves for the delivered (dark coloured lines) and recorded (light coloured lines) integrated luminosities. Figure taken from [19].

the heavy quarks in the forward region have a large boost as they originate from very asymmetric parton collisions, as explained in Section 1.4.1. Thus, their flight distance is on average longer than the one of centrally produced particles. This has a large impact on the decay-time resolution and makes it easier to distinguish the decay products of secondary particles from particles produced in the initial pp collision.

The target instantaneous luminosity of LHCb is about $2 \times 10^{32}\,\mathrm{cm^{-2}\,s^{-1}}$. In order to reach the luminosity goal, the LHCb detector is designed for an average number of inelastic pp collisions of 0.4 per bunch crossing at LHC design conditions. As the maximum number of bunches in the LHC was smaller in 2011 and 2012 with respect to the designed one, the average number of interactions per crossing was increased to about 1.5. Despite this harsh condition, with increased detector occupancies, the physics output was not compromised. The average number of interactions per crossing is changed by defocussing the two beams before the collision independently from the other experiments. The intensity of the proton beams decreases over time while particles collide, but the LHCb experiment is able to keep the instantaneous luminosity constant during a fill by shifting the beams with respect to each other.

The LHCb detector took data during Run I of the LHC in the years 2010, 2011 and 2012 with an average operational efficiency, defined as the ratio of recorded over delivered luminosity (see Figure 2.3), of 93%. Out of the recorded data, about 99% is regarded good and can be used for physics analyses. At the end of 2009 LHCb recorded a very small sample of about 7 $\mu\mathrm{b}^{-1}$ of integrated luminosity at $\sqrt{s} = 0.9$ TeV which have been used to finalize the commissioning of the detector and published its first physics result on prompt K_S^0 production [71]. In 2010, 38 pb^{-1} were recorded at $\sqrt{s} = 7$ TeV that lead to a significant amount of results, especially about b- and c-hadrons production, like the prompt charm production [4]. In 2011, 1.11 fb^{-1} were recorded at $\sqrt{s} = 7$ TeV and this corresponds to the dataset used in this thesis to

perform most of the measurements presented. In 2012, 2.08 fb^{-1} at an increased centre-of-mass energy of $\sqrt{s} = 8$ TeV were recorded. This latter dataset, in combination with the 2011 one, is used to perform the measurements of the decay width difference and of the average decay width in the B_s^0 system, $\Delta\Gamma_s$ and Γ_s, respectively.

LHCb allows the reconstruction of exclusive decays of the b and c hadrons in a variety of leptonic, semileptonic and purely hadronic final states. In order to achieve this goal and extract the physics of interest, the LHCb detector incorporates several specialised sub-detectors. They can be divided into two categories: *tracking system* and *particle identification* detectors. The track reconstruction system comprises a vertex detector, called the Vertex Locator (VELO), and four planar tracking stations: the Tracker Turicensis (TT) located upstream of the dipole magnet and three tracking (T1-T3) stations, located downstream of the magnet. Silicon microstrips are used in TT and the region close to the beam pipe (Inner Tracker, IT) of stations T1-T3, whereas a different technology is employed for the outer part (Outer Tracker, OT). Particle identification (PID) is provided by two Ring Imaging Cherenkov detectors (RICH1 and RICH2), by the calorimeter system, composed of an electromagnetic calorimeter (ECAL) with its Pre-Shower (PS) and Scintillator Pad Detector (SPD) and an hadronic calorimeter (HCAL) and finally by five muon chambers (M1 to M5), all but M1 located behind the calorimeter system. Most of the LHCb sub-detectors are built in two separable halves which can be moved out horizontally for maintenance. The individual detectors are described in detail in [70] and will be summarised in the following sections.

2.2.1   Tracking system

The purpose of the track reconstruction detectors is to measure the trajectories, so-called tracks, of charged particles and their momenta. Charged particles leave signatures in the VELO and TT before the magnet and in the T1-T3 stations after the magnet. Their trajectories are bent by the homogeneous magnetic field in between according to the particle momentum. In order to minimise the interactions of particles with the inactive material, which would lower the detection efficiency and degrade the momentum resolution, special care has been put to reduce the detector material budget. After travelling about 10 m in the LHCb detector, from the VELO to the end of T stations, a particle has traversed about 60% of a radiation length and 20% of an absorption length.

Dipole magnet

In order to measure charged particles momenta, trajectories have to be bent by the presence of a magnetic field. In LHCb this is ensured by a warm dipole magnet [72] placed between the first (TT) and the second group (T1-T3) of tracking stations. It has an angular coverage for the full LHCb acceptance and it provides an integrated magnetic field, $\int B \, \mathrm{d}l$ over $l = 10$ m, of 4 Tm. While aiming at a high magnetic field between the tracking stations in order to improve the momentum resolution, the magnet must have a very low residual field in the surrounding detectors. Thus, the design is influenced by this constraint but also by the boundary conditions of the experimental hall of LHCb. The magnet is composed of two identical coils which are disposed symmetrically with
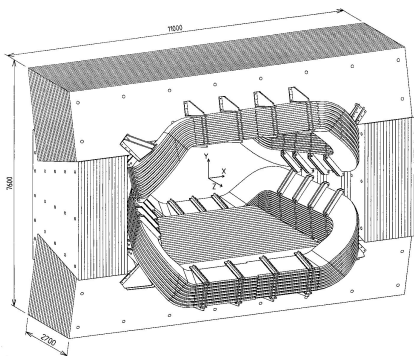
Figure 2.4: Layout of the LHCb dipole magnet. The interaction point lies behind the magnet. Figure taken from [72].
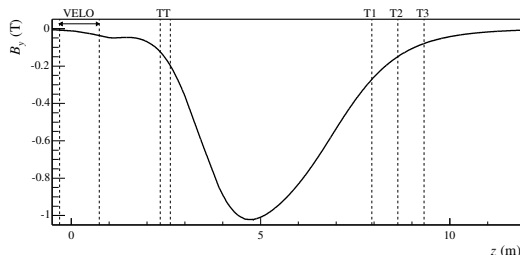
Figure 2.5: The main component B_y of the magnetic field as function z. The position of tracking detectors is indicated with dashed lines. Figure taken from [72].

respect to the horizontal plane; in Figure 2.4 a schematic layout is shown. In order to achieve the required momentum resolution ($\Delta p/p$ of about 0.5% below 20 GeV/c and 0.8% around 100 GeV/c for particles traversing the full tracking system) the integrated magnetic field has to be known with a relative precision of about 10^{-4} and the position of the peak of the magnetic field with an accuracy of few mm. The main component of the magnetic field is pointing in the y direction, B_y. It is shown as a function of the z coordinate in Figure 2.5 (b). Charged particle trajectories are then predominantly bent in the horizontal plane ($x-z$) in opposite directions. Thus, a difference in performances of the left and right sides of the detector leads to asymmetries in the reconstruction of charged particles. An important feature is that the polarity of the magnetic field is switched frequently during the data taking period so that, combining the different datasets, these asymmetries are reduced.

Vertex Locator

The VELO [73] is used to measure the trajectories of particles very close to the interaction region. This information ensures an accurate reconstruction of the vertex positions, enabling a separation of the secondary vertices due to b- and c-hadron decays from the primary vertex (the location of the pp interaction).

The VELO detector consists of 21 stations of silicon detectors, see Figure 2.6. Each station comprises two modules on opposite sides of the detector. One module has two detectors, an R detector and a Φ detector, mounted back to back. The R sensor measures the radial coordinate, r, of the trajectory with circular-shaped strips, subdivided into four 45° sectors. The Φ sensor has strips in approximately radial direction subdivided into two regions, inner and outer, to determine the azimuthal angle of the trajectory, ϕ, defined as the angle between the x-axis and a direction vector in the $x-y$ plane. The strip pitch varies from 40 μm to 100 μm, with the finer granularity close to the beam. The inner strips are placed at 20° angle with respect to the radial direction, while outer strips are at an angle of 10°. The Φ sensors are mounted such that adjacent sensors face opposite directions, such that the strips in adjacent sensors have a stereo angle with respect to each other. This measure improves the reconstruction of the tracks in
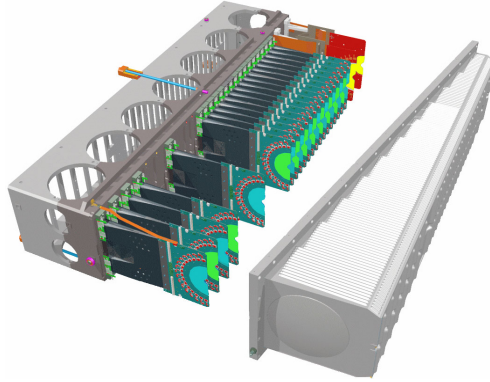
Figure 2.6: A schematic view of the LHCb VELO showing the modules with the silicon sensors on the left and the RF encapsulation on the right, for one half of the detector. Figure taken from [19].
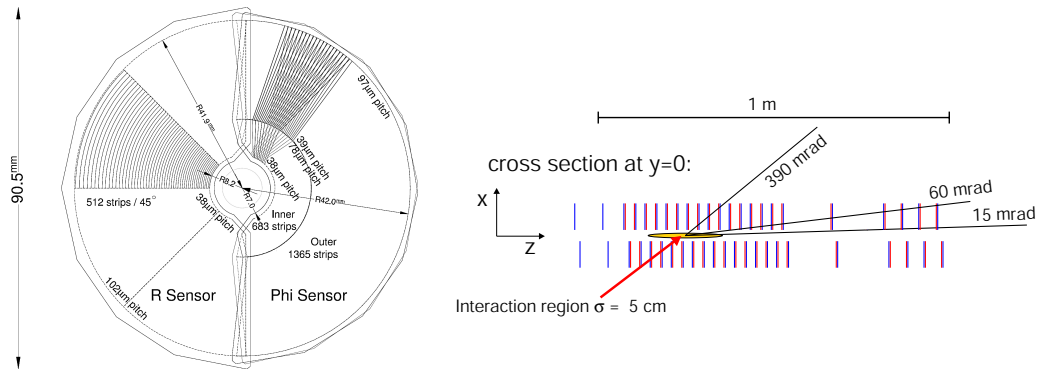
Figure 2.7: A sketch of the lay-out of R and Φ sensors. Figure taken from [73].

Figure 2.8: The placement of VELO modules, top view. Figure taken from [73].

the VELO. The layout of both types is shown in Figure 2.7. Readout for both sensor types is placed at the outer radius. The third coordinate, Z, needed to measure the 3D position of the tracks and vertices is provided by knowledge of the z position of each sensor plane within the experiment.

A sketch of the VELO setup can be seen in Figure 2.8. While covering just 1.8% of the solid angle, it allows to reconstruct roughly 27% of $b\bar{b}$ produced in the pp collisions. Dense packing of modules near the pp interaction point ensures that at least three VELO stations are crossed by a particle within the LHCb angular coverage. It also reduces the average extrapolation distance from the first measured point to the primary vertex, increasing the precision on the position of the vertices. For this reason, the sensitive area is placed at a radial distance of only 7 mm from the beam. However, this does not allow a safe LHC beam injection, therefore the two halves of the VELO can be moved apart whenever needed. Due to this, the position of the sensors has to be optimised, even on a fill by fill basis, to have their centres coinciding with the beam. There is a
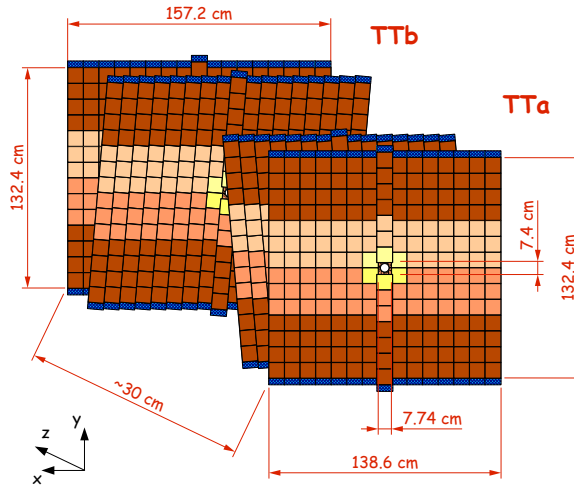
Figure 2.9: Schematic view of the Tracker Turicensis. The readout electronics is indicated in blue. The other colours correspond to different readout sectors. Figure taken from [74].

small overlap between the two detector halves when closed. This aids alignment and ensures the full angular coverage is maintained. The sensors are mounted in a vacuum vessel and are located in a secondary vacuum, about 10^{-4} mbar, separated by the LHC machine Ultra High Vacuum, 10^{-8} mbar, by an RF-box. The surface facing the beam is the so-called RF foil. It is a very thin, 0.3 mm, layer of aluminium to minimise as much as possible the material budget. Nevertheless, the RF foils account for about 40% of the VELO material budget and, thus, significantly degrade the resolution due to multiple scattering.

Silicon trackers

The Silicon Tracker (ST) comprises two detectors: the TT [74] and the IT [75]. They use silicon microstrips with a strip pitch of about 200 μm. Silicon strips offer a good hit resolution and fast response time, needed to operate in regions of high track density and radiation levels. Each of the ST stations is composed by four detector layers with the so-called $x-u-v-x$ arrangement of strips directions. In the TT the four detection layers are arranged in two pairs, (x, u) and (v, x). First and fourth layers have vertical strips, while $u-v$ have layers with strips rotated by $\mp 5°$, respectively. This layout is designed in order to have the best hit resolution along the bending plane, without loosing the stereo view of the tracks.

Tracker turicensis   The geometry of the TT is shown in Figure 2.9. It is about 150 cm wide and 130 cm high and the layers are built up from half modules which themselves consist of seven silicon sensors. The single hit resolution of the TT is about 50 μm. The detector is divided into different readout sections, since the occupancy close to the beam is much higher than in the outer regions. Hits in this detector are used to reconstruct the decay products of long-lived particles, such as the K_S^0 and the Λ, that
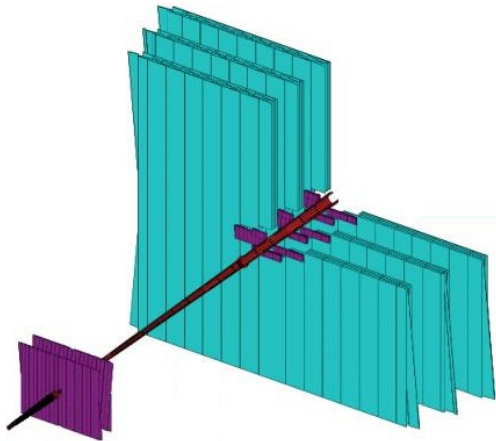
Figure 2.10: Layout of the Outer Tracker (light blue) together with the beam pipe (brown), the TT and the Inner Tracker (purple). Figure taken from [76].
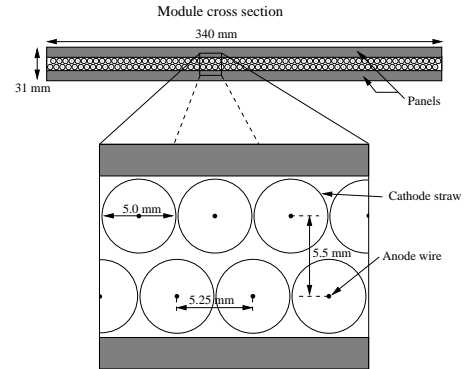
Figure 2.11: Cross section of a straw-tube inside an OT module. Figure taken from [76].

decay mainly outside the fiducial volume of the VELO. Furthermore, the TT allows for the reconstruction of low momentum tracks that are steered out of the detector acceptance by the magnet before reaching the downstream tracking stations.

Inner tracker   The IT covers a 120 cm wide and 40 cm high region. It forms the inner-most area of tracking stations T1-T3, see Figure 2.10, where particle flux is higher $(\sim 5 \times 10^5 \, \text{cm}^{-2} \, \text{s}^{-1})$. Each of the three IT stations is composed of four detector boxes disposed around the beam-pipe in a cross shape. Although this formation only covers 1.3% of the total active area of each tracking station, almost 20% of all charged tracks produced close to the interaction point and traversing the full tracking system pass through this region. Each detector box contains 4 layers of detectors, in the already described $x-u-v-x$ configuration.

Outer tracker

The OT [76] covers the remaining part of the tracking stations T1-T3, as shown in Figure 2.10. It is a drift-time detector which employs straw tubes. Each of the three stations consists of four modules, arranged in the $x - u - v - x$ geometry. Each module contains two staggered layers of drift tubes, see Figure 2.11. The drift tubes are oriented vertically in order to perform better measurements in the bending plane of the experiment. A 25 μm thick wire serving as anode is located in the centre of each straw. The drift tube diameter, 5 mm, and the gas mixture used allow for a drift time across the tube of less than 50 ns and a sufficient drift-coordinate resolution (200 μm). The detector services and supports for the OT are located outside the LHCb acceptance, hence the material budget (3.2% of a radiation length per station) is dominated by the active part of the detector.
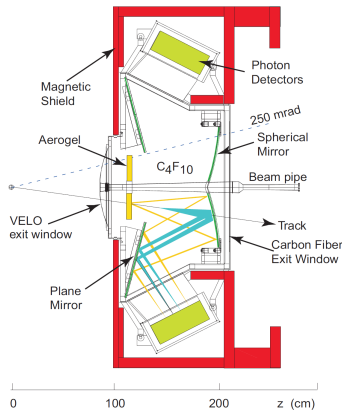
Figure 2.12: Layout of the RICH1 detector, side view. Figure from [77].
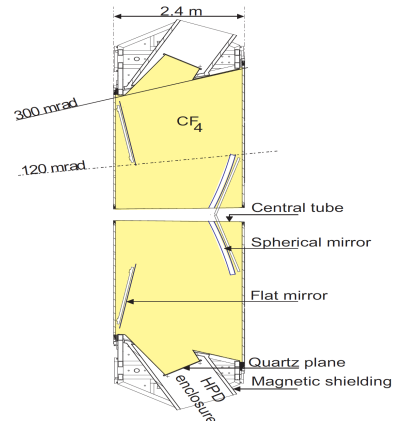
Figure 2.13: Layout of the RICH2 detector, side view. Figure from [77].

2.2.2 Particle identification system

The scope of the particle identification (PID) detectors is to distinguish the different particle species that traverse the LHCb detector. The b hadrons decay mainly in kaons, pions, protons and muons. Since pions are the most abundant particles produced in pp collisions at the LHC, it is crucial to separate them from the other species, in order to suppress combinatorial background. Moreover, muon identification is of primary importance to further reduce the combinatorial background in analyses where the final states include a J/ψ decaying into two muons. Finally, calorimeter is important in order to measure particles energy and for neutral hadrons and photons detection. The particle identification consists of three systems: The RICH detectors, the calorimeter system and the muon stations.

The RICH detectors

The Ring-Imaging Cherenkov (RICH) detectors [77] use the Cherenkov effect to discriminate between pions, kaons and protons. Charged particles emit photons passing through a medium of refraction index n with a velocity, v, larger than the speed of light in that medium ($c' = c/n$). The medium is called radiator. Photons are emitted along a cone with the opening angle, θ_c, given by $\cos\theta_c = 1/(\beta n)$, where $\beta = v/c$. Combining the measurement of the opening angle with the measured momentum, p, from the tracking system allows to calculate the particle's mass, m, as

$$\cos\theta_c = \frac{E}{p\,c\,n} = \frac{1}{n}\sqrt{1 + \left(\frac{mc}{p}\right)^2},\tag{2.1}$$

where E is the particle's energy.

There are two RICH detectors that cover different momentum ranges. The RICH1, placed before the magnet, covers the low momentum range ($\sim$ 2-60 GeV/c), using areogel and C_4F_{10} as radiators. The RICH2, placed downstream of the magnet behind the tracking stations, covers the high momentum range (from $\sim$ 15 GeV/c up to 100 GeV/c
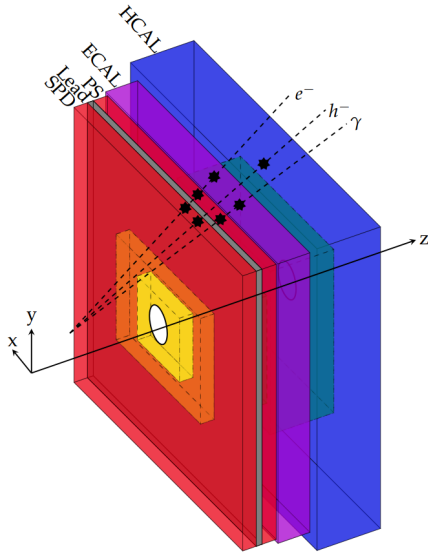
Figure 2.14: Layout of the SPD/PS, ECAL and HCAL showing the segmentation and the interactions of different particle species. Figure from [80].
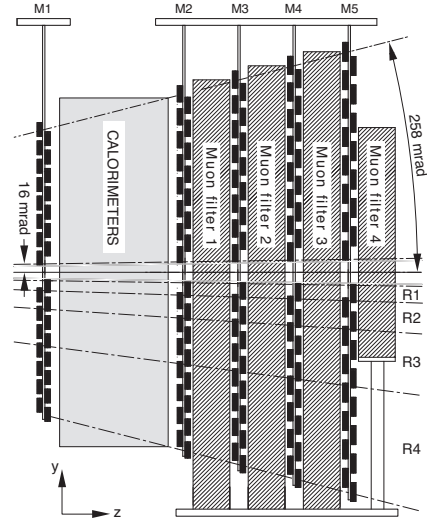
Figure 2.15: Schematic view of the muon system in the y−z plane. Figure from [81].

and beyond) using CF_4 as radiator. The RICH1, shown in Figure 2.12, covers a very wide acceptance region, from ± 25 mrad to ± 250 mrad and ± 300 mrad in the vertical and the horizontal plane, respectively. The RICH2, shown in Figure 2.13, has a limited angular acceptance coverage, from ± 15 mrad to ± 100 mrad and ± 120 mrad in the vertical and the horizontal plane, respectively, but covers the forward region where high momentum particles are mainly produced. Both RICH detectors use a combination of flat and spherical mirrors in order to focus the Cherenkov light on Hybrid Photon Detectors (HPDs), placed outside the acceptance. These detectors reveal photons in the visible spectrum (200-600 nm) and are shielded with iron from the external magnetic field. As an example, the identification efficiency for kaons is almost 95%, with about 5% probability of misidentification of pions. More information on the RICH performance can be found in [78, 79].

Calorimeter

The calorimeter system [82] consists of four detector components, the SPD, the PS, the ECAL and the HCAL calorimeters. It performs many functions: It allows to distinguish electrons, photons and hadrons, as visualised in Figure 2.14, and to measure their energy and position. The measurement of the energy deposited by these particles is also used as an input for the first stage of the trigger system (see Section 2.3). All four detectors are built of alternating plates of absorbing material, lead or iron, and scintillating plates. When a particle deposits parts of its energy or is stopped in the absorber material, energy is released in the form of charged particles and photons. The released energy is converted to photons in the scintillating material. The photons, after having been conducted through wavelength-shifting fibres, are detected

by photomultipliers. The number of detected photons is proportional to the original particle's energy. For an optimal energy resolution, electromagnetic showers from high energy photons have to be fully contained by the ECAL, which has been designed to have a thickness of 25 radiation lengths. On the contrary, for triggering on hadrons, such a good energy resolution is not needed. So, the HCAL thickness is only 5.6 interaction lengths, minimising the occupied space. The whole calorimeter system is segmented in the $x-y$ plane and, due to the larger particle density close to the beam pipe, the segmentation increases in dimension moving away from the beam-pipe with a projective design.

Electromagnetic calorimeter   The SPD/PS are installed directly behind the first muon station. They consists of a 15 mm thick lead converter placed between two almost identical rectangular scintillators. The SPD allows to separate electrons from photons as only charged particles produce scintillating light in the first scintillator. The lead converter, corresponding to 2.5 radiation lengths, initiates electromagnetic showers. The scintillator installed right after allows to discriminate electrons from the overwhelming background of charged and neutral pions as hadrons initiate only small showers in this detector. The ECAL consists of 66 alternating layers of 4 mm thick scintillator and 2 mm thick lead panel, in the plane normal to the beam direction.

Hadronic calorimeter   The HCAL is used for the detection and measurement of the energy of hadrons such as pions and kaons for the first level trigger. It has a similar structure to the ECAL, with alternating layers of iron and scintillator tiles, the latter parallel to the beam axis. The HCAL has the same acceptance coverage as the ECAL.

Muon stations

Muon detection and identification is fundamental in LHCb both for triggering and for the reconstruction of many different decay modes. As muons are long-lived and minimum ionising particles, the muon stations are the last detector along the beam line. The muon system [81] consists of five stations, see Figure 2.15, with angular acceptance from 20 (16) mrad to 306 (258) mrad in the bending (non bending) plane. The first station, M1, is installed before the calorimeter system and its main purpose is to improve the measurement of the transverse momentum in the trigger. The remaining four stations, M2-M5, are placed at the end of the detector and are spaced out by iron absorbers 80 cm thick, in order to avoid the penetration of hadrons. Only muons with a momentum larger than 6 GeV/c cross the entire muon detector since the total thickness of all absorbers (calorimeter and muon system) amounts to 20 interaction lengths. The first three muon stations have a very high spatial resolution in the bending plane in order to measure the direction of the track and the transverse momentum of the muon candidate with a resolution of 20%. The last two stations have a limited spatial resolution, since they are mainly built to identify the muons passing through the detector. The stations consist of Multi-Wire Proportional Chambers, except for the region of M1 close to the beam axis, where a higher particle rate is expected. There, Gas Electron Multipliers are used, since they have a larger radiation tolerance.
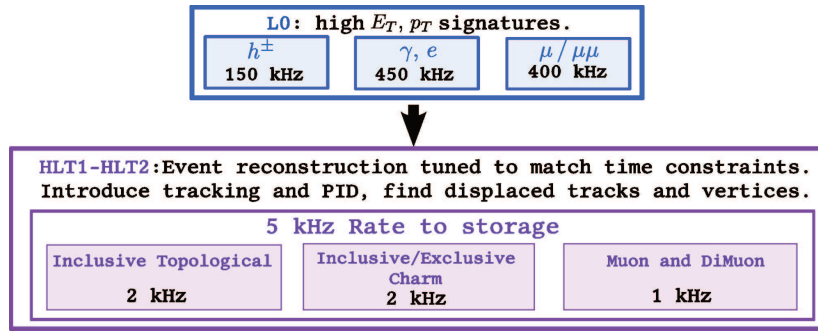
Figure 2.16: Working principle of the LHCb trigger system.

2.3 Trigger system

The nominal LHC rate, including empty bunches, is 40 MHz. This rate is too large to allow data to be written to storage. The main goal of the trigger is to reduce this rate to about 5 kHz, keeping the most relevant pp interactions for subsequent physics analysis. In particular, LHCb is mainly interested in heavy flavour physics and the signatures of these decays are the presence of high transverse momentum (p_T) tracks, high transverse energy (E_T) in the calorimeters and displaced vertices, because b and c hadrons fly on average over few centimetres before they decay. Moreover, the presence of displaced vertices implies that some of the decay products have a large displacement from the pp interaction vertex.

The LHCb trigger system [83] consists of two stages, as shown in the scheme in Figure 2.16:

1. *Hardware Level-0 Trigger*, L0. It reduces the event rate to about 1 MHz: around 450 kHz for events triggered by charged hadrons, 400 kHz for events triggered by muons and 150 kHz for events triggered by electron and photons. This is the maximum rate at which the detector can be read out. Two independent systems are used to select those particles: the L0-muon trigger and the L0-calorimeter trigger.

   The `L0-calorimeter` trigger uses the energy deposit in SPD, PS, ECAL and HCAL. The decision to trigger an event is positive if the transverse energy in a cluster of 2×2 cells is above a certain threshold. The transverse energy of a cluster is defined as $E_T = \sum_{i=1}^{4} E_i \sin \theta_i$, where E_i is the energy deposited in cell i and θ_i is the angle between the z axis and the line that connects the cell centre with the average pp interaction point. Hadrons, photons and electrons are distinguished depending on which calorimeter system the particle is leaving its energy (see Section 2.2.2).

   The `L0-muon` trigger selects the two muons with the highest transverse momentum in each quadrant of the muon stations. The hits in the muon stations are used to reconstruct the muon track. The track direction is then used to estimate the transverse momentum of the muon candidate, assuming it is coming from the pp interaction point and a single kick in the magnetic field. The corresponding event is accepted by the trigger if one of the two transverse momenta or the product of

both is above a certain threshold.

If one of the above L0 trigger decisions is positive, the information of all sub-detectors is read out by the data acquisition system (DAQ). The `L0-muon` efficiency for $B \to J/\psi X$ decays, where the J/ψ meson decays into two muons, is around 70% for $p_T (J/\psi) \approx 1 \, \mathrm{GeV}/c$ and more than 95% at $p_T (J/\psi) \gtrsim 4 \, \mathrm{GeV}/c$ [83].

2. *Software High Level Trigger*, HLT. All events that pass the L0 trigger are processed by the software based HLT. Being completely software based the HLT is flexible and can be changed to vary with beam conditions, energy, luminosity, and physics requirements. It consists of two subsequent stages, the HLT1 and the HLT2. The HLT1 performs a partial event reconstruction to reduce the rate to 40-80 kHz. The HLT2 uses almost fully reconstructed events to reduce the rate to about 3 kHz in 2011 and about 5 kHz in 2012. These events are written to storage and, hence, are available for physics analyses. The HLT uses reconstruction algorithms close to the off-line reconstruction but simplified in some places to meet the timing requirements. Since LHCb performs a wide range of physics analyses, each of them uses a specified trigger configuration, also referred to as trigger lines, that process specific reconstruction methods and selection criteria.

More information on the trigger strategy for the decays analysed here is given in Chapter 5.

2.4   Summary

The essential information of this chapter is briefly summarised here.

- The LHCb experiment is a forward spectrometer dedicated to b- and c-hadrons physics.

- Two beams of protons are accelerated in opposite directions by the Large Hadron Collider. They collide with a centre-of-mass energy of $\sqrt{s} = 7 \, \mathrm{TeV}$ in 2011 and $\sqrt{s} = 8 \, \mathrm{TeV}$ in 2012.

- The tracking detectors that allow to reconstruct the trajectory, the momentum and possibly the decay vertex of a track, as well as the position of the primary proton-proton collision are: The vertex detector (VELO), the Tracker Turicensis (TT) located upstream of the dipole magnet and three tracking (T1-T3) stations, located downstream of the magnet.

- The VELO is a silicon microstrip detector that surrounds the proton-proton interaction region. It measures the trajectories of particles close to this region.

- The particle identification is provided by two Ring Imaging Cherenkov detectors (RICH1 and RICH2), by the calorimeter system and by five muon chambers (M1 to M5).

- The trigger system, composed by a hardware stage (L0) and two software stages (HLT1 and HLT2), allows to reduce the rate from 40 MHz to about 5 kHz, keeping the most relevant proton-proton interactions for subsequent physics analysis.

Event reconstruction

Quality is never an accident; it is always the result of intelligent effort.

— John Ruskin

Charged particle trajectories are reconstructed in LHCb as so-called tracks combining the position information, hits, coming from the different tracking detectors (VELO, TT, IT and OT). The aim of this chapter is to give an overview of the algorithms that are used in LHCb for track reconstruction. Moreover, it is briefly outlined how the reconstructed tracks are linked to the information from the particle identification systems to determine the particle species. The overall reconstruction efficiency of a certain decay channel scales with the track finding efficiency to the power of the number of tracks. Thus, obtaining a high track reconstruction efficiency is particularly important for $H_b \to J/\psi X$ decays, which have many particles in the final state.

The track reconstruction in the VELO is analysed in greater detail. The algorithm used to reconstruct tracks in the VELO introduces a dependence of the reconstruction efficiency on the b-hadron decay time. The correction of this effect is the main challenge of the lifetime measurements presented in this thesis, as it is explained in Chapter 6.

3.1 The LHCb software

The LHCb software is based on the GAUDI framework [84]. Three main software packages are needed to perform an analysis with the data taken by the LHCb experiment.

- **Brunel** The data that have been selected by the trigger system are available for the so-called *off-line reconstruction* process, which is done centrally by the LHCb computing team. It is performed by the BRUNEL software package [85]. It allows the reconstruction of charged tracks by combining the hits from the tracking system. Moreover, BRUNEL also links the particle identification information from the RICH, calorimeter system and the muon chambers to the tracks.

- **DaVinci** The analysis software package DAVINCI [86] applies particle hypotheses to tracks creating the stable particles used to form the decay chain of interest. Within this process the decay tree fitter (DTF) [87] uses the particle tracks built

in the previous step in BRUNEL as inputs and fits simultaneously all vertices specified in the signal decay chain. Moreover, different selection requirements can be applied to increase the signal purity of the sample. The decay tree fitter will be explained in Section 4.2.

- **Moore** The software trigger is implemented in the MOORE [88] software package. The so-called *on-line reconstruction* process is kept as much as possible similar to the off-line reconstruction. Thus, it shares most of the reconstruction and selection algorithms with the BRUNEL and DAVINCI projects. Nevertheless, due to timing requirements in the software trigger, some simplifications are necessary.

The files produced by the reconstruction software are extremely large (about 500 TB in total), so it would be prohibitively resource-intensive to allow LHCb users direct access to them. Therefore, each analysis group can define selection requirements, the so-called stripping selection, with the aim of selecting the events of interest. These stripping selections are then centrally run over the files and the events passing these selections are stored. The output of the stripping is a new file of a more manageable size which can be processed by individual users applying the final selection. The *off-line selection*, including the stripping and the final selection, is discussed in detail for the signal decays used in this analysis in Chapter 5. To profit from improvements in the various reconstruction algorithms, detector calibrations and detector alignments, the raw data are periodically reprocessed as required, typically twice a year, as part of a full scale stripping campaign.

The LHCb Monte Carlo simulation framework   Simulated Monte Carlo (MC) data sets are useful to test analysis strategies and to assess systematic uncertainties. The full MC simulation is done using the following software packages which are built on the GAUDI framework.

- **Gauss** Simulated events are generated using the GAUSS [89] software package. In Monte Carlo, *pp* collisions are simulated using PYTHIA 6.4 [90] with a specific LHCb configuration [91]. Decays of hadronic particles are described by EVTGEN [92], in which final state radiation is generated using PHOTOS [93]. The interaction of the generated particles with the detector and its response are implemented using the GEANT4 toolkit [94] as described in Ref. [95].

- **Boole** The output of the simulated interactions of the particles with the detector is digitized by the BOOLE [96] software package which simulates the detector response.

- **Moore, Brunel and DaVinci** All individual steps of the trigger decision, track reconstruction and analysis software are performed in the same way as on data.

3.2   Track reconstruction at the LHCb experiment

The first step in the track reconstruction is the so-called *pattern recognition* which tries to identify a track, a sequence of hits produced by a charged particle while traversing the detector. The following track types are defined, see also Figure 3.1.
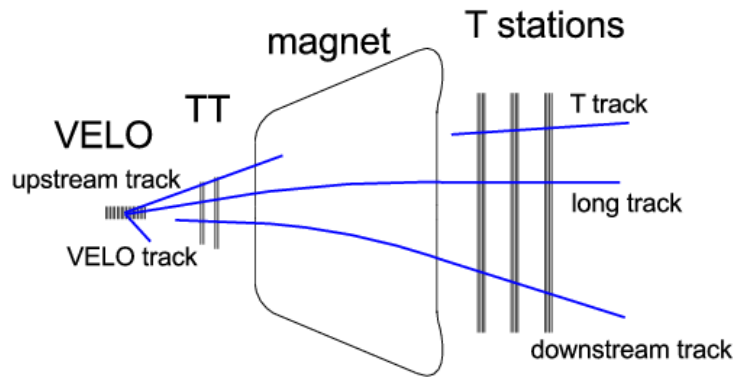
Figure 3.1: Schematic view of the different track types used in LHCb. Figure taken from [97].

- **VELO tracks** contain only information from the VELO. They are used as an input to form Long and Upstream tracks. VELO tracks that cannot be extended as Long or Upstream tracks, typically large angle or backward tracks, can be useful to reconstruct the primary *pp* collision vertex.

- **Long tracks** are associated to particles that traverse the full tracking system. They are formed by a combination of the hits coming from all tracking detectors, from the VELO to the T stations[1], and thus have the most precise momentum resolution. Hence, they are commonly used in most of the physics analysis.

- **Upstream tracks** correspond to particles that are not reconstructed in the T stations or that traverse only the VELO and TT stations. This happens in general for low momentum tracks, since their trajectories are bent out of the detector acceptance by the magnetic field.

- **Downstream tracks** use the hits of the TT and T stations. Usually they are important to reconstruct the decay products of long lived resonances which mostly decay after the VELO, like the K_s^0 or the Λ.

The main algorithm used to reconstruct Long tracks, the so-called *forward tracking*, starts with a search in the VELO detector for straight lines. Subsequently, it exploits a Hough Transform approach [98] to extend VELO tracks in the T stations and pick up hits there. The algorithm that performs the pattern recognition in the VELO is contained in the FastVELO package [99] and it is described in the next section.

The second step in the track reconstruction includes the usage of a Kalman Filter [100] to reconstruct more precisely the trajectory of a particle from the collected measurements. It takes into account effects from multiple scattering and energy loss due to ionization. The χ^2 per degrees of freedom, $\chi^2_{\text{track}}/\text{nDoF}$, of this fit gives a measurement of the quality of the track. It is used to decrease the amount of tracks which do not correspond to a real particle since they contain measurements from several

---

[1]Hits in the TT are added if they are found, but are not necessary to form a Long track.
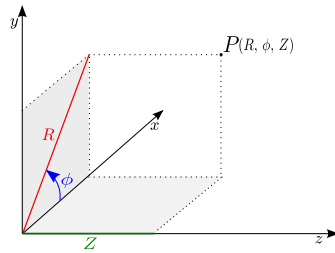
Figure 3.2: A schematic view of the R, φ and Z coordinates of a track in the VELO.

particles or detector noise, so-called ghosts.

The last step consists in the removal of duplicate tracks, so-called clones, which share more than 70% of the hits among themselves. Only the track with the best quality is kept.

3.2.1   Pattern recognition in the vertex detector

In Section 2.2.1 the design of the VELO has been summarised. It is made of two types of silicon sensors, R sensors with strips at constant radius, and Φ sensors with almost radial strips, see Figure 2.7. There are two main assumptions behind the VELO pattern recognition. First, charged-particle tracks are to a good approximation straight lines, due to the negligible magnetic field inside the VELO. Second, they originate from the primary pp interaction region, the so-called primary vertex (PV). These assumptions are needed since the same software package is used also in the trigger. Thus, it has to fulfill tight time constraints and to be very effective suppressing the background. A detailed discussion of this algorithm is beyond the scope of this thesis. However, it is instructive to list in a qualitative way the main features of this algorithm which are relevant to understand the studies described in Chapter 6.

In the FastVELO package [99], the VELO track reconstruction is executed in two subsequential steps: first, a so-called RZ track is formed and then ϕ measurements from the Φ sensors are added in order to obtain a three dimensional track. The R coordinate of a radial strip is defined as the radial distance between the beam axis and the strip itself. The coordinate Z is instead the position of each VELO module along the beam axis. A schematic view is visible in Figure 3.2.

Tracking in R-Z   Most particles are coming directly from the pp interaction point. This means that in the $R-Z$ projection their tracks are straight lines, see Figure 3.3 and Figure 3.4. In this step, only the information coming from the R sensors is used. There are different algorithms available to form a RZ track. The first one starts with four R sensor clusters, so-called quadruplets. The second one is used to reconstruct tracks starting with three R sensor clusters, so-called triplets, but using only unused clusters from the previous step. In order to be sufficiently fast, in the first stage of the software trigger, the HLT1, only the first of these algorithms is used. The second algorithm is instead used in the second stage of the software trigger, the HLT2, and subsequently in the off-line reconstruction.
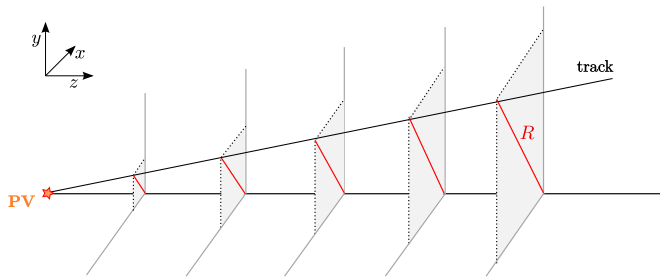
Figure 3.3: A schematic view of the R and Z coordinates of a track that originates from the primary interaction region traversing the VELO detector.
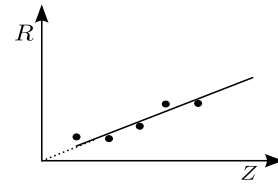
Figure 3.4: $R - Z$ projections of the hits of a track that originates from the primary interaction region.

The R quadruplets are searched starting from the last four sensors, where tracks are most separated, allowing for some inefficiency, meaning that the four hits do not need to be on consecutive sensors but can come from four out of five consecutive sensors. Once a quadruplet is found, the track is extrapolated towards the pp interaction point including close hits in other sensors if possible, allowing again for some missing sensors in between. The R clusters used at this step are then removed so that they cannot be used as input in the subsequent steps of the algorithm. The search for a quadruplet stops if, even at the maximum allowed angle, the track would cross the beam axis far away from the luminous region.

Afterwards, triplets are searched using a similar technique. As three points are not a strong constraint to produce a straight line, using only unused hits reduces the rate of ghosts. Once a triplet is found the track is extended.

Space tracking   The RZ track is then combined with Φ sensor measurements to reconstruct a 3D trajectory[2]. A consistent set of ϕ hits is searched in the Φ sensors next to the R sensors used to reconstruct the RZ track. The starting point is the last Φ sensor which has hits. Making the assumption that the tracks come mainly from the beam line, then the ϕ coordinate of the track is always the same, see the blue track in Figure 3.5. Therefore, the Φ sensor hits with a small distance in ϕ with respect to the previous hit are selected. However, if the track is displaced, it is not insured that the Φ strip involved is the same in each module, as shown in Figure 3.5 with the red track. The track is reconstructed as a space track when at least three Φ clusters in different sensors are found, allowing for some inefficiency, namely a missing sensor. Then, the track is fitted and it has to satisfy a quality criterium, based on the χ^2 of the fit. A check is performed to identify tracks that share more than 70% of the Φ hits. If this is the case, the shortest one or the one with the lower quality is discarded.

Eventually, also a special algorithm to handle tracks not pointing to the pp interaction point is executed. In this algorithm tracks are searched using initially only unused ϕ measurements. This special algorithm, due to time constraints, is executed only in

---

[2]The design of the strips in the Φ sensor is such that they form an angle with respect to radial direction. Moreover the skew of inner and outer sections is reversed. This allows to eliminate ambiguities in the pattern recognition.
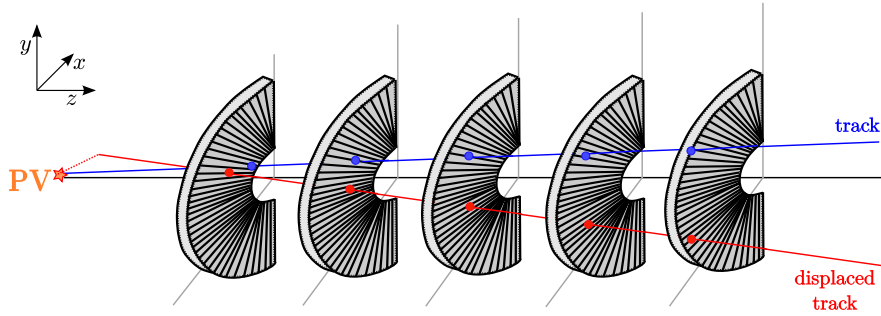
Figure 3.5: A schematic view of the Φ sensor clusters of a track that originates from the primary interaction region (in blue) and a displaced track (in red) traversing the VELO detector.

the HLT2 and in the off-line reconstruction. It is performed only if the number of already found RZ tracks is smaller than 20 or if there are less than 200 RZ tracks but more than 100 space tracks have been found. These criteria are used to ensure that the timing of this special algorithm is reasonable.

The assumptions that are done in the VELO-track reconstruction algorithm makes it difficult to reconstruct largely displaced tracks. These are often tracks associated to b-hadron decay products. A b hadron decays on average after 1 cm but in some cases it can fly up to about 20 cm before its decay. Therefore, the decay products sometimes come from a displaced vertex that is not necessarily on the beam axis or close to the primary interaction region. Similarly, and with a larger effect, decay products of long-lived particles, like the K_s^0 or Λ, are usually not coming from the pp interaction point. These tracks are usually not straight lines in the $R-Z$ projection, see Figure 3.6 and Figure 3.7. Due to these difficulties in reconstructing largely displaced tracks, the VELO reconstruction becomes slightly inefficient for large decay times of the b hadron. This effect does not affect significantly the overall VELO-track finding efficiency, which is measured to be higher than 98% as reported in the next section. However, it cause a bias when performing precision lifetime measurements that was revelead in the course of this thesis. The dependence of the reconstruction efficiency on the b-hadron decay time is examined in greater detail in Chapter 6. The understanding and the correction of this acceptance is the most crucial part of the analysis described in this thesis and it is of paramount importance for all the analyses that rely on an unbiased decay-time spectrum.

3.2.2   Reconstruction performances

The performances of the VELO on important parameters for physics analyses are reviewed in this section. The VELO-track reconstruction efficiency, the primary and secondary vertex resolution and the impact parameter resolution are briefly presented.

The measured VELO-track finding efficiency, ε, for particles traversing the whole detector is measured to be higher than 98% [101] in data collected in 2011. This efficiency is determined in data and simulated samples using a tag an probe method,
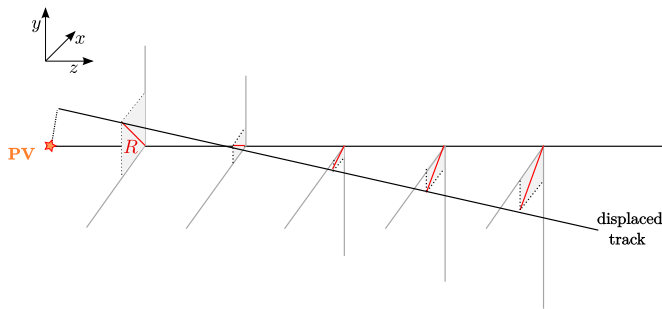
Figure 3.6: A schematic view of the R and Z coordinates of a displaced track that does not originate from the primary interaction region traversing the VELO detector.
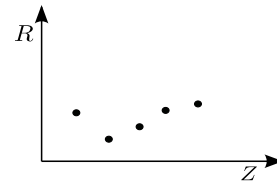

Figure 3.7: $R-Z$ projections of the hits of a displaced track that does not originate from the primary interaction region.

exploiting a large sample of $J/\psi \to \mu^+\mu^-$ available. The VELO-track finding efficiency is shown in Figure 3.8 for data and simulated samples as a function of the momentum, p, the pseudorapidity[3], η, the azimuthal angle, ϕ, and the total number of tracks in the event, N_{track}. The efficiency is weakly dependent on the multiplicity of the event, as the pattern recognition becomes more complex in a higher occupancy environment. The reduced efficiency at $|\phi| \approx \pi/2$ is caused by the extra multiple scattering from the material of the RF foil in the vertical plane. In general, it can be seen that the shape of the efficiency is quite similar in data and in simulation, but quantitatively it is not the same. Thus, depending on the precision level that is required it is not possible to rely on simulated samples.

Tracks reconstructed in the VELO are used to determine the position of the primary vertex. The numbers of tracks used to form a PV ranges from 5, the minimum number required, to around 150. The spatial resolution is found to be 13 μm in y and x direction and 71 μm in z direction [101] for a primary vertex made out of 25 tracks in 2011 data. For data with an average number of visible proton-proton interactions per bunch crossing around 1.3, the average number of tracks in an event in which a candidate B decay has been reconstructed is 120. As the number of reconstructed PVs in the event increases, the resolution degrades. The rate of degradation is approximately 5–10% per additional vertex. The PV vertex resolution for data taken in 2012 is very similar.

The spatial resolution of the b-hadron decay vertex, so-called secondary vertex, is the dominant contribution to the decay-time resolution, as it will be explained in Section 7.2. It is formed out of 2-7 tracks (depending on the final state) and thus its position is less well determined. The resolution is governed by multiple scattering of particles by the detector material, the resolution on the single measurement in the detector and the distance of extrapolation of the tracks from their first hit to the vertex position. It is dominated by the uncertainty on the longitudinal z direction, due to the boost in the forward direction of b-hadron decays, where the spatial resolution is

---

[3]The pseudorapidity is defined as $\eta \equiv -\ln\left(\tan\frac{\theta}{2}\right)$ where θ is the polar angle with respect to the beam-axis.
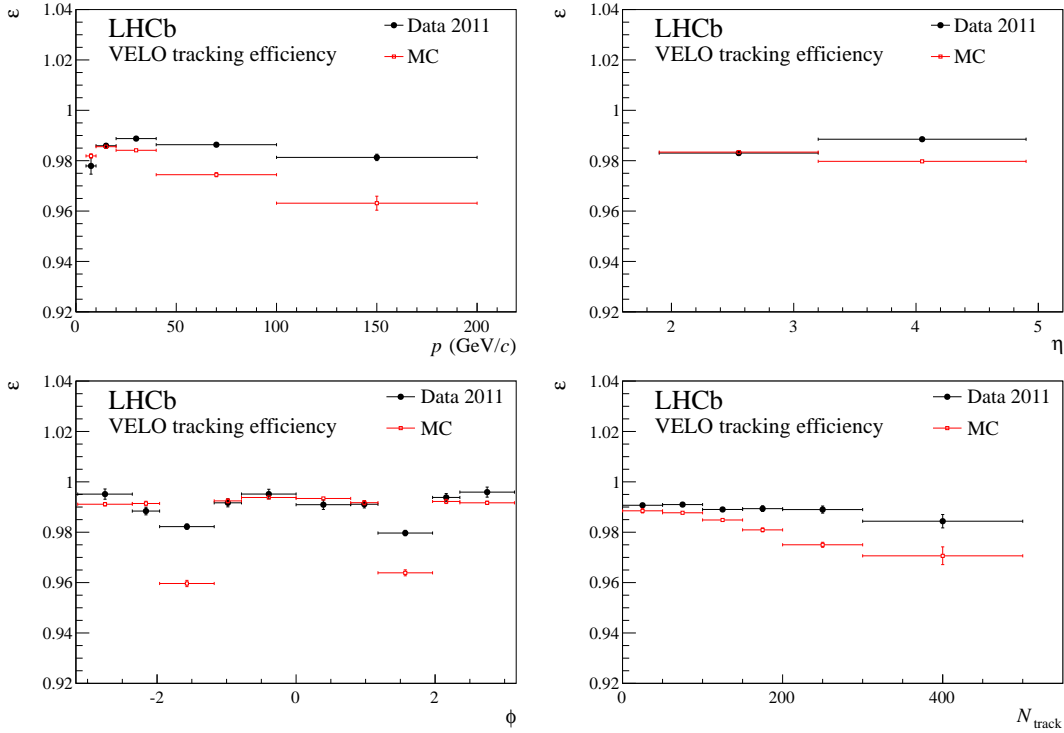
Figure 3.8: Track finding efficiency, ε, in the VELO for the 2011 data and simulation as a function of the momentum, p (top left), the pseudorapidity, η (top right), the azimuthal angle φ (bottom left) and the total number of tracks in the event, N_{track} (bottom right). The simulation has been reweighted to the number of tracks observed in data for the p, η and φ plots. The error bars indicate the statistical uncertainty. Figure from [101].

measured to be about 0.20 mm for typical *b*-hadron decays.

The impact parameter, IP, of a track is defined as the distance between the track and the primary vertex at the track's point of closest approach to the primary vertex. Selection requirements on this quantity are extensively used in LHCb analyses to reduce the contamination of background composed by tracks coming from the PV. The impact parameter resolution of a track is less than $35\,\mu$m in x and y direction for particles with transverse momentum, p_T, larger than 1 GeV/c and it tends to $\sim 12\,\mu$m at large transverse momentum. It degrades for low momenta as multiple scattering increases.

3.3   Particle identification

Particle identification in LHCb is provided by three different detector systems: the calorimeter system, the two RICH detectors and the muon stations.

In the RICH, the measurement of the Cherenkov opening angle combined with the determination of the track's momentum, allows to determine the particle's mass, see Equation 2.1. The muon identification system provides a second discriminating variable

which is based on the distance between the measurements in the muon stations and the track extrapolation. Finally the ECAL algorithm allows to distinguish electrons by matching the charged cluster released in the ECAL with the extrapolated track. The calorimeter system moreover allows to identify neutral pions and photons.

The information obtained from the RICH detectors, the calorimeter and the muon systems is combined for optimal identification of charged particle types (e, μ, π, K, p). The probability of a certain particle hypothesis, x, is calculated by associating a likelihood value, $\mathcal{L}(x)$, to the corresponding track. This likelihood value is calculated relative to the pion, since it is the most abundant particle species produced in the pp interactions at LHCb. The difference of the two logarithmic likelihood values is determined, $\Delta\ln\mathcal{L}_{x\pi} = \ln\mathcal{L}_x - \ln\mathcal{L}_\pi$. The larger this difference is the more likely the reconstructed track can be associated to a particle hypothesis x than to a pion. Pions can be selected when requiring a small or negative value of $\Delta\ln\mathcal{L}_{x\pi}$.

3.4 Summary

The essential information of this chapter is briefly summarised here.

- Different tracking detectors, the VELO, TT and T1-T3 tracking stations, allow charged particle trajectories, tracks, to be reconstructed at LHCb.

- Similar algorithms are used for the so-called on-line and off-line reconstruction of tracks in the trigger and in the subsequent off-line analysis, respectively. However, due to timing constraints in the software trigger, some simplifications or tighter requirements are necessary.

- The algorithm that performs the reconstruction of the tracks in the VELO is implemented in the so-called FASTVELO package.

- The track finding efficiency in the VELO is typically above 98%, with a dependence on the multiplicity of the event, N_{track}, the azimuthal angle, ϕ, and the momentum, p, of the track.

- Largely displaced tracks with respect to the beam line are challenging to reconstruct in the VELO, due to the assumptions made in the algorithm. This is introducing a distortion of the decay-time distribution of b hadrons which has to be corrected in order to perform precise lifetime measurements.

- Charged particles are identified at LHCb by combining the information obtained from the RICH detectors, the calorimeter and the muon systems.

- The difference of the logarithmic likelihood value of a certain particle hypothesis, x, with respect to the pion, $\Delta\ln\mathcal{L}_{x\pi}$, is determined. The larger it is, the more likely the track can be associated to a particle hypothesis x.

Part II

Measurement of the B^+, B^0, B^0_s meson and Λ^0_b baryon lifetimes and determination of $\Delta\Gamma_d/\Gamma_d$

<div style="text-align: right;">

4

</div>

Analysis strategy and tools

I like the challenge of trying different things and wondering whether it's going to work or whether I'm going to fall flat on my face.

— Johnny Depp

This chapter gives an overview of the analysis strategy for the measurement of b-hadron lifetimes. Firstly, the difficulties of the measurement are introduced. Secondly, the method used in LHCb to determine the decay time of a particle is outlined. Thirdly, the different strategies that are commonly used to deal with efficiencies that depend on the b-hadron decay time are briefly reviewed. At last, the Maximum Likelihood formalism that is used by the fit algorithm in this analysis is explained.

4.1 Lifetime measurements

The decay time, t, of a particle in its rest frame is given by

$$t = L\,\frac{m}{|\vec{p}|}\,,\tag{4.1}$$

where L is the flight distance travelled by the b hadron, p is the reconstructed three-momentum and m is its reconstructed invariant mass.

Particles have a constant decay probability therefore the decay time follows an exponential distribution[1], see Figure 4.1(a). Thus, the lifetime can be extracted by a fit to the decay-time distribution. However, several difficulties arise from an experimental point of view.

All the quantities that determine the decay time need to be measured and therefore suffer from experimental uncertainties. To first order, the resolution of the decay length depends on the production vertex resolution and the decay vertex resolution of the candidate. Furthermore, the resolution of the reconstructed mass and of the momentum depend on the momentum resolution of the final state particles. Consequently, the decay-time resolution, $\mathcal{R}(t)$, is a function of phase-space and varies for different decay modes. A typical resolution function is sketched in Figure 4.1(b) and it is examined in

---

[1]The complications that emerge due to neutral meson mixing are discussed in Section 1.5.1.
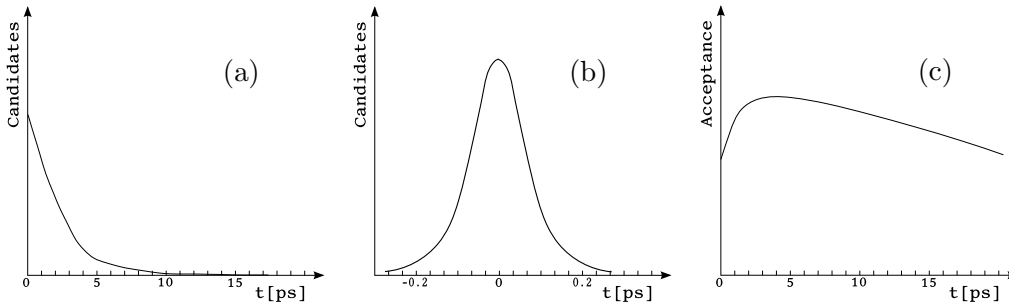
Figure 4.1: Sketches of a typical (a) decay-time distribution; (b) decay-time resolution, and (c) decay-time dependent acceptance of a b hadron.

more detail in Section 7.2. More importantly, efficiencies that depend on the b-hadron decay time can be introduced at any stage of the analysis. In particular, only the shape of these efficiencies is important and not the overall scale, since the latter can be absorbed in a overall normalisation term to which the lifetime is insensitive. Thus, in the following any decay-time dependent efficiency will be referred to as a decay-time acceptance, $\mathrm{Acc}(t)$, as depicted in Figure 4.1(c).

Taking all these elements into account, the b-hadron lifetime, τ_{H_b}, can be extracted modelling the decay-time distribution in the following way

$$\left[e^{-(t/\tau_{H_b})} \otimes \mathcal{R}(t) \right] \times \mathrm{Acc}(t). \tag{4.2}$$

where $\otimes$ denotes the convolution between the exponential decay and the resolution distribution.

In order to perform a precision lifetime measurement it is mandatory to have a good understanding of the decay-time acceptance and to correct for it. Given that the statistical uncertainty expected on the lifetime is of the order of few femtoseconds, these decay-time acceptance must be controlled to a very accurate level. This is the most demanding task of this analysis and it is introduced in Section 4.3 and explained in more details in Chapter 6.

Moreover, the decay-time distribution of a b-hadron candidate is polluted by background events. Thus, another distribution that allows to discriminate between signal and background has to be taken into account. For this purpose, the mass distribution of the b hadron is used.

4.2   Fit of *b*-hadron decay topology

In high energy physics experiments there are two standard approaches to reconstruct a decay chain that proceed via intermediate metastable states, as shown in Figure 4.2. Here, as an example, a b hadron decays into a J/ψ, which decays almost instantaneously into a pair of oppositely charged muons, and another particle X, which also decays into two hadrons, h_1 and h_2.

The first method is a so-called *bottom-up approach*. The first step is to combine all the particles in the final state, like the h_1 and h_2 hadrons in the picture, to intermediate particle, X, in order to reconstruct their production vertex, by constraining them to
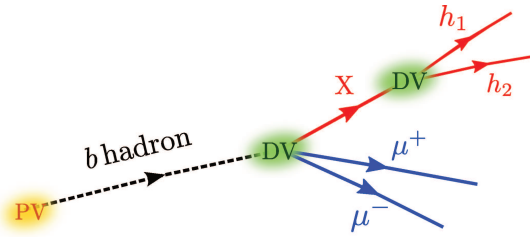
Figure 4.2: Schematic picture of a b-hadron decay chain. It is produced at the pp interaction point, PV, and it decays into a $J/\psi \to \mu^+\mu^-$ and another particle $X \to h_1 h_2$. The J/ψ and X decay vertices, DV, are highlighted.

originate from a common point. Subsequently, intermediate particles are used in turn for the reconstruction of upstream vertices and decays. However, the drawback of this method is that constraints that are upstream of a decay vertex do not contribute to the knowledge of the parameters of the vertex.

An alternative method is the so-called *decay tree fitter* (DTF) [87]. It allows to perform a fit of a complete decay tree with multiple vertices with a simultaneous determination of the position, momentum and decay time of all particles involved.

The positions of the vertices in the decay tree, and the momenta of all particles, constitute the degrees of freedom of the decay tree. Each reconstructed or final state particle is represented by a momentum vector (p_x, p_y, p_z). The mass of a final state particle is not a parameter in the fit, but it is assigned according to the particle hypothesis in the decay tree. Each intermediate particle in the decay tree is modelled by a four momentum vector (p_x, p_y, p_z, E), a decay vertex position (x, y, z) and a decay-time parameter $\theta \equiv L/|\vec{p}|$. If a composite particle has an expected decay length much smaller than the vertex resolution it shares the decay vertex position with its production vertex and does not have a decay-time parameter in the DTF. This is the case for the J/ψ particle in the decay chain. Other information can be specified in a decay tree: So-called internal constraints like the four-momentum conservation at each vertex; relations to external reconstructed objects, like tracks and the primary vertex; and additional external constraints, like mass hypotheses or constraints on the reconstructed mass of the intermediate particles. The global fit to the particle parameters is performed in terms of a Kalman Filter [100]. The χ^2 of this fit, $\chi^2_{\text{DTF}}/\text{nDoF}$, can be used to partially remove decays that originate from wrong particle combinations.

In this analysis, the decay tree fitter is used in different configurations. The decay time of the b-hadron candidate is calculated with the decay tree fitter where the momentum vector of the b-hadron candidate is constrained to point back to the pp interaction point. The reconstructed mass of the b hadron is instead determined from a decay tree fit where the intermediate J/ψ and X particles are constrained to their known masses. This improves the resolution of the b-hadron mass and avoids the introduction of correlations between the decay time and the invariant mass of the b hadron. This allows to use the b-hadron mass in order to discriminate between signal and background.

4.3   Decay-time acceptance correction

At LHCb, b hadrons are produced with an average momentum of about 100 GeV/c and have decay vertices displaced on average by about 1 cm from the primary interaction vertex. Combinatorial background candidates are produced by random combinations of tracks, which tend to have low momentum and originate from a primary pp collision vertex. Conventional selections in the trigger and in the subsequent off-line analysis exploit these features to select b-hadron candidates by requiring that their decay products are energetic and significantly displaced from the primary interaction point. A common discriminating variable is the impact parameter of a track. Usually, b-hadron decay products have an impact parameter that is different from zero, so typical selections require a minimum value for the impact parameter of final state tracks. This allow to significantly reduce the amount of combinatorial background of tracks coming directly from the pp collision vertex. However, it also rejects true b hadrons that have a small decay time such that they are indistinguishable from the background. This introduces a time-dependent acceptance which needs to be taken into account in the analysis. Moreover, there could be also implicit effects, for example at detector level a change in geometry acceptance as a function of the decay time or, as explained in Section 3.2.1, difficulties in reconstructing displaced tracks in the VELO that becomes more relevant for longer decay time.

Experimentally it is challenging to remove or correct all these acceptance effects. Two strategies are used to this purpose: a so-called *relative measurement* of the lifetime of one particle relative to a well-known lifetime particle, or a so-called *absolute measurement*, where all the effects are explicitly taken into account in the analysis.

The advantage of measuring the lifetime through a relative measurement is that the decay-time acceptances to large extent cancel in the ratio of the decay-time distributions, if the control mode has a similar decay topology (similar lifetime, number and types of particles in the final state). The disadvantage is, that there is an irreducible systematic contribution coming from the precision of the input lifetime that limits the total uncertainty.

Absolute measurements do not have this disadvantage, but on the other hand, the decay-time acceptance must be controlled to a very accurate level, especially if the expected statistical uncertainty is low compared to these effects. There are in general two ways to correct the effects introducing a decay-time acceptance. Either, the effect is eliminated at the source investigating the origin of the bias, e.g. by determining the behaviour of the VELO track reconstruction inefficiency for decay products of displaced b hadrons and correcting that behaviour in the data. Alternatively, in case of small effects, the decay-time acceptance function is measured exploiting a control sample that is not affected by the effect. Data-driven methods are usually necessary to obtain greater precision, in order to not be limited by systematic effects.

In this analysis, all lifetimes are obtained through absolute measurements. Several reasons motivated this choice. First, for some of them, like the B^+ or the B^0 meson lifetimes, the expected statistical uncertainty is below the precision of the world average. Thus, performing a relative measurement the systematic uncertainty would be clearly

dominating since there is no available control mode with a better-known lifetime. Second, the same effects that are distorting the decay time distributions of $H_b \to J/\psi X$ decays are relevant also for other analyses. Among them, there is the time-dependent angular analysis of $B_s^0 \to J/\psi\phi$ decays that is performed to measure the average decay width, Γ_s, and the decay width difference, $\Delta\Gamma_s$, in the B_s^0 system, but also the *CP*-violating phase, ϕ_s, which is one of the flagship measurements of the LHCb experiment (see Section 1.5.3). Thus, a detailed investigation of all the contributions to the decay-time acceptance is of vital importance not only for the analysis presented here, but for many others as well. Moreover, since the main effect is coming from the VELO reconstruction efficiency that is dependent on the decay time of the *b* hadron, a successful correction of this effect demonstrates a good understanding of the LHCb detector and of the reconstruction system, giving confidence to other analyses that strongly depend on it.

4.4 Maximum likelihood method

The *b*-hadron lifetimes are obtained by fitting the decay-time distribution after all effects described in the previous section are corrected for by taking the decay-time acceptance into account. The fit algorithm used in this analysis is based on the unbinned maximum likelihood technique. A data sample consists of n data points in the multidimensional observables $\mathbf{x}$. In this analysis, the measured observables $\mathbf{x} = \{m, t\}$ consist of the reconstructed invariant mass, m, of the *b*-hadron candidate and its reconstructed decay time, t. The observables distributions are modelled with a probability density function (PDF), $\mathcal{P}(\mathbf{x}|\vec{\vartheta})$, where $\vec{\vartheta} = \{\vartheta_1, \vartheta_2, ...\}$ is a set of unknown parameters. The likelihood function, $\mathcal{L}(\vec{\vartheta})$, is defined as the product of the PDFs of all reconstructed candidates

$$\mathcal{L}(\vec{\vartheta}) = \prod_i^{\text{candidates}} \mathcal{P}(\mathbf{x_i}|\vec{\vartheta}) . \tag{4.3}$$

The likelihood function is a measure for the probability to obtain the measured quantities for a given choice of parameters $\vec{\vartheta}$. The best estimate for the unknown parameters is the one that maximises the likelihood function. In practice, due to computational reasons, the negative logarithm of the likelihood function is used so that the function

$$-\ln\mathcal{L}(\vec{\vartheta}) = -\sum_i^{\text{candidates}} \ln\mathcal{P}(\mathbf{x_i}|\vec{\vartheta}) \tag{4.4}$$

is minimised during the fitting procedure. This does not affect the properties of the parameter estimation, as the logarithm is a strictly monotonically increasing function. In this analysis the minimisation is performed using the Minuit framework [102] and the fitting algorithm is based on the one developed for the analysis of $B_s^0 \to J/\psi\phi$ decays, documented in [103].

An important assumption behind this analysis is that the invariant mass, m, and the decay time, t, are assumed to be uncorrelated. As a consequence, the PDF describing

the two distributions is factorized into two components

$$\mathcal{P}(m, t|\vec{\vartheta}) = \mathcal{P}_m(m|\vec{\vartheta_m}) \times \mathcal{P}_t(t|\vec{\vartheta_t}), \tag{4.5}$$

where ϑ_m and ϑ_t are the unknown parameters related to the invariant mass and the decay-time distributions, respectively.

Finally, as already stated, the sample is polluted by background events. The PDF can be separated in one part that describes the contribution from the signal component, $\mathcal{S}_{m,t}$, and one that describes the background component, $\mathcal{B}_{m,t}$

$$
\begin{aligned}
\mathcal{P}(m, t|\vec{\vartheta}) &= f_{\text{sig}} \left(\mathcal{S}_m(m|\vec{\vartheta}_m) \times \mathcal{S}_t(t|\vec{\vartheta}_t) \right) \\
&\quad + (1 - f_{\text{sig}}) \left(\mathcal{B}_m(m|\vec{\vartheta}_m) \times \mathcal{B}_t(t|\vec{\vartheta}_t) \right) .
\end{aligned}
\tag{4.6}
$$

The fraction of signal events, f_{sig}, is given by

$$f_{\text{sig}} = \frac{N_{\text{sig}}}{N_{\text{sig}} + N_{\text{bkg}}}, \tag{4.7}$$

where N_{sig} and N_{bkg} are the number of signal and background candidates, respectively. More details about the signal and background PDFs are given in Section 5.6 and Section 7.1.

4.5   Summary and overview of the following chapters

The essential information of this chapter is briefly summarised here.

- The decay time of a particle, t, is obtained using a so-called decay tree fitter that performs a fit of the complete decay chain with multiple vertices determining simultaneously all the relevant parameters of all particles involved.

- The decay-time distribution is distorted by acceptance effects that depend on the b-hadron decay time itself.

- A correction for these effects is mandatory and has to be controlled to a very accurate level.

- The lifetime is extracted by means of an unbinned maximum likelihood fitting technique where the observables are the invariant mass of the b hadron and its decay time.

The rest of this part is organised as follows:

- In Chapter 5 the trigger and off-line selection of the various b-hadron channels is presented.

- In Chapter 6 the origin of the decay-time dependent acceptance that is introduced in the various stages of the analysis is discussed. Different techniques used to correct for the different acceptance effects are introduced and successfully validated.

- In Chapter 7 the maximum likelihood fit used to extract the b-hadron lifetimes is discussed in greater detail together with all the main fit components. The decay-time resolution and the background composition are analysed, before to present the results of the fit.

- In Chapter 8 the systematic uncertainties on the b-hadron lifetime measurements are reported.

- In Chapter 9 the measurement of the lifetime ratios and of the decay width difference in the B^0 system is presented.

Selection of signal candidates

There is no decision that we can make that doesn't come
with some sort of balance or sacrifice.

— Simon Sinek

The first step of the analysis is the reconstruction and the selection of the different b-hadron candidates in order to enhance the signal content of the sample with respect to background pollutions. The B^+, B^0 and B_s^0 mesons and the Λ_b^0 baryon are reconstructed using the exclusive decay modes $B^+ \to J/\psi K^+$, $B^0 \to J/\psi K^{*0}$ and $B^0 \to J/\psi K_S^0$, $B_s^0 \to J/\psi \phi$ and $\Lambda_b^0 \to J/\psi \Lambda$. Collectively, these are referred to as $H_b \to J/\psi X$ decays. First, the topology of these decays is introduced. Second, the selection strategy adopted to perform lifetime measurements is presented, in order to sketch the guidelines behind the subsequent sections. Third, the dataset chosen and the selection requirements applied in the trigger and in the off-line analysis are explained for all decay modes. Finally, the signal yields and mass distributions of all decay channels, after trigger and off-line selection, are given in the last section of this chapter.

5.1 Topology of *b*-hadron decays

The decay topology of the different $H_b \to J/\psi X$ decays is shown in Figure 5.1 (a) for the $B^+ \to J/\psi K^+$ decay mode, in Figure 5.1 (b) for the $B^0 \to J/\psi K^{*0}$ and the $B_s^0 \to J/\psi \phi$ decay modes and in Figure 5.1 (c) for the $B^0 \to J/\psi K_S^0$ and the $\Lambda_b^0 \to J/\psi \Lambda$ decay modes. The b hadrons are produced in the hadronisation of a b quark (or $\bar{b}$) from the pp interaction. They decay weakly, typically after few centimeters of flight distance. The majority of the b-hadron decays have a c hadron in the final state because transitions between the third and the first generation are more suppressed. Among the decay modes which guarantee that all particles are reconstructed in the final state, the most advantageous are those that include the J/ψ resonance in the final state. It decays almost "instantaneously" (the lifetime is approximately 10^{-20} s) into a pair of oppositely charged muons with a branching ratio of $\mathcal{BR}\,(J/\psi \to \mu^+\mu^-) = (5.961 \pm 0.033)\%$.[1] Although this

---

[1] The branching ratios quoted in this section are taken from [14].
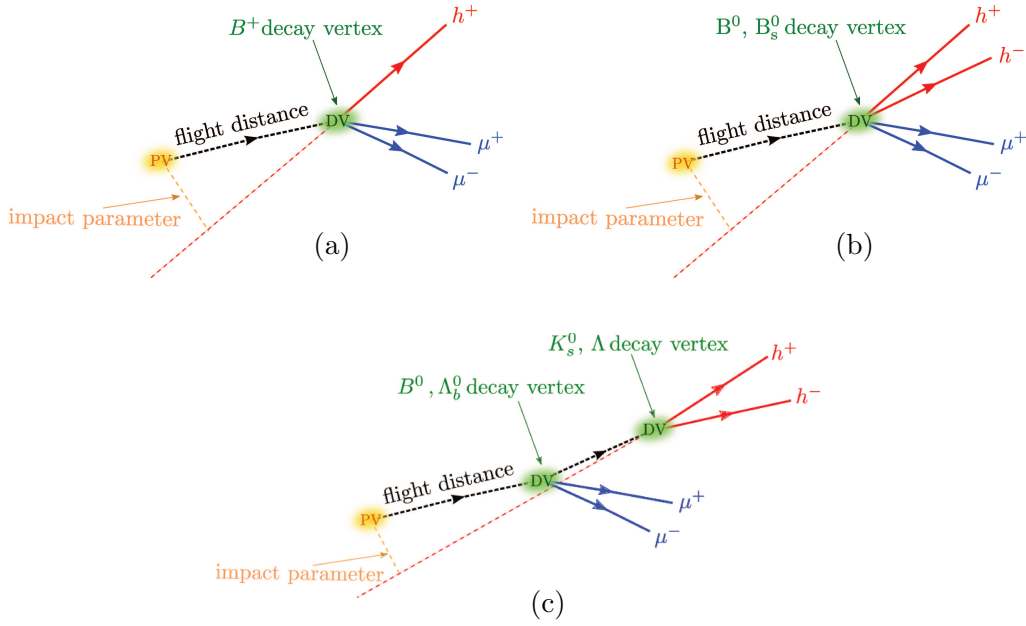
Figure 5.1: Decay topology of the different $H_b \to J/\psi X$ decays: (a) $B^+ \to J/\psi K^+$ decay mode, (b) $B^0 \to J/\psi K^{*0}$ and the $B_s^0 \to J/\psi \phi$ decay modes and (c) $B^0 \to J/\psi K_S^0$ and the $\Lambda_b^0 \to J/\psi \Lambda$ decay modes.

branching ratio is much smaller with respect to the dominant decays into hadronic final states (about 88%), the final state with two muons is much cleaner than hadrons, since the latter are more frequently produced in other processes, leading to a lower signal-to-background ratio. Due to the greater energy loss due to bremsstrahlung photons emitted and to the low resolution that can be achieved in the calorimeters, the final state with two electrons is not considered since a low reconstruction efficiency and momentum resolution is expected in LHCb. In addition, muons are reliably detected by the muon system and they have a high overall reconstruction efficiency, since they are used in all the steps of the trigger, as explained in Section 5.4.

The selected $B^+ \to J/\psi[\mu^+\mu^-]K^+$ decay mode is the one with the largest branching ratio among all of those that contain a J/ψ in the final state. It is the only decay mode used in this work with three stable[2] particles in the final state.

The selected B_s^0 decay mode is $B_s^0 \to J/\psi[\mu^+\mu^-]\phi[K^+K^-]$. The ϕ resonance decays almost instantaneously preferably into a pair of oppositely charged kaons, with a branching ratio of $\mathcal{BR}(\phi \to K^+K^-) = (48.9 \pm 0.5)\%$.

The selected B^0 decay modes are $B^0 \to J/\psi[\mu^+\mu^-]K^*(892)^0[K^+\pi^-]$ and $B^0 \to J/\psi[\mu^+\mu^-]K_S^0[\pi^+\pi^-]$. The $K^*(892)^0$ resonance decays almost instantaneously into a charged kaon and a charged pion with opposite charge, with a branching ratio of $\mathcal{BR}(K^*(892)^0 \to K^+\pi^-) \sim 2/3$. The K_S^0 is one of the two mass eigenstates of the K^0 meson[3]. It is a long-lived particle, with a lifetime $\tau_{K_S^0} = (0.8954 \pm 0.0004) \cdot 10^{-10}\, s$, flying on average few meters before it decays into a pair of oppositely charged pions

---

[2]In this context a particle is considered stable if it does not decay within the LHCb detector.

[3]Similarly to neutral B mesons, also K^0's oscillate. They are an admixture of the two mass eigenstates, K_S^0 and K_L^0, where S and L stands for short and long (referring to the lifetime), respectively.

with a branching ratio of $\mathcal{BR}\left(K_S^0 \to \pi^+\pi^-\right) = (69.20 \pm 0.05)\%$. The fact that the K_S^0 flies so much before its decay, contrary to the resonances mentioned before, means that almost two thirds of the K_S^0 decay outside of the VELO. Thus, their decay products cannot be reconstructed as Long tracks.

Finally, the selected Λ_b^0 decay mode is $\Lambda_b^0 \to J/\psi[\mu^+\mu^-]\,\Lambda[p\pi^-]$. The Λ is a long-lived particle, with a lifetime $\tau_\Lambda = (2.632 \pm 0.020) \cdot 10^{-10}\,s$, flying on average few meters before it decays preferably into a proton and a negatively charged pion with a branching ratio of $\mathcal{BR}\left(\Lambda \to p\pi^-\right) = (63.9 \pm 0.5)\%$.

The overall visible branching ratios of these channels, obtained multiplying the branching ratios of all the intermediate decays, are

$$
\begin{aligned}
\mathcal{BR}\left(B^+ \to J/\psi[\mu^+\mu^-]\,K^+\right) &\simeq 1.016 \cdot 10^{-3}\,, \\
\mathcal{BR}\left(B_s^0 \to J/\psi[\mu^+\mu^-]\,\phi[K^+K^-]\right) &\simeq 3.15 \cdot 10^{-5}\,, \\
\mathcal{BR}\left(B^0 \to J/\psi[\mu^+\mu^-]\,K^*(892)^0[K^+\pi^-]\right) &\simeq 5.30 \cdot 10^{-5}\,, \\
\mathcal{BR}\left(B^0 \to J/\psi[\mu^+\mu^-]\,K_S^0[\pi^+\pi^-]\right) &\simeq 1.8 \cdot 10^{-6}\,, \\
\mathcal{BR}\left(\Lambda_b^0 \to J/\psi[\mu^+\mu^-]\,\Lambda[p\pi^-]\right) &\simeq 2 \cdot 10^{-8}\,.
\end{aligned}
\tag{5.1}
$$

5.2 Data samples

The b-hadron lifetime measurements as well as the measurement of the decay-width difference in the B^0 system are performed using a dataset recorded in 2011 by the LHCb detector at a centre-of-mass energy of $\sqrt{s} = 7\,\text{TeV}$. Several simulated samples are used in the scope of the analysis for preparatory studies and validation of the analysis strategy.

2011 dataset   The full dataset recorded by LHCb in 2011 corresponds to an integrated luminosity of $1.025\,\text{fb}^{-1}$, of which $0.590\,\text{fb}^{-1}$ were recorded with downwards magnet polarity (magnet down) and $0.435\,\text{fb}^{-1}$ with upwards magnet polarity (magnet up). The main data samples used in the analysis are obtained from this sample after applying trigger, stripping, and additional selection requirements, which are presented in the following sections. The FASTVELO software version used for the track reconstruction is v1r5 for both the on-line and the off-line reconstruction.

Simulated dataset   Simulated datasets are a perfect benchmark for the analysis procedure. They are used to perform sanity checks of the analysis strategy and allow to access effects that influence the measurement but cannot be obtained from data. Two categories of simulated data are used: Fully simulated Monte Carlo (MC) datasets and Toy Monte Carlo (ToyMC) datasets. Fully simulated datasets are produced with the algorithms listed in Section 3.1, with trigger decision, reconstruction and software analysis performed in the same way as on data. These samples are centrally produced by the collaboration every time there are important changes in the operation conditions or in the reconstruction software in order to have a simulated sample as close as possible to the actual data taking conditions. However, the production of MC is computing intensive and is expensive in terms of storage space so typically the production happens once per year of data taking. On the other hand, Toy Monte Carlo samples consist

of pseudo-experiments where only the phenomenological distributions of interest are reproduced, without a full description of particle interactions. Therefore, they require a comparatively fast simulation time and small storage. This type of simulation is also used throughout the analysis, in particular for the validation of the fit and the estimation of some systematic uncertainties.

5.3   Event selection strategy

As discussed in Section 4.4, the major physics parameters are extracted from the decay-time distributions of the different b hadrons. The strategy of this analysis is to use a so called time-unbiased event selection. It is intended to select b-hadron candidates with minimal distortion of the decay-time distributions. These selections generally avoid cutting on variables that are highly correlated to the b-hadron decay time, such as impact parameter of final state particles with respect to primary vertices. The consequence of this strategy is that a very high level of so-called prompt background, consisting of combinations of tracks originating from the primary vertex, is kept in the region of small decay time. The prompt background is very important for the calibration of the decay-time resolution in data, as explained in Section 7.2. However, in order to increase the signal to background ratio when measuring the b-hadrons lifetimes, it is better to remove this background cutting directly on the b-hadron decay time.

In order to fulfill the tight processing time constraints, some of the already existing trigger and stripping lines that select $H_b \rightarrow J/\psi\, X$ decays include selection requirements that introduce a non-trivial acceptance in the decay-time distribution. The choice of the trigger and the stripping lines used for this analysis is driven by the size of the systematic effects on the lifetime. Only those lines that introduce a systematic uncertainty contribution that is below the expected statistical uncertainty are used.

5.4   Trigger selection

Before being available for the analysis, an event has to be selected by a specific trigger algorithm, see Section 2.3. As the trigger lines introduce efficiencies that depend on the b-hadron decay-time distribution, the strategy is to use as few lines as possible while retaining a high signal yield. The reconstruction of each of the $H_b \rightarrow J/\psi\, X$ decays is similar and starts selecting $J/\psi \rightarrow \mu^+\mu^-$ decays in the trigger.

Hardware Trigger (L0)   On the hardware stage two trigger configurations are selected for this analysis: The single–muon and the dimuon line. The former selects all the events where there is at least one muon candidate with a transverse momentum above 1.4 GeV/c. The latter selects all the events with two muon candidates that have a transverse momentum larger than 0.56 GeV/c and 0.48 GeV/c, respectively.

High Level Trigger   The subsequent software trigger is composed of two stages.

The first stage, HLT1, performs a partial event reconstruction. In this analysis the so-called `HLT1DiMuonHighMass` trigger line is used since it is the one of the lines

with the highest efficiency for signal candidates while keeping a uniform efficiency as a function of decay time. It requires events to have two oppositely charged muons. First of all, the fast on-line version of FASTVELO is executed, followed by the reconstruction of the pp interaction vertex (PV). Subsequently the tracks candidates are filtered: Only VELO track candidates which have sufficient muon hits associated are used as input to reconstruct the forward trajectory, see Section 3.2. These tracks are fitted with a fast version of the off-line Kalman fitter [100], and the corresponding $\chi^2_{\mathrm{track}}/\mathrm{nDoF}$ is required to be less than 4. The two muon tracks are then combined if their distance of closest approach (DOCA) is below 0.2 mm. The dimuon vertex is fitted and required to have a reasonable fit quality, with a $\chi^2_{\mathrm{vtx}}/\mathrm{nDoF}$ below 25. The dimuon invariant mass, $m(\mu^+\mu^-)$, is required to be larger than 2.7 GeV/c^2, the transverse muons momenta larger than 0.5 GeV/c and the muons momenta larger than 6 GeV/c.

At the second stage, HLT2, a full event reconstruction is performed, calculating the position of each PV using all available charged particles in the event. The average number of PVs in each triggered event is approximately 2.0. The longitudinal (z) position of the PVs is known to a precision of approximately 0.05 mm.

To reduce the rate of triggered events even more two strategies are used. Especially for calibration samples the strategy is to randomly select a certain amount of events using a deterministic prescale. For physics samples, if possible, different selection requirements are applied to remove events which are not interesting for the analysis. These selection requirements, however, introduce distortions in the decay-time distribution.

The line used for this analysis is the so-called `HLT2DiMuonDetachedJPsi` trigger line. Events are retained for further processing if they contain a $J/\psi \to \mu^+\mu^-$ pair, with an invariant mass within 120 MeV/c^2 of the known J/ψ mass [14], that forms a vertex, $\chi^2_{\mathrm{vtx}}/\mathrm{nDoF}$ below 25, that is significantly displaced from the PV. If multiple PVs are reconstructed in the event the PV with the minimum value of the impact parameter is associated with the J/ψ candidate. The displacement of the J/ψ candidate is estimated putting a requirement on the flight distance (FD) significance (FDS), FD/σ_{FD}, to be above 3. This selection forces the J/ψ candidate to be separated from the PV and these candidates are said to be detached. This introduces a non-uniform acceptance as function of decay time.

There is also another HLT2 line that is used in order to determine the non-uniform acceptance aforementioned, called `HLT2DiMuonJPsi`. It has exactly the same selection as the previous one but the flight distance significance requirement, such that the acceptance is uniform as function of decay time. However, in order to cope with the LHCb bandwidth limitation, this line is scaled by a factor equal to 0.2 in the second half of the 2011 data taking period.

The relevant HLT1 and HLT2 trigger line selections are summarised in Table 5.1.

The trigger line which selected an event and all detector hits which were used to form the given trigger candidate are saved when writing an event to storage. This allows to check if the off-line reconstructed signal candidate was used in the decision process of a specific trigger line. Three categories of trigger event types are defined

    1. *Triggered On Signal* (TOS): The signal under study is sufficient to trigger the

Table 5.1: Relevant HLT1 and HLT2 trigger line selections used in the analysis. If thresholds changed, they are given as first half 2011/second half 2011. A '–' implies that no requirement is applied on the corresponding parameter.

	HLT1DiMuonHighMass	HLT2DiMuonJPsi	HLT2DiMuonDetachedJPsi
$p_{\mathrm{T}}[\,\mathrm{GeV}/c\,]$	> 0.5	$-$	$-$
$p\,[\,\mathrm{GeV}/c\,]$	> 6	$-$	$-$
$\chi^2_{\mathrm{track}}/\mathrm{nDoF}$	< 4	< 5	< 5
DOCA $[\,\mathrm{mm}\,]$	< 0.2	$-$	$-$
$m(\mu^+\mu^-)\,[\,\mathrm{GeV}/c^2\,]$	> 2.7	$M_{J/\psi} \pm 0.12$	$M_{J/\psi} \pm 0.12$
$\chi^2_{\mathrm{vtx}}/\mathrm{nDoF}$	< 25	< 25	< 25
FDS	$-$	$-$	> 3
Prescale	1	$1/0.2$	1

event.

2. *Triggered Independent of Signal* (TIS): The event would also have been triggered without the signal under study.

3. *Decision Trigger* (DEC): The event is always positively triggered if there is a candidate passing the selection. It is a mixture of TOS and TIS candidates plus all of the candidates where neither the signal nor the rest of the event was sufficient to generate a positive trigger decision.

In this analysis, in order to fully control reconstruction effects, only TOS trigger lines are used to be sure that a signal candidate which is used in the analysis has been used in the trigger decision. In the case of $H_b \to J/\psi\,X$ decays and dimuon triggers, the trigger decision is TOS if both muons of the J/ψ are responsible for the trigger.

The accepted fraction of $H_b \to J/\psi\,X$ events with respect to all triggered events is about 75% when `HLT1DiMuonHighMass TOS` and `HLT2DiMuonDetachedJPsi TOS` events are considered. It reduces to about 40% when the `HLT1DiMuonHighMass TOS` and the `HLT2DiMuonJPsi TOS` trigger lines are used, due to the hard prescale of the latter.

5.5   Stripping and final selection of $b \to J/\psi\,X$ decays

Historically, so-called exclusive $B^+ \to J/\psi K^+$, $B^0 \to J/\psi K^{*0}$, $B^0_s \to J/\psi\phi$, $B^0 \to J/\psi K^0_{\mathrm{S}}$ and $\Lambda^0_b \to J/\psi\Lambda$ stripping lines have been developed to directly select the candidates of interest for each decay mode. The selection requirements included in these stripping lines were developed in order to select events without using variables directly related to the b-hadron decay time. However, in the course of this thesis, it was revealed that several decay-time acceptance effects non-trivial to correct where introduced due to the stripping selection requirements, as it will be explained in detail in Section 6.3.3 and Section 6.3.4. Thus, in order to avoid these requirements, for all the $H_b \to J/\psi\,X$ decay channels, a so-called inclusive stripping line which selects only detached J/ψ is used, namely `FullDSTDiMuonJpsi2MuMuDetachedLine`. Each J/ψ

Table 5.2: *Selection criteria used to identify $J/\psi \to \mu^+ \mu^-$ candidates. A '–' implies that no requirement was applied on the corresponding parameter. In the stripping, the J/ψ is reconstructed first in each event and is used as the common starting point for reconstructing $B^+ \to J/\psi K^+$, $B^0 \to J/\psi K^{*0}$, $B_s^0 \to J/\psi \phi$, $B^0 \to J/\psi K_s^0$ and $\Lambda_b^0 \to J/\psi \Lambda$ decays. Final refer to the value of the selection requirement used when applying the final selection to enrich the sample with signal.*

	Variable	Stripping	Final selection
$\mu^\pm$	$\chi^2_{\text{track}}/\text{nDoF}$	< 5	< 4
	$\Delta\ln\mathcal{L}_{\mu\pi}$	> 0	> 0
	p_T	> 550 MeV/c	> 550 MeV/c
$J/\psi \to \mu^+\mu^-$	$\chi^2_{\text{vtx}}/\text{nDoF}$	< 16	< 16
	FDS	> 3	> 3
	$m(\mu^+\mu^-)$	$\in [3030, 3150]$ MeV/c^2	$\in [3030, 3150]$ MeV/c^2

candidate is used as the starting point to build each of the five exclusive modes. The b-hadron candidate is reconstructed off-line adding the X candidate to every selected J/ψ candidate.

5.5.1   Selection of J/ψ candidates

The off-line sample of J/ψ meson candidates is selected by requiring each muon to have a good quality track with a $\chi^2_{\text{track}}/\text{nDoF}$ smaller than 4. This is a common value used in most of the LHCb analysis.   The muons are required to have a positive muon probability, $\Delta\ln\mathcal{L}_{\mu\pi}$ greater than 0, to minimise misidentification. Each muon is required to have a transverse momentum, p_T, greater than 550 MeV/c. This largely reduces the number of muons originating directly from the PV.

The two oppositely-charged muons are used to form a J/ψ candidate. The fit of a common vertex is required to be of a certain quality. This is achieved by selecting only those candidates with a $\chi^2_{\text{vtx}}/\text{nDoF}$ smaller than 16. The invariant mass of the two muons, $m(\mu^+\mu^-)$, must be in the range $[3030, 3150]$ MeV/c^2. Finally, the J/ψ candidate has to be displaced from the PV by more than three times its flight distance uncertainty. This requirement is the same as the one used in the HLT2 selection, however the decay-time acceptance introduced is slightly different. This is due to the fact that in the stripping, in order to choose the correct PV when several PVs are present in the event, the χ^2 of the impact parameter, χ^2_{IP}, is used instead of the impact parameter value (used in the HLT2). The impact parameter χ^2_{IP} is approximately the IP significance, IP/σ_{IP}, to the second power. In particular, off-line the PV with the minimum value of the impact parameter χ^2_{IP} is associated with the J/ψ candidate. Moreover, the position of the PV found in the off-line selection is different with respect to the on-line one, due to simplifications used in the on-line reconstruction. This is discussed in detail in Section 6.4. The requirements used to select J/ψ candidates are summarised in Table 5.2.

5.5.2   Selection of *b*-hadron candidates

The *b*-hadron candidate selection is performed by applying kinematic and particle identification criteria to the final-state tracks, the details of which are reported in Section 5.5.3 to Section 5.5.7. No requirements are placed on variables that are highly correlated to the *b*-hadron decay time, thereby avoiding the introduction of additional biases.

The reconstruction efficiency of a track depends, among others, on the location of the track itself within the LHCb detector. Especially at the edges of the detector it is not possible to have a homogeneous track reconstruction efficiency. Therefore, a so-called *fiducial region* is defined. All final-state particles are required to have a pseudorapidity in the range $2.0 < \eta < 4.5$. In addition, the *z*-position of the PV (z_{PV}) is required to be within $100 \, \mathrm{mm}$ of the nominal interaction point, where the standard deviation of the z_{PV} distribution is approximately $47 \, \mathrm{mm}$. These criteria cause a reduction of approximately 10% in signal yield but define a fiducial region where the reconstruction efficiency is largely uniform.

As explained in Section 4.2, the decay time t is computed using a kinematic decay tree fit (DTF), involving all final-state tracks from the *b*-hadron candidate with a constraint on the position of the associated PV. Unlike in the trigger, the position of each PV is calculated using all available charged particles in the event after the removal of the *b*-hadron candidate final-state tracks. This is necessary to prevent the final-state tracks from biasing the PV position towards the *b*-hadron decay vertex and helps to reduce the tails of the decay-time resolution function. This prescription does not bias the measured lifetime using simulated events as shown in detail in Chapter 6. The χ^2 of the fit, $\chi^2_{\mathrm{DTF}}/\mathrm{nDoF}$, is useful to discriminate between signal and background. In particular, it is required to be smaller than 5. In cases where there are multiple *b*-hadron candidates per event, the candidate with the smallest χ^2_{DTF} is chosen. This requirement does not introduce any bias on the measured lifetime, as explained in Section 8.12.

Studies of simulated events, explained in Chapter 6, show that in the case of $B^0 \to J/\psi \, K^{*0}$ ($B^0_s \to J/\psi \, \phi$) decays, imposing requirements on χ^2_{DTF} introduces a dependence of the selection efficiency on the decay time if the K^+ and π^- (K^+ and K^-) tracks are included in the DTF. If no correction is applied to the decay-time distribution, the measured lifetime is biased by approximately $-2 \, \mathrm{fs}$ relative to the generated value. Using simulated events it is found that this effect is correlated to the opening angle between the K^+ and π^- (K^+ and K^-) from the K^{*0} (ϕ) decay. No effect is observed for the muons coming from the J/ψ decay due to the larger opening angle in this case. To remove the effect, the calculation of χ^2_{DTF} for the $B^0 \to J/\psi \, K^{*0}$ and $B^0_s \to J/\psi \, \phi$ channels is performed with an alternative DTF in which the assigned track parameter uncertainties of the kaon and pion are increased in such a way that their contribution to the *b*-hadron vertex position is negligible.

Candidates are required to have a decay time t in the range $[0.3, 14.0] \, \mathrm{ps}$. The lower bound on the decay time suppresses a large fraction of the prompt combinatorial background without removing a large fraction of signal candidates, while the upper bound is introduced to reduce the sensitivity to long-lived background candidates. In the case of the $B^0 \to J/\psi \, K^0_{\mathrm{S}}$ and $\Lambda^0_b \to J/\psi \, \Lambda$ decays, the lower bound is increased to $0.45 \, \mathrm{ps}$ to compensate for the worse decay time resolution in these modes, see Section 7.2.

Table 5.3: *Selection criteria used to identify $B^+ \to J/\psi K^+$ candidates. The J/ψ selection criteria are reported in Table 5.2. A '–' implies that no requirement is applied on the corresponding parameter.*

	Variable	Stripping	Final selection
all tracks	$\chi^2_{\text{track}}/\text{nDoF}$	< 5	< 4
K^+	$\Delta \ln \mathcal{L}_{K\pi}$	–	> 0
	p_T	–	> 1 GeV/c
	p	–	> 10 GeV/c
$B^+ \to J/\psi K^+$	$m(J/\psi K^+)$	–	$\in [5170, 5400] \text{MeV}/c^2$
	χ^2_{IP}	–	< 25
	$\chi^2_{\text{IP,next PV}}$	–	> 50
	$\chi^2_{\text{DTF}}/\text{nDoF}$	–	< 5
	t	–	$\in [0.3, 14.0]$ ps

The χ^2 of the IP, χ^2_{IP}, is required to be smaller than 25 to ensure that the b hadron originates from the PV. Usually, there is more than one PV in the event. To avoid misidentification of the PV, b-hadron candidates are removed if they have a $\chi^2_{\text{IP,next PV}}$ with respect to the second nearest PV, so-called next best PV, smaller than 50. This requirement is found to distort the decay-time distribution, as it is explained in Chapter 6, but reduces a source of background due to the incorrect association of the b hadron to its production vertex.

5.5.3   Selection of $B^+ \to J/\psi K^+$ decays

The B^+ candidates are reconstructed by combining the J/ψ candidates, selected as explained in Section 5.5.1, with a charged particle that is identified as a kaon with $\Delta \ln \mathcal{L}_{K\pi}$ greater than zero. The kaon candidates are required to have p_T larger than $1\,\text{GeV}/c$ and p larger than $10\,\text{GeV}/c$. The subsequent stage of the selection is to combine the kaon with the J/ψ to build the B^+ candidate. The χ^2_{DTF} of the fit, which has 5 degrees of freedom, is required to be less than 25. This ensures a good quality of the vertex formed by the J/ψ and the kaon candidate. The invariant mass, $m(J/\psi K^+)$, must be in the range $[5170, 5400]\,\text{MeV}/c^2$. The selected mass range is very wide to allow a detailed investigation of potential combinatorial background. The asymmetric lower bound is chosen to remove contributions from incompletely reconstructed $B^0 \to J/\psi K^{*0}$ decays, with $K^0(892)^* \to K^+\pi^-$, see Section 7.3. Multiple B^+ candidates are found in less than 0.02% of selected events. The selection criteria used to identify $B^+ \to J/\psi K^+$ decays are summarised in Table 5.3.

5.5.4   Selection of $B^0 \to J/\psi K^{*0}$ decays

The K^{*0} candidates are reconstructed by combining two oppositely charged particles that are identified as a kaon and a pion, with $\Delta \ln \mathcal{L}_{K\pi}$ greater and smaller than 0, respectively. The pion and K^{*0} must have p_T greater than $0.3\,\text{GeV}/c$ and $1.5\,\text{GeV}/c$,

Table 5.4: Selection criteria used to identify $B^0 \to J/\psi K^{*0}$ candidates. The J/ψ selection criteria are reported in Table 5.2. A '−' implies that no requirement is applied on the corresponding parameter.

	Variable	Stripping	Final selection
all tracks	$\chi^2_{\text{track}}/\text{nDoF}$	< 5	< 4
$K^{*0} \to K^+\pi^-$	$\Delta\ln\mathcal{L}_{K\pi}\,(K^+)$	−	> 0
	$\Delta\ln\mathcal{L}_{\pi K}\,(\pi^+)$	−	< 0
	$p_T\,(K^*(892)^0)$	−	> 1.5 GeV/c
	$p_T\,(\pi^-)$	−	> 0.3 GeV/c
	$m(K^+\pi^-)$	−	$\in [826,\,966]\,\text{MeV}/c^2$
$B^0 \to J/\psi K^*(892)^0$	$m(J/\psi K^+\pi^-)$	−	$\in [5150,\,5340]\text{MeV}/c^2$
	χ^2_{IP}	−	< 25
	$\chi^2_{\text{IP,next PV}}$	−	> 50
	$\chi^2_{\text{DTF}}/\text{nDoF}$	−	< 5
	t	−	$\in [0.3,\,14.0]$ ps

respectively. The invariant mass, $m(K^+\pi^-)$, must be in the range $[826, 966]\,\text{MeV}/c^2$.

The B^0 candidates are reconstructed by combining the J/ψ, selected as explained in Section 5.5.1, and K^{*0} candidates. The invariant mass, $m(J/\psi K^+\pi^-)$, must be in the range $[5150, 5340]\,\text{MeV}/c^2$, where the upper bound is chosen to remove the contribution from $B^0_s \to J/\psi \overline{K}^{*0}$ decays. The χ^2_{DTF} of the fit, which has 3 degrees of freedom, is required to be less than 15. Multiple B^0 candidates are found in 2.2% of selected events. The selection criteria used to identify $B^0 \to J/\psi K^{*0}$ decays are summarised in Table 5.4.

5.5.5   Selection of $B^0 \to J/\psi K^0_S$ decays

The K^0_S candidates are formed from the combination of two oppositely charged particles that are identified as pions and reconstructed as Downstream tracks. This is necessary since studies of simulated signal decays demonstrate that an inefficiency depending on the b-hadron decay time is introduced by the reconstruction of the decay products of the long-lived K^0_S and Λ particles using Long tracks, see Chapter 6. Even so, it is found that the acceptance of the TT still depends on the origin of the tracks. This effect is removed by further tightening of the requirement on the position of the PV to $z_{\text{PV}} > -50\,\text{mm}$.

The Downstream pions are required to have p_T greater than $0.1\,\text{GeV}/c$ and p greater than $2\,\text{GeV}/c$. The K^0_S candidate must have p_T greater than $1\,\text{GeV}/c$ and be well separated from the B^0 decay vertex, to suppress potential background from $B^0 \to J/\psi K^{*0}$ decays where the kaon has been misidentified as a pion. The χ^2 of the K^0_S vertex fit must be less than 25 and the invariant mass of the dipion system, $m(\pi^+\pi^-)$, must be within $15\,\text{MeV}/c^2$ of the known K^0_S mass [14]. For subsequent stages of the selection, $m(\pi^+\pi^-)$ is constrained to the known K^0_S mass.

The invariant mass, $m(J/\psi\pi^+\pi^-)$, of the J/ψ, selected as explained in Section 5.5.1,

Table 5.5: *Selection criteria used to identify $B^0 \to J/\psi K_S^0$ candidates. The J/ψ selection criteria are reported in Table 5.2. A '–' implies that no requirement is applied on the corresponding parameter.*

	Variable	Stripping	Final selection
$\mu^\pm$	$\chi^2_{\text{track}}/\text{nDoF}$	< 5	< 4
$\pi^\pm$	$\chi^2_{\text{track}}/\text{nDoF}$	> 5000	< 10
$K_S^0 \to \pi^+\pi^-$	$p_{\text{T}}(\pi^\pm)$	–	$> 0.25\,\text{GeV}/c$
	$p(\pi^\pm)$	–	$> 2\,\text{GeV}/c$
	$p_{\text{T}}(K_S^0)$	–	$> 1\,\text{GeV}/c$
	$\chi^2_{\text{vtx}}/\text{nDoF}(K_S^0)$	–	< 25
	FDS wrt B^0 vtx (K_S^0)	–	> 3
	$|m(\pi\pi) - m(K_S^0)|$	–	$< 15\,\text{MeV}/c^2$
$B^0 \to J/\psi K_S^0$	$m(J/\psi\,\pi^+\pi^-)$	–	$\in [5150, 5340]\,\text{MeV}/c^2$
	χ^2_{IP}	–	< 25
	$\chi^2_{\text{IP,next PV}}$	–	> 50
	$\chi^2_{\text{DTF}}/\text{nDoF}$	–	< 5
	t	–	$\in [0.45, 14.0]\,\text{ps}$

and K_S^0 candidate combination must be in the range $[5150, 5340]\,\text{MeV}/c^2$, where the upper bound is chosen to remove the contribution from $B_s^0 \to J/\psi K_S^0$ decays. The χ^2_{DTF} of the fit, which has 6 degrees of freedom, is required to be less than 30. Multiple B^0 candidates are found in less than 0.4% of selected events. The selection criteria used to identify $B^0 \to J/\psi K_S^0$ decays are summarised in Table 5.5.

5.5.6 Selection of $B_s^0 \to J/\psi\phi$ decays

The ϕ candidates are formed from two oppositely charged particles that have been identified as kaons and originate from a common vertex. The K^+K^- pair is required to have p_{T} larger than $1\,\text{GeV}/c$. The invariant mass of the K^+K^- pair, $m(K^+K^-)$, must be in the range $[990, 1050]\,\text{MeV}/c^2$.

The B_s^0 candidates are reconstructed by combining the J/ψ candidate, selected as explained in Section 5.5.1, with the K^+K^- pair, requiring the invariant mass, $m(J/\psi K^+K^-)$, to be in the range $[5200, 5550]\,\text{MeV}/c^2$. The χ^2_{DTF} of the fit, which has 3 degrees of freedom, is required to be less than 15. Multiple B_s^0 candidates are found in less than 2.0% of selected events. The selection criteria used to identify $B_s^0 \to J/\psi\phi$ decays are summarised in Table 5.6.

5.5.7 Selection of $\Lambda_b^0 \to J/\psi\Lambda$ decays

The selection of $\Lambda_b^0 \to J/\psi\Lambda$ candidates follows a similar approach to that adopted for $B^0 \to J/\psi K_S^0$ decays. Only protons and pions reconstructed as Downstream tracks are used to reconstruct the Λ candidates. The pions are required to have p_{T} larger than

Table 5.6: Selection criteria used to identify $B_s^0 \to J/\psi\phi$ candidates. The J/ψ selection criteria are reported in Table 5.2. A '–' implies that no requirement is applied on the corresponding parameter.

	Variable	Stripping	Final selection
all tracks	$\chi^2_{\text{track}}/\text{nDoF}$	< 5	< 4
$\phi \to K^+K^-$	$\Delta\ln\mathcal{L}_{K\pi}\,(K^\pm)$	–	> 0
	$p_T\,(\phi)$	–	$> 1.0\,\text{GeV}/c$
	$m(K^+K^-)$	–	$\in [1008, 1032]\,\text{MeV}/c^2$
$B_s^0 \to J/\psi\phi$	$m(J/\psi\,K^+K^-)$	–	$\in [5200, 5550]\,\text{MeV}/c^2$
	χ^2_{IP}	–	< 25
	$\chi^2_{\text{IP,next PV}}$	–	> 50
	$\chi^2_{\text{DTF}}/\text{nDoF}$	–	< 5
	t	–	$\in [0.3, 14.0]\,\text{ps}$

$0.1\,\text{GeV}/c$, while pions and protons must have p larger than $2\,\text{GeV}/c$. The Λ candidate must be well separated from the Λ_b^0 decay vertex and have p_T larger than $1\,\text{GeV}/c$. The χ^2 of the Λ vertex fit must be less than 25 and $m(p\pi^-)$ must be within $6\,\text{MeV}/c^2$ of the known Λ mass [14]. For subsequent stages of the selection, $m(p\pi^-)$ is constrained to the known Λ mass.

The invariant mass, $m(J/\psi p\pi^-)$, of the J/ψ, selected as explained in Section 5.5.1, and Λ candidate combination must be in the range $[5470, 5770]\,\text{MeV}/c^2$. The χ^2_{DTF} of the fit, which has 6 degrees of freedom, is required to be less than 30. Multiple Λ_b^0 candidates are found in less than 0.5% of selected events. The selection criteria used to identify $\Lambda_b^0 \to J/\psi\Lambda$ decays are summarised in Table 5.7.

5.6 Invariant mass distributions and determination of signal yields

To visualise the effect of the selection requirements explained in the previous sections the invariant mass distributions of the different b-hadron candidates after the application of the final selection are shown in Figures 5.2 and 5.3. The estimated signal and background yields for the five $H_b \to J/\psi X$ channels are reported in Table 5.9.

The signal distribution in all the b-hadron decay modes is described by the sum of two Gaussian distributions, $\mathcal{G}_1$ and $\mathcal{G}_2$, with a common mean, m_{H_b},

$$PDF(m) = N_f \cdot [f_{\sigma_1} \cdot \mathcal{G}_1\,(m_{H_b},\,\sigma_1; m) + (1 - f_{\sigma_1}) \cdot \mathcal{G}_2\,(m_{H_b},\,\sigma_2; m)]\,, \qquad (5.2)$$

where N_f is a normalisation factor. Here f_{σ_1} is the fraction of the first Gaussian distribution and σ_1 and σ_2 are the widths of the first and second Gaussian distribution, respectively. The usage of two different widths is due to the fact that the momentum resolution depends on the momentum of the final state particles. Therefore, also the mass resolution does not behave as a pure single Gaussian. For this analysis, the double

Table 5.7: Selection criteria used to identify $\Lambda_b^0 \to J/\psi\Lambda$ candidates. The J/ψ selection criteria are reported in Table 5.2. A '–' implies that no requirement is applied on the corresponding parameter.

	Variable	Stripping	Final selection
$\mu^{\pm}$	$\chi^2_{\text{track}}/\text{nDoF}$	< 5	< 4
p and π^-	$\chi^2_{\text{track}}/\text{nDoF}$	> 5000	< 10
$\Lambda \to p\pi^-$	$p_{\text{T}}\,(\pi^-)$	–	$> 0.1\,\text{GeV}/c$
	$p_{\text{T}}\,(p)$	–	$> 0.5\,\text{GeV}/c$
	$p\,(p,\pi^-)$	–	$> 2\,\text{GeV}/c$
	$p_{\text{T}}(\Lambda)$	–	$> 1\,\text{GeV}/c$
	$\chi^2_{\text{vtx}}/\text{nDoF}\,(\Lambda)$	–	< 25
	FDS wrt Λ_b^0 vtx (Λ)	–	> 3
	$|m(p\pi^-) - m(\Lambda)|$	–	$< 6\,\text{MeV}/c^2$
$\Lambda_b^0 \to J/\psi\Lambda$	$m(J/\psi\, p\pi^-)$	-	$\in [5470,\ 5740]\text{MeV}/\text{c}^2$
	χ^2_{IP}	–	< 25
	$\chi^2_{\text{IP,next PV}}$	–	> 50
	$\chi^2_{\text{DTF}}/\text{nDoF}$	–	< 5
	t	–	$\in [0.45, 14.0]\,\text{ps}$

Gaussian is found to describe the data quite well. The background is modelled by an exponential function with constant α_m, $\exp^{\alpha_m \cdot m}$. A more detailed investigation of the background is given in Section 7.3. All these parameters are free to vary in the fit.

The signal and background parameters are obtained performing an unbinned maximum likelihood fit to the b-hadron invariant mass distribution, as described in Section 4.4. The results of the fit are summarised in Table 5.8. The quality of the fit can be judged by the *pull distribution*. The pull in each mass bin i is defined as

$$\text{pull}_i = \frac{x_i - \mathcal{P}(m)_i}{\sigma_i}, \tag{5.3}$$

where x_i is the number of entries in bin i, σ_i is the statistical uncertainty of this bin and $\mathcal{P}(m)_i$ is the value of the PDF at the centre of bin i. The distribution is given in the lower part of each figure. All the pull points lie within the interval [-2,+2], showing a good quality of the fit.
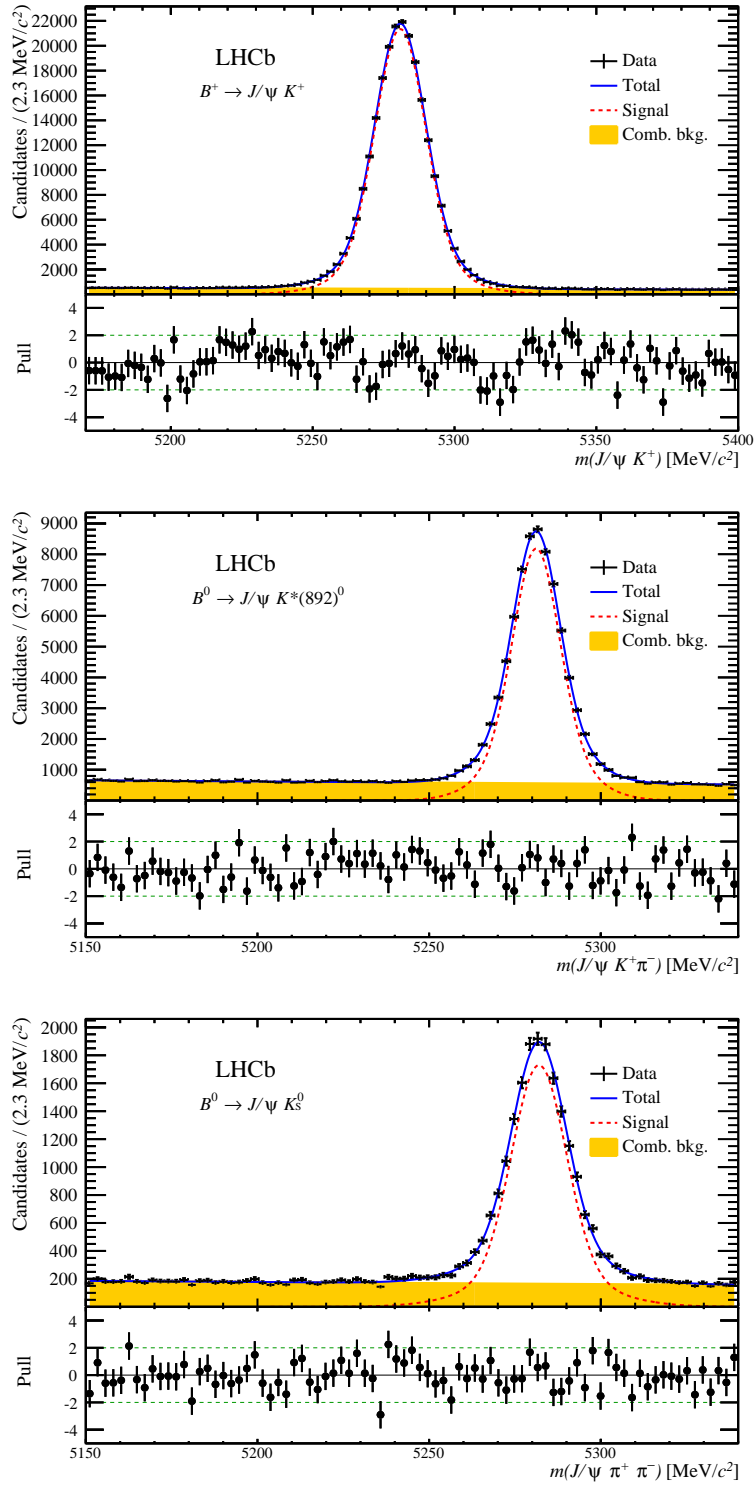
Figure 5.2: Mass distributions of $B^+ \to J/\psi K^+$, $B^0 \to J/\psi K^{*0}$ and $B^0 \to J/\psi K_S^0$ candidates and their associate fit residual in bin uncertainty units (pulls). The data are shown by the black points; the total fit function by the blue solid line; the signal contribution by the red dashed line and the combinatorial background contribution by the yellow filled area.
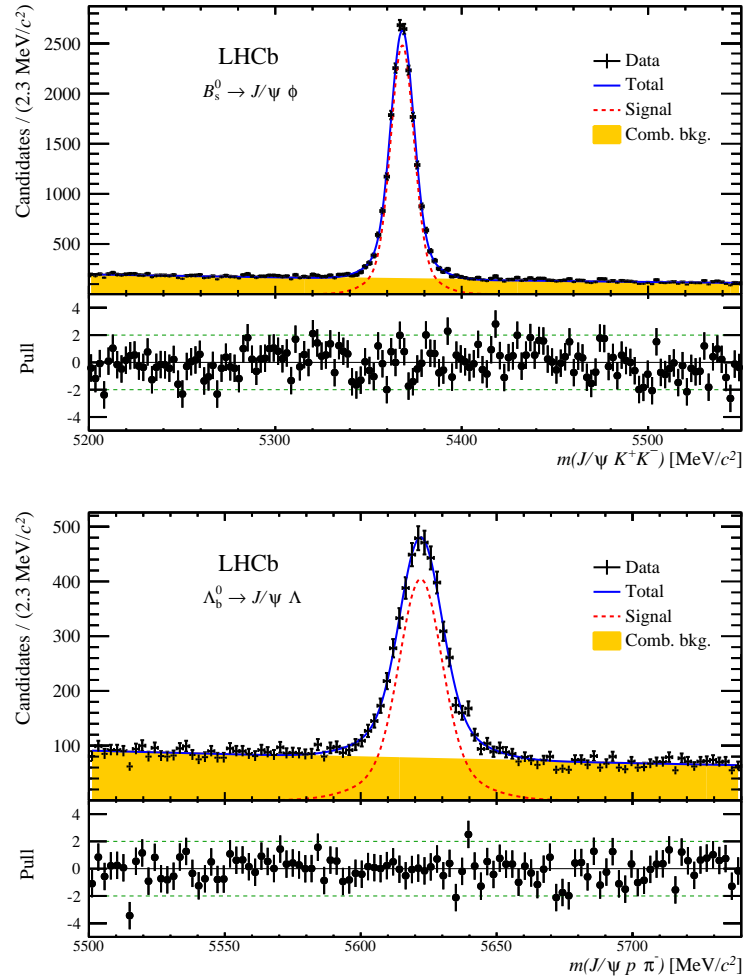
Figure 5.3: Mass distributions of $B_s^0 \to J/\psi\phi$ and $\Lambda_b^0 \to J/\psi\Lambda$ candidates their associate fit residual in bin uncertainty units (pulls). The data are shown by the black points; the total fit function by the blue solid line; the signal contribution by the red dashed line and the combinatorial background contribution by the yellow filled area.

Table 5.8: Fit values of the parameters used in the fit to the b-hadron invariant mass distribution after the application of the off-line selection. The uncertainty is statistical only.

Channel	m_{H_b} [MeV/c^2]	σ_1 [MeV/c^2]	σ_2 [MeV/c^2]	f_{σ_1}	f_{sig}	α_m
$B^+ \to J/\psi K^+$	5280.89 ± 0.02	8.70 ± 0.06	17.5 ± 0.4	0.78 ± 0.01	0.836 ± 0.001	0.00151 ± 0.00007
$B^0 \to J/\psi K^{*0}$	5281.18 ± 0.04	6.5 ± 0.1	12.2 ± 0.5	0.65 ± 0.04	0.589 ± 0.002	0.0012 ± 0.0001
$B^0 \to J/\psi K_S^0$	5282.01 ± 0.09	7.8 ± 0.3	17.3 ± 2.5	0.75 ± 0.05	0.547 ± 0.008	0.0009 ± 0.0003
$B_s^0 \to J/\psi \phi$	5368.17 ± 0.06	6.0 ± 0.2	13.7 ± 1.1	0.75 ± 0.04	0.452 ± 0.003	0.00162 ± 0.00007
$\Lambda_b^0 \to J/\psi \Lambda$	5622.1 ± 0.2	7.5 ± 0.5	17.1 ± 3.0	0.70 ± 0.09	0.333 ± 0.008	0.0015 ± 0.0002

Table 5.9: Estimated signal and background yields for the five $H_b \to J/\psi X$ channels selected using the criteria described in Section 5.5.3 to 5.5.7.

Channel	Signal yield	Background yield
$B^+ \to J/\psi K^+$	$229\,434 \pm 503$	$44\,083 \pm 261$
$B^0 \to J/\psi K^{*0}$	$70\,534 \pm 312$	$48\,366 \pm 276$
$B^0 \to J/\psi K_S^0$	$17\,045 \pm 175$	$14\,350 \pm 167$
$B_s^0 \to J/\psi \phi$	$18\,662 \pm 152$	$22\,514 \pm 165$
$\Lambda_b^0 \to J/\psi \Lambda$	$3\,960 \pm\ \ 89$	$8\,022 \pm 110$

## 5.7   Summary

The essential information of this chapter is briefly summarised here.

- The analysis uses the dataset recorded by LHCb in 2011 at a centre-of-mass energy of 7 TeV. This corresponds to an integrated luminosity of 1 fb^{-1}.

- The trigger, stripping and off-line selections are intended to identify *b*-hadron candidates with minimal distortion of the decay-time distributions.

- In order to fulfil the tight time constraints in the trigger and in the stripping, the already existing trigger and stripping lines that select $H_b \to J/\psi X$ decays include some selection requirements that introduce a non-trivial decay-time dependent acceptance that biases the decay-time distribution. These effects will be described in Chapter 6.

- The estimated signal yields obtained from a fit of the *b*-hadron invariant mass distributions after the full selection is applied are given in Table 5.9.

6

Decay-time acceptance

Be precise. A lack of precision is dangerous when the margin of error is small.

— Donald Rumsfeld

The main challenge in the measurements reported is understanding and controlling the detector acceptance, reconstruction and selection efficiencies that depend upon the b-hadron decay time, globally referred to as the decay-time acceptance. In this chapter they are analysed in detail. First, the origin of the different effects that distorts the b-hadron decay-time distribution is discussed and the different sources of decay-time dependent reconstruction and selection efficiencies are listed. They can be classified into two main categories: So-called lower and upper decay-time acceptance. They are separately analysed and addressed in the subsequent sections of this chapter. Finally, an overview of all the corrections performed is given.

6.1 Origin of the decay-time acceptance

The aim of this section is to provide a complete and detailed overview about the origin of the decay-time acceptance in the different $H_b \to J/\psi\,X$ channels. In order to understand the different sources of the decay-time acceptance it is useful to study simulated Monte Carlo samples. However, as pointed out already in Section 3.2.2, simulated samples do not describe perfectly data distributions. Thus, the size of the different effects that distorts the b-hadron decay-time distribution cannot be estimated in MC. In order to rely on simulated samples as less as possible, they are used to understand the origin of the decay-time acceptance and to develop techniques to remove it that can be applied in data without using MC information. However, the main advantage of MC is that it is possible to check that all the corrections developed remove the bias on the lifetime measurements completely.

The decay-time acceptance is obtained from Monte Carlo by dividing the decay-time distribution of the b-hadron signal candidates that are reconstructed and that pass the selection (see Chapter 5) by the generated theory distribution. The latter represents the decay-time distribution of the candidates before any reconstruction or selection
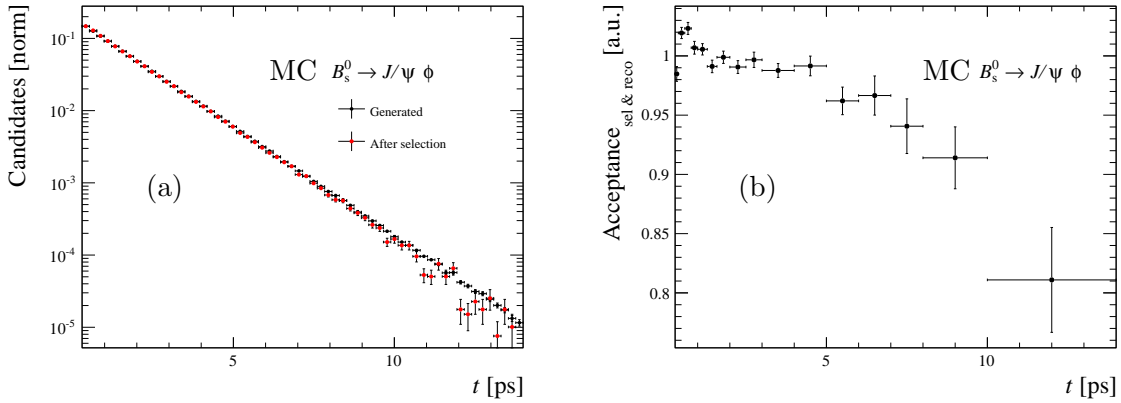
Figure 6.1: (a) Decay-time distribution in simulated MC sample of the $B_s^0 \to J/\psi\phi$ signal candidates that are reconstructed and that pass the selection (red) and generated decay-time distribution of the candidates before any reconstruction or selection requirement is applied (black). The individual distributions are normalised to the same area. (b) Decay-time acceptance obtained dividing these two decay time distributions.

requirement is applied. These two distributions, normalised to the same area, are shown in Figure 6.1 (a) in red and black, respectively, for the $B_s^0 \to J/\psi\phi$ decay mode. The decay-time acceptance, Acceptance$_{\text{sel \& reco}}$, is obtained dividing these two distributions and it is shown in Figure 6.1 (b). It is important to note that only the shape of the acceptance is interesting and not the overall scale, thus the y-axis is given in arbitrary units.

The decay-time acceptance can be divided into two contributions. In the detached HLT2 trigger, `HLT2DiMuonDetachedJPsi`, and in the according stripping selection a requirement on the displacement of the J/ψ candidate from the primary vertex, FD/σ_{FD}, is used (see Section 5.4). It is useful to suppress background due to combinations of tracks that come from the PV, but clearly it also removes short-lived b hadrons. The acceptance introduced by this requirement is shown in Figure 6.2 (b) as a function of the b-hadron decay time. It is obtained dividing the normalised decay-time distribution of b-hadron candidates passing this selection requirement over that of candidates that are reconstructed and that pass the full selection but this requirement. This selection requirement affects mainly b hadrons with small decay time, below 2 ps, thus the corresponding decay-time acceptance is referred to as lower decay-time acceptance. Even if the inefficiency at low decay time is not large, due to the fact that most of the events have a decay time below 2 ps its effect is rather large.

Leaving out the requirement on the displacement of the J/ψ candidate from the primary vertex, $H_b \to J/\psi X$ candidates are reconstructed and selected using an approach where no explicit selection requirements related to the b-hadron decay time are required, but a trivial one on the decay time itself. Therefore, a flat decay-time acceptance was expected. Dividing the decay-time distribution of these b-hadron candidates by the generated one, the decay-time acceptance shown in Figure 6.2 (a) is obtained. The origin of this decay-time acceptance has been a long-standing puzzle within the LHCb

(a) Upper acceptance   (b) Lower acceptance
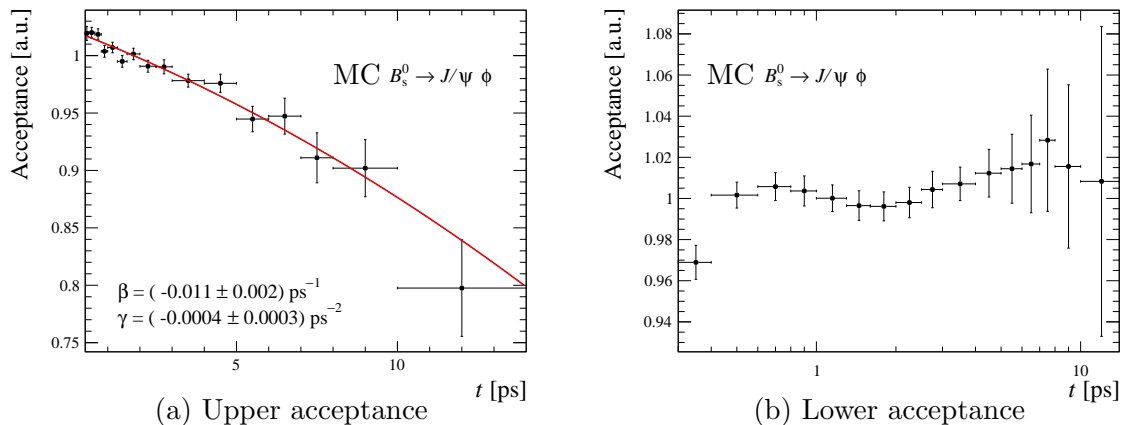
Figure 6.2: (a) Decay-time acceptance of all the selection and reconstruction requirements but the displacement of the J/ψ candidate from the PV in $B_s^0 \to J/\psi\phi$ MC sample. Superimposed in red there is the result of a fit with a parabolic function, see Equation 6.1. (b) Decay-time acceptance of the requirement on the displacement of the J/ψ candidate from the PV used in the detached HLT2 trigger `HLT2DiMuonDetachedJPsi` *and in the stripping selection (note the logarithmic scale on the x axis) for candidates that are reconstructed and that pass the full selection but this requirement in $B_s^0 \to J/\psi\phi$ MC sample.*

collaboration. It was first observed in simulated data during the measurement of the CP-violating phase ϕ_s in the decay $B_s^0 \to J/\psi\phi$ [54]. On the whole, this acceptance shows a decrease of the efficiency to reconstruct and select b-hadron candidates as a function of the decay time. It is referred to as upper decay-time acceptance since b hadrons with a large decay time are more affected by this effect. Superimposed in Figure 6.2 (a) there is the result of a fit with a quadratic function described by

$$\mathrm{PDF}(t) \propto \left(1 + \beta t + \gamma t^2\right), \tag{6.1}$$

where t is the reconstructed b-hadron decay time and the β and γ factors parameterise the observed decay-time acceptance. If there were no acceptance effects then the β and γ factors would be zero, however a value of $\beta \sim \mathcal{O}(10^{-2})\,\mathrm{ps}^{-1}$ is observed. Ignoring such acceptance effects in MC studies results in a significant underestimation of the measured $B_s^0 \to J/\psi\phi$ effective lifetime of $\mathcal{O}(20)\,\mathrm{fs}$. Similar effects have been observed in all the others $H_b \to J/\psi X$ modes.

With the data recorded at LHCb in 2011 the expected statistical precision on the b-hadron lifetimes is about few femtoseconds for the B^+ and the B^0 decay modes, where a smaller statistical uncertainty with respect to the other b hadrons is expected. Thus, precise knowledge of the decay-time acceptance is critical in order to correct for all the biasing effects and to control the size of the systematic uncertainties related to these corrections.

The study of the decay-time acceptance is organised as follows. First simulated signal samples are analysed in more detail to determine the multiple origins of the decay-

time acceptance, as described in Section 6.2. It can be divided into three categories depending on the origin of the bias: the VELO-track reconstruction inefficiency, which is the largest contribution and it is explained in Section 6.3.2, the method used to reconstruct the primary vertex and the final analysis selection, discussed in Section 6.3.3 and Section 6.3.4, and finally the trigger and stripping requirement on the detachment of the J/ψ, treated in Section 6.4. The $B_s^0 \to J/\psi\phi$ channel is used frequently as an example, when possible, to discuss the different biases, since it is affected by all the different decay-time biasing effects.

6.2   Anatomy of the decay-time acceptance

A detailed study of the decay-time acceptance is performed in simulated MC signal samples to identify the reconstruction, trigger and selection requirements responsible for lifetime biases. For each $H_b \to J/\psi X$ decay channel the lifetime is extracted by means of a fit to the decay-time distribution using a single exponential convoluted with a decay-time resolution function to model it.[1] The fit is repeated for each step of the analysis, namely the reconstruction, selection and trigger requirements are introduced sequentially. In reality, a candidate has to pass the trigger requirements before to be available for the subsequent selection stage. However, since it is known that the trigger requirement on the displacement of the J/ψ candidate from the primary vertex is introducing a decay-time dependent acceptance whose origin is understood, all the other selection requirements are analysed first.

The result of this procedure is shown in Figure 6.3 for the $B^+ \to J/\psi K^+$, $B^0 \to J/\psi K^{*0}$ and $B_s^0 \to J/\psi\phi$ decay channels. The complete explanation of the analysis steps in Figure 6.3 can be found in Appendix A. The first point in these plots represent the fitted value of the lifetime at the generation stage. The only requirement applied at this step is that all the particles in the final state have to roughly be within the LHCb detector acceptance. Comparing this value with the last point, representing the fitted lifetime value at the end of the full reconstruction and selection procedure, the bias introduced on the lifetime measurement is estimated. First of all, it should be noticed that the trend is very similar for these three decay modes which manifest a total bias equal to

$$\Delta\tau_{B^+ \to J/\psi K^+} \quad \sim \quad -19\,\mathrm{fs}\,, \tag{6.2}$$

$$\Delta\tau_{B^0 \to J/\psi K^{*0}} \quad \sim \quad -16\,\mathrm{fs}\,, \tag{6.3}$$

$$\Delta\tau_{B_s^0 \to J/\psi\phi} \quad \sim \quad -18\,\mathrm{fs}\,. \tag{6.4}$$

Analysing the Figure 6.3 in greater details it is possible to identify few analysis steps where there is a significant change in the lifetime which is consistent among the different b-hadrons channels. The first step where a bias is consistently visible in all decay channels is step number 2, that corresponds to the requirement that all the particles in the final state have enough hits in the VELO detector to be reconstructed, see Section 3.2.1. Clearly, the main bias is introduced in step number 4, that corresponds

---

[1]For more details on the fit procedure and on the decay-time resolution function used in this analysis see Section 7.1.

to the requirement that all the particles in the final state are reconstructed as VELO tracks. These two effects are addressed in Section 6.3.1 and in Section 6.3.2, respectively. Additional stages of the track reconstruction do not introduce any further bias. Concerning the selection requirements it is possible to see that especially for the $B^0 \to J/\psi K^{*0}$ and $B_s^0 \to J/\psi \phi$ decay channels there are some significant biases in the last four points (steps number 9-12). Step number 9 corresponds to the requirement on the good quality of the K^{*0} or ϕ decay vertex, namely $\chi^2_{\text{vtx}}/\text{nDoF} < 16$. The steps number 10-12 are related to the different requirements used to select the B^0 or B_s^0 meson, namely $\chi^2_{\text{IP}} < 25$, $\chi^2_{\text{DTF}}/\text{nDoF} < 5$ and $\chi^2_{\text{IP,next PV}} > 50$, respectively. These selection-related effects are treated in detail in Section 6.3.3 and Section 6.3.4. Finally, concerning the trigger requirements, there is a clear trend visible in all the decay channels. Steps number 16 and 17 are related to the requirement on the flight distance significance imposed on the J/ψ candidate in the trigger and in the stripping which clearly bias the decay-time distribution. This effect is analysed in Section 6.4. Moreover, there is also a bias on step number 14 related to the HLT1 selection, which in principle does not contain any lifetime biasing requirement. This trigger bias is analysed in Section 6.3.5.

Concerning the $B^0 \to J/\psi K_S^0$ and $\Lambda_b^0 \to J/\psi \Lambda$ decay channels, the corresponding plots showing the lifetime as a function of the different analysis steps are shown in Figure 6.4. In this case only the two muons coming from the J/ψ are reconstructed as Long tracks while the two final state tracks coming from the K_S^0 and the Λ are reconstructed as Downstream tracks. This explains why the step corresponding to the requirement that the muons are reconstructed as VELO tracks, step number 5, is less pronounced that in the other channels. Therefore, also the overall bias is smaller in these two decay channels

$$\Delta\tau_{B^0 \to J/\psi K_S^0} \quad \sim \quad -12\,\text{fs}\,, \tag{6.5}$$

$$\Delta\tau_{\Lambda_b^0 \to J/\psi\Lambda} \quad \sim \quad -6\,\text{fs}\,. \tag{6.6}$$

No visible biases are arising in these two channels from the selection, but a small one at step number 7, while the trigger requirements in steps number 19-20 cause basically no bias with respect to the other channels.

6.3   Upper decay-time acceptance

In this section all the decay-time dependent acceptances that are introduced in the reconstruction and in the selection process, but the requirement on the displacement of the J/ψ candidate from the PV, are addressed. Within each subsection, every biasing effect is presented and a procedure to correct for it is explained and validated.

6.3.1   Geometrical acceptance of the vertex detector

The largest variation of the acceptance with the decay time is introduced by the track reconstruction in the VELO. The track finding algorithm used in the VELO has been introduced in Section 3.2.1. In order to be reconstructible in the VELO, tracks
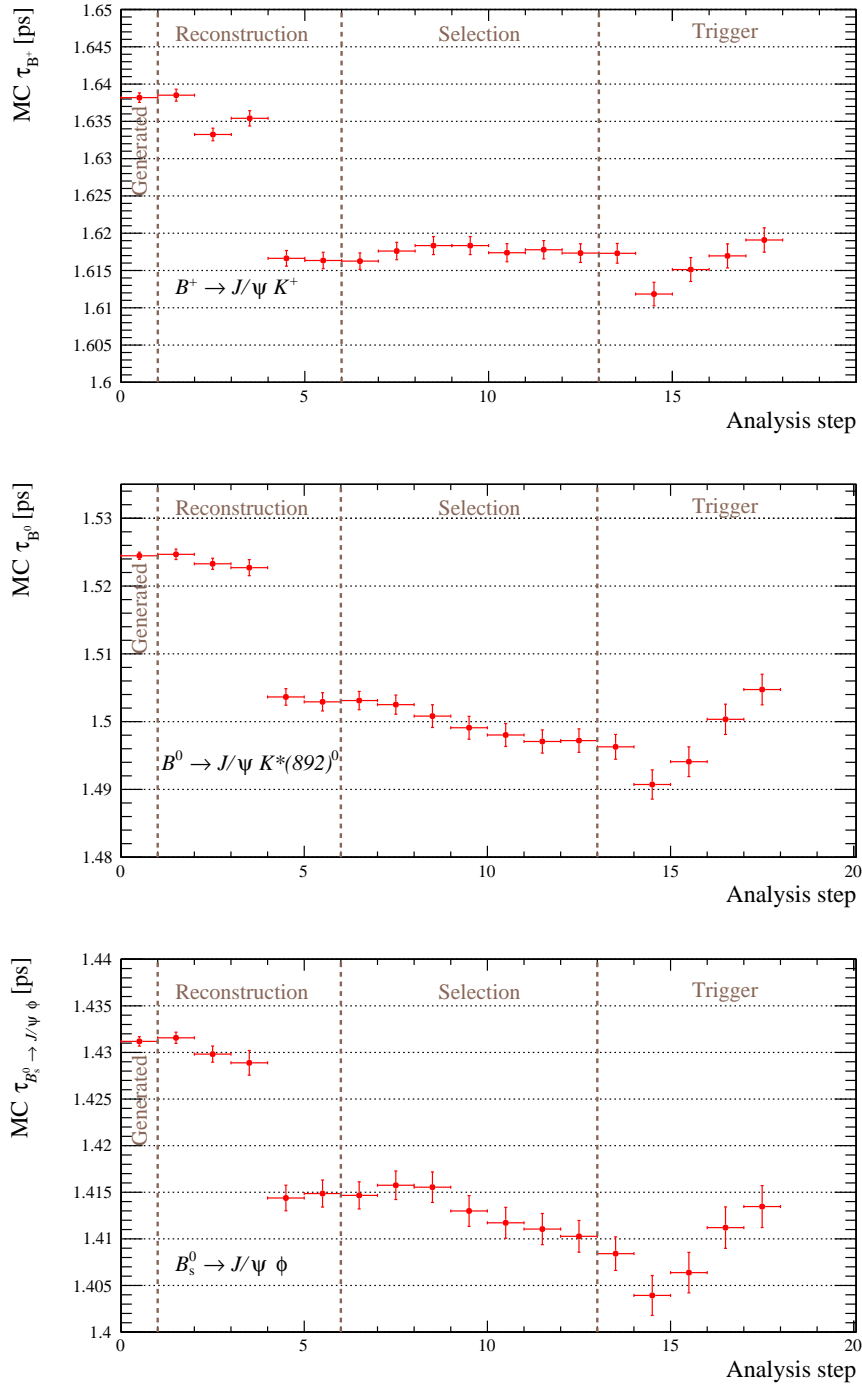
Figure 6.3: Measured lifetime in simulated Monte Carlo samples of $B^+ \to J/\psi K^+$, $B^0 \to J/\psi K^{*0}$ and $B_s^0 \to J/\psi \phi$ decay channels as a function of the different reconstruction, selection and trigger requirements used in the analysis. For a detailed explanation of the analysis steps see Appendix A.
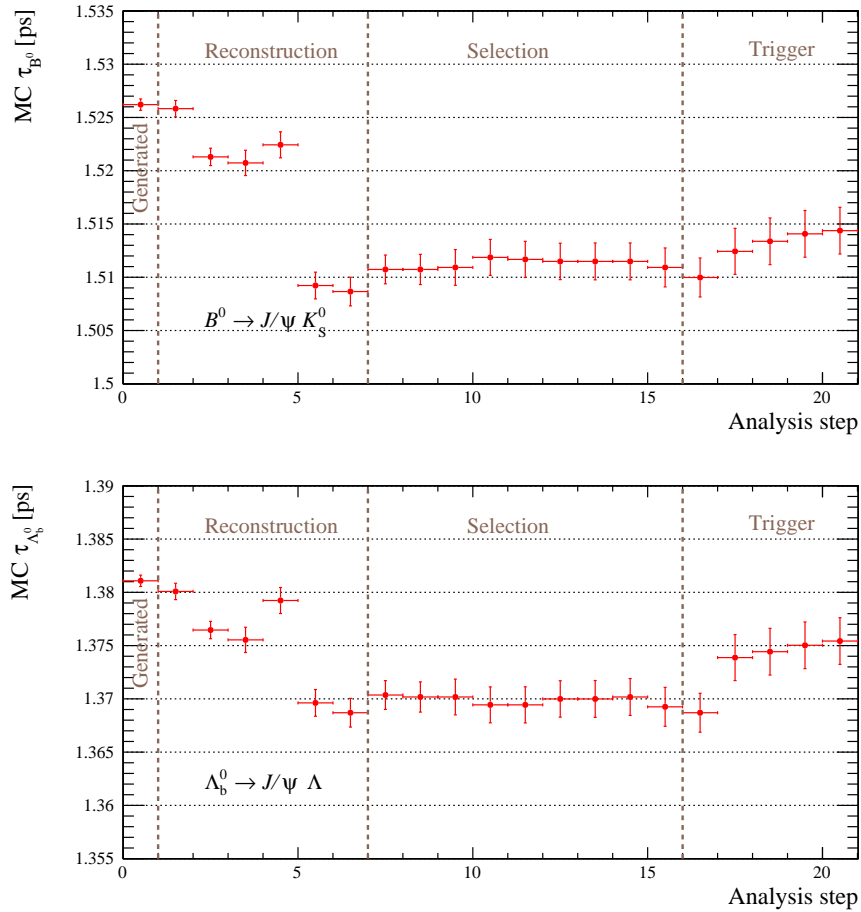
Figure 6.4: Measured lifetime in simulated Monte Carlo samples of $B^0 \to J/\psi K_S^0$ and $\Lambda_b^0 \to J/\psi \Lambda$ decay channels as a function of the different reconstruction, selection and trigger requirements used in the analysis. For a detailed explanation of the analysis steps see Appendix A.
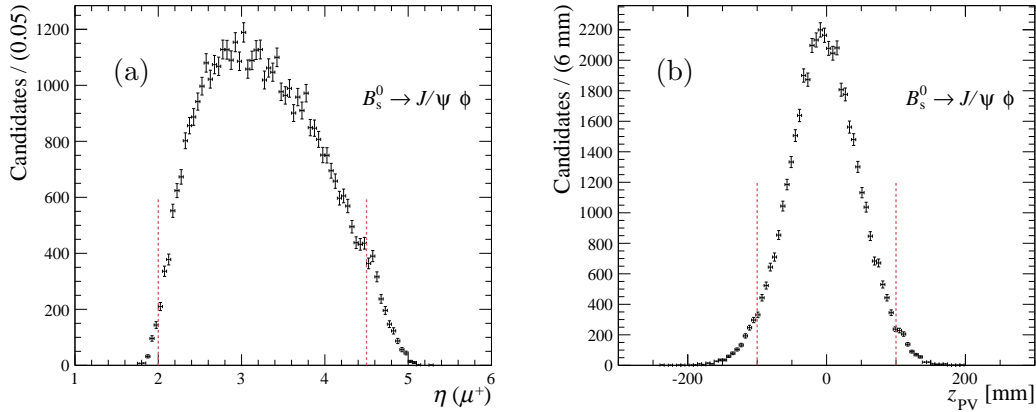
Figure 6.5: Distributions of (a) the pseudorapidity, η of the positive muon and (b) the z-position of the PV, z_{PV}, from $B_s^0 \to J/\psi\phi$ events. The red lines delimit the fiducial region introduced to ensure a more homogeneous reconstruction.

need to have hits in at least four different R sensors if they are reconstructed in the HLT1 trigger or at least three different R sensors if they are reconstructed in the HLT2 or off-line. Removing all final-state particles that do not meet these requirements is introducing a bias up to 5 fs, as visible in step number 2 of Figure 6.3. This is a pure geometrical effect since at this stage tracks are not yet reconstructed by the software algorithm. The z position of the PV (z_{PV}) has a spread of few centimeters, so if an event belongs to the tails of this distribution, especially when the b hadron has a long decay time, it is possible that the decay products do not leave enough hits in the VELO. Moreover there could be difficulties reconstructing tracks that are close to the edges of the LHCb angular acceptance. A so-called fiducial region is define in order to reduce these effects. All final-state particles are required to have a pseudorapidity in the range $2.0 < \eta < 4.5$. In addition, the z-position of the PV is required to be within 100 mm of the nominal interaction point for $B^+ \to J/\psi K^+$, $B^0 \to J/\psi K^{*0}$ and $B_s^0 \to J/\psi\phi$ decay channels. Both distributions as well as the fiducial region are shown in Figure 6.5. For $B^0 \to J/\psi K_S^0$ and $\Lambda_b^0 \to J/\psi\Lambda$ decay channels this fiducial region is not enough. It is found that the acceptance of the TT, whose information is necessary to build a Downstream track, still depends on the origin of the tracks. This effect is removed by further tightening of the requirement on the position of the PV to $z_{PV} > -50$ mm. These criteria cause a reduction of approximately 10% in signal yield but define a fiducial region where the efficiency for a track to be reconstructible is largely uniform. Moreover, outside this region, the correction for the VELO reconstruction inefficiency, which is explained in the next section, works visibly worse.

6.3.2 Acceptance effects of reconstruction in the vertex detector

The track finding procedure in the VELO assumes that tracks originate approximately from the interaction region. As explained in Section 3.2.1, in the case of long-lived b-hadron candidates this assumption is less justified, leading to a loss of reconstruction

$\beta = (0.0009 \pm 0.0018)$ ps^{-1}
$\gamma = (-0.0012 \pm 0.0003)$ ps^{-2}

(a) before correction

$\beta = (0.0013 \pm 0.0019)$ ps^{-1}
$\gamma = (-0.00033 \pm 0.00029)$ ps^{-2}

(b) after correction
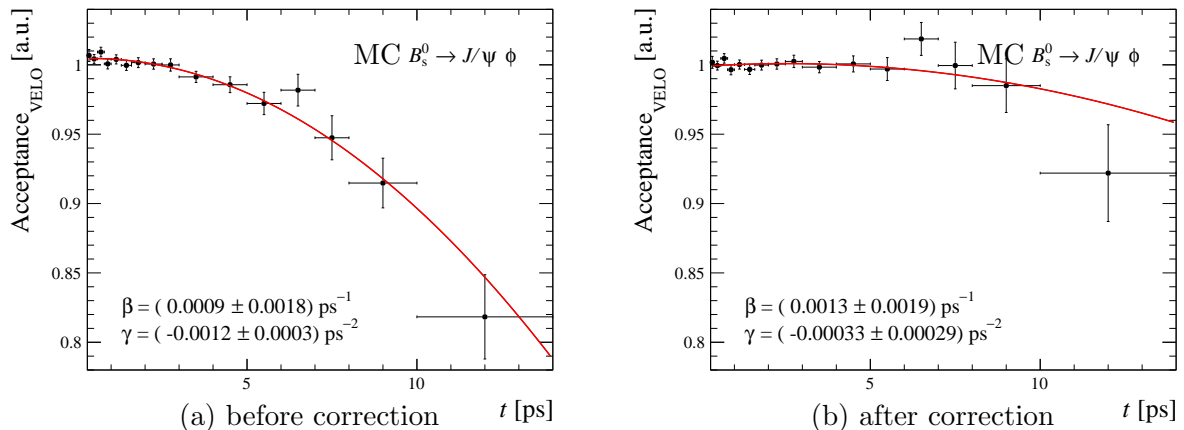
Figure 6.6: *Acceptance introduced by the reconstruction of the b-hadron decay products as VELO tracks as a function of the b-hadron decay time from simulated MC $B_s^0 \to J/\psi\phi$ sample (a) before any correction is applied and (b) using the per-event weights derived in Section 6.3.2.*
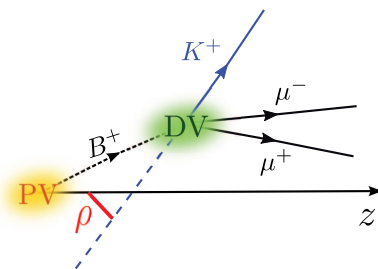
Figure 6.7: *Sketch of a $B^+ \to J/\psi K^+$ decay showing the distance of closest approach of a track, the kaon in this example, to the z-axis, so-called ρ.*

efficiency for charged particle tracks from the b-hadron decay. The acceptance introduced by the reconstruction of the tracks in the VELO detector as a function of the decay time is shown in Figure 6.6 (a) for simulated $B_s^0 \to J/\psi\phi$ decays. Since no selection requirements but the fiducial region are applied at this stage, the statistics available in MC is such that a deviation from the basically linear behaviour found in Figure 6.2 (a) is visible. This acceptance shows a parabolic behaviour and it is fitted with the function define in Equation 6.1. The results for the fit parameters are shown in the figure. Clearly, the acceptance is not uniform as a function of the decay time and this is the origin of the lifetime bias at step number 4 in Figure 6.3.

An useful quantity to parameterise the VELO-track reconstruction efficiency is the distance of closest approach of a track to the z-axis, ρ, sketched in Figure 6.7 for the kaon coming from a $B^+ \to J/\psi K^+$ decay. It is defined as

$$\rho \equiv \frac{|(\boldsymbol{d} - \boldsymbol{v}) \cdot (\boldsymbol{p} \times \hat{\boldsymbol{z}})|}{|\boldsymbol{p} \times \hat{\boldsymbol{z}}|}, \tag{6.7}$$

where $\boldsymbol{p}$ is the momentum of the final-state track from a b-hadron candidate decaying at point $\boldsymbol{d}$, $\hat{\boldsymbol{z}}$ is a unit vector along the z-axis and $\boldsymbol{v}$ is the origin of the VELO coordinate
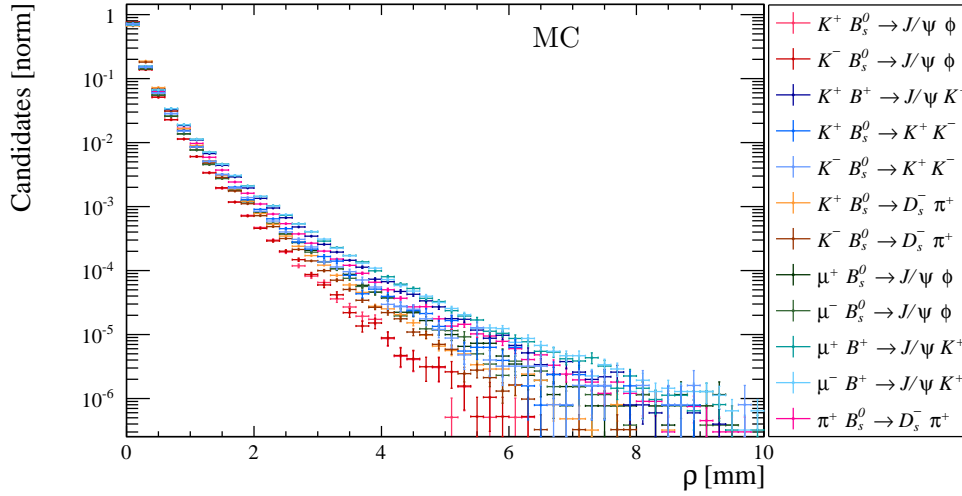
Figure 6.8: Distributions of ρ for different final state tracks coming from several decay channels in simulated MC (note the logarithmic scale on the y-axis). The different color points represents the different tracks as shown in the legend.

system. In simulated Monte Carlo samples, $\boldsymbol{v} = (0,0,0)$ corresponds to the centre of the LHCb coordinate system. Instead, during data taking the position of the LHCb VELO is moved and centred around the LHC beam line, which is monitored as a function of time. It can be seen in Figure 6.5 (b) that the z position of the PV is slightly shifted with respect to zero. For the calculation of ρ only shifts in the x and y directions are relevant. On average, in 2011 data the shift is 0.459 mm in the x direction and -0.015 mm in the y direction. For a proper calculation of the ρ variable, these shifts are adjusted event by event. In Figure 6.8 it is shown the ρ distribution for different final state tracks coming from several decay channels in simulated MC. The distributions are peaked near 0 mm, but clearly show large tails which extend out to 10 mm. For comparison, the diameter of VELO sensors is about 42 mm.

The VELO-track reconstruction efficiency, $\varepsilon_{\mathrm{VELO}}(\rho)$, extracted from simulated MC samples as a function of the track displacement ρ is shown in Figure 6.9 for the same tracks used in Figure 6.8. From these simulated b-hadron decays, it is observed that the effect is largely independent from the decay. The VELO-track reconstruction efficiency can be empirically parameterised by

$$\varepsilon_{\mathrm{VELO}}(\rho) = a(1 + c\rho^2), \tag{6.8}$$

where the parameters a and c are determined from an unbinned fit to the efficiency distribution. Even though these tracks have different kinematic properties and different ρ distributions they have very similar VELO-track reconstruction efficiencies. This motivates the usage of an unique control sample to determine this efficiency directly from data in order to be able to remove the corresponding lifetime bias. It is important to note that only the shape, thus the c parameter, is relevant and not the overall scale, the a parameter, which can be absorbed in the PDF normalisation. The small differences between the VELO-track reconstruction efficiencies of different tracks that can be seen
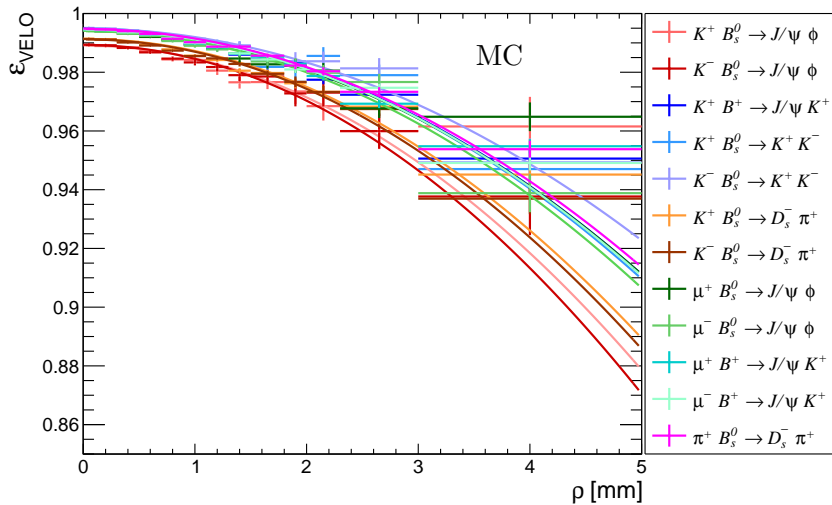
Figure 6.9: VELO-track reconstruction efficiency for different tracks coming from several decay channels in simulated MC as a function of the track displacement, ρ, as defined in Equation 6.7. The solid lines show the result of an unbinned maximum likelihood fit using the parameterisation in Equation 6.8 to the data.

in Figure 6.9 are correlated to the opening angle between the tracks coming from the same resonance and a slight dependence on the different phase space of the various decays. They are taken into account in the analysis as explained in the next section.

Correction for the acceptance effects of reconstruction in the vertex detector

This section introduces a method which has been developed to extract the VELO-track reconstruction efficiency directly from data without having to rely on simulated Monte Carlo samples. The technique is first described and validated on a simulated MC signal sample, before showing the results in data. The method leverages the fact that a large sample of $B^+ \to J/\psi K^+$ candidates is available in data and that, as explained in the previous section, the efficiency is similar for all particles. Using a control sample of $B^+ \to J/\psi K^+$ candidates where the K^+ is reconstructed as a Downstream track, the VELO-track reconstruction efficiency, $\varepsilon_{\text{VELO}}(\rho)$, is computed as the fraction of these tracks that are also reconstructed as Long tracks, using a so-called tag and probe technique. Indeed, the main difference among Downstream and Long tracks is that the latter use VELO tracks while the former not, so the VELO-track reconstruction efficiency can be determined. In the data and MC samples, when a Downstream track can be prolonged in the VELO and therefore is reconstructed also as a Long track, the Downstream track is removed. Thus, in order to determine the VELO-track reconstruction efficiency, the data and MC samples have to be processed with the software used to determine Downstream tracks. Performing an unbinned fit to the efficiency distribution it is possible to extract the a and c parameters of the function introduced in Equation 6.8. Since different configurations of the VELO reconstruction algorithms, FASTVELO (see Section 3.2.1), are used within the LHCb HLT1 software trigger (on-line) and during the subsequent HLT2 and off-line processing (collectively

(a) On-line reconstruction   (b) Off-line reconstruction
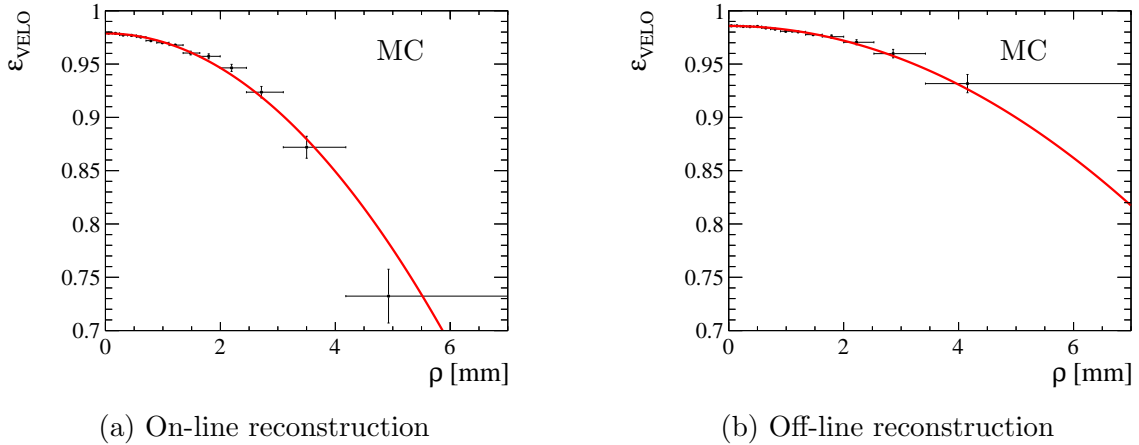
Figure 6.10: VELO-track reconstruction efficiency in simulated MC for kaon tracks reconstructed using the (a) on-line and (b) off-line algorithms as a function of the kaon displacement, ρ, as defined in Equation 6.7. The red solid lines show the results of an unbinned maximum likelihood fit using the parameterisation in Equation 6.8 to the data (black points).

called off-line), it is necessary to evaluate two different efficiencies.

Figure 6.10 shows the VELO-track reconstruction efficiency obtained using this method and Table 6.1 shows the corresponding fit results using the function defined in Equation 6.8. The stronger dependence of the on-line efficiency as a function of ρ is due to the tighter requirements used in the first stage of the software trigger such that it satisfies the required processing time.

The distortion to the decay-time distribution caused by the VELO-track reconstruction is corrected for by weighting each b-hadron candidate by the inverse of the product of the per-track efficiencies

$$w = 1 / \left(\prod_{i=1}^{N_{\text{tracks}}} \varepsilon^i_{\text{VELO}}(\rho_i) \right) . \tag{6.9}$$

The chosen efficiency depends on whether the particle is reconstructed with the on-line or off-line variant of the algorithm. Studies on simulated data show that tracks found by the on-line tracking algorithm that is used in the HLT1 are also found by the off-line tracking algorithm that is used in the second stage of the trigger, HLT2, and in the subsequent off-line selection. Thus, for tracks that are reconstructed in the HLT1 trigger, no additional effects are introduced by the subsequent stages of the reconstruction. In all the $H_b \to J/\psi X$ decay channels the muons coming from the J/ψ are used in every trigger stages, while the other particle tracks are reconstructed only by the off-line software version. Thus, the efficiency weight, for example, for each $B_s^0 \to J/\psi \phi$ candidate takes the form

$$w_{B_s^0 \to J/\psi \phi} = 1 / \left(\varepsilon^{\mu^+}_{\text{VELO,on-line}} \, \varepsilon^{\mu^-}_{\text{VELO,on-line}} \, \varepsilon^{K^+}_{\text{VELO,off-line}} \, \varepsilon^{K^-}_{\text{VELO,off-line}} \right) , \tag{6.10}$$

since the two muons are required to be reconstructed on-line, while the two kaons are reconstructed off-line. In the case of the $B^0 \to J/\psi K_S^0$ and $\Lambda_b^0 \to J/\psi \Lambda$ channels,

Table 6.1: *VELO reconstruction efficiency fitted parameters in simulated MC for kaon tracks reconstructed with the on-line and off-line algorithms. In both cases, the correlation coefficient between a and c is 0.2.*

	a	$c\,[\,\mathrm{mm}^{-2}]$
On-line	0.9788 ± 0.0001	-0.0083 ± 0.0003
Off-line	0.9857 ± 0.0001	-0.0035 ± 0.0002

since no VELO information is used when reconstructing the K_{S}^0 and Λ particles, the candidate weighting functions take the form $w = 1/\left(\varepsilon_{\mathrm{VELO,on-line}}^{\mu^+}\ \varepsilon_{\mathrm{VELO,on-line}}^{\mu^-}\right)$.

This method neglects correlations among the reconstruction efficiencies of the different particle tracks coming from the same b hadron. The efficiency to reconstruct a b-hadron decay product is correlated to that of the other decay products. This can be understood as the phase space of the decay products is correlated and the production vertex is the same. Thus, if a track is already reconstructed is more likely that also the other tracks can be reconstructed as well. Defining a fiducial region the correlations are significantly reduced, as the more inhomogeneous detector regions are ignored. Nevertheless, neglecting them leads to a remaining lifetime bias. Furthermore, studies on simulated data show that the efficiency for kaons and pions from the decay of ϕ and K^{*0} mesons is slightly smaller than for the kaon in $B^+ \to J/\psi\,K^+$ decays as can bee seen in Figure 6.9 (see Section 6.3.4). In addition, there are kinematic differences between the calibration B^+ sample and the signal samples. All together, if these effects are neglected, the lifetime bias is about 2-4 fs depending on the decay channel considered.

In order to account for these effects, the VELO-track reconstruction efficiency obtained from the tag and probe technique is compared with the true efficiency distribution available in each $H_b \to J/\psi\,X$ MC sample for every particle in the final state. Defining $\epsilon^{X|Y}$ as the efficiency to reconstruct the track X in the VELO given that the track Y has been already reconstructed, the total efficiency to reconstruct, for example, a $B_s^0 \to J/\psi\,\phi$ candidate, taking correlations and the different phase space into account, can be written as[2]

$$\epsilon(B_s^0 \to J/\psi\,\phi) = \varepsilon_{\mathrm{VELO,on-line}}^{\mu^-}\ \varepsilon_{\mathrm{VELO,on-line}}^{\mu^+|\mu^-}\ \varepsilon_{\mathrm{VELO,off-line}}^{K^+|\mu^+\mu^-}\ \varepsilon_{\mathrm{VELO,off-line}}^{K^-|K^+\mu^+\mu^-}. \qquad (6.11)$$

These individual efficiencies, $\epsilon^{X|Y}$, can be obtained for each particle in the final state only using the MC true efficiency since using the tag and probe technique the two muons coming from the J/ψ are always already reconstructed. Moreover, these individual efficiencies can be extracted separately from the corresponding simulated MC sample for each $H_b \to J/\psi\,X$ decay mode, therefore taking the different phase space into account. The true individual VELO-track reconstruction efficiencies obtained in this way are then fitted using the function in Equation 6.8. As an example, in Figure 6.11 the on-line VELO-track reconstruction efficiency obtained using the tag and probe technique is compared with the true efficiencies, $\varepsilon_{\mathrm{VELO,on-line}}^{\mu^-}$ and $\varepsilon_{\mathrm{VELO,on-line}}^{\mu^+|\mu^-}$, where

---

[2]The ordering of the particles in the formula is due to the fact that in data the muons are reconstructed first since they are used in the trigger, while the ordering of the charges is arbitrary.
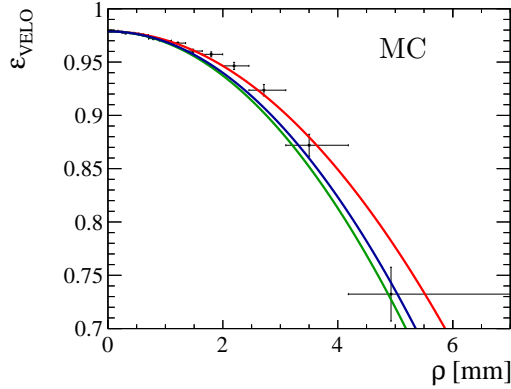
Figure 6.11: VELO-track reconstruction efficiency in simulated MC for kaon tracks reconstructed using the tag and probe technique and the on-line algorithm as a function of the kaon displacement, ρ, as defined in Equation 6.7. The red solid line show the result of an unbinned maximum likelihood fit using the parameterisation in Equation 6.8 to the data (black points). In green and blue it is shown the result of a fit to the true VELO-track reconstruction efficiency distributions $\varepsilon_{\mathrm{VELO,on-line}}^{\mu^-}$ and $\varepsilon_{\mathrm{VELO,on-line}}^{\mu^+|\mu^-}$, respectively.

the muons originate from a $B_s^0 \to J/\psi\phi$ candidate. It is possible to see that, due to correlations among the reconstruction efficiencies and different phase space, the curves do not coincide. These differences are taken into account calculating so-called scaling factors. They are determined by dividing the c parameters obtained from the fit of the MC true efficiencies by those derived from the $B^+ \to J/\psi K^+$ control sample using the tag and probe technique. These scaling factors are then included in the weight calculation of Equation 6.9, multiplying the corresponding c parameter. They have typical sizes in the range $[1.04, 1.65]$, depending on the decay mode and final-state particle being considered. If more statistics will be available in the control sample, binning the VELO efficiency for multiple variables such as the pseudorapidity or the number of tracks in the event is expected to reduce the shift of the scaling factors from unity.

The usage of these per-event weights removes completely the effect due to the VELO reconstruction inefficiency, as shown in Figure 6.6 (b). Here, the efficiency to reconstruct tracks in the VELO detector as a function of the decay-time is shown for $B_s^0 \to J/\psi\phi$ decays, where the per-event correction is introduced. The efficiency is fitted with the function introduced in Equation 6.1. The values of the β and γ parameters are basically consistent with zero within the uncertainty.

Applying the same technique to a data sample of $B^+ \to J/\psi K^+$ decays yields qualitatively similar behaviour for $\varepsilon_{\mathrm{VELO}}(\rho)$. Here, there is the complication that the sample is polluted by background candidates. In order to take them into account, the B^+ meson mass is modelled using the same PDF described in Section 5.6. This fit is used to assign to each candidate a weight that quantify the probability of a given event to be considered as a signal candidate depending on the value of the mass, so-called sWeights [104] (see Appendix B for more information). Thus, the VELO-track

(a) On-line reconstruction (b) Off-line reconstruction
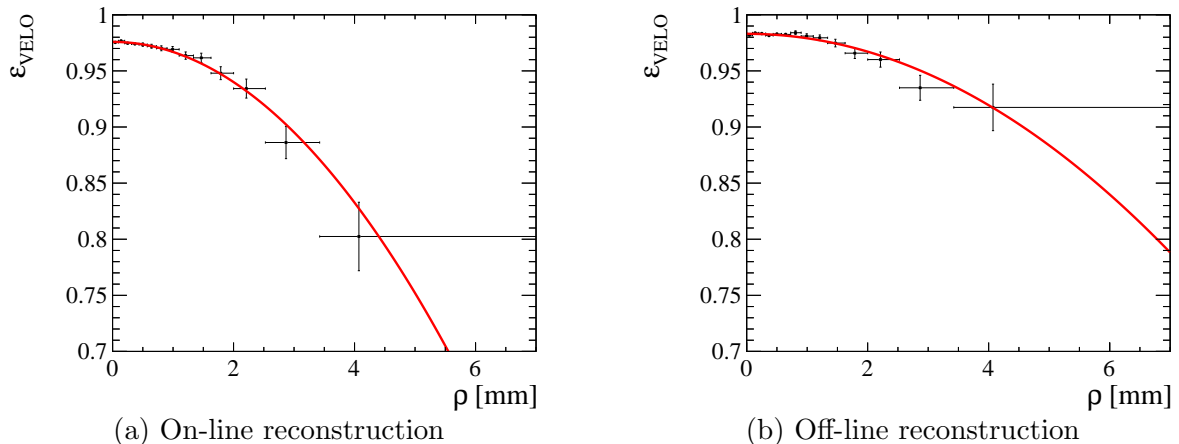
Figure 6.12: VELO-track reconstruction efficiency for kaon tracks reconstructed using the (a) on-line and (b) off-line algorithms as a function of the kaon displacement ρ, as defined in Equation 6.7. The red solid lines show the results of an unbinned maximum likelihood fit using the parameterisation in Equation 6.8 to the background subtracted data (black points).

Table 6.2: VELO reconstruction efficiency fitted parameters in data for kaon tracks reconstructed with the on-line and off-line algorithms. In both cases, the correlation coefficient between a and c is 0.2.

	a	$c\,[\,\mathrm{mm}^{-2}]$
On-line	0.9759 ± 0.0005	-0.0093 ± 0.0007
Off-line	0.9831 ± 0.0004	-0.0041 ± 0.0005

reconstruction efficiency can be isolated for signal candidates. In Figure 6.12 is visible the VELO-track reconstruction efficiency obtained using this method and Table 6.2 shows the corresponding fit results. There is a 10% discrepancy among the c parameters obtained in data and in simulated MC, see Table 6.2 and Table 6.1, which is due to slightly different conditions used in the simulated MC sample, like misalignment of the VELO modules that is worse in data than in MC or the presence of dead channels that are non implemented in MC.

The scaling factors obtained from simulated MC are multiplied to the c parameter obtained with the data-driven approach. Their effect on the lifetime is quite limited, since neglecting this correction there is only a 2-4 fs bias in the different b-hadrons lifetimes. Being conservative, since this part of the correction is derived from simulated MC, half of it is taken as a systematic uncertainty.

The remaining lifetime biasing effects due to the off-line selection are small compared to the VELO-track reconstruction efficiency. They will be analysed briefly in the next sections.
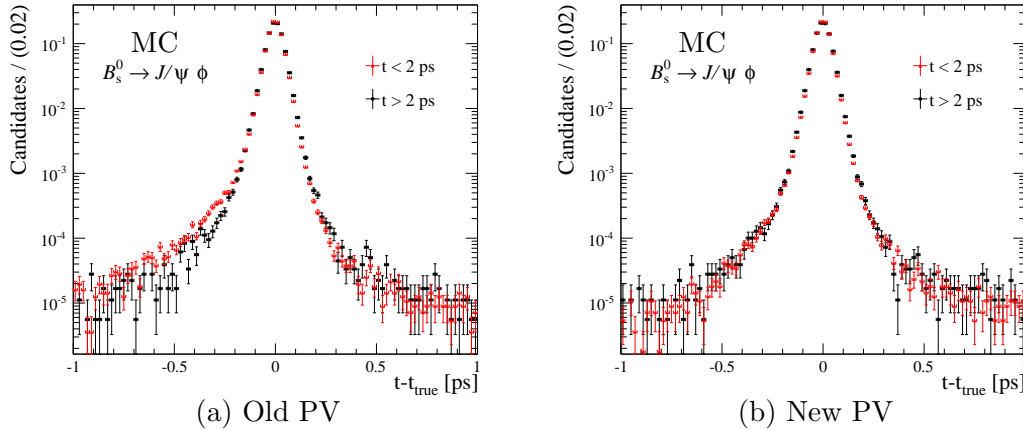
Figure 6.13: MC distribution of the b-hadron decay time residuals, $t - t_{\text{true}}$, for selected $B_s^0 \rightarrow J/\psi\phi$ candidates (a) using the old strategy to refit the PV and (b) using the new strategy developed for this analysis.

6.3.3 Primary vertex finding acceptance

The b-hadron decay time is computed as part of a kinematic decay tree fit (DTF) involving all final state tracks from the b candidate along with a constraint on the position of the primary vertex from which the b candidate originates, see Section 4.3. Prior to performing the decay tree fit, the position of each PV is re-calculated after removing the tracks coming from the b-hadron candidate and using only the remaining tracks to determine the position of the PV. This is necessary in order to prevent the b-hadron final state tracks biasing the PV position towards the b decay-vertex which would subsequently cause a decay-time bias. This effect is important especially if the PV is only constrained by few tracks and if the b hadron has a low decay time such that the decay vertex is closed to the PV. Since the minimum number of tracks necessary to find a PV is five, it is possible that most of them are coming from short-lived b-hadron candidates. However, even after the position of the PV is re-calculated in this way a bias in the decay-time distribution is still present.

In simulated Monte Carlo samples it is possible to check for each reconstructed decay time, t, of a b-hadron candidate the true value of it, t_{true}, that corresponds to the generated value. The MC distribution of the residuals, $t - t_{\text{true}}$, is shown in Figure 6.13 (a) for selected $B_s^0 \rightarrow J/\psi\phi$ candidates. Black and red points represent B_s^0 candidates with a reconstructed decay time greater or lower than 2 ps, respectively. It can be seen that b-hadron candidates with small decay times tend to have their decay times underestimated, leading to a negative tail in the residual distribution.

This is the origin of the decay-time bias due to the χ^2_{IP} and $\chi^2_{\text{IP,next PV}}$ requirements shown in steps 10-12 of Figure 6.3. Since the position of the PV is biased, short-lived b-hadron candidates are preferentially selected as their impact parameter with respect to the biased PV is on average smaller. This is visible in Figure 6.14, where the acceptance due to these two selection requirements is shown as a function of the reconstructed decay time. The acceptance is obtained dividing the normalised decay-time distribution of b-hadron candidates that pass the full selection by that of b-hadron candidates that pass
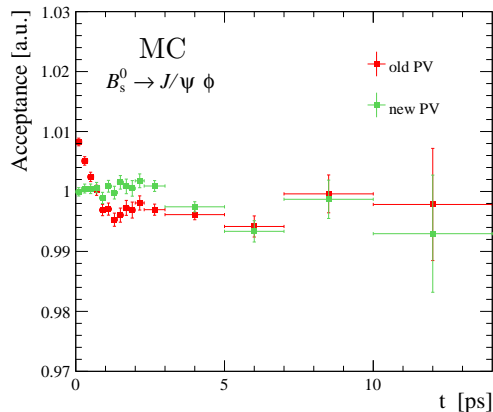
Figure 6.14: Decay-time dependent acceptance in a MC $B_s^0 \rightarrow J/\psi\phi$ sample of the χ^2_{IP} and $\chi^2_{\mathrm{IP,next\ PV}}$ B_s^0 candidate requirements with respect to the remaining selection procedure.

the full selection but these two requirements. The red points show the distribution before any correction is applied and especially below 2 ps the efficiency to select b hadrons is clearly higher.

This effect is removed by using an alternative PV refitting procedure. The nominal method simply removes the b-hadron final state tracks and refind the position of the PV using the remaining tracks that were originally used to form the PV. However, it is possible the tracks that are belonging to the PV are neglected, since they were discarded when the PV was searched including the b-hadron final state tracks. An alternative approach is to start the search for the PV from scratch using all tracks in the event, minus the b-hadron final state tracks. The MC distribution of the residuals, $t - t_{\mathrm{true}}$, is shown in Figure 6.13 (b) for selected $B_s^0 \rightarrow J/\psi\phi$ candidates. Here the PV used to constraint the direction of the b hadron is determined using the new PV refitting procedure. The residual distribution is now symmetric and fully compatible for small and high b-hadrons decay time. This procedure completely eliminates the bias at low decay time introduced by the b-hadron selection, as it is shown in Figure 6.14 by the green distribution.

6.3.4 Selection acceptance

Another biasing effect that is arising during the selection procedure is due to the requirement on the goodness of the vertex formed by the two kaons coming from the ϕ resonance or the kaon and the pion coming from the K^{*0} resonance. Imposing the $\chi^2_{\mathrm{vtx}}/\mathrm{nDoF}$ to be smaller than 16 causes a 3-2 fs bias, as shown in step number 9 in Figure 6.3. The decay-time acceptance due to this requirement is shown in Figure 6.15 (a) for $B_s^0 \rightarrow J/\psi\phi$ candidates in simulated MC sample. The data distribution is fitted with the function defined in Equation 6.1 and the fit result is shown in the figure. The same study for $B^0 \rightarrow J/\psi K^{*0}$ gives a smaller bias. On the other hand, the same requirement for the two muons coming from the J/ψ gives instead a negligible bias. It is found that this effect is correlated to the opening angle between the two decay products of the resonance. The distribution of the opening angle, α, between the K^+ and π^-,
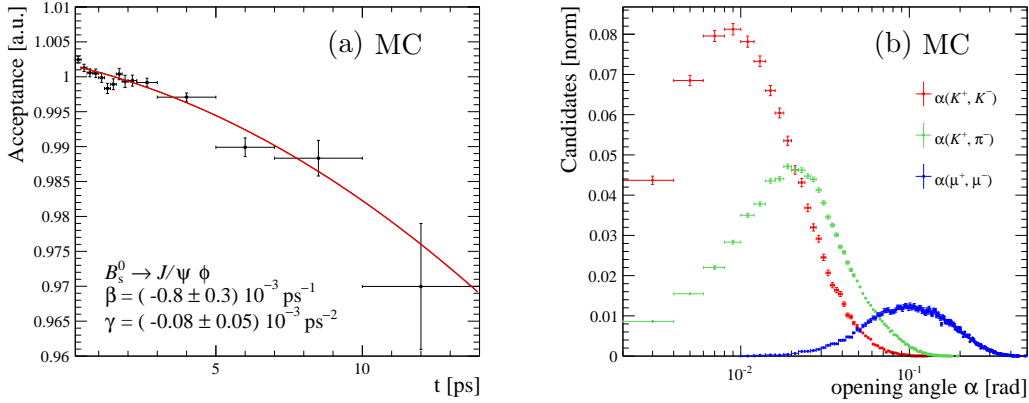
Figure 6.15: (a) Decay-time acceptance introduced by the requirement on the goodness of the vertex, $\chi^2_{\mathrm{vtx}}/\mathrm{nDoF} < 16$, formed by the two kaons coming from the ϕ resonance. Superimposed there is a fit with the function defined in Equation 6.1 and the result of the fit. (b) Distributions of the opening angle, α, between the K^+ and K^- from the ϕ, the K^+ and π^- from the K^{*0}, and the μ^+ and μ^- from the J/ψ represented by the green, red and blue data points, respectively.

the K^+ and K^-, and the μ^+ and μ^-, is visible in Figure 6.15 (b) in green, red and blue, respectively. Indeed, the bias due to the vertex quality requirement decreases if the opening angle is larger. The connection between the opening angle and the decay-time bias appears to be related to the fact that if the opening angle is very small ($\mathcal{O}(0.001\,\mathrm{rad})$) the two decay products are not enough separated inside the VELO and they traverse same Φ sensor. Since the first sensors are at a radial distance of 7 mm from the beam, this effect is greater if the b-hadron decay vertex (and thus also the K^{*0} and ϕ decay vertices) is displaced by a similar amount. This can be seen in Figure 6.16, where the Φ sensor clusters of K^+ and K^- tracks, with the same opening angle, are sketched in case of a displaced B^0_s (in red) or a non displaced B^0_s (in blue). It is possible to see that when the kaons originate from a displaced B^0_s and have a small opening angle, their tracks share the first hit in the VELO. Due to this reason, these tracks are causing on average a worse $\chi^2_{\mathrm{vtx}}/\mathrm{nDoF}$ so that these events are often rejected during the selection procedure.

Moreover, for the same reason the two decay products with a small opening angle are also sometimes not reconstructed in the VELO. This causes a worse VELO-track reconstruction efficiency at large ρ for these tracks. This effect is visible in Figure 6.9, where the two kaons coming from the $B^0_s \to J/\psi\phi$ decay channel exhibit a greater drop with respect to the two muons coming from the same decay. Thi effect is already included in the scaling factors derived from simulated MC samples, as described in Section 6.3.2.

A possible solution to move around the bias due to the requirement on the $\chi^2_{\mathrm{vtx}}/\mathrm{nDoF}$ is to remove this requirement from the selection. However, this is not enough as the bias is then propagated to the $\chi^2_{\mathrm{DTF}}/\mathrm{nDoF}$ selection requirement on the b-hadron candidate, see Figure 6.17 (a). Removing also this requirement would increase the background component significantly. Thus, to remove the effect, besides removing the $\chi^2_{\mathrm{vtx}}/\mathrm{nDoF}$
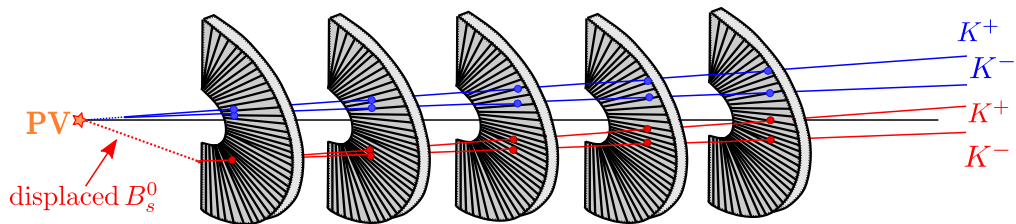
Figure 6.16: Schematic view of the Φ sensor clusters of K^+ and K^- tracks coming from the decay of a displaced B_s^0 (in red) or a non displaced B_s^0 (in blue).

(a) before correction

(b) after correction
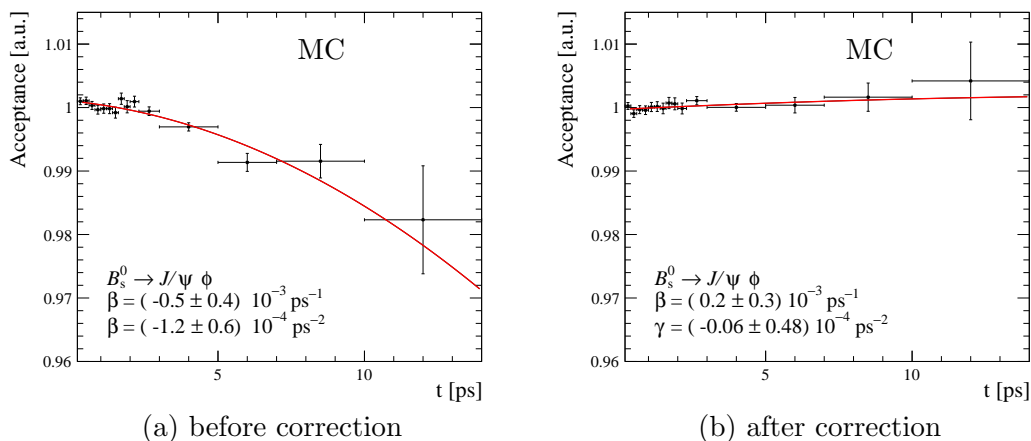
Figure 6.17: (a) Decay-time acceptance introduced by the requirement on the goodness of the B_s^0 vertex, $\chi^2_{\mathrm{DTF}}/\mathrm{nDoF} < 5$, when the selection requirement on the $\chi^2_{\mathrm{vtx}}/\mathrm{nDoF}$ of the ϕ resonance is removed. (b) The same decay-time acceptance is shown after the usage of the alternative DTF described in the text. In both figures, superimposed there is a fit with the function defined in Equation 6.1 and the result of the fit.

requirement on the ϕ and K^{*0} decay vertex, the calculation of the $\chi^2_{\mathrm{DTF}}/\mathrm{nDoF}$ for the $B^0 \to J/\psi\, K^{*0}$ and $B_s^0 \to J/\psi\, \phi$ channels is performed with an alternative decay tree fit in which the assigned track parameter uncertainties of the kaon and pion are increased in such a way that their contribution to the b-hadron vertex position is negligible. This completely remove the acceptance effect, as it is shown in Figure 6.17 (b).

6.3.5 Trigger acceptance

As discussed in Section 5.4, in the first stage of the software trigger only quantities that are uncorrelated to the b-hadron decay time are used. Usually, in other analyses involving the decay of a b hadron to a $J/\psi X$ final state, like the measurement of the CP-violating phase ϕ_s in the decay $B_s^0 \to J/\psi\phi$ [5], a so-called DEC trigger was used in order to enhance the available statistics. As explained in Section 5.4 a DEC DiMuon trigger can use a pair of muons coming from the signal candidate decay, from the rest of the event or even from a mixture of the two. However, it is the origin of the rather large bias visible in step 14 in Figure 6.3. In order to have a positive decision from a DiMuon trigger like the one used in the HLT1, two muons have to be reconstructed. Usually these are the two muons coming from the J/ψ meson decay, but if one of the

two is not reconstructed in the trigger the event can still be triggered by a DEC trigger line if another independent muon is reconstructed. Due to the selection requirement used in the trigger, the two muon tracks have to be close in space. This happens more frequently if the J/ψ decays close to the PV, since in this region there are many other muons directly produced at the pp collision vertex. As a result, the HLT1 DEC efficiency is larger for short-lived b hadrons, since the decay vertex of the b hadron coincides with the decay vertex of the J/ψ. In order to remove this effect, only TOS triggers, where both muons have to come from the signal J/ψ, are used in this analysis. In this way one is sure that a signal candidate which is used in the analysis has been used in the trigger decision.

6.4   Lower decay-time acceptance

The efficiency of the second stage of the software trigger depends on the b-hadron decay time, see Figure 6.2 (b), as it requires that the J/ψ meson is significantly displaced from the PV. The decay-time dependence of this efficiency, $\varepsilon_{\text{trigger}}(t)$, is obtained for each $H_b \rightarrow J/\psi X$ decay mode using the same technique developed in [5] and explained in details in [105]. This technique exploits a corresponding sample of $H_b \rightarrow J/\psi X$ candidates that are selected without any displacement requirement. For each channel, the control sample corresponds to approximately 40% of the total number of signal candidates due to limitations in the bandwidth available. A maximum likelihood fit is performed to the unbinned invariant mass distribution $m(J/\psi X)$ of every b-hadron candidate to determine the fraction of signal decays that survive the decay-time biasing trigger requirements as a function of decay time.

The same technique is used to determine the decay-time dependent acceptance of the triggered candidates caused by the stripping selection, $\varepsilon_{\text{stripping}|\text{trigger}}(t)$, which is introduced by the same requirement on the detachment of the J/ψ mesons in the sample used to reconstruct the b-hadron decays. Due to the fact that the position of the PV found in the off-line selection is different with respect to the on-line one, due to simplifications used in the on-line reconstruction, the usage of this requirement in the stripping adds a small additional effect. The combined acceptance, Acceptance$_{\text{trigger \& stripping}}(t)$, is given by the product of Acceptance$_{\text{trigger}}(t)$ and Acceptance$_{\text{stripping}|\text{trigger}}(t)$.

The expected decay-time acceptance is a curve starting from zero for vanishing b-hadron decay time with a plateau at large decay times. However, the acceptance reaches a maximum around 0.6 ps and then drops down before reaching the plateau at large decay times. This is visible in Figure 6.18, which shows $\varepsilon_{\text{trigger \& stripping}}(t)$ obtained for the different $H_b \rightarrow J/\psi X$ channels as a function of decay time. Studies using simulated events show that dip near 1.5 ps appears because of the PV reconstruction. In the software trigger some final-state tracks of short-lived b-hadron decays may be used to reconstruct an additional fake PV close to the true b-hadron decay vertex, since they are not eliminated as done in the off-line analysis. As a result the reconstructed J/ψ meson does not satisfy the displacement requirement, leading to a decrease in efficiency. This happens more frequently for short-lived b hadrons and the drop is more pronounced depending on the number of signal tracks that are coming from the PV. This is visible in Figure 6.18 comparing the drop of $B^+ \rightarrow J/\psi K^+$ (two tracks from the
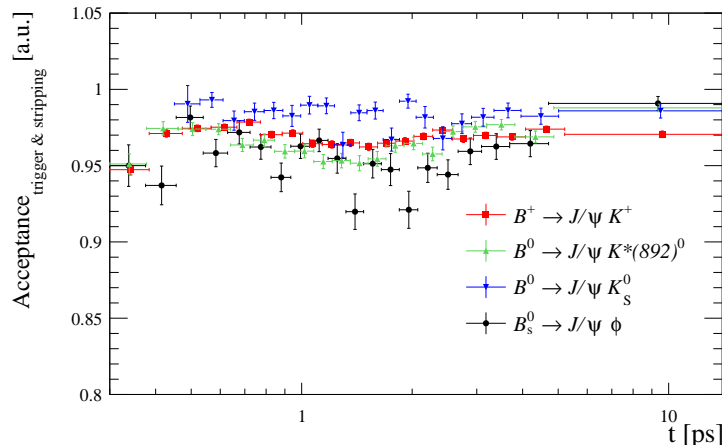
Figure 6.18: Combined trigger and selection acceptance, Acceptance$_{\text{trigger \& stripping}}(t)$,
for the different $H_b \rightarrow J/\psi X$ *candidates.*

PV) events to that of $B^0 \rightarrow J/\psi K^{*0}$ (three tracks from the PV) events. This effect is
more significant in simulated samples due to the higher statistics available.

The acceptance parameterisation for each channel is used in the fit to measure the
corresponding b-hadron lifetime. An exception is made for the $\Lambda_b^0 \rightarrow J/\psi \Lambda$ channel
where, owing to its smaller event yield, Acceptance$_{\text{trigger \& stripping}}(t)$ measured with
$B^0 \rightarrow J/\psi K_S^0$ decays is used instead. The validity of this approach is checked using
large samples of simulated events.

6.5 Overview of the acceptance corrections

The lifetime as a function of the different analysis steps is shown in Figure 6.19
and Figure 6.20 for the different b hadrons. The red points refer to the lifetime value
extracted from a sample where all the corrections previously mentioned are not included,
as presented in Section 6.2. Green points indicate the lifetime value extracted from
a sample where all the corrections explained in this chapter are included. In all the
different b-hadron samples the departure from the generated lifetime, $\Delta\tau$, is found to
be basically compatible with zero within the statistical precision of each simulated
sample. However, there are still small remaining biases that are consistent among all
b-hadron channels. This is the case, for example, for the last step in the selection
procedure, step number 12 in Figure 6.19 and number 15 in Figure 6.20. It is possible
to see in Figure 6.14 that, even after the new PV refitting procedure, there is still a
decay-time dependent acceptance at large decay times. Similar results are found for all
the other channels. However the impact of these small remaining biases to the lifetime
measurements and to the total systematic uncertainty is very small, so that further
investigations were not necessary. Thus, the measured lifetimes in the data sample are
simply corrected by each $\Delta\tau$ and a corresponding systematic uncertainty is assigned,
given by the size of the statistical uncertainty on the fitted lifetime for each simulated
signal mode.
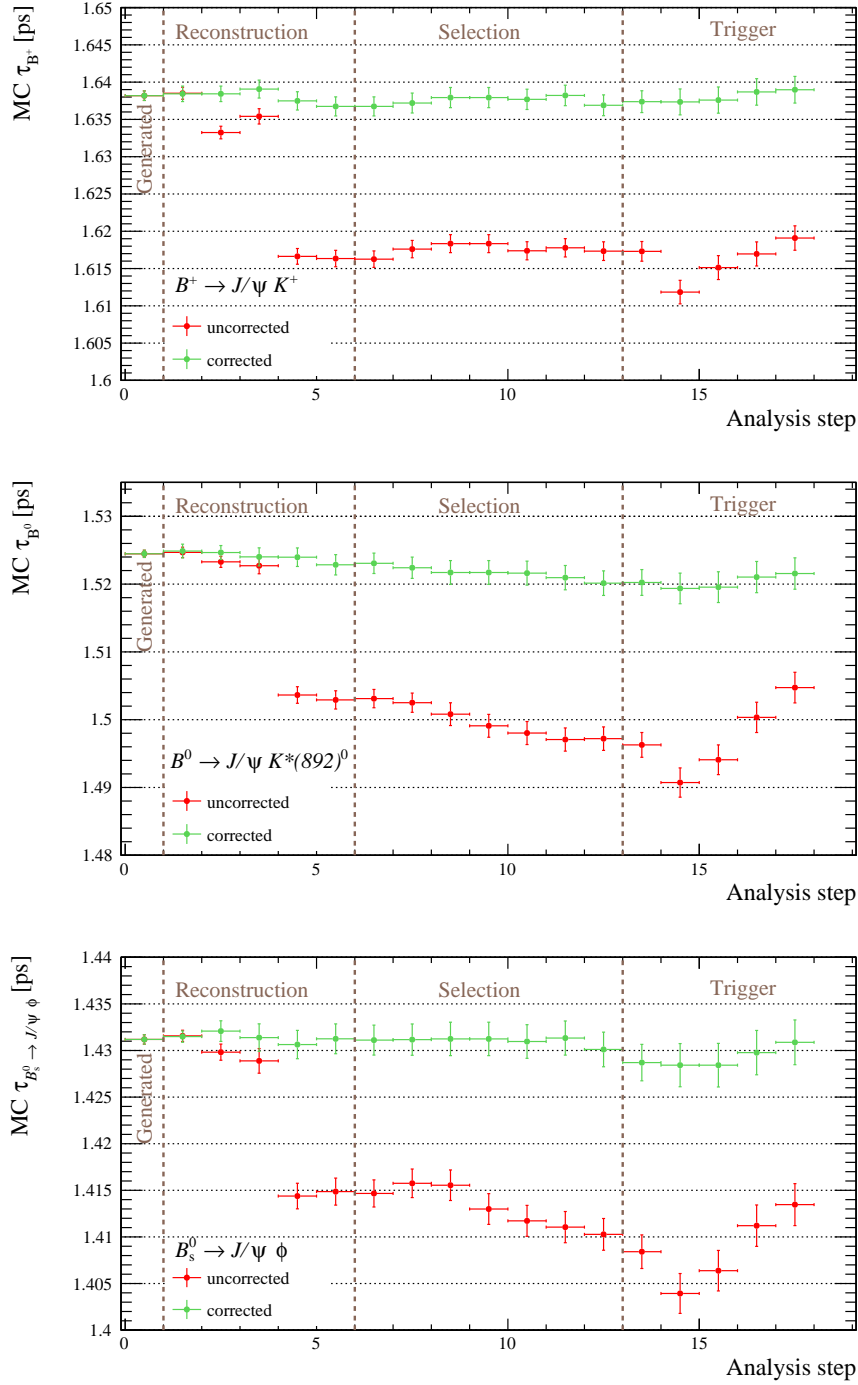
Figure 6.19: Measured lifetime in simulated Monte Carlo samples of $B^+ \to J/\psi K^+$, $B^0 \to J/\psi K^{*0}$ and $B_s^0 \to J/\psi \phi$ decay channels as a function of the different reconstruction, selection and trigger requirements used in the analysis. All the corrections for the decay-time biasing effects highlighted by the red curve are taken into account in the green distribution. For a detailed explanation of the analysis steps see Appendix A.
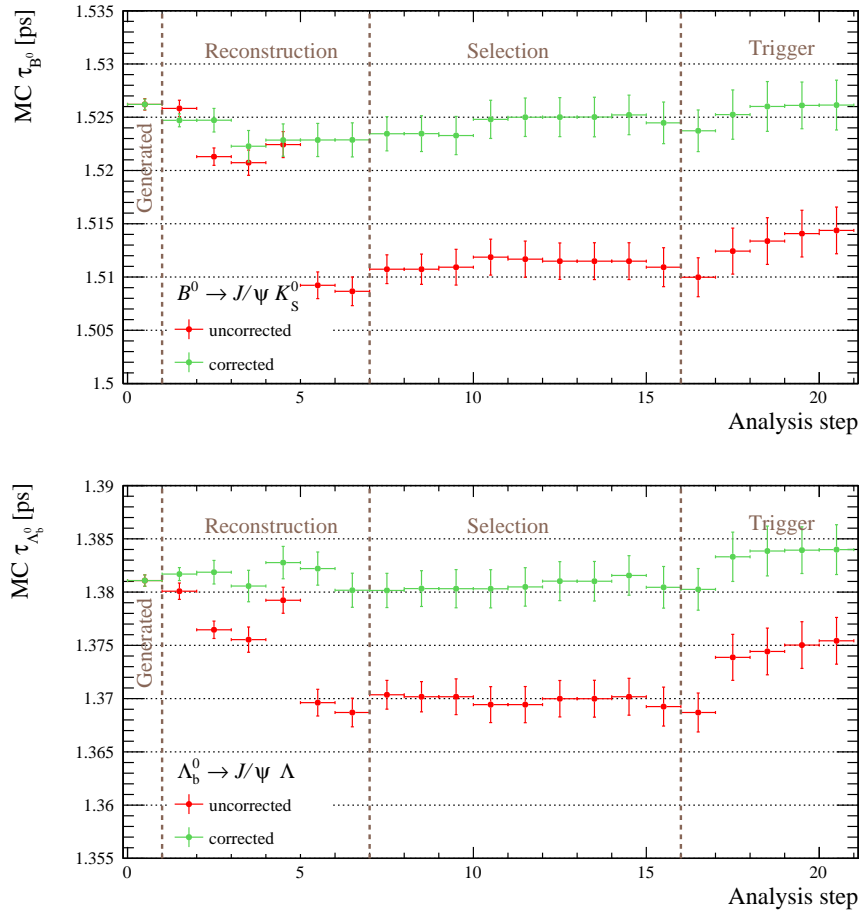
Figure 6.20: Measured lifetime in simulated Monte Carlo samples of $B^0 \to J/\psi K_S^0$ and $\Lambda_b^0 \to J/\psi \Lambda$ decay channels as a function of the different reconstruction, selection and trigger requirements used in the analysis. All the corrections for the decay-time biasing effects highlighted by the red curve are taken into account in the green distribution. For a detailed explanation of the analysis steps see Appendix A.

6.6 Summary

Different techniques have been developed in order to correct the decay-time dependent acceptance effects that are introduced in the different stages of the analysis. They are briefly summarised here.

1. A fiducial region where the efficiency for a track to be reconstructible is largely uniform is introduced. It is defined by requiring the final state tracks to have a pseudorapidity in the range $2.0 < \eta < 4.5$ and the z position of the PV to be within 100 mm of the nominal interaction point for the $B^+ \to J/\psi K^+$, $B^0 \to J/\psi K^{*0}$ and $B_s^0 \to J/\psi \phi$ decay channels. For the $B^0 \to J/\psi K_S^0$ and $\Lambda_b^0 \to J/\psi \Lambda$ decay channels, this requirement is more strict and the z position of the PV has to be greater than -50 mm.

2. To correct for the VELO-track reconstruction efficiency loss at large b-hadron decay times a data-driven technique has been developed. The VELO-track efficiency as a function of the displacement of a track with respect to the z axis, ρ, is derived from a $B^+ \to J/\psi K^+$ control sample. Each b-hadron candidate is weighted by the inverse of the product of the per-track efficiencies. A small correction to this procedure (about 10%) is taken from Monte Carlo simulated samples in order to consider correlations among the reconstruction efficiencies of different tracks and kinematic differences between the calibration B^+ sample and the signal sample.

3. The position of the primary vertex has been found to be biased towards the b-hadron decay vertex. This causes an underestimation of the b-hadron decay-time, especially below 2 ps, and subsequently a decay-time dependent acceptance when selection requirements that use the position of the PV are introduced in the analysis. A new strategy to find the position of the PV has been developed in order to remove this effect.

4. The quality of the vertex fit turned out to be worse for tracks with narrow opening angle and large displacement. Thus, the selection requirement on the goodness of the vertex formed by the two kaons coming from the ϕ resonance or the kaon and the pion coming from the K^{*0} resonance introduce a decay-time acceptance. This effect is removed avoiding this selection requirement and performing the calculation of the χ^2_{DTF} for the $B^0 \to J/\psi K^{*0}$ and $B^0_s \to J/\psi \phi$ channels with an alternative decay tree fit in which the kaon and pion contribution to the b-hadron vertex position is neglected.

5. In the first stage of the software trigger so-called TOS trigger lines need to be used to be sure that a signal candidate which is used in the analysis has been as well used in the trigger decision.

6. A requirement on the displacement of the J/ψ from the PV is used in the trigger and in the stripping selection. A parameterisation of the decay-time dependent acceptance introduced by this requirement is obtained from data using a corresponding limited size sample of $H_b \to J/\psi X$ candidates that are selected without any displacement requirement.

The lifetime as a function of the different analysis steps after all these corrections have been implemented is shown in green Figure 6.19 and Figure 6.20 for the different b hadrons.

7

All models are wrong. Some are useful.

— George E. P. Box

Once that all the methods developed in order to correct for the decay-time dependent acceptance, explained in Chapter 6, are taken into account in the analysis, it is possible to extract the lifetime of the different b hadrons performing an unbinned maximum likelihood fit. In this chapter, all the necessary components needed in order to perform this fit are introduced, before the results of the fit are presented. Firstly, the fit strategy is summarised followed by a consistency check to validate the fit procedure. Secondly, the decay-time resolution is introduced. Thirdly, the background is analysed in detail. Finally, the fit results are reported in the last section of this chapter.

7.1 Maximum Likelihood fit

For each channel, the lifetime is determined from a two-dimensional maximum likelihood fit to the unbinned invariant mass, $m(J/\psi X)$, and decay time, t, distributions, as introduced in Section 4.4. The baseline fit model is the so-called **classical fit**, cFit, where both the signal part and the background part of the probability density function, PDF, are explicitly modelled. The PDF is constructed as

$$\mathcal{P}(m, t| \overrightarrow{\vartheta}) \;\; = \;\; f_{\text{sig}} \left(\mathcal{S}_m(m| \overrightarrow{\vartheta}_m) \times \mathcal{S}_t(t| \overrightarrow{\vartheta}_t) \right) \tag{7.1}$$
$$+ (1 - f_{\text{sig}}) \left(\mathcal{B}_m(m| \overrightarrow{\vartheta}_m) \times \mathcal{B}_t(t| \overrightarrow{\vartheta}_t) \right) ,$$

where f_{sig} is the signal fraction, determined in the fit, and $\mathcal{S}_m \times \mathcal{S}_t$ and $\mathcal{B}_m \times \mathcal{B}_t$ are the mass and the decay time distribution PDFs for the signal and background components, respectively. A systematic uncertainty is assigned to the assumption that the mass and decay-time PDFs factorise, see Chapter 8.

Mass component The signal mass PDF, $\mathcal{S}_m$, has been introduced in Section 5.6. It is modelled by the sum of two Gaussian distributions

$$\mathcal{S}_m \propto f_{\sigma_1} \cdot \mathcal{G}_1 \left(m_{H_b}, \sigma_1; m \right) + (1 - f_{\sigma_1}) \cdot \mathcal{G}_2 \left(m_{H_b}, \sigma_2; m \right) , \tag{7.2}$$

up to a normalisation factor. The parameters of the mass distribution left free in the fit are the common mean, m_{H_b}, the widths of the two Gaussian distributions, σ_1 and σ_2, and the fraction of the first Gaussian distribution, f_{σ_1}. The background mass distribution, $\mathcal{B}_m$, is modelled by an exponential function with a single free parameter, α_m. A single fit to the mass distribution alone gives the results listed in Table 5.8.

In summary, the parameters describing the mass PDF consist of $\overrightarrow{\vartheta}_m = \{m_{H_b}, \sigma_1, \sigma_2, f_{\sigma_1}, \alpha_m\}$. In the fit to data these mass parameters are left free to vary and they are obtained simultaneously with the decay-time parameters.

Decay-time component The expected signal b-hadron decay time distribution is described by an exponential function with decay constant given by the b-hadron lifetime, τ_{H_b}. The signal decay time PDF, $\mathcal{S}_t$, is obtained by multiplying the exponential function by the combined t-dependent trigger and selection efficiency, $\mathrm{Acc}\,(t)$, described in Section 6.4. For each channel the exponential function is convoluted with a Gaussian resolution distribution, $\mathcal{R}\,(t)$, with width σ and mean Δ (see Section 7.2.1) that are fixed in the fit. Thus, the signal decay time PDF is

$$\mathcal{S}_t \propto \left[e^{-(t'/\tau_{H_b})} \otimes \mathcal{R}\,(t, t') \right] \times \mathrm{Acc}\,(t), \tag{7.3}$$

up to a normalisation factor.

From inspection of background events in the b-hadron invariant mass distribution, see Section 7.3, the background decay time PDF, $\mathcal{B}_t$, is well modelled by a sum of three exponential functions with different decay constants, τ_{B_1}, τ_{B_2} and τ_{B_3}

$$\mathcal{B}_t \propto \left[f_{B_1}\, e^{-(t'/\tau_{B_1})} + f_{B_2}\, e^{-(t'/\tau_{B_2})} + (1 - f_{B_1} - f_{B_2})\, e^{-(t'/\tau_{B_3})} \otimes \mathcal{R}\,(t, t') \right]. \tag{7.4}$$

Here, f_{B_1} and f_{B_2} are the fractions of the first and the second exponential function, respectively.

In summary, the parameters describing the decay-time PDF consist of $\overrightarrow{\vartheta}_t = \{\tau_{H_b}, f_{B_1}, \tau_{B_1}, f_{B_2}, \tau_{B_2}, f_{B_3}, \tau_{B_3}, \sigma, \Delta\}$. In the fit to data all but the last two decay-time parameters are left free to vary.

The negative log-likelihood, constructed as

$$-\ln \mathcal{L}(\overrightarrow{\vartheta}) = -\alpha \sum_i^{\mathrm{candidates}} w_i \ln \mathcal{P}(m, t | \overrightarrow{\vartheta}), \tag{7.5}$$

is minimised in the fit in order to estimate the parameters $\overrightarrow{\vartheta}$, where the weights w_i correspond to the per-candidate correction for the VELO reconstruction efficiency described in Section 6.3.2. The factor $\alpha = \sum_i w_i / \sum_i w_i^2$ is used to include the effect of the weights in the determination of the uncertainties [104].

7.1.1   Validation of the fit procedure

The fit procedure is validated using Toy Monte Carlo, where the mass and the decay-time distributions of the b hadrons are generated according to the PDFs used in
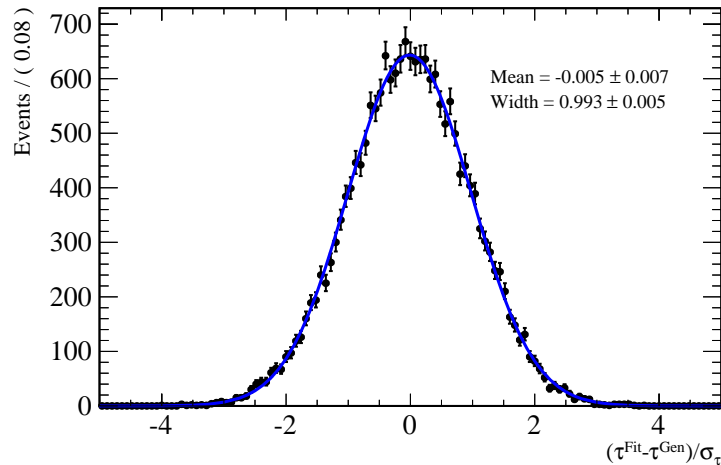
Figure 7.1: Results of 10 000 toy-experiments. The pull distribution for the lifetime, τ, as defined in Equation 7.6, is shown. The data are shown by the black points. The distribution is fitted with a Gaussian distribution represented by the blue solid line.

the fit. In each toy experiment, the number of generated events is set to the number of events available in data. The result of the fit on data for all free parameters is used when generating the mass and the decay-time distribution. Moreover, the decay-time acceptance effects discussed in Chapter 6 are also taken into account simulating a linear acceptance as a function of the decay time. This allows for a verification of the per-candidate correction as well. The generated sample is then fitted in the same way as the data sample, using the same fitting technique. Thus, this method does not probe effects due to wrong underlying theory models. These effects are studied in Chapter 8 as part of the systematic uncertainties.

For each generated data sample, i, the fit results, $\vartheta_i^{\mathrm{Fit}}$, are saved together with the uncertainty estimate on each fitted parameter, σ_{ϑ_i}, and the value used in the generation, $\vartheta_i^{\mathrm{Gen}}$. Using these quantities the so-called pull of each parameter is calculated as

$$\mathrm{pull}_i = \frac{\vartheta_i^{\mathrm{Fit}} - \vartheta_i^{\mathrm{Gen}}}{\sigma_{\vartheta_i}} \ . \tag{7.6}$$

This procedure is repeated 10 000 times. In the Gaussian limit, if the PDFs are implemented correctly in the fit algorithm and the uncertainty estimation is correct, the pulls of the fitted parameters follow a Gaussian distribution with mean equal to zero and width equal to one.

One example of such a toy study for the $\Lambda_b^0 \to J/\psi\Lambda$ decay is shown in Figure 7.1. It shows the pull distribution of the lifetime. It can be seen that the pull distribution is well described by a Gaussian with a mean compatible with zero and a width compatible with one. This is the lowest statistics decay mode analysed. It is also the sample where the highest fraction of combinatorial background is measured, see Section 5.6, so these are the worse conditions of all channels. Nevertheless, it was verified that also in the other decay modes the estimate of the lifetime is unbiased.

7.1.2   Alternative fit procedure

In the classical fit, as described in Section 7.1, the background components are modelled explicitly. An alternative approach is the so-called **sFit** method [104]. In this case, the background in the decay-time distribution is not explicitly modelled but subtracted in advance. This is obtained by using a single fit to the invariant mass as discriminating variable to assign a weight, $W_s(m_i)$, to each candidate. This weight, often referred to as sWeight, corresponds to the probability of a given event to be considered as a signal candidate depending on the measured invariant mass. Events that are likely to be background are assigned small or negative weights. For more information see Appendix B. Then, a maximum likelihood fit is performed where each candidate is weighted by $W_s(m_i)$. The fit minimises the negative log likelihood function

$$-\ln\mathcal{L}(\overrightarrow{\vartheta}) = -\alpha_s \sum_i^{\text{candidates}} w_i W_s(m_i) \ln\mathcal{P}(m,\, t|\, \overrightarrow{\vartheta}), \qquad (7.7)$$

in order to estimate the parameters $\overrightarrow{\vartheta}$, where the weights w_i, as before, correspond to the per-candidate correction for the VELO reconstruction efficiency described in Section 6.3.2. The factor $\alpha_s = \sum_i(w_i \cdot W_s(m_i))/\sum_i(w_i \cdot W_s(m_i))^2$ is used to include the effect of the VELO reconstruction efficiency and mass distribution weights in the estimation of the uncertainties. The difference between the results of the two fitting procedures is used to estimate the systematic uncertainty on the background description.

The sFit technique, as the cFit, is only valid if the discriminating variable is independent from all other observables. As already stated before, the mass is assumed to be uncorrelated with the decay time.

7.2   Decay-time resolution

The reconstructed decay time, t, of a particle in its rest frame is given by Equation 4.1. It is defined in terms of the reconstructed decay length, L, the momentum, p, and the invariant mass, m, of the particle in the LHCb frame. The uncertainty on the decay length and the momentum are basically uncorrelated in LHCb. Thus, the decay-time uncertainty can be expressed in terms of the decay-length uncertainty, σ_L, and the momentum uncertainty, σ_p, as

$$\sigma_t^2 = \left(\frac{m}{p}\right)^2 \sigma_l^2 + \left(\frac{t}{p}\right)^2 \sigma_p^2. \qquad (7.8)$$

It can be seen that there is an explicit dependence on the decay time in the second term of the right-hand side equation. However, for small decay times, up to a few times the b-hadron lifetime, the uncertainty is dominated by the resolution on the decay length, which in turn is dominated by the secondary vertex resolution of the VELO. For large decay times instead, it is dominated by the momentum resolution. As an example, for an average b-hadron momentum of $p = 100\,\text{GeV}/c$ and a decay time of 1 ps, a secondary vertex resolution of about $\sigma_l = 200\,\mu m$ and a relative momentum resolution of $\sigma_p/p = 0.4\%$, the first term on the right hand side of Equation 7.8 is about

20 times larger than the second term. The two contributions are approximately equal only at several times the b-hadrons lifetimes. Therefore, the momentum resolution plays only a small role for this analysis.

The resolution on the decay time is a necessary component of the probability density function in order to perform precise lifetime measurements. However, the most stringent demands on the decay time resolution stem from the requirement to resolve the fast oscillations induced by B_s^0–$\bar{B}_s^0$ mixing in other important LHCb analysis [106]. At LHCb an excellent decay-time resolution, about 3% of the b-hadron lifetime, is achieved thanks to several reasons. First of all, b hadrons are highly boosted in the forward direction, see Section 1.4.1. Thus, the decay vertex of a b hadron is on average well separated from the pp interaction point. Moreover, the VELO detector provides an excellent vertex resolution. A good momentum resolution is obtained due to the attention given in the minimisation of the amount of material particles traverse in order to reduce effects from multiple scattering.

Overall, the decay-time resolution at LHCb is small compared to b-hadron lifetimes, therefore its effect when performing lifetime measurements is very limited. This is a fortiori valid in this analysis since the events below 0.3/0.45 ps are removed by the off-line selection requirements. Therefore a simplified resolution model is used and possible systematic effects related to the choice of resolution model are discussed in Chapter 8.

7.2.1 Decay-time resolution in simulated samples

Using the $H_b \to J/\psi X$ simulated Monte Carlo samples introduced in Section 5.2 it is possible to have direct information on the decay-time resolution. It is determined from the difference between the reconstructed decay-time of the selected b-hadron candidate and the corresponding generated value. The decay-time resolution is shown in Figure 7.2 for the different $H_b \to J/\psi X$ decay modes. The mean value and the root mean square, RMS, of these distributions are summarised in Table 7.1 for all different $H_b \to J/\psi X$ decays. The decay-time resolution is about 40 fs for $B^+ \to J/\psi K^+$, $B^0 \to J/\psi K^{*0}$ and $B_s^0 \to J/\psi\phi$ decay modes, where all the final state particles are reconstructed as Long tracks. It increases to about 60 fs for the $B^0 \to J/\psi K_S^0$ and $\Lambda_b^0 \to J/\psi\Lambda$ decay modes, where the decay products of the long-lived K_S^0 and Λ are reconstructed as Downstream tracks. Moreover, there is an offset in the decay-time resolution of 1 fs at most.

Empirically, the decay-time resolution distributions in Figure 7.2 can be modelled using various Gaussian distributions with different widths. In this analysis the baseline model used to parameterise the decay-time resolution is a single Gaussian distribution

$$\mathcal{R}(t) = \mathcal{G}(\Delta, \sigma; t) \equiv \frac{1}{\sqrt{2\pi}\sigma} e^{-\left[(t-\Delta)^2/(2\sigma^2)\right]}, \tag{7.9}$$

where σ represents the width of the Gaussian distribution and Δ represents the mean. Both are fixed in the fit used to extract the lifetime of the different b hadrons. The width is fixed to 45 fs for $B^+ \to J/\psi K^+$, $B^0 \to J/\psi K^{*0}$ and $B_s^0 \to J/\psi\phi$ decay modes, and to 65 fs for $B^0 \to J/\psi K_S^0$ and $\Lambda_b^0 \to J/\psi\Lambda$ decay modes in order to take into account the observation of a decay-time resolution in data on average 10% worse than in simulated Monte Carlo (see next section). The mean of the decay-time resolution is

Table 7.1: Mean value and RMS of the decay-time resolution distributions extracted from simulated Monte Carlo.

Channel	Mean [fs]	RMS [fs]
$B^+ \to J/\psi K^+$	-0.379 ± 0.004	39.40 ± 0.03
$B^0 \to J/\psi K^{*0}$	-0.209 ± 0.006	39.02 ± 0.04
$B^0 \to J/\psi K^0_S$	+0.622 ± 0.007	58.92 ± 0.06
$B^0_s \to J/\psi\phi$	+0.146 ± 0.007	42.15 ± 0.05
$\Lambda^0_b \to J/\psi\Lambda$	+1.012 ± 0.008	62.31 ± 0.06

set to zero since it is irrelevant when performing lifetime measurements as it results just in a change of normalisation. In effect, the signal and background distributions, the former modelled by an exponential function with argument $-(t/\tau_{H_b})$, are convoluted with the resolution distribution. An offset in the Gaussian distribution results in an exponential with an argument proportional to the sum $(-t/\tau_{H_b} + \Delta)$. This term is just the product of two exponentials, where the second one is a constant term than can be simply absorbed in the overall normalisation of the PDF.

7.2.2   Decay-time resolution in data samples

The decay-time resolution depends on the topology of the decay and is calibrated for each final state on data. The calibration method uses so-called prompt combinations that mimic the signal candidates. They are obtained combining a J/ψ that is produced at the pp interaction point with one or two particles, depending on the final state of interest, coming from the PV as well. Thus, all the particles used to obtain a fake signal candidate are prompt, which means directly produced at the PV. Therefore, their lifetime is by construction equal to zero and any value different from zero in the decay-time distribution is attributed to the decay-time resolution. Using a sample of prompt J/ψ background events, the decay-time resolution for $H_b \to J/\psi X$ channels reconstructed using Long tracks has been measured to be approximately 45 fs [5]. The resolution is about 10% worse in data than in the corresponding simulated events.

Concerning the $B^0 \to J/\psi K^0_S$ and $\Lambda^0_b \to J/\psi\Lambda$ channels, the decay-time resolution has been studied in data for the $B^0_s \to J/\psi K^0_S$ channel in a previous analysis [107]. In this study the K^0_S final state particle tracks are reconstructed as Long tracks if the VELO information is available, as Downstream tracks otherwise. However, in the analysis reported in this thesis, the K^0_S and the Λ decay products are instead reconstructed using Downstream tracks only, so a different decay-time resolution is expected and thus a separate study has been performed. This study has been done only for the $B^0 \to J/\psi K^0_S$ decay channel, due to the low statistics available in data for the $\Lambda^0_b \to J/\psi\Lambda$ channel. However, the Monte Carlo studies reported in the previous section support the assumption that a similar decay-time resolution is expected in these two channels.

Using the same technique as explained before, a fake signal candidate can be obtained combining a J/ψ particle that is produced at the PV with two other particles from the
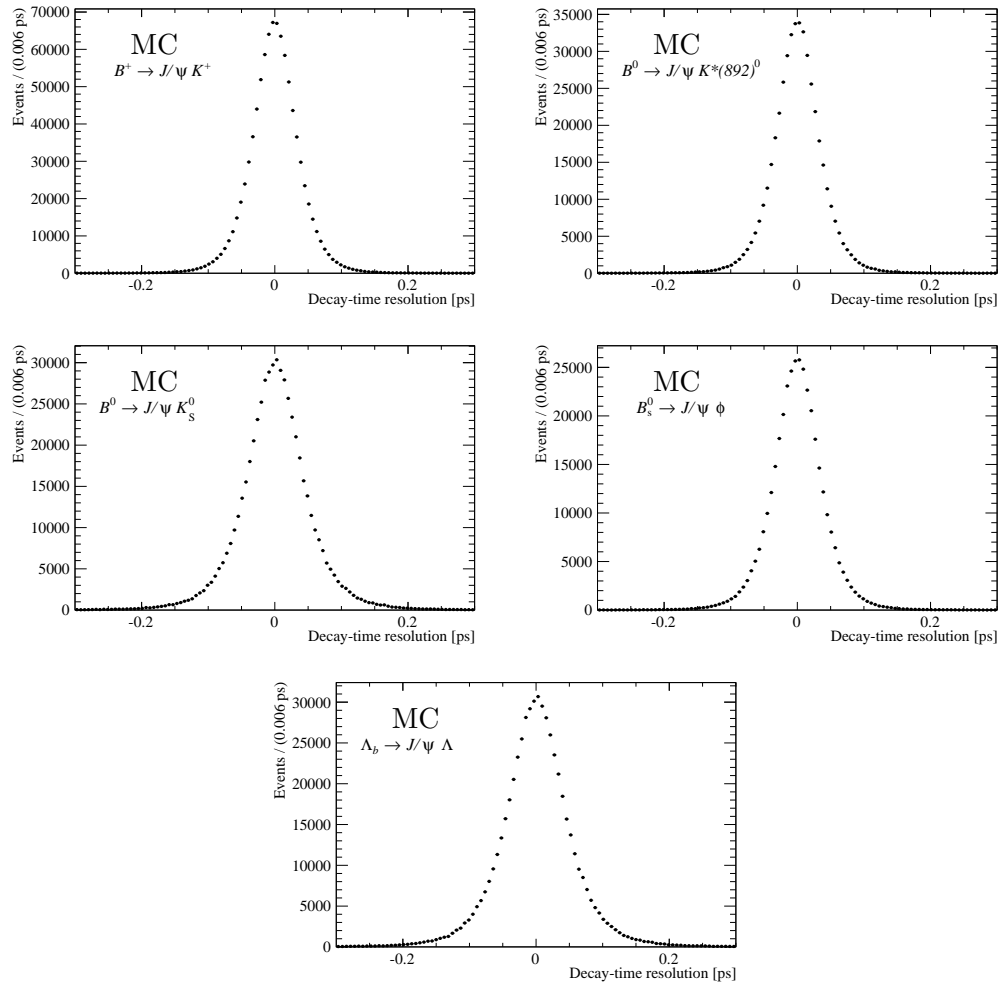
Figure 7.2: Decay-time resolution of $B^+ \to J/\psi K^+$, $B^0 \to J/\psi K^{*0}$, $B^0 \to J/\psi K^0_S$, $B^0_s \to J/\psi \phi$ and $\Lambda^0_b \to J/\psi \Lambda$ candidates in the simulated Monte Carlo sample.

Table 7.2: Fit results of the mean and effective decay-time resolution of the double Gaussian, 2 $\mathcal{G}$, distribution and of the triple Gaussian distribution, 3 $\mathcal{G}$, used to model the decay-time resolution of $B^0 \to J/\psi K_\mathrm{S}^0$ event in data.

$B^0 \to J/\psi K_\mathrm{S}^0$	Long K_S^0	Downstream K_S^0
Mean Δ [fs]	-3.9±0.4	-4.7±0.3
$\sigma_{\mathcal{R},\mathrm{eff}}$ 2 $\mathcal{G}$ [fs]	49.6±1.1	62.0±1.0
$\sigma_{\mathcal{R},\mathrm{eff}}$ 3 $\mathcal{G}$ [fs]	65.0±1.3	105.6±1.5

PV as well, the tracks of the latter being Downstream tracks. For comparison, the decay-time resolution has been studied also in the case where only Long tracks are used to reconstruct the final state particles.

Two different PDFs are used to parameterise the decay-time distribution: a sum of two Gaussian distributions with the same mean, Δ, but two different widths, $\sigma_{\mathcal{R},1}$ and $\sigma_{\mathcal{R},2}$, and a sum of three Gaussian distributions, again with the same mean but three different widths

$$\mathcal{R}_{2\mathcal{G}}(t) \propto f_{\mathcal{R},1} \cdot \mathcal{G}_1(\Delta, \sigma_{\mathcal{R},1}; t) + (1 - f_{\mathcal{R},1}) \cdot \mathcal{G}_2(\Delta, \sigma_{\mathcal{R},2}; t) , \qquad (7.10)$$

$$\mathcal{R}_{3\mathcal{G}}(t) \propto f_{\mathcal{R},1} \cdot \mathcal{G}_1(\Delta, \sigma_{\mathcal{R},1}; t) + f_{\mathcal{R},2} \cdot \mathcal{G}_2(\Delta, \sigma_{\mathcal{R},2}; t)$$
$$+ (1 - f_{\mathcal{R},1} - f_{\mathcal{R},2}) \cdot \mathcal{G}_3(\Delta, \sigma_{\mathcal{R},3}; t) . \qquad (7.11)$$

The motivation behind the usage of a triple Gaussian distribution is that, in case Downstream tracks are used, the decay-time resolution exhibits longer tails with respect to the case where only Long tracks are used, see Figure 7.2. The overall effective decay-time resolution, $\sigma_{\mathcal{R},\mathrm{eff}}$, is calculated by taking the weighted average of the widths of the Gaussian distributions. In case a double Gaussian distribution is used, it is calculated as

$$\sigma_{\mathcal{R},\mathrm{eff}} = \sqrt{f_{\mathcal{R},1}^2 \cdot \sigma_{\mathcal{R},1}^2 + (1 - f_{\mathcal{R},1})^2 \cdot \sigma_{\mathcal{R},2}^2} . \qquad (7.12)$$

The mean and the effective decay-time resolution of the double Gaussian and of the triple Gaussian distributions are summarised in Table 7.2, for both scenarios where only Long tracks or only Downstream tracks are used to reconstruct the K_S^0 final-state particles. It is possible to see that the decay-time resolution in case two Gaussian distributions are used is about 65 fs when Downstream tracks are used, almost 50% worse than the one obtained when Long tracks are used. This motivates to move the lower decay-time bound in the off-line selection to 0.45 ps instead of 0.3 ps for the $B^0 \to J/\psi K_\mathrm{S}^0$ and the $\Lambda_b^0 \to J/\psi \Lambda$ channels, to have a similar suppression as the other channels on the background that originates from combinations of tracks coming from the PV. The effect of the longer tails is clearly visible when the third Gaussian is taken into account. Since the baseline decay-time resolution model that is used in this analysis neglects this contribution, possible systematic effects related to this choice are analysed and discussed in Chapter 8.

7.3   Background composition and modelling

When measuring b-hadron lifetimes it is essential that a correct parameterisation is used to model the decay-time distribution of background events. This section is dedicated to motivate the PDF that describes the combinatorial background, which is the dominant contribution to the total background of $H_b \to J/\psi X$ events. Afterwards, physics backgrounds that may peak around the b-hadron mass are analysed and their effects on the measured b-hadron lifetime are quantified.

7.3.1   Combinatorial background

The combinatorial background is produced by random combinations of tracks. It can be classified into two components according to their different origins and decay-time distributions; so-called prompt and long-lived backgrounds.

Prompt background events consist of fake b hadrons composed by tracks that originate from the same primary vertex and are, therefore, expected to have a decay time of zero ps. Since the detector has a non-perfect decay-time resolution, see Section 7.2, this delta function is smeared and decay-times different from zero are measured. On the other hand, after the off-line selection only events with a decay time greater than 0.3 ps for the channels $B^+ \to J/\psi K^+$, $B^0 \to J/\psi K^{*0}$ and $B_s^0 \to J/\psi \phi$ and greater than 0.45 ps for the channels $B^0 \to J/\psi K_S^0$ and $\Lambda_b^0 \to J/\psi \Lambda$ are kept. This threshold corresponds to approximately seven times the decay-time resolution in the corresponding channels. Thus, this component is largely reduced. Long-lived background events are caused by fake b-hadron candidates made out of combinations of tracks from the associated PV with tracks from other sources, mainly decays of other particles.

These backgrounds can be well described as the sum of three exponential functions, as formulated in Equation 7.4. This parameterisation does not correspond to a physical model but is rather motivated by the observed shape in data, see Figure 7.4 (a). The results of the fit performed in data using this parameterisation are summarised in Table 7.6. The lower "lifetime" component, τ_{B_3}, has an average lifetime of about 100 or 250 fs for the decay modes were only Long or also Downstream tracks are used, respectively. This background component, which constitutes a fraction of about 50% of the total background in all the decay modes, most likely originates from the tail of prompt events shifted by two to three times the decay-time resolution. The second contribution, τ_{B_2}, has a fraction of about 40% and an average lifetime of about 500 or 800 fs, for the decay modes were only Long or also Downstream tracks are used, respectively. Finally, the last component, τ_{B_1}, which includes about 10% of the background events, has a very long lifetime, similar to or even larger than the expected b-hadron lifetime.

A pure background sample to verify the fit model for the background is obtained from events that have a reconstructed b-hadron mass which is much smaller or much larger than the real b-hadron mass. The mass sidebands are defined around the b-hadron
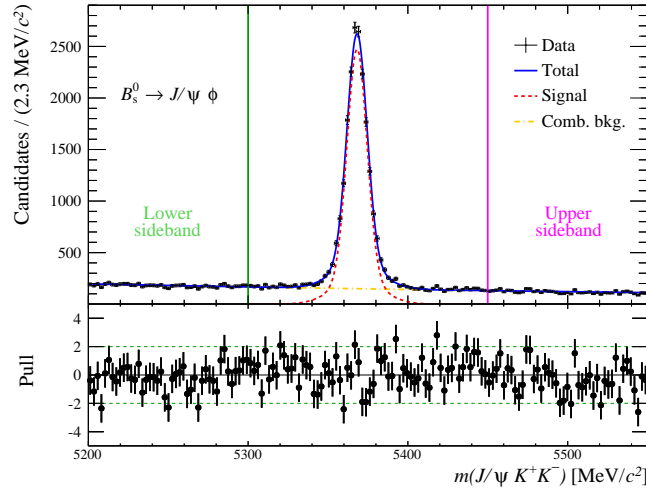
Figure 7.3: Invariant mass distribution of $B_s^0 \to J/\psi\phi$ candidates indicating the upper and lower sideband used to determine the decay-time background distribution.

mass as

$$[5170, 5200] < m_{B^+} \, [\,\mathrm{MeV}/c^2] < [5350, 5400] \,, \tag{7.13}$$

$$[5150, 5240] < m_{B^0} \, [\,\mathrm{MeV}/c^2] < [5320, 5340] \,, \tag{7.14}$$

$$[5200, 5300] < m_{B_s^0} \, [\,\mathrm{MeV}/c^2] < [5450, 5550] \,, \tag{7.15}$$

$$[5500, 5570] < m_{\Lambda_b^0} \, [\,\mathrm{MeV}/c^2] < [5670, 5740] \,. \tag{7.16}$$

A visualisation of the mass sidebands can be seen in Figure 7.3 for the $B_s^0 \to J/\psi\phi$ decay. The signal region is chosen such that, $|m_{H_b} - m_{H_b,\,\mathrm{PDG}}| < 30\,\mathrm{MeV}/c^2$. The decay-time distributions of the candidates in the sidebands, suitably scaled in order to take into account the widths of the sidebands compared to the total invariant mass range, can be compared to the projections of the background decay-time distribution obtained from the fit. By modelling the decay-time background distribution with three or two exponentials functions, it is possible to judge the quality of each fit by looking at the pull distribution. The projections of these fits can be seen in Figure 7.4 (a) and (b) for the $B_s^0 \to J/\psi\phi$ decay mode. Here, the total fit function is represented by the blue solid line; the signal contribution by the red dashed line and the combinatorial background contribution by the yellow dashed-dotted line. The expected background distribution obtained from the lower and upper sidebands, rescaled in order to match the number of background candidates expected in the full mass region, is shown by the green and the pink points, respectively. It is clear that adding a third exponential function to model the long-lived component of the background in the fit improves significantly the description of the data. Similar conclusions are found for all the other $H_b \to J/\psi X$ decay modes.

Until now an underlying assumption has been made. It is important to verify that the background distributions in the sidebands are compatible to those in the signal region. This is an important prerequisite for the fitting procedure to work. It can be
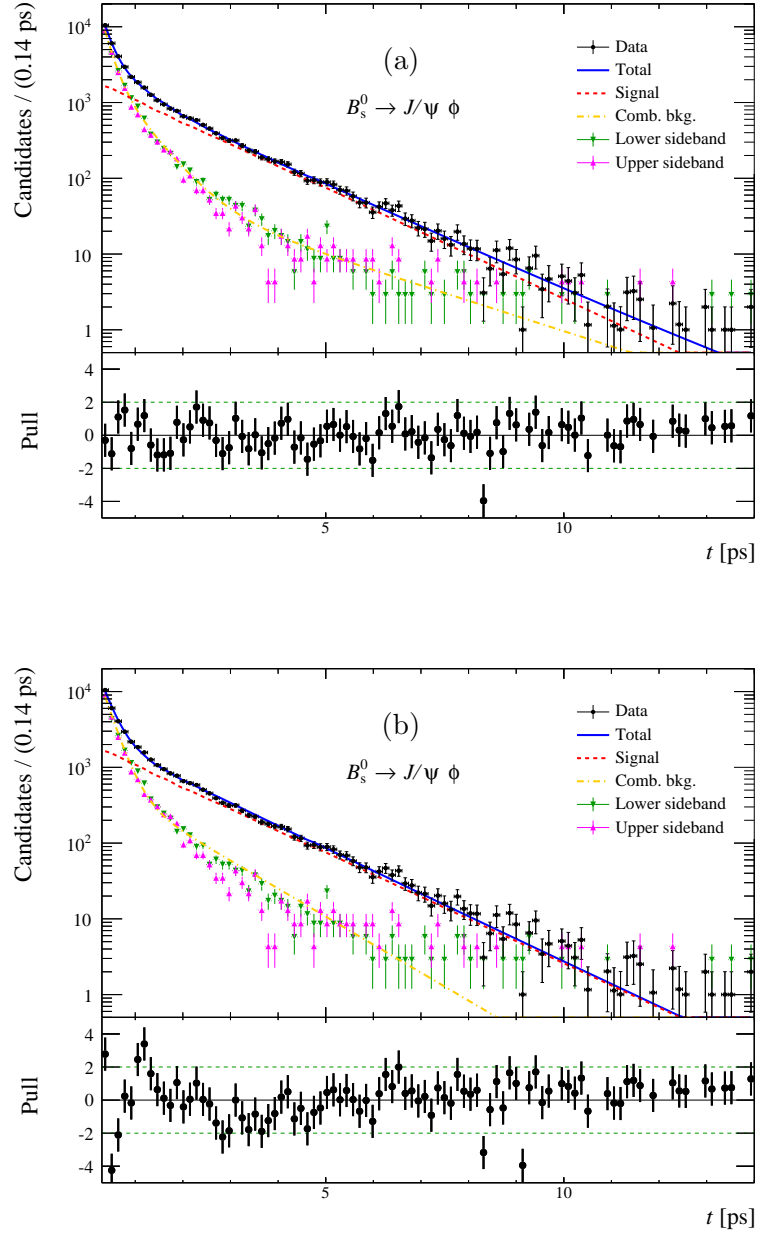
Figure 7.4: Distribution of the decay time of $B_s^0 \rightarrow J/\psi\phi$ candidates and their associated residual uncertainties (pulls). The fit function used to model the background is constituted by (a) three exponentials and (b) two exponentials. The data are shown by the black points; the total fit function by the blue solid line; the signal contribution by the red dashed line and the combinatorial background contribution by the yellow dashed-dotted line. The expected background distribution obtained from the lower and upper sidebands is shown by the green and the pink points, respectively.
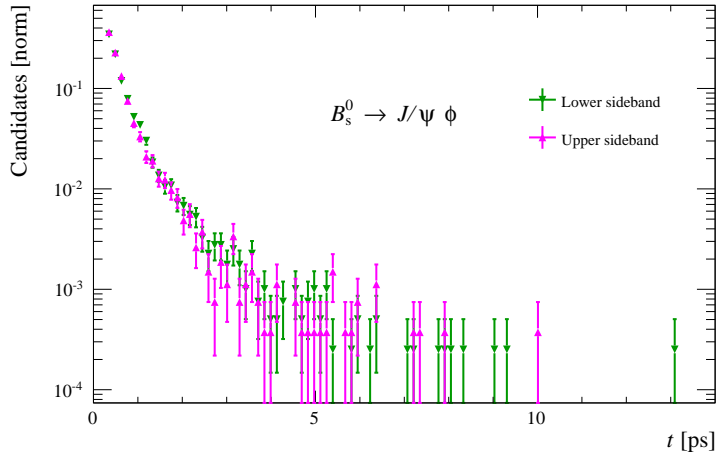
Figure 7.5: Distribution of the decay time of $B_s^0 \rightarrow J/\psi\phi$ background events extracted from the low sideband, green full triangle down points, and the upper sideband, pink full triangle up points. The two distributions are normalised to the same area. For the definition of the sideband see Equation 7.15.

done by comparing the distributions from the lower and the upper sideband. If the agreement is good, then it is reasonable to assume that they can be extrapolated to the signal region. In Figure 7.5 the decay-time distributions for the upper, pink data points, and lower, green data points, sidebands are shown, normalised to the same area, for the $B_s^0 \rightarrow J/\psi\phi$ decay mode. The agreement is very good in the entire decay-time range. Similar conclusions are found for all the other $H_b \rightarrow J/\psi X$ decay modes.

Any small difference in the two sidebands can be quantified comparing the results from the cFit and the alternative fitting method that performs a different treatment of the background, the sFit, as described in Section 7.1.2. As a sanity check, in Figure 7.6 the normalised distributions of $B_s^0 \rightarrow J/\psi\phi$ background events extracted from the sidebands, black full square points, and using the sPlot technique, red full circle points, are shown. The sPlot technique, see Appendix B, allows to unfold the background decay-time distribution making use of sWeights, as introduced in Section 7.1.2. The agreement among the two distributions is very good and similar results are found for all the other $H_b \rightarrow J/\psi X$ decay modes. Moreover, since the two fit procedures give fully compatible results, it is possible to conclude that any small difference between the combinatorial background in the sidebands and underneath the peak can be safely neglected.

7.3.2   Physics backgrounds

Apart from the combinatorial background, there are additional contributions from physics backgrounds. These are candidates from other decay channels that pass the b-hadron selection. As these are mostly candidates from others $H_b \rightarrow J/\psi X$ decays, their mass distribution could also generate a peak around the b-hadron mass. Thus, these contributions are called peaking backgrounds. The model that has been described
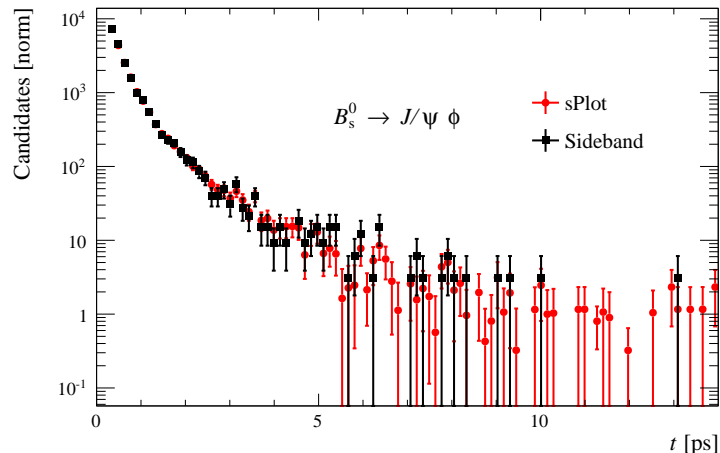
Figure 7.6: Distribution of the decay time of $B_s^0 \to J/\psi\phi$ background events extracted from the sidebands, black full square points, and using the sPlot technique, red full circle points. The two distributions are normalised to the same area. The sPlot technique is explained in Appendix B.

in the previous section neglects completely any peaking background component. Since their impact is found to be small, the default fit does not include such components. However, the effect of peaking background is treated as a systematic uncertainty and is explained in more detail in this section.

$B^+ \to J/\psi K^+$ channel

Concerning the $B^+ \to J/\psi K^+$ sample the only component that has been isolated is a so-called feed-down contribution from $B^0 \to J/\psi K^{*0}$ candidates that pass the selection. This could happen if the pion coming from the decay of the $K^{*0} \to K^+\pi^-$ is not reconstructed. Since the mass and momentum of the pion are missing in the computation of the b hadron mass, this background contributes in the lower mass window range. Its impact is clearly visible if the B^+ invariant mass range is enlarged from $m(J/\psi K^+) \in [5170, 5400] \, \mathrm{MeV}/c^2$ to $m(J/\psi K^+) \in [5150, 5400] \, \mathrm{MeV}/c^2$. The fit to the B^+ mass distribution in this enlarged range is shown in Figure 7.7, where only events with a decay time larger than $0.6 \, \mathrm{ps}$ are considered. This decay-time range is considered to further suppress the contribution from the prompt background in order to enhance the effect of the feed-down $B^0 \to J/\psi K^{*0}$ background. It is possible to see that a linear model does not describe the background nicely, especially around the lower edge of the distribution, as confirmed by the pull distribution (see Equation 5.3) at the bottom of the figure. By running the selection used to isolate $B^+ \to J/\psi K^+$ decays in a sample of $B^0 \to J/\psi K^{*0}$ simulated Monte Carlo events, it is possible to study the invariant mass distribution of this feed-down contribution. It is shown in Figure 7.8, and indicates a clear peaking structure below $5170 \, \mathrm{MeV}/c^2$. In order to remove this contribution, the strategy is to reduce the B^+ mass range to $m(J/\psi K^+) \in [5170, 5400] \, \mathrm{MeV}/c^2$, as already anticipated in the selection chapter. This new lower mass requirement is indicated by
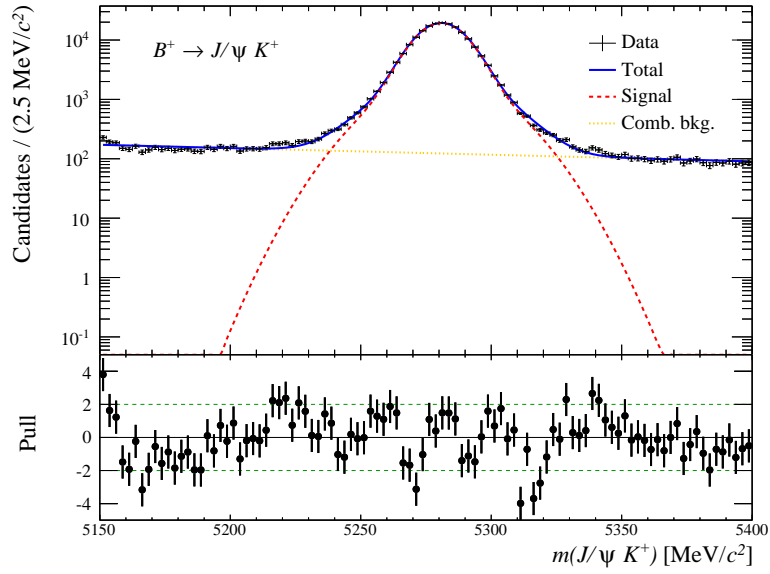
Figure 7.7: $B^+ \to J/\psi K^+$ *candidates mass distribution in the range* $m(J/\psi K^+) \in [5150, 5400] \,\mathrm{MeV}/c^2$ *for candidates with a decay time larger than* $0.6 \,\mathrm{ps}$. *The presence of feed-down from* $B^0 \to J/\psi K^{*0}$ *is visible in the lower limit of the mass window.*
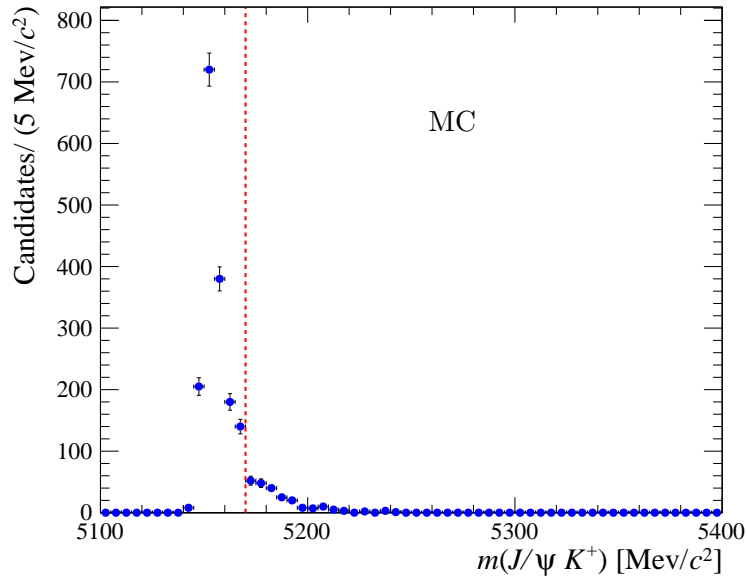
Figure 7.8: Mass distribution of simulated Monte Carlo $B^0 \to J/\psi K^{*0}$ *candidates that pass the selection used to isolate* $B^+ \to J/\psi K^+$ *decays.*
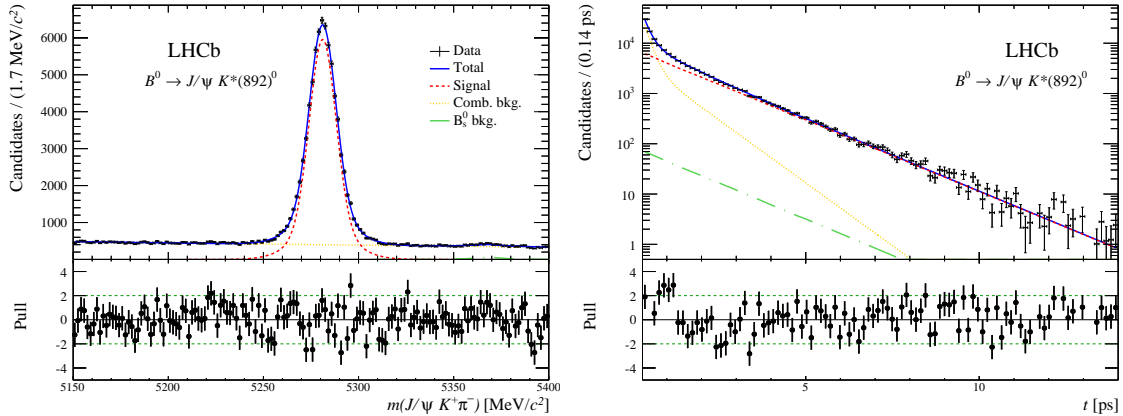
Figure 7.9: Fit projections of the $B^0 \to J/\psi K^{*0}$ candidates mass (left) and decay-time (right) distributions. The data are shown by the black points; the total fit function by the blue solid line; the signal contribution by the red dashed line; the combinatorial background contribution by the yellow dotted line and the B_s^0 contribution by the green dotted-dashed line.

the red dashed line in Figure 7.8. In this way, the remaining feed-down contribution from $B^0 \to J/\psi K^{*0}$ is negligible and can be safely ignored in the analysis.

$B^0 \to J/\psi K^{*0}$ channel

Concerning the $B^0 \to J/\psi K^{*0}$ channel, a detailed analysis of any possible peaking background has been performed and the only contribution that cannot be neglected is due to $B_s^0 \to J/\psi K^{*0}$ events passing the $B^0 \to J/\psi K^{*0}$ selection. In the mass distribution this contribution is shifted by about 85 MeV/c^2 with respect to the B^0 signal peak, since it is centred around the B_s^0 mass. It is preferable to directly remove this background component selecting only events whose invariant mass is below 5340 MeV/c^2, as anticipated in the selection chapter. In this way this component is completely removed without loosing sensitivity on the final result.

As a cross-check, to estimate the size of the lifetime bias due to this contamination, this background component has been explicitly included in the fit. The mass distribution model chosen for the $B_s^0 \to J/\psi K^{*0}$ component is a double Gaussian distribution with a common mean and two different widths. The mean and the two widths of the distribution are fixed to the values obtained from the $B_s^0 \to J/\psi \phi$ fit in data, see Table 7.5, while the fraction between the two Gaussian distributions and the total fraction of the B_s^0 component are left free to vary in the fit. The decay-time distribution is modelled by a single exponential with the lifetime fixed to the expected B_s^0 effective lifetime, 1.5 ps [2]. The projections of the fit to the B^0 mass and decay-time distributions are shown in Figure 7.9. A $B_s^0 \to J/\psi K^{*0}$ background fraction of 0.4% is found. The mass and decay-time projections of this background component are shown by the dotted-dashed green line. The result of the B^0 lifetime shows a deviation of 0.4 fs with respect to the nominal value obtained ignoring this component. This value could have been assigned as a systematic uncertainty since this background component is neglected in the baseline
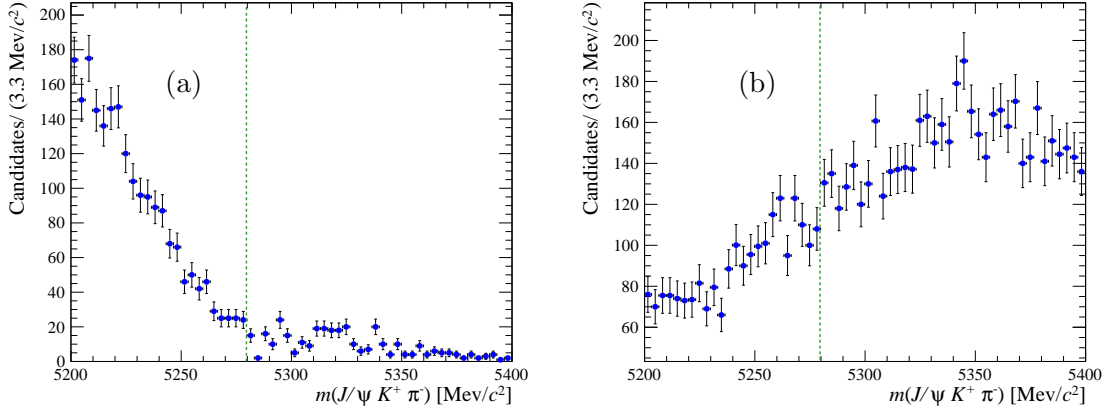
Figure 7.10: Distributions of $m(J/\psi K\pi)$ for events in the $B_s^0 \to J/\psi\phi$ lower (a) and upper (b) sideband. No peak is visible at the nominal B^0 mass, 5279.58 ± 0.17 MeV/c^2 [14], pointed by the green dashed line.

fit. However, in this way one has to rely on the assumptions that the fit parameter values of the $B_s^0 \to J/\psi\phi$ mass model can be used for the $B_s^0 \to J/\psi K^{*0}$ channel as well as the B_s^0 effective lifetime value used as an input in the fit. Thus, it was preferred to remove this background component, as already stated.

$B_s^0 \to J/\psi\phi$ channel

Potential peaking backgrounds to the $B_s^0 \to J/\psi\phi$ channel are $B^0 \to J/\psi K^{*0}[K^+\pi^-]$ and $\Lambda_b^0 \to J/\psi p K^-$ events. The pion or the proton in the final state can be incorrectly identified as a kaon such that they look like the decay product of a ϕ meson decaying into two kaons. The amount of these events can be estimated by studying events in the sidebands of the $m(J/\psi K^+K^-)$ data distribution where one of the kaons has its mass hypothesis replaced with that of the pion or proton, respectively.

Concerning the $B^0 \to J/\psi K^{*0}[K^+\pi^-]$ misidentified background, Figures 7.10 (a) and (b) show the distributions of the $m(J/\psi K^+\pi^-)$ invariant mass for events in the $B_s^0 \to J/\psi\phi$ lower and upper sideband, respectively. Each event appears twice in the plots as it is possible to assign the pion hypothesis separately to both kaons in the final state. No peak is visible at the nominal B^0 mass, 5279.58 ± 0.17 MeV/c^2 [14], thus it is possible to conclude that the contamination due to $B^0 \to J/\psi K^{*0}[K^+\pi^-]$ misidentified background is negligible, since from simulated sample this contribution is expected to be present in the sidebands.

Concerning the $\Lambda_b^0 \to J/\psi p K^-$ misidentified background, Figures 7.11 (a) and (b) show the distributions of the $m(J/\psi p K^-)$ invariant mass for events in the $B_s^0 \to J/\psi\phi$ lower and upper sideband, respectively. A peak at the nominal Λ_b^0 mass, 5619.4 ± 0.7 MeV/c^2 [14], is visible in the data, especially in the lower sideband. These events are identified as originating from $\Lambda_b^0 \to J/\psi p K^-$ decays where the proton in the final state is misidentified as a kaon. As above, each event appears twice in the plots
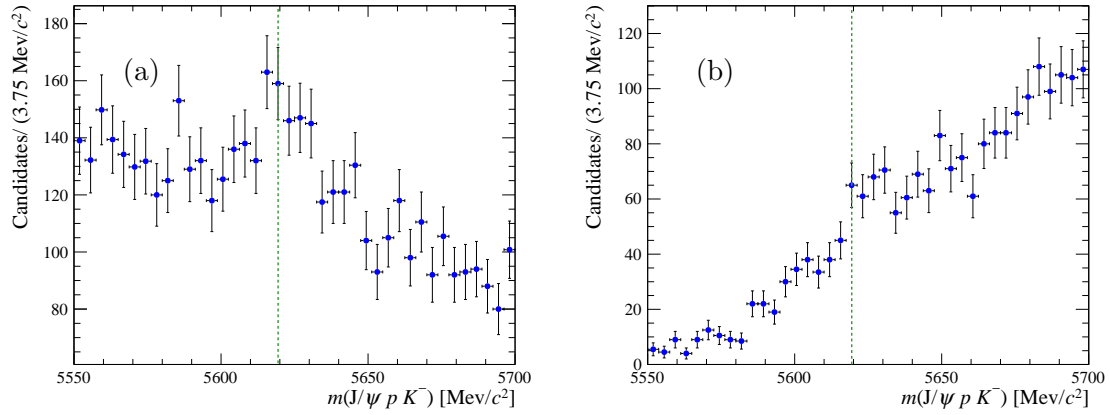
Figure 7.11: Distributions of $m(J/\psi pK^-)$ for events in the $B_s^0 \to J/\psi \phi$ lower (a) and upper (b) sideband. A peak at the nominal Λ_b^0 mass, 5619.4 ± 0.7 MeV/c^2 [14], is visible in the lower sideband, as pointed by the green dashed line.

as it is possible to assign the proton hypothesis separately to both kaons in the final state. From a fit of the $m(J/\psi pK^-)$ distribution in the $B_s^0 \to J/\psi \phi$ lower sideband, the number of misidentified $\Lambda_b^0 \to J/\psi pK^-$ events is estimated to be 190 ± 65. Using a simulated $\Lambda_b^0 \to J/\psi pK^-$ Monte Carlo sample it is possible to extrapolate this yield to get the expected number of misidentified $\Lambda_b^0 \to J/\psi pK^-$ events in the full $B_s^0 \to J/\psi \phi$ mass distribution range. The selection used to isolate $B_s^0 \to J/\psi \phi$ decays is applied to a $\Lambda_b^0 \to J/\psi pK^-$ simulated Monte Carlo sample. The invariant mass distribution of events that pass the selection is modelled with a single Gaussian distribution, $\mathcal{G}(\mu_{\Lambda_b^0}, \sigma_{\Lambda_b^0}; m)$, where the mean and the width are left free to vary in the fit. A linear polynomial is used to describe a small background contribution present in MC, with coefficient $a_{\Lambda_b^0}$. The projections of the fit to the $J/\psi pK^-$ invariant mass distribution in the $B_s^0 \to J/\psi \phi$ mass range are shown in Figure 7.12 (a) and the results of the fit are summarised in Table 7.3. Taking into account the fraction of events that appear in the lower sideband region it is possible to extrapolate the number of events obtained in data in the lower sideband to the full mass range, obtaining a contribution of 2436 ± 834 Λ_b^0 events. This corresponds to about 6% of the total number of events. Since this contribution is not negligible, a check has been performed to estimate the bias on the B_s^0 effective lifetime due to this background component that is neglected in the baseline fit. In order to do so, it is necessary to estimate in MC the lifetime of the $\Lambda_b^0 \to J/\psi pK^-$ events that pass the $B_s^0 \to J/\psi \phi$ selection. Using the fit to the invariant mass distribution shown in Figure 7.12 (a) and the sFit technique to statistically subtract the background contribution from the $\Lambda_b^0 \to J/\psi pK^-$ decay-time distribution, it is possible to isolate the $\Lambda_b^0 \to J/\psi pK^-$ signal component. The decay-time signal component is fitted using an exponential function, with decay constant $\tau_{\Lambda_b^0}$. The projection of this fit is shown in Figure 7.12 (b) and the lifetime value is reported in Table 7.3.

This background component is then included in the fit of the $B_s^0 \to J/\psi \phi$ sample. The mass and decay-time parameters of this component are fixed to the values reported in Table 7.3, while the total fraction is fixed to the extrapolated value from data. The
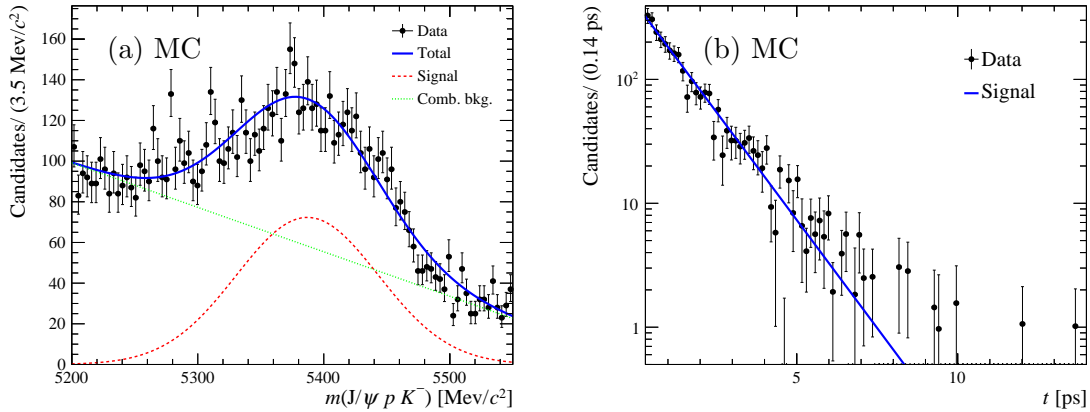
Figure 7.12: Distribution of $m(J/\psi KK)$ and $t(J/\psi KK)$ for simulated $\Lambda_b^0 \to J/\psi pK$ MC events passing the $B_s^0 \to J/\psi\phi$ selection. The solid blue line shows the result of a fit to the data. The signal contribution is indicated by the red dotted line and the combinatorial background contribution is indicated by the green dashed line.

Table 7.3: Parameters determined from the fit to a simulated $\Lambda_b^0 \to J/\psi pK^-$ Monte Carlo sample, where the events are passing the full $B_s^0 \to J/\psi\phi$ selection.

Parameter	Value
$\mu_{\Lambda_b^0}$	$5387.0 \pm 2.6 \, \mathrm{MeV}/c^2$
$\sigma_{\Lambda_b^0}$	$56.4 \pm 3.0 \, \mathrm{MeV}/c^2$
$a_{\Lambda_b^0}$	-0.6281 ± 0.027
N_{Bkg}	6086 ± 197
N_{Sig}	2913 ± 189
$\tau_{\Lambda_b^0}$	$1.244 \pm 0.042 \, \mathrm{ps}$

projections of the fit to the B_s^0 mass and decay time are shown in Figure 7.13. The B_s^0 effective lifetime shows a deviation of 0.35 fs with respect to the nominal result after the inclusion of the $\Lambda_b^0 \to J/\psi pK^-$ misidentified background. This bias is taken into account as a systematic uncertainty on the final result.

$B^0 \to J/\psi K_S^0$ channel

There are three potential peaking backgrounds to the $B^0 \to J/\psi K_S^0$ channel. The first contribution that cannot be neglected is analogous to the $B^0 \to J/\psi K^{*0}$ decay mode. It is due to $B_s^0 \to J/\psi K_S^0$ events passing the $B^0 \to J/\psi K_S^0$ selection. In the mass distribution this contribution is shifted by about 85 MeV/c^2 with respect to the B^0 signal peak since it is centred around the B_s^0 mass. Thus, this component is directly removed selecting only events whose invariant mass is below 5340 MeV/c^2, as anticipated in the selection chapter. In this way this component is completely removed without loosing sensitivity on the final result.

Other potential peaking backgrounds to the $B^0 \to J/\psi K_S^0$ channel, analogously to the $B_s^0 \to J/\psi\phi$ channel, are $B^0 \to J/\psi K^{*0}[K^+\pi^-]$ and $\Lambda_b^0 \to J/\psi\Lambda[p\pi^-]$ events. The kaon
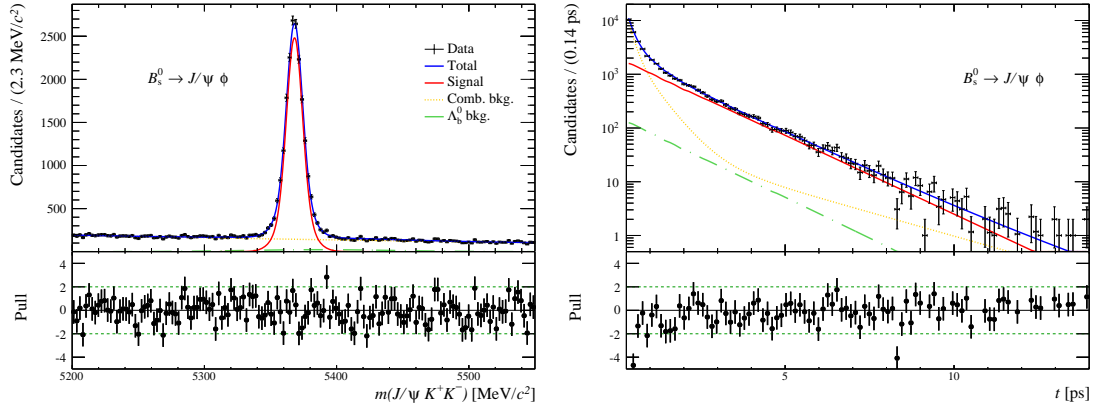
Figure 7.13: Fit projections of the $B_s^0 \to J/\psi \phi$ candidates mass (left) and decay-time (right) distributions. The data are shown by the black points; the total fit function by the blue solid line; the signal contribution by the red dashed line; the combinatorial background contribution by the yellow dotted line and the Λ_b^0 contribution by the green dotted-dashed line.

or the proton in the final state can be incorrectly identified as a pion such that they look like the decay product of a K_S^0 meson, that decays into two pions. The amount of these events can be estimated, as in the previous section, by studying events in the sidebands of the $m(J/\psi \pi^+ \pi^-)$ data distribution, after replacing the pion mass hypothesis with that of the kaon or the proton, respectively. No significant $B^0 \to J/\psi K^{*0}$ background is observed, thanks mainly to the selection requirement on the flight distance significance of the K_S^0, which forces the K_S^0 to be well separated from the B^0 decay vertex. On the other hand, a small contamination of the Λ_b^0 background is visible. As explained in the previous section, it is possible to estimate the expected number of these background events making use of a simulated Monte Carlo $\Lambda_b^0 \to J/\psi \Lambda [p\pi^-]$ sample. About 200 ± 87 events are expected in the full $B^0 \to J/\psi K_S^0$ mass distribution, which is about 0.6% of the total number of events. The nominal fit is therefore performed without this background. In order to estimate the bias on the lifetime due to this assumption, the fit is also performed explicitly including this component. The B^0 effective lifetime shows a deviation of 0.3 fs with respect to the nominal result. This bias is taken into account as a systematic uncertainty on the final result.

$\Lambda_b^0 \to J/\psi \Lambda$ channel

Similarly to the other channels, a potential peaking background to the $\Lambda_b^0 \to J/\psi \Lambda$ channel is due to $B^0 \to J/\psi K_S^0 [\pi^+ \pi^-]$ events passing the $\Lambda_b^0 \to J/\psi \Lambda$ selection when one of the pion is misidentified as a proton. Looking at the $m(J/\psi p\pi)$ sidebands a small amount of this background is found. Using a simulated $B^0 \to J/\psi K_S^0$ Monte Carlo sample the total amount of this background is estimated to be equal to about 4% of the total number of candidates, with 470 ± 120 $B^0 \to J/\psi K_S^0$ events in the $\Lambda_b^0 \to J/\psi \Lambda$ invariant mass distribution. Therefore, the fit is performed explicitly including this component to estimate the bias of the Λ_b^0 lifetime. It shows a deviation of 1.1 fs with respect to the nominal result. This bias is taken into account as a systematic uncertainty.

Table 7.4: Fit results for the B^+, B^0 mesons and Λ_b^0 baryon lifetimes and B_s^0 meson effective lifetime in Monte Carlo samples are shown in the first column. In the second column, it is shown the result of a fit to the Monte Carlo sample before any reconstruction or selection requirement is applied. In the third column, the difference between the first and second column results is shown. All the uncertainties are statistical only.

Lifetime	MC value [ps]	Generated value [ps]	Lifetime correction [ps]
$\tau_{B^+ \to J/\psi K^+}$	1.6411 ± 0.0017	1.63818 ± 0.00064	$+0.003 \pm 0.0017$
$\tau_{B^0 \to J/\psi K^{*0}}$	1.5226 ± 0.0023	$1.52447 \pm \pm 0.00053$	-0.0019 ± 0.0023
$\tau_{B^0 \to J/\psi K_S^0}$	1.5279 ± 0.0029	1.52545 ± 0.00061	$+0.0025 \pm 0.0029$
$\tau_{\Lambda_b^0 \to J/\psi \Lambda}$	1.3840 ± 0.0037	1.38049 ± 0.00061	$+0.0035 \pm 0.0037$
$\tau_{B_s^0 \to J/\psi \phi}$	1.4307 ± 0.0024	1.43119 ± 0.00050	-0.0005 ± 0.0024

7.4   Fit results

In this section the results obtained from the two-dimensional maximum likelihood fit explained in Section 7.1 are shown. Before to present the results of the fit on the data samples, the results obtained on the Monte Carlo simulated samples are discussed.

Fit of the Monte Carlo samples   The results of the fit to the different b-hadrons simulated MC samples are summarised in Table 7.4. Here, the lifetime of the different b hadrons, obtained using the same fitting technique of data, is reported in the first column. In particular, the weights used to perform the per-candidate correction for the VELO reconstruction efficiency as well as the correction for the acceptance introduced by the t-dependent trigger and selection efficiency are included. The result of this fit can be compared to the value of the lifetime that is used in the generation of the Monte Carlo sample. In order to not double count systematic effects due to the fitting procedure, which are addressed separately (see Chapter 8), the generated lifetime value is obtained from a fit to the Monte Carlo sample before any reconstruction, trigger or selection requirement is applied. This value is shown in the second column of Table 7.4. Finally, in the third column, the differences between the first and the second column results are shown. In this case, the uncertainty corresponds to the uncertainty on the fitted MC lifetime. This difference is used to quantify the remaining lifetime bias in the MC sample. It is subtracted as a correction from the fitted values of the b-hadron lifetimes in data and the corresponding uncertainty is assigned as a systematic uncertainty on this correction, due to the limited size of the MC sample.

Fit of data samples   The fit values of the b-hadron lifetimes obtained performing the two-dimensional maximum likelihood fit explained in Section 7.1 are reported in Table 7.7. The mass and the decay-time distributions of the different b hadrons used in the fit are shown in Figure 7.14 and Figure 7.15. The quality of the fit can be judged by the pull distribution, as defined in Equation 5.3, given in the lower part of each figure. Most of the pull points lie within the interval [-2,+2], showing a good quality of the fit. The fit values of the parameters describing the invariant mass distribution can be found in Table 7.5, while those used to parameterise the decay-time distribution are

Table 7.5: *Fit values of the parameters used in the fit of the b-hadron invariant mass distribution after the application of the off-line selection. The uncertainty is statistical only.*

Channel	m_{H_b} [MeV/c²]	σ_1 [MeV/c²]	σ_2 [MeV/c²]	f_{σ_1}	f_{sig}	α_m
$B^+ \to J/\psi K^+$	5280.88 ± 0.02	8.89 ± 0.05	18.9 ± 0.3	0.78 ± 0.01	0.814 ± 0.008	0.00149 ± 0.00007
$B^0 \to J/\psi K^{*0}$	5281.17 ± 0.04	6.8 ± 0.1	13.4 ± 0.4	0.72 ± 0.02	0.593 ± 0.002	0.0013 ± 0.0001
$B^0 \to J/\psi K^0_S$	5281.97 ± 0.08	7.6 ± 0.3	15.1 ± 1.2	0.70 ± 0.05	0.543 ± 0.005	0.0007 ± 0.0001
$B^0_s \to J/\psi \phi$	5368.19 ± 0.06	6.2 ± 0.1	14.7 ± 1.0	0.80 ± 0.02	0.453 ± 0.003	0.00162 ± 0.00007
$\Lambda^0_b \to J/\psi \Lambda$	5622.0 ± 0.2	7.4 ± 0.6	15.5 ± 2.5	0.67 ± 0.11	0.330 ± 0.007	0.0014 ± 0.0002

Table 7.6: *Fit values of the parameters used in the fit of the b-hadron decay-time distribution after the application of the off-line selection. The uncertainty is statistical only.*

Channel	τ_{B_1} [ps]	τ_{B_2} [ps]	τ_{B_3} [ps]	f_{B_1}	f_{B_2}
$B^+ \to J/\psi K^+$	1.55 ± 0.06	0.26 ± 0.02	0.108 ± 0.007	0.118 ± 0.007	0.39 ± 0.06
$B^0 \to J/\psi K^{*0}$	1.40 ± 0.07	0.50 ± 0.03	0.135 ± 0.005	0.12 ± 0.02	0.47 ± 0.02
$B^0 \to J/\psi K^0_S$	3.5 ± 1.1	0.84 ± 0.05	0.26 ± 0.01	0.039 ± 0.006	0.43 ± 0.04
$B^0_s \to J/\psi \phi$	2.2 ± 0.2	0.53 ± 0.04	0.161 ± 0.008	0.06 ± 0.01	0.43 ± 0.04
$\Lambda^0_b \to J/\psi \Lambda$	2.2 ± 0.3	0.72 ± 0.13	0.24 ± 0.03	0.12 ± 0.04	0.44 ± 0.07

reported in Table 7.6. The fitted lifetime values are then corrected for the remaining lifetime bias measured in simulated Monte Carlo samples, see Table 7.4. The resulting corrected lifetime values for the different b hadrons are shown in the second column of Table 7.7.

Table 7.7: *Fit results for the B^+, B^0 mesons and Λ^0_b baryon lifetimes and B^0_s meson effective lifetime in data are shown in the first column. In the second column the fit value is corrected with the lifetime correction factor extracted from the simulated Monte Carlo sample, see Table 7.4. The uncertainty is statistical only.*

Lifetime	Fit Value [ps]	Corrected Value [ps]
$\tau_{B^+ \to J/\psi K^+}$	1.6398 ± 0.0035	1.637 ± 0.004
$\tau_{B^0 \to J/\psi K^{*0}}$	1.5219 ± 0.0061	1.524 ± 0.006
$\tau_{B^0 \to J/\psi K^0_S}$	1.5011 ± 0.0128	1.499 ± 0.013
$\tau_{\Lambda^0_b \to J/\psi \Lambda}$	1.4188 ± 0.0265	1.415 ± 0.027
$\tau_{B^0_s \to J/\psi \phi}$	1.4808 ± 0.0114	1.480 ± 0.011
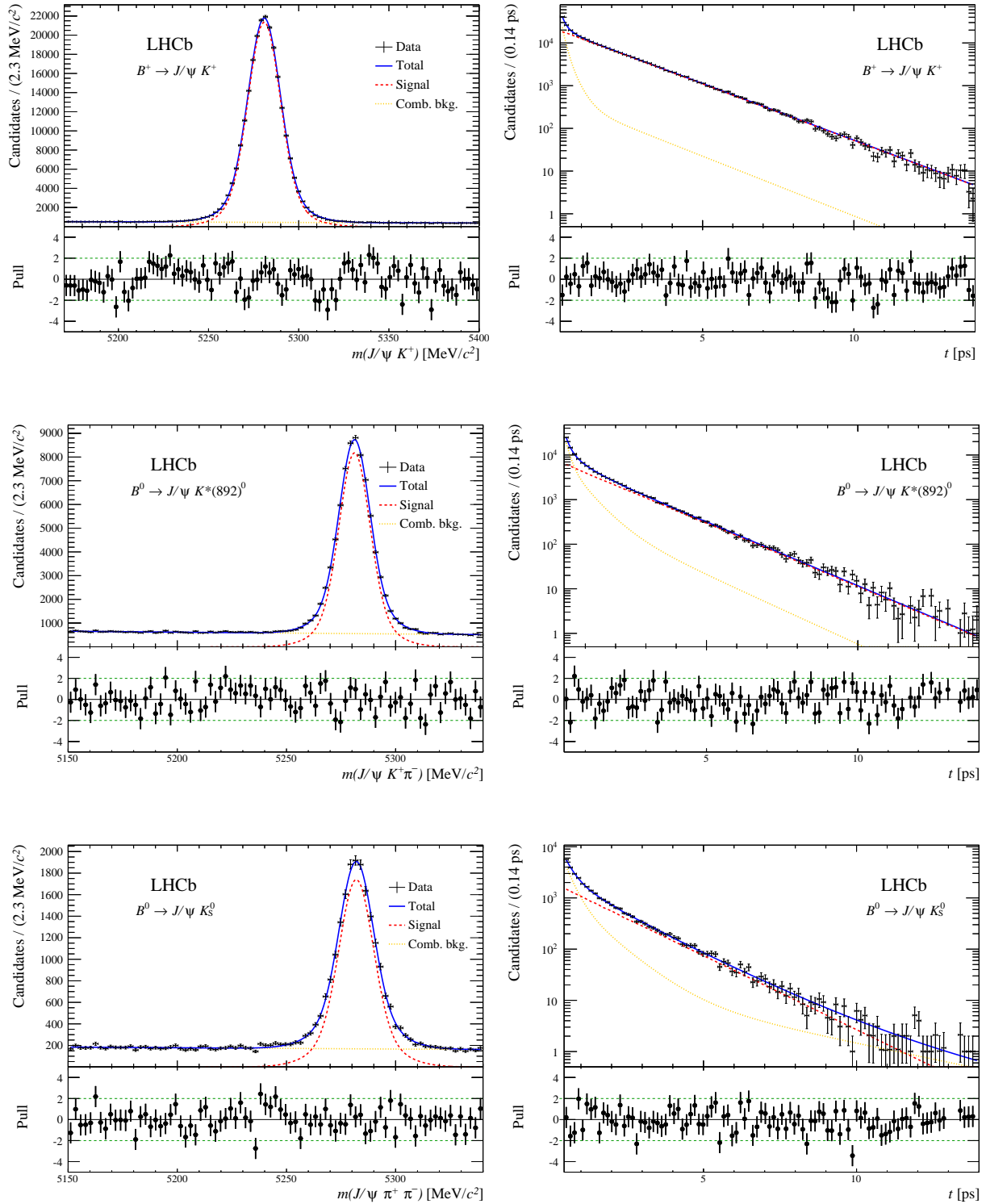
Figure 7.14: Distributions of the (left) mass and (right) decay time of $B^+ \to J/\psi K^+$, $B^0 \to J/\psi K^{*0}$ and $B^0 \to J/\psi K_S^0$ candidates and their associated residual uncertainties (pulls). The data are shown by the black points; the total fit function by the blue solid line; the signal contribution by the red dashed line and the combinatorial background contribution by the yellow dotted line.
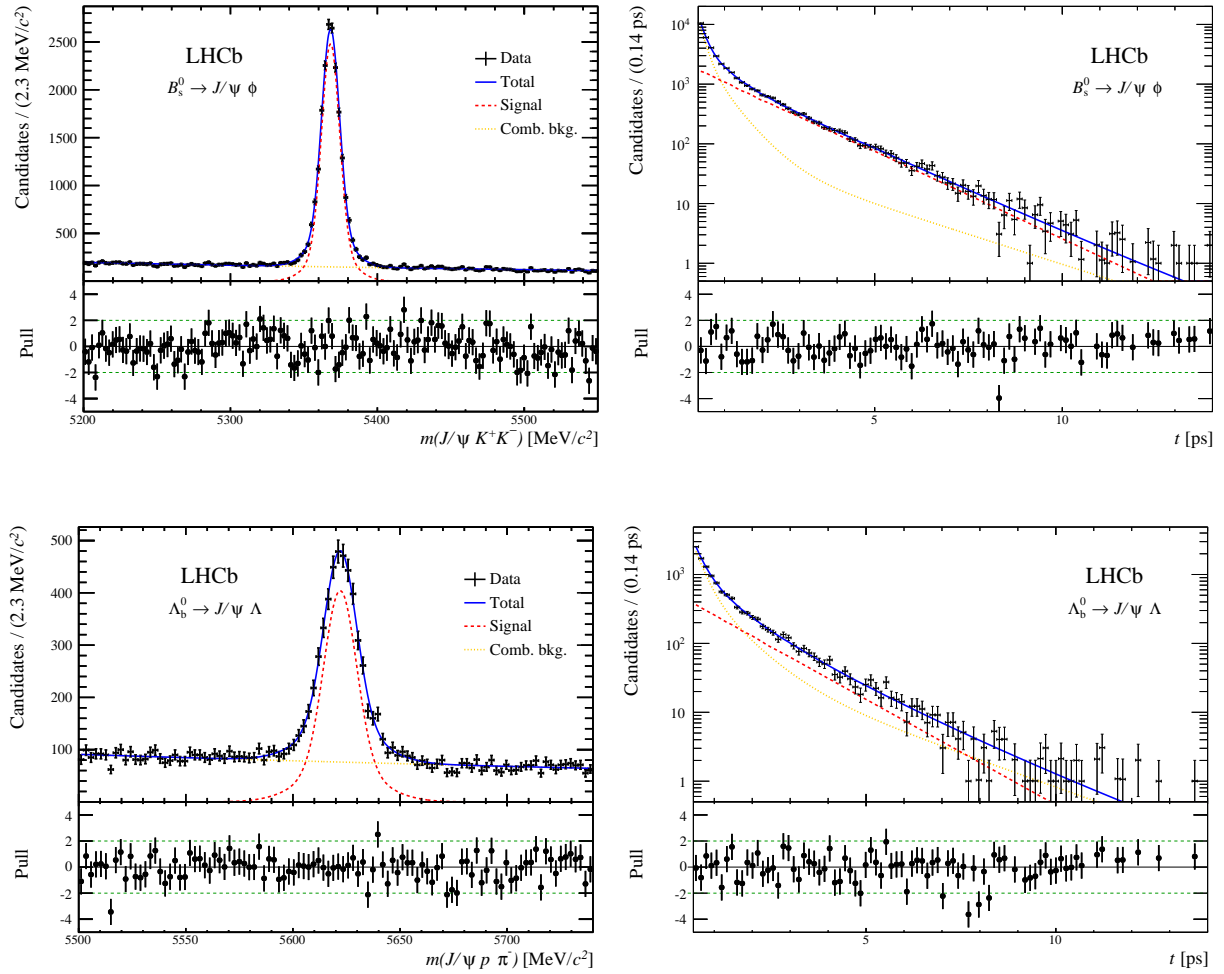
Figure 7.15: Distributions of the (left) mass and (right) decay time of $B_s^0 \to J/\psi\phi$ and $\Lambda_b^0 \to J/\psi\Lambda$ candidates and their associated residual uncertainties (pulls). The data are shown by the black points; the total fit function by the blue solid line; the signal contribution by the red dashed line and the combinatorial background contribution by the yellow dotted line.

7.5   Summary

The essential information of this chapter is briefly summarised here.

- The lifetime of each b hadron is extracted by means of an unbinned maximum likelihood fit to the b-hadron invariant mass and decay-time distributions.

- The VELO reconstruction acceptance is corrected using a per event weight, as described in Section 6.3.2, while the trigger acceptance effects are corrected by taking into account the parameterisation of the trigger acceptance in the fit, see Equation 7.3.

- The resolution is fixed in the fit to 45 fs for $B^+ \to J/\psi K^+$, $B^0 \to J/\psi K^{*0}$ and $B^0_s \to J/\psi \phi$ decay modes, and to 65 fs for $B^0 \to J/\psi K^0_S$ and $\Lambda^0_b \to J/\psi \Lambda$ decay modes.

- The background of all the b hadrons is mainly formed by random combinations of tracks that pass the selection procedure, therefore this is the only component that is parameterised in the fit.

- Other sources of physics background, candidates from other decay channels that pass the b-hadron selection and that could peak in the b-hadron mass distribution, have been investigated. When they were found to be non negligible, the effect on the lifetime measurement is estimated by including their contribution in the fit and a corresponding systematic uncertainty is assigned.

- The estimated lifetimes of the different b hadrons obtained from the fit are given in Table 7.7.

8

Systematic uncertainties

There is no such uncertainty as a sure thing.

— Robert Burns

A large number of systematic studies has been performed to test the robustness of the determination of the lifetimes of the different b hadrons. Systematic effects can arise due to multiple sources and they can bias the measured lifetime value. In this chapter the studies of all these effects are summarised. First, the effects that are related to the decay-time acceptance correction are discussed. Second, the systematic uncertainties that are connected to the fit technique and to the data modelling are analysed. Then, lifetime biases that are affecting the B_s^0 and B^0 effective lifetime measurements are investigated. Afterwards, the effects due to the length and momentum scale uncertainty are shortly presented. Finally, some consistency checks that were performed but where no bias is observed are briefly listed.

8.1 Track reconstruction efficiency in the vertex detector

The VELO-track reconstruction efficiency correction is the main challenge of this analysis. The systematic uncertainty related to it can be split into two components. The first uncertainty is due to the finite size of the $B^+ \to J/\psi\, K^+$ sample, reconstructed using Downstream kaon tracks, which is used to determine the per-candidate efficiency weights and leads to a statistical uncertainty on the $\varepsilon_{\mathrm{VELO}}(\rho)$ parameterisation. The lifetime fits are repeated after varying the parameters by $\pm 1\sigma$ and the largest difference between the lifetimes is assigned as the uncertainty.

The second uncertainty is due to the scaling factors, which are used to correct the efficiency for phase-space effects. This part of the correction relies on simulated samples. Comparing the results for the VELO-track reconstruction inefficiency in data and MC in Table 6.2 and Table 6.1, respectively, a 10 % discrepancy is found. In order to conservatively take into account possible effects coming from differences between data and simulated sample, the lifetime fit is repeated using the unscaled efficiency and half of the variation in fit results is assigned as a systematic uncertainty. These two contributions, which are of roughly the same size, are added in quadrature and reported

Table 8.1: VELO-track reconstruction efficiency fit results for kaon tracks reconstructed using the off-line and on-line algorithms, in different bins of transverse momentum of the track and track multiplicity.

p_T [GeV/c]	n_{Tracks}	Online		Offline	
		a	c [mm^{-2}]	a	c [mm^{-2}]
$[0, 2]$	$[0, 150]$	0.9789 ± 0.0009	-0.0069 ± 0.0010	0.9877 ± 0.0007	-0.0018 ± 0.0005
$[2, 30]$	$[0, 150]$	0.9777 ± 0.0006	-0.0097 ± 0.0016	0.9847 ± 0.0005	-0.0051 ± 0.0012
$[0, 2]$	$[150, 1200]$	0.9739 ± 0.0015	-0.0102 ± 0.0013	0.9811 ± 0.0014	-0.0052 ± 0.0009
$[2, 30]$	$[150, 1200]$	0.9704 ± 0.0008	-0.0137 ± 0.0020	0.9765 ± 0.0007	-0.0079 ± 0.0016

in Table 8.3. Together they represent one of the largest systematic contributions for the $B^+ \to J/\psi K^+$, $B^0 \to J/\psi K^{*0}$ and $B_s^0 \to J/\psi \phi$ decay channels. For the $B^0 \to J/\psi K_S^0$ and $\Lambda_b^0 \to J/\psi \Lambda$ decay channels their effect is limited due to the fact that in this case only the muon tracks are reconstructed as Long tracks and suffer from VELO-track reconstruction inefficiency.

A number of additional consistency checks are performed to investigate a possible mismodelling of the VELO-track reconstruction efficiency. First, the track finding VELO efficiencies shown in Figure 3.8 exhibit a dependency on the number of tracks in the event and on the momentum of the tracks. Thus, $\varepsilon_{\mathrm{VELO}}(\rho)$ is evaluated in two bins of track transverse momentum and two bins of track multiplicity using the same method described in Section 6.3.2. These efficiencies are shown in Figure 8.1 and Figure 8.2 for the on-line and the off-line version of the FastVELO algorithm, respectively. These curves are parameterised with the function introduced in Equation 6.8 and the results of the fit are summarised in Table 8.1. The c parameters determined from these fits are used to calculate a new per-event weight to correct for the VELO-track reconstruction efficiency. Using both data and simulated events, the change in the lifetimes observed after repeating the fit with these new weights is less than half of the effect due to the statistical uncertainty on the $\varepsilon_{\mathrm{VELO}}(\rho)$ parameterisation. Therefore, no further systematic uncertainty is assigned.

Second, also motivated by the track finding VELO efficiencies shown in Figure 3.8, the dependence of the VELO-track reconstruction efficiency on the azimuthal angle, ϕ, of each track is studied by independently evaluating the efficiency in four ϕ quadrants for both data and simulation. The small dependence observed does not lead to significant changes in the lifetimes.

Third, to assess the sensitivity to the choice of parameterisation for $\varepsilon_{\mathrm{VELO}}(\rho)$ (Equation 6.8), the results are compared to those with a linear model for the efficiency

$$\varepsilon_{\mathrm{VELO}}(\rho) = a(1 + b\rho)\,. \tag{8.1}$$

The effect is found to be negligible and no systematic uncertainty is applied.

Finally, the efficiency is determined separately for both positive and negative kaons and found to be compatible.
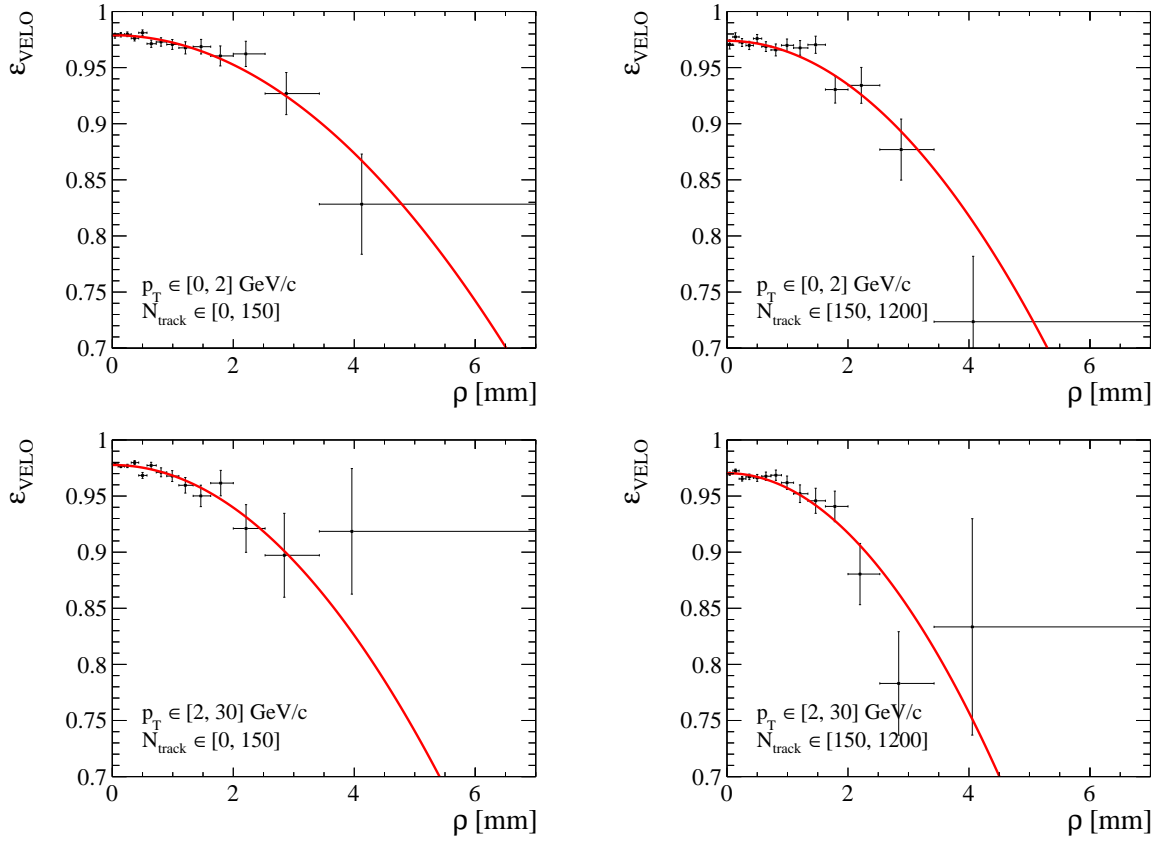
Figure 8.1: VELO-track reconstruction efficiency for kaon tracks reconstructed using the on-line algorithms as a function of the kaon displacement ρ, as defined in Equation 6.7, in different bins of transverse momentum of the track and track multiplicity. The red solid lines show the result of an unbinned maximum likelihood fit using the parameterisation in Equation 6.8 to the background subtracted data (black points).
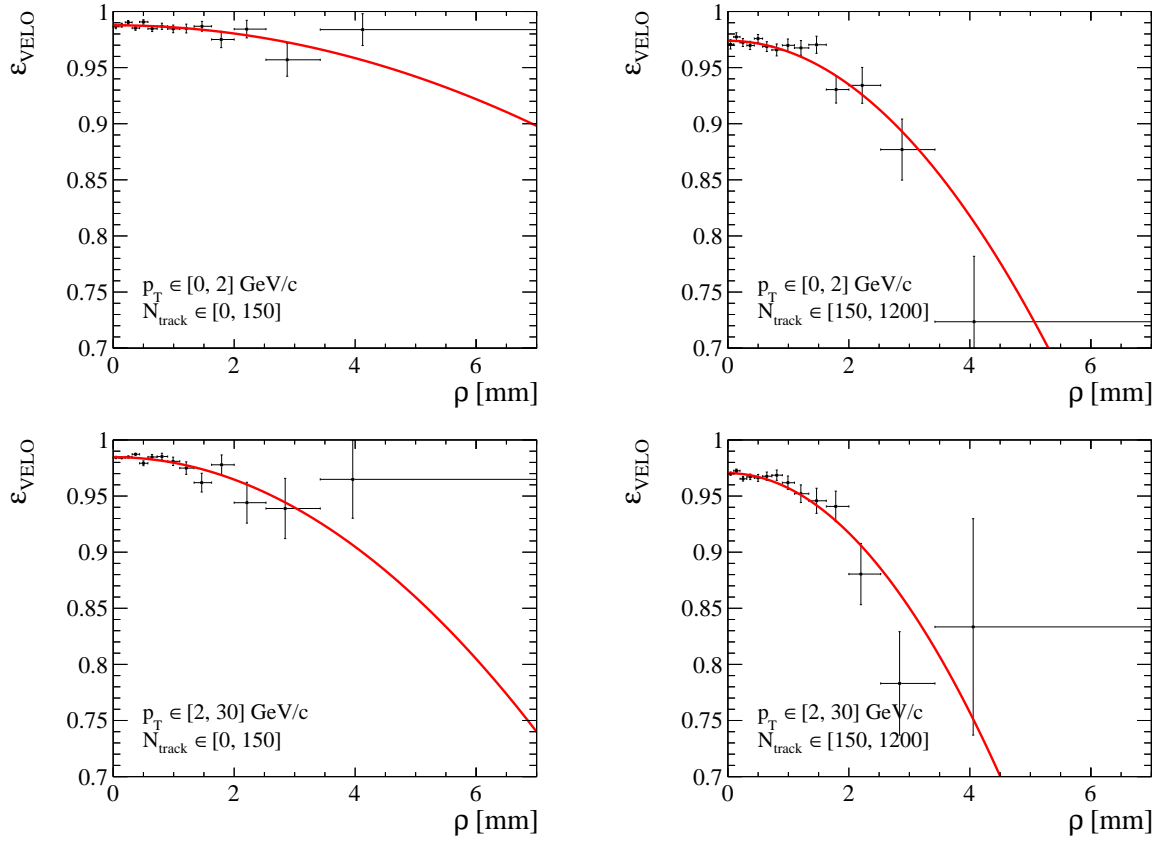
Figure 8.2: VELO-track reconstruction efficiency for kaon tracks reconstructed using the off-line algorithms as a function of the kaon displacement ρ, as defined in Equation 6.7, in different bins of transverse momentum of the track and track multiplicity. The red solid lines show the result of an unbinned maximum likelihood fit using the parameterisation in Equation 6.8 to the background subtracted data (black points).

8.2 Validation of the analysis method in simulated samples

The techniques described in Chapter 6 to correct the decay-time dependent efficiencies introduced in the different stages of the analysis have been validated on simulated data. The lifetime is fitted in each simulated signal mode and the deviation from the generated lifetime, $\Delta\tau$, is found to be compatible with zero within the statistical precision of each simulated sample, as shown in Figure 6.19 and Figure 6.20 for the different b hadrons. However, since it is known that the procedure developed do not remove completely some biases, the measured lifetimes in the data samples are corrected for the individual $\Delta\tau$. A corresponding systematic uncertainty is assigned, given by the size of the statistical uncertainty on the fitted lifetime for each simulated signal mode, since within this uncertainty it is not possible to identify further biases.

8.3 Correction for the trigger and stripping acceptance effects

For each signal decay mode, the effect of the limited size of the control sample used to estimate the combined trigger and stripping selection efficiency due to the requirement on the displacement of J/ψ candidates is evaluated by repeating the fits with $\varepsilon_{\text{trigger \& stripping}}(t)$ randomly fluctuated within its statistical uncertainty. The standard deviation of the distribution of lifetimes obtained is assigned as a systematic uncertainty.

8.4 Correlation between invariant mass and decay time

The assumption that $m(J/\psi X)$ is independent of the decay time is crucial to the validity of the likelihood fits used in this study. It is tested in data by re-evaluating the signal weights of the alternative fit in bins of decay time and then refitting the entire sample using the modified weights. Clearly, the background contribution changes in different decay-time bins since the prompt contribution is dominant at low decay-times. Moreover, also the width of the second signal Gaussian distribution, see Equation 5.2, shows a slight dependence on the decay-time. This procedure provides new estimates of the lifetime, τ_i, in each bin i. A clear trend is observed for the lifetime variation, $\tau - \tau_i$, among the different decay modes. The systematic uncertainty for each decay mode is evaluated as the sum in quadrature of the lifetime variations, each weighted by the fraction of signal events in the corresponding bin, N_i^{sig}, in the following way

$$\sigma^{\text{mass}-\text{time corr.}} = \sqrt{\frac{\sum_i (\tau - \tau_i)^2 \cdot N_i^{\text{sig}}}{\sum_i N_i^{\text{sig}}}} \ . \tag{8.2}$$

Part of this uncertainty is also of statistical nature, since the lifetimes in each bin i are estimated from sub-samples of the sample that is used to determine the nominal lifetime value, so this systematic uncertainty is a conservative upper limit for any effect due to correlations between invariant mass and decay time.

Table 8.2: Fit results for the B^+, B^0 mesons and Λ_b^0 baryon lifetimes and B_s^0 meson effective lifetime using the alternative fit technique. The uncertainty is statistical only.

Lifetime	Fit Value [ps]
$\tau_{B^+ \to J/\psi K^+}$	1.6399 ± 0.0036
$\tau_{B^0 \to J/\psi K^{*0}}$	1.5217 ± 0.0063
$\tau_{B^0 \to J/\psi K_S^0}$	1.4989 ± 0.0131
$\tau_{\Lambda_b^0 \to J/\psi \Lambda}$	1.4197 ± 0.0275
$\tau_{B_s^0 \to J/\psi \phi}$	1.4804 ± 0.0117

8.5   Modelling of the data distribution

The alternative likelihood fit explained in Section 7.1.2 does not assume any model for the decay time distribution associated with the combinatorial background. Therefore, the systematic uncertainty associated to the modelling of this background is evaluated by taking the difference in lifetimes measured by the nominal and alternative fit methods.

The fit values of the b-hadron lifetimes obtained performing the alternative fit are reported in Table 8.2. The mass and the decay time distributions of the different b hadrons used in the fit are shown in Figure 8.3 and Figure 8.4 together with the fit projections.

The fit uses a double Gaussian distribution to describe the $m(J/\psi X)$ distribution of signal candidates. This assumption is tested by repeating the fit using a so-called double-sided Apollonios function, see Appendix C, where the mean and width parameters are varied in the fit and the remaining parameters are fixed to those from simulation. The differences in lifetime with respect to the default results are nevertheless small and are taken as systematic uncertainties.

8.6   Decay-time resolution

The systematic uncertainty related to the choice of 45 fs for the width of the decay-time resolution function (65 fs in the case of $B^0 \to J/\psi K_S^0$ and $\Lambda_b^0 \to J/\psi \Lambda$) is evaluated by changing the width by ± 15 fs and repeating the fit. This change in width is larger than the estimated uncertainty on the resolution and leads to a negligible change in the fit results. Consequently, no systematic uncertainty is assigned. Furthermore, to test the sensitivity of the lifetimes to potential mismodelling of the long tails in the resolution, the resolution model is changed from a single Gaussian function to a sum of two or three Gaussian functions with parameters fixed from data. Repeating the fit with the new resolution model causes no significant change to the lifetimes and no systematic uncertainty is assigned.
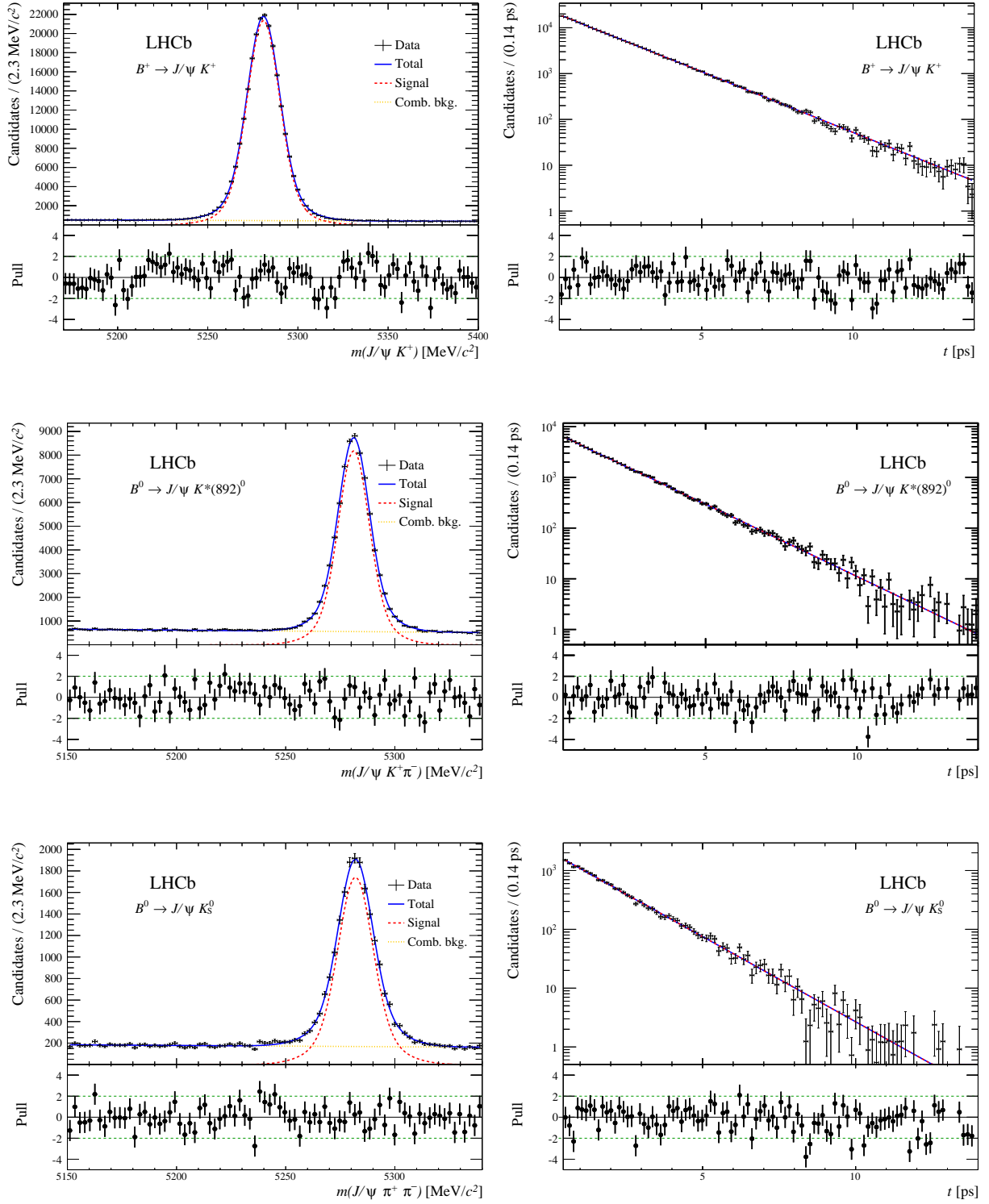
Figure 8.3: Distributions of the (left) mass and (right) decay time of $B^+ \to J/\psi K^+$, $B^0 \to J/\psi K^{*0}$ and $B^0 \to J/\psi K^0_S$ candidates and their associated residual uncertainties (pulls). The alternative likelihood fit described in Section 7.1.2 has been used. The data are shown by the black points; the total fit function by the blue solid line; the signal contribution by the red dashed line and the combinatorial background contribution by the yellow dotted line.
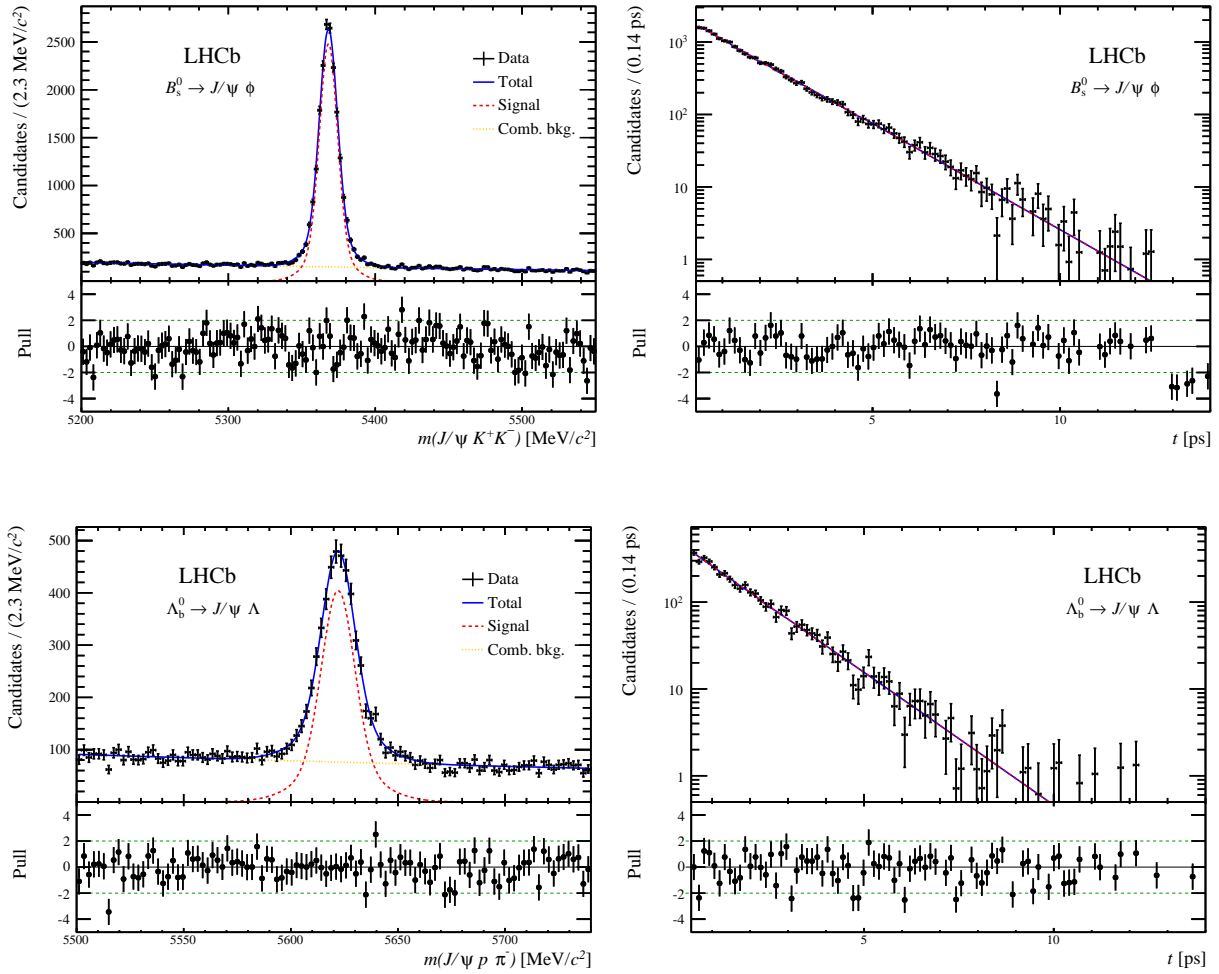
Figure 8.4: Distributions of the (left) mass and (right) decay time of $B_s^0 \to J/\psi\phi$ and $\Lambda_b^0 \to J/\psi\Lambda$ candidates and their associated residual uncertainties (pulls). The alternative likelihood fit described in Section 7.1.2 has been used. The data are shown by the black points; the total fit function by the blue solid line; the signal contribution by the red dashed line and the combinatorial background contribution by the yellow dotted line.

8.7   Background composition

As described in Section 7.3 the dominant background in each channel is combinatorial in nature. It is also possible for backgrounds to arise due to misreconstruction of b-hadron decays where the particle identification has failed. The presence of such backgrounds is checked by inspecting events in the sidebands of the signal and re-assigning the mass hypotheses of at least one of the final-state hadrons, as explained in Section 7.3. The only contributions that have an impact are $\Lambda_b^0 \to J/\psi\, pK^-$ decays in the $B_s^0 \to J/\psi\,\phi$ channel, where a proton is misidentified as a kaon, and the cross-feed component between $B^0 \to J/\psi\, K_S^0$ and $\Lambda_b^0 \to J/\psi\,\Lambda$ decays, where pion and protons are misidentified. In the case of $B_s^0 \to J/\psi\,\phi$ decays, the fit is repeated including a contribution of $\Lambda_b^0 \to J/\psi\, pK^-$ decays. The two-dimensional PDF is determined from simulation, while the yield is found to be about 6% from the sidebands of the B_s^0 sample. This leads to the effective lifetime changing by 0.4 fs, which is assigned as a systematic uncertainty. A similar procedure is used to determine the invariant mass shape of the cross-feed background between $B^0 \to J/\psi\, K_S^0$ and $\Lambda_b^0 \to J/\psi\,\Lambda$ decays, while the decay time is modelled with the exponential distribution of the corresponding signal mode. A fit to both data samples is performed in order to constrain the yield of the background and the resulting change in lifetime of 0.3 fs and 1.1 fs for B^0 and Λ_b^0, respectively, is assigned as a systematic uncertainty.

Another potential source of background is the incorrect association of signal b hadrons to another PV, which results in an erroneous reconstruction of the decay time. Since the fitting procedure ignores this contribution, a systematic uncertainty is evaluated by repeating the fit after including in the background model a component describing the incorrectly associated candidates. This model is determined in data using a sample of $B^+ \to J/\psi\, K^+$ decay, where most statistics is available to perform the study. For each event the decay time is calculated with respect to a randomly chosen PV from the previous selected event. This procedure clearly provides a completely wrong PV to which the candidate is associated and selected. In studies of simulated events the fraction of this background is less than 0.1%. Repeating the fit in data, considering conservatively a 1% contribution of this background, results in the lifetime changing by only 0.1 fs and, therefore, no systematic uncertainty is assigned.

8.8 B_s^0 effective lifetime

In the $B_s^0 \to J/\psi\,\phi$ channel, the B_s^0 is a pseudoscalar meson decaying into two vector mesons, as explained in Section 1.5.3. The final state is a mixture of different polarisations, namely CP even ($l = 0,\ 2$) and CP odd ($l = 1$) eigenstates. They can be separated by means of an angular analysis. The measurement of the effective lifetime in the $B_s^0 \to J/\psi\,\phi$ channel is performed integrating over the angular distributions of the final-state particles and is, in the case of uniform angular efficiency, insensitive to the different polarisations of the final state [5]. To check if the angular acceptance introduced by the detector geometry and event selection can affect the measured lifetime, the events are weighted by the inverse of the angular efficiency determined in Ref. [5]. Repeating the fit with the weighted dataset leads to a shift of the lifetime of

$-1.0\,\text{fs}$, the same as is observed in simulation. The final result is corrected by this shift, which is also assigned as a systematic uncertainty.

The $B_s^0 \rightarrow J/\psi\phi$ sample is composed predominately by the resonant P-wave $\phi \rightarrow K^+K^-$. Additionally, a small S-wave K^+K^- component is present. The B_s^0 effective lifetime could also be biased due to this small CP-odd S-wave component that is ignored in the fit. For the $m(K^+K^-)$ mass range used in this analysis (see Section 5.5.6) the Ref. [108] indicates that the S-wave contribution is 1.1%. The effect of ignoring such a component is evaluated by generating ToyMC samples with an additional 1% CP-odd component. Repeating the fit ignoring this distribution on 500 ToyMC experiments it is possible to estimate the bias on the effective lifetime. A change in the lifetime of $-1.2\,\text{fs}$ is observed, which is used to correct the final lifetime and is also taken as a systematic uncertainty.

Finally, as described in Section 5.5.6, only events with a decay time larger than $0.3\,\text{ps}$ are considered in the nominal fit. This offset leads to a different relative contribution of the heavy and light mass eigenstates such that the lifetime extracted from the exponential fit does not correspond to the effective lifetime defined in Equation 1.40. A correction of $-0.3\,\text{fs}$ is applied to account for this effect.

8.9 Production asymmetry

The presence of a production asymmetry between B^0 and $\overline{B}^0$ mesons, see Section 1.4.1, could bias the measured $B^0 \rightarrow J/\psi K_S^0$ effective lifetime by adding additional terms in Equation 1.40. Assuming no direct CP violation and a vanishing decay-width difference in the B^0 system, $\Delta\Gamma_d$, the expected shift in the $B^0 \rightarrow J/\psi K_S^0$ effective lifetime is

$$\Delta\tau_{B^0 \rightarrow J/\psi K_S^0} \approx A_P(B^0)\, \mathcal{A}_{CP}^{\text{mix}}\, \Delta m_d\, \frac{\left(\Gamma_d^2 - \Delta m_d^2\right)}{\left(\Gamma_d^2 + \Delta m_d^2\right)^2}\,. \tag{8.3}$$

The detailed calculation can be found in Appendix D. The production asymmetry is measured to be $A_\text{P}(B^0) = (0.6 \pm 0.9)\%$ [109], the uncertainty of which is used to estimate a corresponding systematic uncertainty on the $B^0 \rightarrow J/\psi K_S^0$ lifetime of 1.1 fs. No uncertainty is assigned to the $B^0 \rightarrow J/\psi K^{*0}$ lifetime since this decay mode is flavour-specific, see Section 1.5.1, and the production asymmetry cancels in the untagged decay rate.

For the B_s^0 system, the rapid oscillations, due to the large value of $\Delta m_s = 17.768 \pm 0.024\,\text{ps}^{-1}$ [110], reduce the effect of a production asymmetry, reported as $A_\text{P}(B_s^0) = (4 \pm 8)\%$ in Ref. [109], to a negligible level. Hence, no corresponding systematic uncertainty is assigned.

8.10 Length scale uncertainty

The decay time is proportional to the measured flight distance of the b-hadron candidate, as defined in Equation 4.1. The accuracy of this distance measurement

depends on the uncertainty on the positions of the VELO modules along the beam direction (z-axis). It is evaluated by comparing detector survey data with the track-based alignment.

There are two contributions to this uncertainty. The first comes from the knowledge of the overall length of the VELO. If the length of the VELO is underestimated by 1%, this would result directly in a 1% shorter measured decay time. At the time of the assembly the length of the baseplate of the VELO has been measured with an accuracy of approximately 100 μm [101] over the whole length of the VELO (1 m). This results in a z-scale uncertainty of 0.01%. The second contribution to this systematic effect is due to a possible relative shift of the individual modules within the VELO. A track-based alignment [111], based on histogramming hit residuals and on minimising the χ^2, has been used to evaluate this contribution. It is found that this effect is dominated by the uncertainty on the relative z-position of the first two modules that are hit by a particle. The uncertainty on the z-scale due to track-based alignment is estimated to be equal to 0.02% [110].

The uncertainties from these two contributions are added in quadrature to obtain the final uncertainty on the z-scale, which is 0.022 %. This translates into a 0.022% relative uncertainty on the lifetime measurements due to the uncertainty on the length scale at LHCb.

8.11 Momentum scale uncertainty

The decay time is proportional to the measured momentum, p, over the measured invariant mass, m, of the b-hadron candidate, as defined in Equation 4.1. Therefore, the effect of the accuracy to which the momentum is measured at LHCb has to be evaluated. However, since the momentum scale uncertainty influences both the measured momentum and the invariant mass of the b-hadron candidate, the effect partially cancels. A simplified test of the effect of incorrect momentum measurement on the lifetime is performed. Comparing the b-hadrons average reconstructed mass with respect to the world average mass [14], deviations from the nominal values are found to be within 0.1%. Scaling the momentum by 0.1% (or exaggerating the effect by 0.5%) and re-computing the mass m, a relative change of about $2 \cdot 10^{-5} (9 \cdot 10^{-5})$ on the ratio m/p is found. Therefore, the change on the lifetime is negligible.

8.12 Consistency checks

Several consistency checks are performed to study the stability of the measured lifetimes, by comparing the results obtained using different subsets of the data in terms of magnet polarity, data taking period, b-hadron and track kinematic variables, number of PVs in the event and track multiplicity. In all cases, no significant trend is observed and all lifetimes are compatible with the nominal results.

If multiple signal candidates are found in one event after the off-line selection procedure, the candidate with the smallest $\chi^2_{\mathrm{DTF}}/\mathrm{nDoF}$ is chosen. As a result, only one b-hadron candidate per event is available for the subsequent stages of the analysis.

Table 8.3: Statistical and systematic uncertainties (in femtoseconds) for the values of the b-hadron lifetimes. The total systematic uncertainty is obtained by combining the individual contributions in quadrature.

Source	$\tau_{B^+ \to J/\psi K^+}$	$\tau_{B^0 \to J/\psi K^{*0}}$	$\tau_{B^0 \to J/\psi K^0_S}$	$\tau_{\Lambda^0_b \to J/\psi \Lambda}$	$\tau_{B^0_s \to J/\psi \phi}$
Statistical uncertainty	3.5	6.1	12.8	26.5	11.4
VELO reconstruction	2.0	2.3	0.9	0.5	2.3
Simulation sample size	1.7	2.3	2.9	3.7	2.4
Mass-time correlation	1.4	1.8	2.1	3.0	0.7
Trigger and selection eff.	1.1	1.2	2.0	2.0	2.5
Background modelling	0.1	0.2	2.2	2.1	0.4
Mass modelling	0.1	0.2	0.4	0.2	0.5
Peaking background	–	–	0.3	1.1	0.4
Effective lifetime bias	–	–	–	–	1.6
B^0 production asym.	–	–	1.1	–	–
LHCb length scale	0.4	0.3	0.3	0.3	0.3
Total systematic	3.2	3.9	4.9	5.7	4.6

In order to verify that this method is not introducing any decay-time bias, a random candidate is selected every time that there is more than one *b*-hadron candidate in the event and the lifetime is evaluated again. The shift of the lifetime with respect to the nominal result is found to be negligible and thus, no systematic uncertainty is assigned.

8.13 Summary

In this section the different contributions to the systematic uncertainty on the measurements of the lifetimes of the different *b*-hadrons have been presented. They are summarised in Table 8.3 where the quadratic sum, which represents the total systematic uncertainty assigned, is also reported. It can be seen that for the B^+ lifetime the systematic uncertainty is of the same size as the statistical uncertainty, while for all the other channels the systematic contribution is well below the statistical one.

There is no clear dominating contribution to the systematic uncertainty. However, the main contributions are due to the decay-time acceptance correction, namely the VELO-track reconstruction efficiency correction and the finite size of the simulated samples used to validate the corrections. It is expected that these contributions can easily be improved in the future. The size of the simulated samples can be enlarged by generating more events and the uncertainty on the VELO-track reconstruction efficiency correction will be reduced with a larger $B^+ \to J/\psi K^+$ control sample that will be available collecting more data.

9
Lifetime ratios and $\Delta\Gamma_d/\Gamma_d$ measurement

Physics is about questioning, studying, probing nature. You probe, and,
if you're lucky, you get strange clues.

— Lene Hau

Using the lifetime measurements reported in Section 7.4, several lifetime ratios are determined. They represent useful inputs for comparisons with the corresponding theoretical predictions and to confirm the validity of the *CPT* theorem. Finally, the measurement of the decay width difference in the B^0 system over the average decay width, $\Delta\Gamma_d/\Gamma_d$, is derived following the method introduced in Section 1.5.2.

9.1 Lifetime ratios

From a theoretical point of view lifetime ratios are well-defined quantities, since many uncertainties cancel in the ratio. Moreover, also from an experimental point of view lifetime ratios are robust quantities, since many systematic uncertainties that are completely correlated among the different b-hadrons decay modes can be neglected.

In order to better compare the experimental results with the theoretical predictions, the lifetime measurements determined in Section 7.4 are used to calculate lifetime ratios. Table 9.1 reports the ratios of the B^+ and Λ_b^0 lifetimes and B_s^0 effective lifetime to the B^0 effective lifetime measured in the flavour-specific $B^0 \to J/\psi K^{*0}$ channel. This decay mode provides a better normalisation than the $B^0 \to J/\psi K_S^0$ channel due to the lower statistical uncertainty and due to the fact that the $B^0 \to J/\psi K^{*0}$ effective lifetime only depends quadratically on $\Delta\Gamma_d/\Gamma_d$, as shown in Equation 1.42.

All ratios are consistent with SM predictions [40, 43, 44, 47, 48], as presented in Table 1.6 and with previous measurements [2]. The B_s^0 lifetime used in the ratio determination is the effective lifetime evaluated in the $J/\psi\phi$ final state and not the average B_s^0 lifetime, which will be derived in the next part. Thus, this ratio cannot be compared to the theoretical one shown in Table 1.6.

Table 9.1: Lifetime ratios for the B^+, B_s^0 mesons and Λ_b^0 baryon to the B^0 lifetime measured in the flavour-specific $B^0 \to J/\psi K^{*0}$ channel. The uncertainty is statistical only.

Ratio	Value
$\tau_{B^+}/\tau_{B^0 \to J/\psi K^{*0}}$	1.074 ± 0.005
$\tau_{B_s^0 \to J/\psi\phi}/\tau_{B^0 \to J/\psi K^{*0}}$	0.971 ± 0.009
$\tau_{\Lambda_b^0}/\tau_{B^0 \to J/\psi K^{*0}}$	0.929 ± 0.018

Table 9.2: Fit results for the B^+, B^-, B^0, $\bar{B}^0$ mesons and Λ_b^0 and $\bar{\Lambda}_b^0$ baryon lifetimes. The uncertainty is statistical only.

Lifetime	Fit value [ps]
τ_{B^+}	1.6382 ± 0.0050
τ_{B^-}	1.6352 ± 0.0051
τ_{B^0}	1.5237 ± 0.0086
$\tau_{\bar{B}^0}$	1.5240 ± 0.0087
$\tau_{\Lambda_b^0}$	1.3722 ± 0.0361
$\tau_{\bar{\Lambda}_b^0}$	1.4602 ± 0.0391

Furthermore, the ratios τ_{B^+}/τ_{B^-}, $\tau_{\Lambda_b^0}/\tau_{\bar{\Lambda}_b^0}$ and $\tau_{B^0 \to J/\psi K^{*0}}/\tau_{\bar{B}^0 \to J/\psi \bar{K}^{*0}}$ are calculated. Measuring any of these ratios different from unity would indicate a violation of CPT invariance which predicts that a particle and the corresponding antiparticle must have the same lifetime. Since neutral B^0 mesons exhibit the phenomenon of mixing, in the ratio $\tau_{B^0 \to J/\psi K^{*0}}/\tau_{\bar{B}^0 \to J/\psi \bar{K}^{*0}}$ the flavour of the B^0 is tagged at the moment of the decay and it does not necessarily correspond to the flavour at production. Thus, if this ratio is different from unity, it could also indicate that $\Delta\Gamma_d$ is non-zero and $B^0 \to J/\psi K^{*0}$ is not 100% flavour-specific.

The lifetimes used to determine this second set of ratios are evaluated using the same procedure described in Chapter 7, splitting the B^+, B^0 and Λ_b^0 samples in order to separate decays originating by a particle or by the corresponding antiparticle. In particular, the B^+ (B^-) decays can be distinguished by the charge of the kaon in the final state, K^+ (K^-). Similarly, the B^0 ($\bar{B}^0$) decays can be distinguished by the charge of the kaon in the final state, K^+ (K^-), and the Λ_b^0 ($\bar{\Lambda}_b^0$) decays can be distinguished by the charge of the pion in the final state, π^- (π^+). The fit results for these lifetimes are shown in Table 9.2. From these values, the τ_{B^+}/τ_{B^-}, $\tau_{\Lambda_b^0}/\tau_{\bar{\Lambda}_b^0}$ and $\tau_{B^0 \to J/\psi K^{*0}}/\tau_{\bar{B}^0 \to J/\psi \bar{K}^{*0}}$ ratios are derived. They are listed in Table 9.3. No statistically significant deviation from unity of these set of ratios is observed.

The majority of the systematic uncertainties described in Chapter 8 can be propagated to the lifetime ratio measurements. They are reported in Table 9.4. However, some of the uncertainties are correlated between the individual lifetimes and cancel in the ratio.

Table 9.3: *Ratios of the B^+, B^0 and the Λ_b^0 lifetime with respect to the lifetime of the corresponding antiparticle. The uncertainty is statistical only.*

Ratio	Value
τ_{B^+}/τ_{B^-}	1.002 ± 0.004
$\tau_{\Lambda_b^0}/\tau_{\overline{\Lambda}_b^0}$	0.940 ± 0.035
$\tau_{B^0 \to J/\psi K^{*0}}/\tau_{\overline{B}^0 \to J/\psi \overline{K}^{*0}}$	1.000 ± 0.008

Table 9.4: *Statistical and systematic uncertainties (in units of 10^{-3}) for the lifetime ratios. For brevity, τ_{B^0} $\left(\tau_{\overline{B}^0}\right)$ corresponds to the measurement of $\tau_{B^0 \to J/\psi K^{*0}}$ $\left(\tau_{\overline{B}^0 \to J/\psi \overline{K}^{*0}}\right)$. The total systematic uncertainty is obtained by combining the individual contributions in quadrature.*

Source	τ_{B^+}/τ_{B^0}	$\tau_{B_s^0}/\tau_{B^0}$	$\tau_{\Lambda_b^0}/\tau_{B^0}$	τ_{B^+}/τ_{B^-}	$\tau_{\Lambda_b^0}/\tau_{\overline{\Lambda}_b^0}$	$\tau_{B^0}/\tau_{\overline{B}^0}$
Statistical uncertainty	5.0	8.5	18.0	4.0	35.0	8.0
VELO reconstruction	1.6	1.7	1.1	–	–	–
Simulation sample size	2.0	2.2	2.8	2.1	5.3	3.0
Mass-time correlation	1.6	1.2	2.3	–	–	–
Trigger and selection eff.	1.1	1.8	1.5	–	–	–
Background modelling	0.3	0.1	1.5	0.2	3.0	1.4
Mass modelling	0.2	0.4	0.2	0.1	0.2	0.2
Peaking background	–	0.3	0.7	–	–	–
Effective lifetime bias	–	1.0	–	–	–	–
B^0 production asym.	–	–	–	–	–	8.5
Total systematic	3.2	3.7	4.4	2.1	6.1	9.1

For the first set of ratios, the systematic uncertainty from the VELO-reconstruction efficiency weights, in particular from the finite size of the $B^+ \to J/\psi K^+$ control sample, and the LHCb length scale are considered as fully correlated and thus neglected. For the second set of ratios, also other systematic uncertainties, as indicated in Table 9.4, cancel, since the ratio is formed from lifetimes measured using the same decay mode. In contrast to the situation for the measurement of the B^0 lifetime in the $B^0 \to J/\psi K^{*0}$ mode, the B^0 production asymmetry does lead to a systematic uncertainty on the measurement of $\tau_{B^0 \to J/\psi K^{*0}}/\tau_{\overline{B}^0 \to J/\psi \overline{K}^{*0}}$ since terms like $A_P \cos(\Delta m_d t)$ do not cancel in the decay rates describing the decays of B^0 and $\overline{B}^0$ mesons to $J/\psi K^{*0}$ and $J/\psi \overline{K}^{*0}$ final states. The detailed calculation can be found in Appendix D. The effect of candidates where the flavour, via the particle identification of the decay products, has not been correctly assigned is investigated and found to be negligible.

In general, the systematic uncertainty is much smaller than the statistical uncertainty and it is dominated by the limited size of the simulated sample. The only exception is the ratio $\tau_{B^0}/\tau_{\overline{B}^0}$, which is dominated by the uncertainty on the B^0 production asymmetry.

Table 9.5: *Statistical and systematic uncertainties (in units of 10^{-3}) for $\Delta\Gamma_d/\Gamma_d$. The total systematic uncertainty is obtained by combining the individual contributions in quadrature.*

Source	$\Delta\Gamma_d/\Gamma_d$
Statistical uncertainty	25.0
VELO reconstruction	4.1
Simulation sample size	6.3
Mass-time correlation	4.7
Trigger and selection eff.	4.0
Background modelling	3.8
Mass modelling	0.8
Peaking background	0.5
B^0 production asym.	1.9
Total systematic	10.7

9.2 Measurement of $\Delta\Gamma_d/\Gamma_d$

As already introduced in Section 1.5.2, it is possible to determine the decay width difference between the mass eigenstates in the B^0 system over the average decay width, $\Delta\Gamma_d/\Gamma_d$, from the ratio of the effective B^0 lifetime measurements in a flavour specific decay (like $B^0 \to J/\psi K^{*0}$) and in a decay to a CP eigenstate (like $B^0 \to J/\psi K_S^0$). Defining the ratio of these two lifetimes as $R \equiv \tau_{B^0 \to J/\psi K_S^0}/\tau_{B^0 \to J/\psi K^*(892)^0}$, the following expression for $\Delta\Gamma_d/\Gamma_d$ is obtained

$$\frac{\Delta\Gamma_d}{\Gamma_d} = \frac{2}{\cos(2\beta)}(R-1) + \frac{2}{\cos(2\beta)^2}(R-1)^2 + \mathcal{O}(R-1)^3 \,. \tag{9.1}$$

Making use of $\beta = (21.5^{+0.8}_{-0.7})°$ [2] and substituting the measurements of the $B^0 \to J/\psi K^{*0}$ and $B^0 \to J/\psi K_S^0$ effective lifetimes listed in Table 7.7, the decay width difference over the average decay width in the B^0 system is determined to be

$$\frac{\Delta\Gamma_d}{\Gamma_d} = 0.044 \pm 0.025 \,. \tag{9.2}$$

Again, almost all of the systematic uncertainties described in Chapter 8 can be propagated to this measurement. The detailed list of all the contributions is reported in Table 9.5. The only systematic uncertainties that are considered as fully correlated are the contributons from the VELO-reconstruction efficiency weights, in particular related to the finite size of the $B^+ \to J/\psi K^+$ control sample, and the LHCb length scale. The systematic uncertainty due to the uncertainty on the β measurement is found to be negligible.

The systematic uncertainty on this measurement is considerably smaller than the statistical uncertainty. It is dominated by the uncertainty on the limited size of the simulated sample thus it can be easily reduced in the future.

Part III

Measurement of Γ_s and $\Delta\Gamma_s$

<div style="text-align: right;">

10

</div>

Average decay width and decay width difference in the B_s^0 system

<div style="text-align: right;">

In cauda venenum. (The poison (is) in the tail.)

— Fedro

</div>

The techniques developed to correct the decay-time dependent acceptance in order to perform the b-hadrons lifetime measurements are important also in other analyses in order to obtain an unbiased b-hadron decay-time distribution. In particular, they are fundamental in order to obtain a measurement of the average decay width, Γ_s, and the decay width difference, $\Delta\Gamma_s$, in the B_s^0 system. To this purpose, a time-dependent angular analysis of $B_s^0 \to J/\psi\phi$ decays is needed, as explained in Section 1.5.3. In this chapter, the strategy used to implement the corrections developed in Chapter 6 into this analysis is reviewed, emphasizing the differences with respect to the strategy followed for the b-hadrons lifetime measurements. Finally, the measurement of Γ_s and $\Delta\Gamma_s$ is reported.

10.1   Data sample

The measurement of Γ_s and $\Delta\Gamma_s$ is performed using the full dataset recorded in 2011 and 2012 at a centre-of-mass energy of $\sqrt{s} = 7$ TeV and $\sqrt{s} = 8$ TeV, respectively. This dataset corresponds to an integrated luminosity of about 3.0 fb^{-1}, namely $\mathcal{L} = 0.99$ fb^{-1} in 2011 and $\mathcal{L} = 2.04$ fb^{-1} in 2012. The events used in this analysis stem from this sample and pass the trigger, stripping and final analysis selection requirements, which are presented in the following sections. The FASTVELO version used for the track reconstruction in 2012 data is v1r11 for both the on-line and the off-line reconstruction. This is different than the version used during the 2011 data taking, v1r5. In order to be as much as possible consistent in both datasets, the 2011 dataset was reprocessed with the FASTVELO v1r11 track-reconstruction version for the off-line reconstruction. However, the on-line reconstruction version, v1r5, cannot be modified since after a trigger decision is taken the events that are not selected are deleted. This implies that the correction of the lifetime bias which is related to inefficiencies in the VELO-

<div style="text-align: center;">

151

</div>

track reconstruction must be determined separately for the different years of data taking.

The Monte Carlo samples used for this analysis have been produced with similar conditions to those used during the data taking in 2011 and 2012, in particular using the same FastVELO version as in data. With respect to the MC samples used for the b-hadron lifetimes analysis, the generated values used for the different particle properties, like the mass and the lifetime, have been updated to the 2012 version of the PDG [14]. In particular, the values used in the generation for Γ_s and $\Delta\Gamma_s$ are $\Gamma_s = 0.6653 \, \mathrm{ps}^{-1}$ and $\Delta\Gamma_s = 0.0917 \, \mathrm{ps}^{-1}$.

10.2   Analysis strategy

As already introduced in Section 1.5.3, the $B_s^0 \to J/\psi\phi$ final state is a superposition of CP-even and CP-odd states depending upon the relative orbital angular momentum of the J/ψ and the ϕ. This decay proceeds predominantly via the ϕ resonance, subsequently decaying to a K^+K^- pair which is in a P-wave configuration. However, the same final state can also be produced with a K^+K^- pair in a S-wave configuration.

This decay allows to determine the CP-violating phase ϕ_s, which originates from the interference between B_s^0 meson decay amplitudes to CP eigenstates directly or via mixing. Since it is precisely predicted by the SM [27], a measurement of this phase significantly different from the SM prediction would provide a strong evidence for processes beyond the SM. In order to measure it, CP-even and CP-odd components have to be disentangled by analysing the distribution of the reconstructed decay angles of the final-state particles. In this way, the decay widths of the light and the heavy B_s^0 mass eigenstates, which allow to determine Γ_s and $\Delta\Gamma_s$, are also measured.

A detailed discussion of the experimental details of this analysis is beyond the scope of this thesis and can be found in Ref. [5, 28]. Here, the strategy of the measurement is briefly summarised, with particular emphasis on the choices that affect the B_s^0 decay-time distribution and thus the determination of Γ_s and $\Delta\Gamma_s$. These parameters of interest are extracted by fitting the measured decay-time and angular distributions of the reconstructed $B_s^0 \to J/\psi\phi$ decays, as introduced in Section 1.5.3. In this analysis, the decay angles defined in the helicity basis are used. The helicity angles are denoted by $\Omega = (\theta_\mathrm{K}, \theta_\mu, \varphi_h)$ and they are visualised in Figure 10.1. The polar angle θ_K (θ_μ) is the angle between the K^+ (μ^+) momentum and the direction opposite to the B_s^0 momentum in the K^+K^- ($\mu^+\mu^-$) centre-of-mass system. The azimuthal angle between the K^+K^- and $\mu^+\mu^-$ decay planes is φ_h. This angle is defined by a rotation from the K^- side of the K^+K^- plane to the μ^+ side of the $\mu^+\mu^-$ plane. The rotation is positive in the $\mu^+\mu^-$ direction in the B_s^0 rest frame.

One challenge of this analysis is that the production flavour of the B_s^0 mesons must be determined to distinguish between the decay rates of B_s^0 and $\overline{B}_s^0$ in the fit. The separation of the sample is achieved with so-called flavour tagging algorithms [112]. They exploit either the hadronisation properties of the signal B_s^0 meson or the properties of a second b-hadron that is produced from the $b\bar{b}$ quark pair and thus correlated to the signal B_s^0 meson.
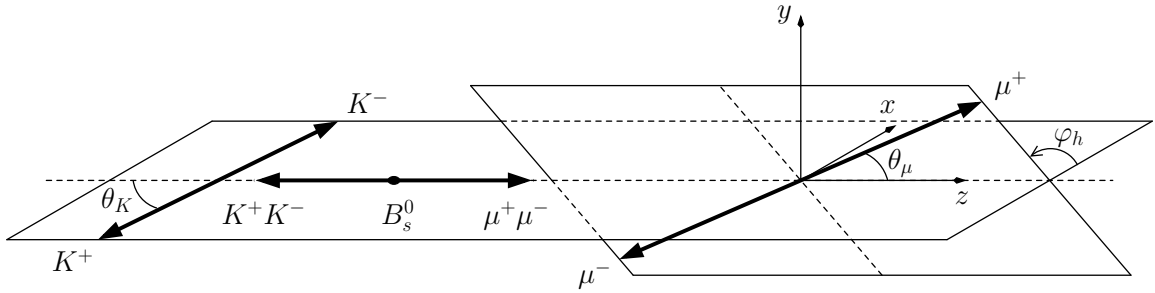
Figure 10.1: Definition of helicity angles as discussed in the text. Figure taken from Ref. [5].

Moreover, the measured decay-time and angular distributions are distorted by acceptance effects introduced by the geometrical coverage of the detector, by the track reconstruction and by trigger and selection requirements. The rest of this chapter is devoted to explain the strategy used to determine the B_s^0 decay-time acceptance and the results obtained.

10.3   Trigger and off-line selection

The sensitivity of the decay-time and angular distributions to the physics observables increases with the number of reconstructed $B_s^0 \to J/\psi\phi$ signal decays, while it decreases with the amount of background polluting the event sample. The specific selection criteria are optimised to maximise the sensitivity on ϕ_s. This implies that some selection requirements that have been used in order to perform the b-hadron lifetime measurements are not suitable for this analysis. They have been introduced in order to reduce the decay-time acceptance effects. However, they also reduce the statistical power of the sample. In this section, the trigger lines and the selection criteria used to isolate $B_s^0 \to J/\psi\phi$ candidates are discussed, highlighting the differences with respect to the criteria used for the B_s^0 effective lifetime determination, explained in Chapter 5.

10.3.1   Trigger selection

The trigger strategy is to include more trigger lines with respect to the B_s^0 effective lifetime measurement in order to increase the number of signal candidates available for the subsequent stages of the analysis. However, this introduce more time-dependent acceptances that have to be modeled. In addition to the HLT1 trigger line described in Section 5.4, namely `HLT1DiMuonHighMass`, which does not contain any decay-time biasing requirement, two other HLT1 lines are introduced, so-called `Hlt1TrackMuon` and `Hlt1TrackAllL0`. The former line requires a positive L0-Muon, meaning a single muon, or L0-DiMuon, meaning two muons, decision of the hardware trigger. The latter line requires a positive L0-Physics decision, meaning that either the L0 calorimeter or the L0 muon trigger have selected the event. Both trigger lines select single tracks depending on their impact parameter, IP, and their impact parameter $\chi^2_{\rm IP}$. Tracks from decays of B_s^0 candidates have in general a higher $\chi^2_{\rm IP}$ than tracks from the pp interaction point.

Table 10.1: Relevant HLT1 trigger line selections used in 2011 for the determination of $\Delta\Gamma_s$ and Γ_s. A '−' implies that no requirement is applied on the corresponding parameter.

	HLT1DiMuonHighMass	Hlt1TrackMuon	Hlt1TrackAllL0
L0	L0-Muon or L0-DiMuon	L0-Muon or L0-DiMuon	L0-Physics
$p_{\mathrm{T}}\,[\,\mathrm{GeV}/c\,]$	> 0.5	> 1.0	> 1.7
$p\,[\,\mathrm{GeV}/c\,]$	> 6	> 8	> 10
$\chi^2_{\mathrm{track}}/\mathrm{nDoF}$	< 4	< 2	< 2
DOCA $[\,\mathrm{mm}\,]$	< 0.2	−	−
$m(\mu^+\mu^-)\,[\,\mathrm{GeV}/c^2\,]$	> 2.7	−	−
$\chi^2_{\mathrm{vtx}}/\mathrm{nDoF}$	< 25	−	−
IP $[\,\mathrm{mm}\,]$	−	> 0.1	> 0.1
χ^2_{IP}	−	> 16	> 16

Therefore these trigger lines are more efficient for B_s^0 with a large decay time than for those with a small decay time. In addition, a minimum $\chi^2_{\mathrm{track}}/\mathrm{nDoF}$ of the track fit is required and selection criteria on the transverse momentum and momentum of the tracks are applied. All selection criteria of these lines are summarised in Table 10.1 and Table 10.2 for 2011 and 2012 data, respectively.

Each event has to satisfy the criteria of at least one of these HLT1 trigger lines. Afterwards, the signal decay has to pass the decay-time dependent HLT2 line also used to perform *b*-hadrons lifetime measurements, namely HLT2DiMuonDetachedJPsi. The selection used in 2011 and 2012 for this HLT2 line is listed in Table 10.3. All the trigger lines use only B_s^0 decay products to take the decision in order to avoid the introduction of a decay-time acceptance, as explained in Section 6.3.5. This trigger strategy retains approximately 90% of all the B_s^0 candidates that would pass the remaining off-line selection and that are triggered, without any selection on the trigger line.

It is possible to divide the full sample into two subsamples

1. **HLT1 unbiased**: candidates that pass the Hlt1DiMuonHighMass and Hlt2DiMuonDetachedJPsi requirements.

2. **HLT1 biased**: candidates that pass the Hlt1TrackMuon or Hlt1TrackAllL0 requirements and that are subsequently triggered by the Hlt2DiMuonDetachedJPsi line. In order to avoid an overlap with the HLT1 unbiased subsample, the events must not be triggered by the Hlt1DiMuonHighMass line.

In the end both subsamples have a distorted decay-time distribution as both require the detached HLT2 line. However this classification is useful to understand the procedure used to derive the decay-time dependent acceptance of these trigger categories, described in Section 10.4.2.

10.3.2   Off-line selection

The detailed selection requirements are listed in Table 10.4 for the stripping and the subsequent final selection. The main difference with respect to the selection illustrated in Section 5.5.6 is that the fiducial requirements are not used. Even if they help

Table 10.2: *Relevant HLT1 trigger line selections used in 2012 for the determination of $\Delta\Gamma_s$ and Γ_s. If thresholds changed, the approximate corresponding integrated luminosity collected is indicated in the second row. A '–' implies that no requirement is applied on the corresponding parameter.*

	HLT1DiMuonHighMass	Hlt1TrackMuon	Hlt1TrackAllL0
L0	L0-Muon or L0-DiMuon	L0-Muon or L0-DiMuon	L0-Physics
$p_{\mathrm{T}}[\,\mathrm{GeV}/c\,]$	> 0.5	> 1.0	$> 1.35/1.7/1.6$ $(1/611/1428\ \mathrm{pb}^{-1})$
$p\,[\,\mathrm{GeV}/c\,]$	$> 1/6/3$ $(6/606/1428\ \mathrm{pb}^{-1})$	$> 8/3$ $(630/2410\ \mathrm{pb}^{-1})$	$> 1/10/3$ $(6/606/1428\ \mathrm{pb}^{-1})$
$\chi^2_{\mathrm{track}}/\mathrm{nDoF}$	$< 5/3$ $(6/2034\ \mathrm{pb}^{-1})$	$< 3/2.5$ $(70/1970\ \mathrm{pb}^{-1})$	$< 2.25/2/1.5/2$ $(6/61/271/1702\ \mathrm{pb}^{-1})$
DOCA $[\,\mathrm{mm}\,]$	< 0.2	–	–
$m(\mu^+\mu^-)\,[\,\mathrm{GeV}/c^2\,]$	> 2.7	–	–
$\chi^2_{\mathrm{vtx}}/\mathrm{nDoF}$	< 25	–	–
IP $[\,\mathrm{mm}\,]$	–	> 0.1	> 0.1
χ^2_{IP}	–	> 16	> 16

Table 10.3: *Relevant HLT2 trigger line selections used in the analysis. If thresholds changed, they are given as 2011/2012. A '–' implies that no requirement is applied on the corresponding parameter.*

	HLT2DiMuonJPsi	HLT2DiMuonDetachedJPsi
$\chi^2_{\mathrm{track}}/\mathrm{nDoF}$	$< 5/4$	$< 5/4$
$m(\mu^+\mu^-)\,[\,\mathrm{GeV}/c^2\,]$	$M_{J/\psi} \pm 0.12$	$M_{J/\psi} \pm 0.12$
$\chi^2_{\mathrm{vtx}}/\mathrm{nDoF}$	< 25	< 25
FDS	–	> 3
Prescale	yes	–

Table 10.4: Selection criteria used to identify $B_s^0 \to J/\psi\phi$ candidates for the determination of $\Delta\Gamma_s$ and Γ_s. A '−' implies that no requirement is applied on the corresponding parameter.

	Variable	Stripping	Final selection
all tracks	$\chi^2_{\text{track}}/\text{nDoF}$	< 5	< 4
$J/\psi \to \mu^+\mu^-$	$\Delta\ln\mathcal{L}_{\mu\pi}\ (\mu^\pm)$	> 0	> 0
	$p_T\ (\mu^\pm)$	$-$	$> 500\ \text{MeV}/c$
	$\chi^2_{\text{vtx}}/\text{nDoF}\ (J/\psi)$	< 16	< 16
	$m(\mu^+\mu^-)$	$\in [3030, 3150]\ \text{MeV}/c^2$	$\in [3030, 3150]\ \text{MeV}/c^2$
$\phi \to K^+K^-$	$\Delta\ln\mathcal{L}_{K\pi}\ (K^\pm)$	> -2	> 0
	$p_T\ (\phi)$	$> 1.0\ \text{GeV}/c$	$> 1.0\ \text{GeV}/c$
	$\chi^2_{\text{vtx}}/\text{nDoF}\ (\phi)$	< 25	< 16
	$m(K^+K^-)$	$\in [980, 1050]\ \text{MeV}/c^2$	$\in [990, 1050]\ \text{MeV}/c^2$
$B_s^0 \to J/\psi\phi$	$m(J/\psi\,K^+K^-)$	$\in [5200, 5550]\ \text{MeV}/c^2$	$\in [5200, 5550]\ \text{MeV}/c^2$
	$\chi^2_{\text{vtx}}/\text{nDoF}(B_s^0)$	< 20	< 10
	χ^2_{IP}	$-$	< 25
	$\chi^2_{\text{IP,next PV}}$	$-$	> 50
	$\chi^2_{\text{DTF}}/\text{nDoF}$	$-$	< 5
	t	$> 0.2\ \text{ps}$	$\in [0.3, 14.0]\ \text{ps}$

significantly defining a region where the efficiency for a track to be reconstructible is quite uniform, they also cause a significant reduction of the statistical power of the sample of about 10%. This would result in an increase of the statistical uncertainty on ϕ_s. The second main difference is the presence of the selection requirement on the good quality of the vertex, $\chi^2_{\text{vtx}}/\text{nDoF}$, formed by the decay products of the ϕ and of the B_s^0. As explained in Section 6.3.4, these requirements cause a loss of signal candidates with a large B_s^0 decay-time. However, the lifetime bias introduced is small, around 1 fs, compared to the significant amount of background that is introduced due to the absence of these two selection criteria. Thus, it was decided to keep these selection requirements. Finally, the last main difference is the absence of the selection requirement on the flight distance significance, FDS, of the J/ψ with respect to the PV. This is due to the fact that since in this analysis the presence of the $\chi^2_{\text{vtx}}/\text{nDoF}$ requirement is tolerated, a different stripping line which contains this requirement is available. It is a $B_s^0 \to J/\psi\phi$ exclusive stripping line, instead of the inclusive J/ψ stripping line used to select the b-hadron lifetime measurements sample, and it does not contain the FDS requirement.

10.4 Decay-time acceptance

The decay-time acceptance introduced by the reconstruction, trigger and selection requirements is divided, as explained in Section 6.3.2, in a lower and upper decay-time acceptance. These two contributions are analysed separately in the next two sections.

Table 10.5: Residuals measured in Toy MC on the parameters Γ_s and $\Delta\Gamma_s$ for different parameterisations of the upper decay-time acceptance. About 90 000 events are generated including a linear only, quadratic only or quadratic parameterisation of the acceptance and then fitted assuming a flat acceptance. The results are shown in the left, middle and right column, respectively.

Parameter	Residual		
	linear only ($\gamma = 0$)	quadratic only ($\beta = 0$)	quadratic ($\gamma, \beta \neq 0$)
Γ_s	0.255 ± 0.005 ps^{-1}	0.279 ± 0.006 ps^{-1}	0.251 ± 0.005 ps^{-1}
$\Delta\Gamma_s$	-0.0003 ± 0.0007 ps^{-1}	-0.0056 ± 0.0006 ps^{-1}	-0.0060 ± 0.0008 ps^{-1}

10.4.1 Upper decay-time acceptance

The upper decay-time acceptance is introduced by the reconstruction and selection requirements. If this time-dependent acceptance could be parameterised with a linear function, $(1 + \beta t)$, it would have an effect only on the value of Γ_s, leaving $\Delta\Gamma_s$ unbiased. This can be understood since, if β is small, it is possible to write

$$(1 + \beta t)\, e^{-\Gamma_H t} \approx e^{-(\Gamma_H - \beta)t} \;\; \text{and} \;\; (1 + \beta t)\, e^{-\Gamma_L t} \approx e^{-(\Gamma_L - \beta)t}, \qquad (10.1)$$

where Γ_L and Γ_H are the decay width of the light and heavy mass eigenstates, respectively. Since $\Delta\Gamma_s \equiv \Gamma_L - \Gamma_H$ and the correction is independent on the decay time, it just cancels when performing the difference between the two decay widths. This statement has been verified using Toy Monte Carlo where a linear decay-time acceptance is introduced in the generation of the sample and subsequently is ignored in the fit performed to extract the values of Γ_s and $\Delta\Gamma_s$. The result of this procedure is shown in the first column in Table 10.5. Here, the residuals, defined as the difference between the generated value and the fitted value, are shown. It is possible to see that while Γ_s is clearly biased, the parameter $\Delta\Gamma_s$ is instead unaffected. This scenario would make the correction procedure for the decay-time acceptance easier. Since the correction is time-independent, it would be possible to derive the value of the β parameter separately and then to subtract this quantity by the Γ_s measurement extracted from the fit.

However, it is found that the upper decay-time acceptance cannot be parameterised by a linear function. It is obtained in simulated $B_s^0 \to J/\psi\phi$ MC samples dividing the normalised decay-time distribution of reconstructed and selected candidates by the generated one. It is shown in Figure 10.2 (a) and (b) for the MC samples reproducing the 2011 and the 2012 data taking conditions, respectively. Here, only the HLT1 unbiased trigger lines and no HLT2 lines are applied since the decay-time acceptance introduced by the biasing trigger lines is explained in the next section. The decay-time acceptance is parameterised with the function

$$\text{PDF}(t) \propto (1 + \beta t + \gamma t^2). \qquad (10.2)$$

The fitted values of the β and γ parameters are reported in the figure. It is possible to see that the decay-time dependent acceptance is larger in 2012 data taking conditions with respect to 2011, as the γ parameter almost double.
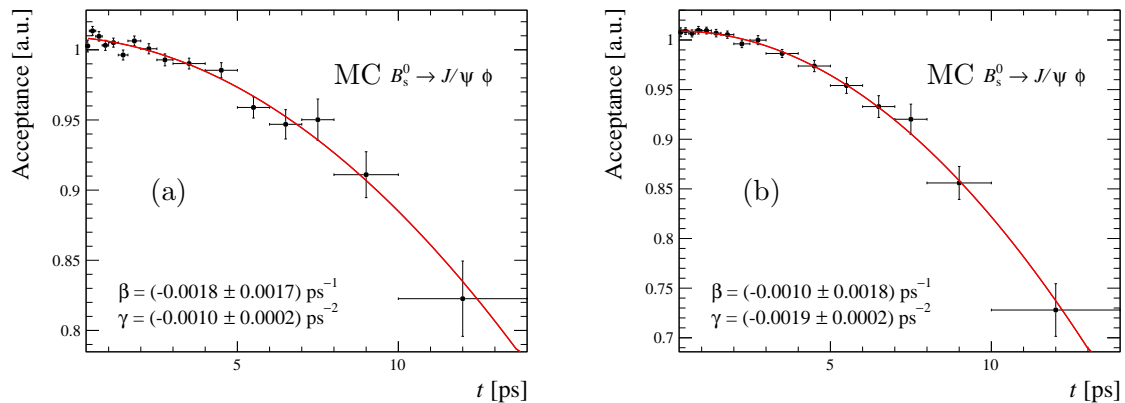
Figure 10.2: Decay-time acceptance obtained in simulated MC sample of the $B_s^0 \rightarrow J/\psi\phi$ signal candidates dividing the normalised decay-time distributions of reconstructed and selected candidates by the generated decay-time distribution, for (a) 2011 and (b) 2012 data taking conditions.

If a quadratic acceptance is considered, the correction of the decay width in Equation 10.1 becomes time-dependent and also $\Delta\Gamma_s$ is biased. This result is confirmed by Toy MC, since the residuals shown in the second and in the third column in Table 10.5, corresponding to a quadratic only ($\beta = 0$) or a quadratic decay-time acceptance, are significantly different from zero. The size of these biases is confirmed when fitting large simulated MC samples with 2011 and 2012 data taking conditions when no upper decay-time correction is included. In this case, since the effect is time-dependent, it is essential to include the correction for the decay-time acceptance directly in the fit using a similar strategy to that used to perform the b-hadrons lifetime measurements.

As explained in Section 6.3.2 the origin of this decay-time dependent acceptance is mainly due to the VELO-track reconstruction inefficiency at large B_s^0 decay time. Thus, the correction to this effect is evaluated using a similar procedure as the method developed for the $H_b \rightarrow J/\psi X$ lifetime measurements. Since different versions of the VELO track reconstruction algorithm have been used within the LHCb HLT1 software trigger in 2011 and 2012, as well as different data taking conditions, the efficiency is evaluated separately for the two years and for the on-line and off-line version of the algorithm. Figure 10.3 shows the VELO-track reconstruction efficiencies obtained in 2011 and 2012 data and Table 10.6 shows the corresponding fit results obtained using the parameterisation introduced in Equation 6.8. These results can be compared to those obtained with the 2011 data and the FASTVELO version v1r5, see Table 6.2. It can be seen that, despite some changes in the selection of the data, the on-line 2011 c parameters are in good agreement, which is expected since the FASTVELO version is the same. The 2011 off-line c parameter is instead half the corresponding value obtained with the old FASTVELO version. This is due to some improvements that have been build in the algorithm before the 2012 data taking period in order to partially recover the loss of VELO-track reconstruction efficiency for displaced tracks with large ρ. It

(a) On-line reconstruction 2011

(c) Off-line reconstruction 2011

(b) On-line reconstruction 2012

(d) Off-line reconstruction 2012
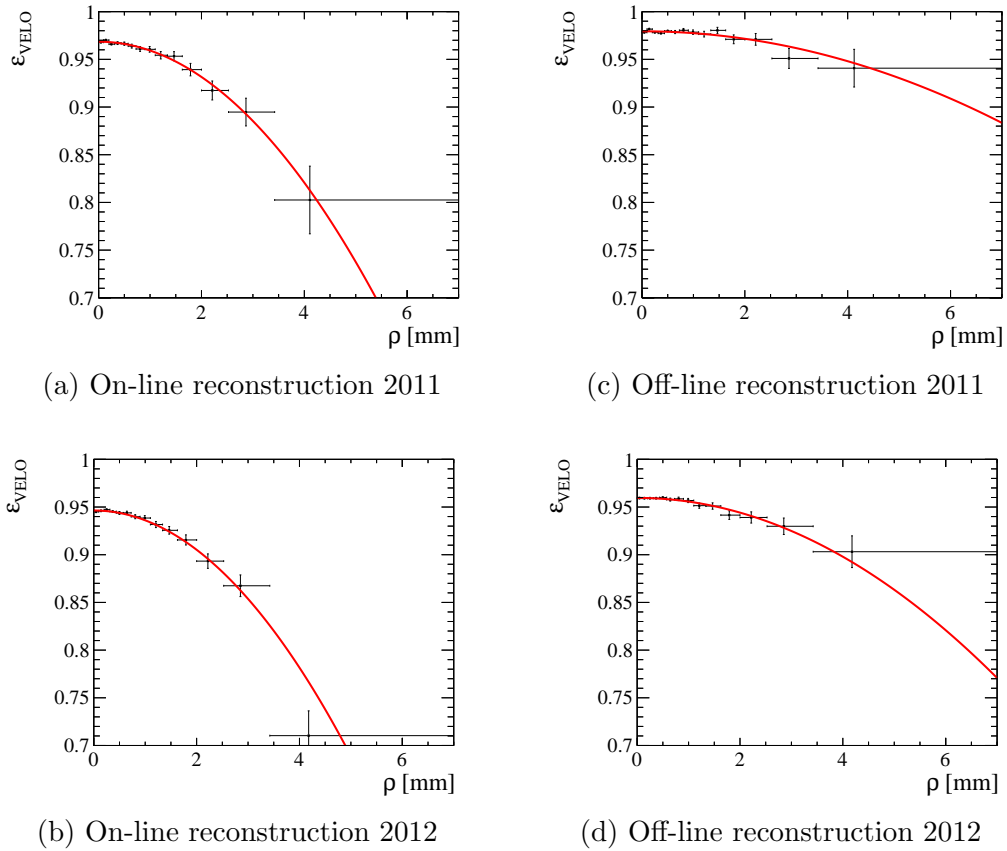
Figure 10.3: VELO-track reconstruction efficiency for kaon tracks reconstructed using the (a-b) on-line and (c-d) off-line algorithms as a function of the kaon displacement ρ, as defined in Equation 6.7. The red solid lines show the result of an unbinned maximum likelihood fit using the parameterisation in Equation 6.8 to the background subtracted data (black points). The top (bottom) plots show 2011 (2012) data.

was expected to get a similar improvement also for 2012 data. However, it can be seen that the on-line and off-line c parameters in 2012 data are similar to those obtained with the old FASTVELO version. This trend is confirmed by the Monte Carlo samples and it is seen as well in the worse decay-time acceptance shown in Figure 10.2 for the 2012 MC sample with respect to the 2011 sample.

One of the main reasons for this worse inefficiency in 2012 data is that the z position of the primary vertex is significantly shifted in 2012 data, where a mean of almost 25 mm is observed, with respect to 2011 data, where a shift of only 3 mm is observed. It can be seen in Figure 10.4 comparing the black (2012) and the red (2011) z_{PV} distributions. The same shift is also simulated in MC samples. Due to the absence of a fiducial region limiting the tails of the z_{PV} distribution, the reconstruction efficiency is significantly worse in 2012 data.

Another consequence of the absence of a fiducial region is that the correlation between the VELO-track reconstruction efficiencies of the different B_s^0 decay products is higher. These correlations are taken into account using a similar procedure to the
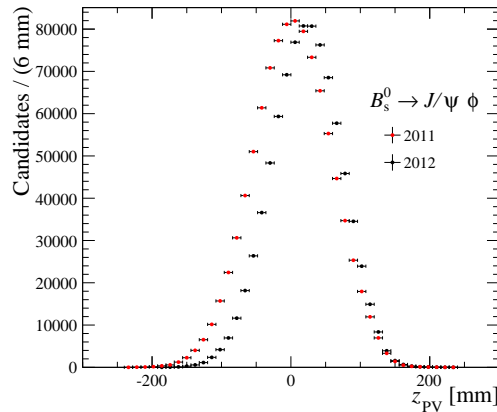
Figure 10.4: Distributions of the z-position of the PV, z_{PV}, from $B_s^0 \to J/\psi\phi$ events in 2011 (red points) and 2012 (black).

one described in Section 6.3.2.

The distortion to the decay-time distribution caused by the VELO-track reconstruction is corrected for by weighting each b-hadron candidate by the inverse of the product of the per-track efficiencies, similarly to the procedure followed in Section 6.3.2. In particular, since in most of the events both muon tracks are reconstructed using the on-line tracking algorithm that is used in the HLT1, the efficiency weight for each $B_s^0 \to J/\psi\phi$ candidate takes the form

$$w_{\mathrm{HLT1 \; unbiased}} = 1/\left(\varepsilon_{\mathrm{VELO,on-line}}^{\mu^+} \; \varepsilon_{\mathrm{VELO,on-line}}^{\mu^-} \; \varepsilon_{\mathrm{VELO,off-line}}^{K^+} \; \varepsilon_{\mathrm{VELO,off-line}}^{K^-}\right), \quad (10.3)$$

However, in this analysis there is a complication arising due to the fact that the trigger strategy is different with respect to the b-hadron lifetime measurements. In particular, the `Hlt1TrackMuon` line requires only one muon, instead of two, passing the trigger selection criteria to retain the corresponding event. The `Hlt1TrackAllL0` instead requires only one muon or one kaon to trigger the event. Overall, these two trigger lines increase the statistics of the sample by about 15% (20%) in 2011 (2012). However, the `Hlt1TrackAllL0` contributes with only 2%. In the data sample the information about which particle in the event, among the B_s^0 decay products, is responsible for the trigger is missing. Thus, the strategy for these two HLT1 lines is to consider that only the

Table 10.6: VELO reconstruction efficiency fitted parameters in data for kaon tracks reconstructed with the on-line and off-line algorithms in 2011 and 2012.

	a	$c \; [\mathrm{mm}^{-2}]$
On-line 2011	0.9685 ± 0.0006	-0.0096 ± 0.0008
Off-line 2011	0.9794 ± 0.0005	-0.0021 ± 0.0004
On-line 2012	0.9563 ± 0.0004	-0.0105 ± 0.0006
Off-line 2012	0.9721 ± 0.0004	-0.0036 ± 0.0004

muon with the highest transverse momentum is responsible for it and thus reconstructed using the on-line tracking algorithm that is used in the HLT1. In this case the weight is calculated as

$$w_{\text{HLT1 biased}} = 1/\left(\varepsilon_{\text{VELO,on-line}}^{\mu^{\text{high } \text{PT}}} \; \varepsilon_{\text{VELO,off-line}}^{\mu^{\text{low } \text{PT}}} \; \varepsilon_{\text{VELO,off-line}}^{K^{+}} \; \varepsilon_{\text{VELO,off-line}}^{K^{-}} \right). \quad (10.4)$$

This approach is tested in a simulated MC sample, as discussed in Section 10.4.3 and the difference of Γ_s and $\Delta\Gamma_s$ with respect to the generated value is considered as a systematic uncertainty.

10.4.2 Lower decay-time acceptance

The lower decay-time acceptance histograms are calculated separately for the two subsamples, HLT1 unbiased and HLT1 biased, rather than being split in a part describing the HLT1 and a part describing the HLT2 effects. The acceptances for both subsamples are determined with a completely data-driven technique and the procedure is discussed in the following.

The acceptance of the HLT1 unbiased sample is obtained using the same method described in Section 6.4. It exploits a limited size sample selected with a trigger line, (Hlt2DiMuonJPsi), that use the same selection, apart from the cut on the J/ψ flight distance significance. For the HLT1 biased sample, there is no corresponding reference line available. Therefore, the acceptance is determined by dividing the HLT1 biased decay-time distribution by the decay-time distribution of candidates that pass a fully decay-time independent trigger selection, HLT unbiased (Hlt1DiMuonHighMass and Hlt2DiMuonJPsi)

$$\text{Acceptance (t)} = \frac{\text{HLT1 biased events}}{\text{HLT unbiased}}. \quad (10.5)$$

The decay-time acceptance histograms are shown in Figure 10.5. Note that the y-axis of the acceptance histograms is given in arbitrary units. Since the data taking conditions are different between 2011 and 2012, like a different number of PVs or track multiplicity, they are determined separately for the two years. A significant acceptance drop for low decay time is visible for the HLT1 biased sample, reflecting the effects of the IP requirements in the trigger selection.

10.4.3 Validation of the decay-time acceptance corrections

The lower decay-time acceptance is accounted for by including a parameterisation of the trigger acceptance shown in Figure 10.5 in the fit to the decay-time and angular distributions. The upper decay-time acceptance is corrected event by event in the fit with the VELO-track reconstruction efficiency weights derived in Section 10.4.1. In order to validate these data-driven techniques, the fitted values of Γ_s and $\Delta\Gamma_s$, obtained in the MC sample after these decay-time acceptance corrections are included in the fit, are compared with the generated value. Due to the absence of a fiducial region and the presence of some selection requirements that introduce a decay-time dependent acceptance, a small remaining lifetime bias is expected. Thus, the result of this validation procedure on the MC sample is used to assign a systematic uncertainty to the correction technique. In Table 10.7 the results of fits to the MC sample using the
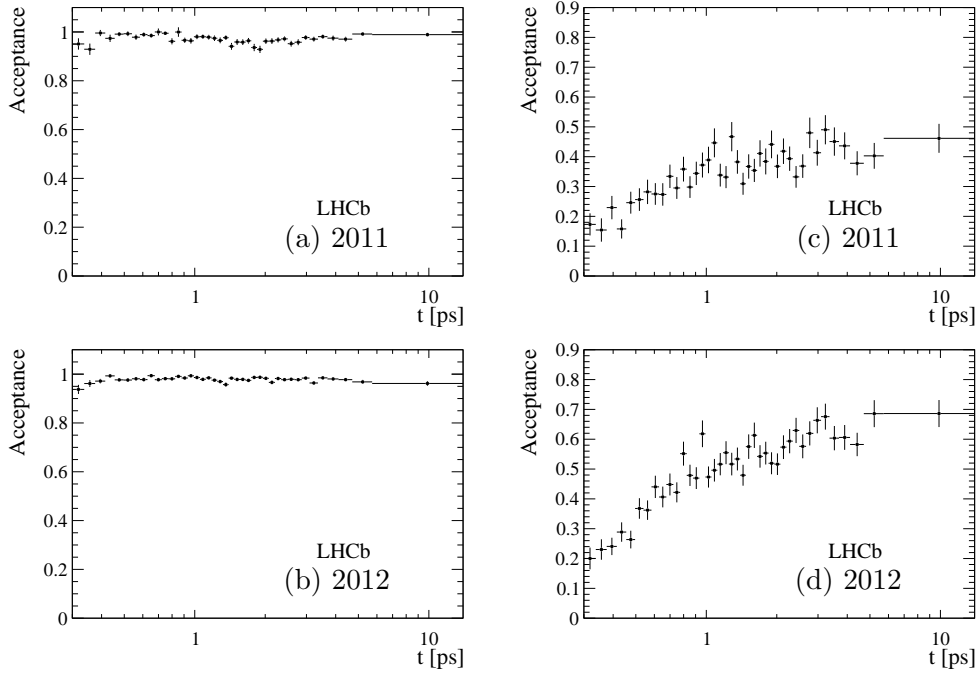
Figure 10.5: B_s^0 decay time acceptances determined for (a-b) HLT1 unbiased events and for (c-d) HLT1 biased events. The top (bottom) plots show 2011 (2012) data.

HLT1 unbiased sample only and the whole sample are shown. In the second column, the pull on the corresponding parameter θ, defined as $(\theta_{\mathrm{fit}} - \theta_{\mathrm{generated}})/\sigma_{\theta_{\mathrm{fit}}}$, is shown. In the third column, the corresponding expected pull on data is reported, obtained from the MC one by scaling the statistical uncertainty accordingly. It is possible to see that the bias on Γ_s get worse when fitting the whole sample, due to the non-perfect procedure used to correct for the HLT1 biased sample. On the contrary, the bias on $\Delta\Gamma_s$ is partially compensated by the bias introduced when fitting the HLT1 biased sample such that the bias obtained fitting the whole sample is smaller. However, since these fit results are used to assign a systematic uncertainty on the correction procedure, in order to take into account possible differences between MC samples and data, the largest of these discrepancies is considered. So this procedure results in a systematic uncertainty equal to 32% of the statistical uncertainty for $\Delta\Gamma_s$ and a systematic uncertainty equal to 26% of the statistical uncertainty for Γ_s.

10.5   Results

The Γ_s and $\Delta\Gamma_s$ measurements are performed by factorising the fit process into two independent fits [113]. First, a fit to the B_s^0 invariant mass distribution is perfomed, and the yield of $B_s^0 \to J/\psi\phi$ signal candidates is measured to be 95690 ± 350. It is used to determine the signal and background probabilities of each candidate [104]. By using the signal probability, the $B_s^0 \to J/\psi\phi$ signal decay-time and helicity-angle distributions are isolated. These distributions are shown in Figure 10.6, together with the one-dimensional projections of the fit superimposed. The differently dashed lines

Table 10.7: *Results from a fit to the decay-time and angular distribution in simulated* $B_s^0 \to J/\psi\phi$ *signal events using the whole sample or the HLT1 unbiased sample only. The residual pull of each parameter with respect to the MC generated value is also shown, using both the MC (second column) and data (third column) statistical uncertainties.*

Trigger	Parameter	Value	Pull MC	Expected pull data
HLT1 unbiased	Γ_s	0.66496 ± 0.00032	-1.1	-0.16
	$\Delta\Gamma_s$	0.08877 ± 0.00099	-3.0	-0.32
All HLT1	Γ_s	0.66471 ± 0.00028	-2.5	-0.26
	$\Delta\Gamma_s$	0.09000 ± 0.00088	-1.9	-0.18

show the different final state components: *CP*-even, *CP*-odd and S-wave.

As already introduced in Section 1.5.3, Γ_L is mainly determined by the *CP*-even component and Γ_H by the *CP*-odd component. Looking at the decay-time fit projections for the *CP*-even and *CP*-odd components in Figure 10.6, it is possible to see that the slopes of the decay-time distributions are different. Thus, a value of $\Delta\Gamma_s$ different from zero is expected. The values of the decay width difference, $\Delta\Gamma_s$, and the average decay width, Γ_s, in the B_s^0 system extracted from the fit are

$$\begin{aligned} \Delta\Gamma_s &= 0.0805 \pm 0.0091\,\mathrm{ps}^{-1}, \\ \Gamma_s &= 0.6603 \pm 0.0027\,\mathrm{ps}^{-1}. \end{aligned}$$

Here the uncertainty is the statistical only. The systematic uncertainties are listed in Table 10.8. The majority of them is evaluated using a similar approach to the one used to evaluate the systematic uncertainties on the *b*-hadron lifetimes. One difference is the uncertainty due to the residual bias found in simulated MC samples, evaluated following the procedure described in Section 10.4.3. This contribution replaces the one due to the simulated sample size, since the bias found is significant with respect to the statistical uncertainty of the simulated sample. Moreover, there is an additional contribution due to the procedure used to correct for the angular-dependent acceptance. Since the acceptance is taken from simulated samples, a systematic uncertainty is assigned to take into account differences between data and simulated samples and due to the limited size of the simulated sample itself. Overall, the systematic uncertainties for Γ_s and $\Delta\Gamma_s$ are dominated by the decay-time acceptance correction. Nevertheless, they are still small compared to the statistical uncertainty.

10.6 Summary

The essential information of this chapter is briefly summarised here.

- The decay width difference, $\Delta\Gamma_s$, and the average decay width, Γ_s, in the B_s^0 system are extracted from a fit to the measured decay-time and angular distributions of the reconstructed $B_s^0 \to J/\psi\phi$ decays.

- The decay-time dependent acceptance introduce a significant bias in the values of $\Delta\Gamma_s$ and Γ_s which have to be taken into account.
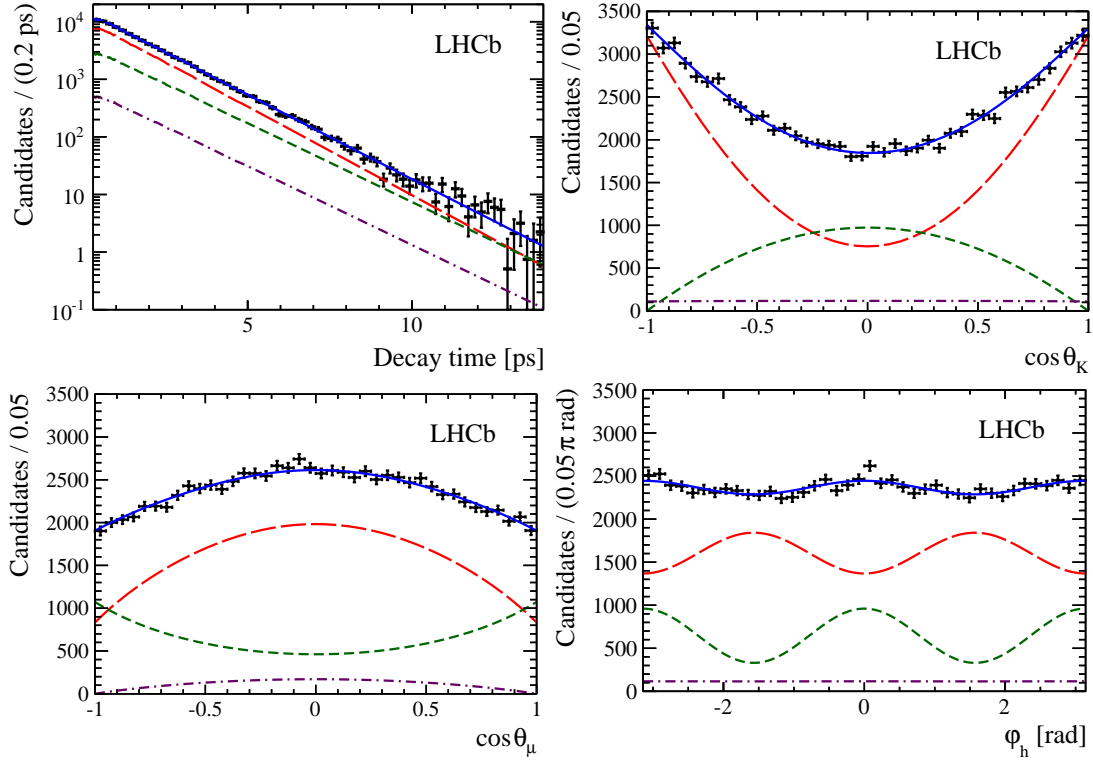
Figure 10.6:   Decay-time and helicity-angle distributions of $B_s^0 \to J/\psi\phi$ decays (data points) with the one-dimensional projections of the fit superimposed. The solid blue line shows the total signal contribution, which is composed of CP-even (long-dashed red), CP-odd (short-dashed green) and S-wave (dotted-dashed purple) contributions. Figure taken from Ref. [113]

Table 10.8: Statistical and systematic uncertainties for Γ_s and $\Delta\Gamma_s$. The total systematic uncertainty is obtained by combining the individual contributions in quadrature.

Source	Γ_s [ps^{-1}]	$\Delta\Gamma_s$ [ps^{-1}]
Statistical uncertainty	0.0027	0.0091
VELO reconstruction	0.0005	0.0002
Residual bias in simulation	0.0007	0.0029
Mass factorisation	–	0.0007
Trigger efficiency	0.0011	0.0009
Background and mass modelling	0.0001	0.0008
Peaking background	0.0005	0.0004
LHCb length scale	0.0002	–
Angular efficiency	0.0001	0.0002
Total systematic	0.0015	0.0033

- The $B_s^0 \to J/\psi\phi$ selection criteria are optimised to maximise the sensitivity on the CP violating phase, ϕ_s, which is also extracted in this analysis. This implies that some selection requirements that have been used in order to perform the b-hadron lifetime measurements are not suitable for this analysis. This introduces a larger bias on $\Delta\Gamma_s$ and Γ_s.

- The main origin of the decay-time acceptance is due to the VELO reconstruction inefficiency for largely displaced tracks. It is corrected using a per event weight, as described in Section 10.4.1, while the trigger acceptance is corrected by taking into account a parameterisation of the time-dependent trigger acceptance in the fit, see Section 10.4.2.

- The correction procedure is validated on a large simulated sample and the remaining bias is taken as a systematic uncertainty.

- The values of $\Delta\Gamma_s$ and Γ_s are measured to be $\Delta\Gamma_s = 0.0805 \pm 0.0091 \pm 0.0033\,\mathrm{ps}^{-1}$ and $\Gamma_s = 0.6603 \pm 0.0027 \pm 0.0015\,\mathrm{ps}^{-1}$.

Part IV

Conclusion

11

Results and conclusion

The gratification comes in the doing, not in the results.

— James Dean

In this thesis the analysis developed to measure the lifetime of several b hadrons, namely the B^+, B^0, B_s^0 mesons and the Λ_b^0 baryon has been presented. The data sample collected by the LHCb detector in 2011 has been used, corresponding to an integrated luminosity of 1 fb^{-1}. The different b-hadrons decay modes that were chosen have a J/ψ in the final state and have been triggered and selected in a uniform way. The main challenge of this work consisted in the understanding and controlling of the different decay-time acceptance effects introduced in different stages of the analysis. These effects were found to be related to the geometrical detector acceptance and to the reconstruction and selection efficiencies that depend upon the b-hadron decay time. The main contribution is coming from the decay-time dependent efficiency to reconstruct particle tracks in the vertex detector and several data-driven techniques have been developed to remove these effects.

The measured b-hadron lifetimes are

$$
\begin{aligned}
\tau_{B^+\to J/\psi K^+} &= 1.637 \pm 0.004 \text{ (stat.)} \pm 0.003 \text{ (syst.)} \text{ ps,} \\
\tau_{B^0\to J/\psi K^{*0}} &= 1.524 \pm 0.006 \text{ (stat.)} \pm 0.004 \text{ (syst.)} \text{ ps,} \\
\tau_{B^0\to J/\psi K_S^0} &= 1.499 \pm 0.013 \text{ (stat.)} \pm 0.005 \text{ (syst.)} \text{ ps,} \\
\tau_{\Lambda_b^0\to J/\psi \Lambda} &= 1.415 \pm 0.027 \text{ (stat.)} \pm 0.006 \text{ (syst.)} \text{ ps,} \\
\tau_{B_s^0\to J/\psi \phi} &= 1.480 \pm 0.011 \text{ (stat.)} \pm 0.005 \text{ (syst.)} \text{ ps.}
\end{aligned}
$$

Due to the non-negligible value of $\Delta\Gamma_s$, it is important to note that the B_s^0 lifetime measurement listed above is the B_s^0 effective lifetime in the $B_s^0 \to J/\psi\phi$ final state.

These lifetimes were used to determine several lifetime ratios. They represent an important test of the validity of the theoretical tool used to determine several b-hadrons observables, the heavy quark expansion (HQE). Ratios of b-hadron lifetimes can be theoretically predicted with higher accuracy than absolute lifetimes since many terms in the HQE and their potential uncertainties cancel. The ratios of the B^+ and Λ_b^0 lifetimes

and B_s^0 effective lifetime to the B^0 lifetime in the flavour-specific $B^0 \to J/\psi K^{*0}$ channel are measured to be

$$
\begin{aligned}
\tau_{B^+}/\tau_{B^0 \to J/\psi K^{*0}} &= 1.074 \pm 0.005 \text{ (stat.)} \pm 0.003 \text{ (syst.)}, \\
\tau_{B_s^0 \to J/\psi \phi}/\tau_{B^0 \to J/\psi K^{*0}} &= 0.971 \pm 0.009 \text{ (stat.)} \pm 0.004 \text{ (syst.)}, \\
\tau_{\Lambda_b^0}/\tau_{B^0 \to J/\psi K^{*0}} &= 0.929 \pm 0.018 \text{ (stat.)} \pm 0.004 \text{ (syst.)}.
\end{aligned}
$$

Furthermore, the ratios τ_{B^+}/τ_{B^-}, $\tau_{\Lambda_b^0}/\tau_{\overline{\Lambda}_b^0}$ and $\tau_{B^0 \to J/\psi K^{*0}}/\tau_{\overline{B}^0 \to J/\psi \overline{K}^{*0}}$ have been measured. These ratios are a test of the CPT theorem that foresees the same lifetime for a particle and the corresponding antiparticle. They are measured to be

$$
\begin{aligned}
\tau_{B^+}/\tau_{B^-} &= 1.002 \pm 0.004 \text{ (stat.)} \pm 0.002 \text{ (syst.)}, \\
\tau_{\Lambda_b^0}/\tau_{\overline{\Lambda}_b^0} &= 0.940 \pm 0.035 \text{ (stat.)} \pm 0.006 \text{ (syst.)}, \\
\tau_{B^0 \to J/\psi K^{*0}}/\tau_{\overline{B}^0 \to J/\psi \overline{K}^{*0}} &= 1.000 \pm 0.008 \text{ (stat.)} \pm 0.009 \text{ (syst.)}.
\end{aligned}
$$

The effective lifetimes of $B^0 \to J/\psi K^{*0}$ and $B^0 \to J/\psi K_S^0$ decays were used to derive a measurement of $\Delta\Gamma_d/\Gamma_d$

$$
\frac{\Delta\Gamma_d}{\Gamma_d} = -0.044 \pm 0.025 \text{ (stat.)} \pm 0.011 \text{ (syst.)}. \tag{11.1}
$$

Finally, the techniques developed to correct the decay-time dependent acceptance in order to perform the b-hadrons lifetime measurements were used to obtain a measurement of the average decay width, Γ_s, and the decay width difference, $\Delta\Gamma_s$, in the B_s^0 system. To this scope, a time-dependent angular fit of $B_s^0 \to J/\psi \phi$ decays has been used, where the corrections for the different lifetime biasing effects have been included. Using the full data sample recorded by the LHCb detector in 2011 and 2012, corresponding to an integrated luminosity of 3 fb^{-1}, they are measured to be

$$
\begin{aligned}
\Delta\Gamma_s &= 0.0805 \pm 0.0091 \text{ (stat.)} \pm 0.0033 \text{ (syst.)} \text{ ps}^{-1}, \\
\Gamma_s &= 0.6603 \pm 0.0027 \text{ (stat.)} \pm 0.0015 \text{ (syst.)} \text{ ps}^{-1}.
\end{aligned}
$$

All the results presented in this thesis are summarised in Table 11.1. Here, the values measured within this work are shown together with the updated world average as given by the Heavy Flavour Averaging Group (HFAG) [2], which includes all the measurements up to Fall 2014. The theoretical predictions, introduced in Section 1.6.4, are given as well. With the exception of the $\Lambda_b^0 \to J/\psi \Lambda$ channel, these are the single most precise measurements of the b-hadron lifetimes. All the lifetime results are compatible with previous world averages, see Table 1.6. The reported $\tau_{\Lambda_b^0 \to J/\psi \Lambda}$ is smaller by approximately 2σ than another measurement performed by the LHCb collaboration [114], which has been published in the course of this thesis work. This measurement exploits the full LHCb dataset and a decay channel, $\Lambda_b^0 \to J/\psi p K^-$, which provides a larger number of events with respect to the one used in this thesis. This Λ_b^0 decay mode was first seen by LHCb [115]. The Λ_b^0 baryon lifetime is determined from a relative measurement with respect to the well-known B^0 lifetime and it is measured to be $\tau_{\Lambda_b^0} = 1.479 \pm 0.009 \text{ (stat.)} \pm 0.010 \text{ (syst.)}$ ps. This is the most precise measurement to date. The average between this LHCb measurement and the one

Table 11.1: *Results obtained in this work, updated world average values [2] and theoretical predictions [1,39,40,42,44,47,48] for b-hadron lifetimes, lifetime ratios and decay width in the B_s^0 and in the B^0 system, $\Delta\Gamma_s$ and $\Delta\Gamma_d/\Gamma_d$. The uncertainty of the results presented in this work is obtained by combining the statistical and systematic contributions in quadrature.*

| Observable	This work	New world average	Prediction
τ_{B^+} [ps]	1.637 ± 0.005	1.638 ± 0.004	-
τ_{B^0} [ps]	1.524 ± 0.007	1.520 ± 0.004	-
$\tau_{B_s^0}$ [ps]	1.514 ± 0.007	1.509 ± 0.004	-
$\tau_{B_s^0 \to J/\psi\phi}$ [ps]	1.480 ± 0.012	1.429 ± 0.088	-
$\tau_{\Lambda_b^0}$ [ps]	1.415 ± 0.028	1.467 ± 0.010	-
τ_{B^+}/τ_{B^-}	1.002 ± 0.004	-	1
$\tau_{\Lambda_b^0}/\tau_{\overline{\Lambda}_b^0}$	0.940 ± 0.036	-	1
$\tau_{B^0 \to J/\psi K^{*0}}/\tau_{\overline{B}^0 \to J/\psi \overline{K}^{*0}}$	1.000 ± 0.012	-	1
τ_{B^+}/τ_{B^0}	1.074 ± 0.006	1.076 ± 0.004	1.01-1.11
$\tau_{B_s^0}/\tau_{B^0}$	0.994 ± 0.007	0.993 ± 0.004	0.99-1.01
$\tau_{\Lambda_b^0}/\tau_{B^0}$	0.929 ± 0.018	0.965 ± 0.007	0.86 - 1.01
$\Delta\Gamma_s$ [ps^{-1}]	0.0805 ± 0.0097	0.077 ± 0.007	0.087 ± 0.021
$\Delta\Gamma_d/\Gamma_d$	-0.044 ± 0.027	0.001 ± 0.010	(0.0042 ± 0.0008)
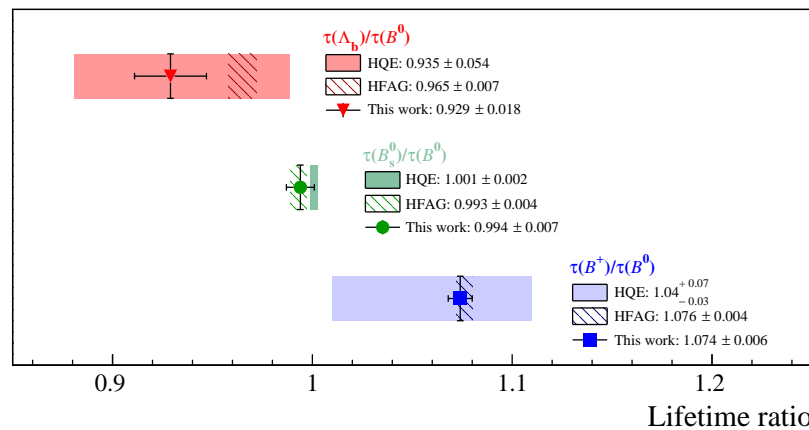
Figure 11.1: *Status of the experimental results obtained in this work, updated world average values from HFAG [2] and HQE theoretical predictions [1] for the ratios of b-hadron lifetimes.*
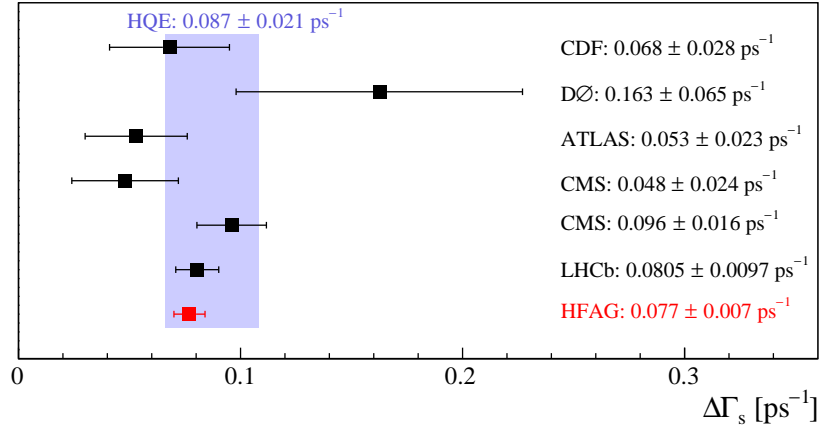
Figure 11.2: Overview of the status of the experimental results for $\Delta\Gamma_s$, updated world average values from HFAG [2] and HQE [1] theoretical predictions.

presented in this thesis is $\tau^{\text{LHCb}}_{\Lambda^0_b} = 1.468 \pm 0.009\,(\text{stat.}) \pm 0.008\,(\text{syst.})$ ps.

All lifetime ratios are consistent with HQE predictions [1, 39, 40] and contributed significantly to reduce the uncertainty of the updated world averages [2]. The current status is shown in Figure 11.1 where a comparison of the experimental results presented in this thesis, updated world averages [2] and HQE predictions [1] is visible. It is possible to see that in most cases the HQE predictions are significantly less precise than the experimental results, strongly limited by a lack of up-to-date values of some matrix elements determined from lattice QCD calculations that are used in the HQE [116, 117]. One of the greater improvements achieved in this work is due to the precise determination of the average B^0_s lifetime, $\tau_{B^0_s} \equiv 1/\Gamma_s = 1.514 \pm 0.006\,(\text{stat.}) \pm 0.003\,(\text{syst.})$ ps, and of the B^0 lifetime. They are used to determine the $\tau_{B^0_s}/\tau_{B^0}$ ratio. This is the ratio where the most precise theoretical predictions are available and so it is of great importance to reduce the experimental uncertainty.

Concerning the second set of lifetime ratios, τ_{B^+}/τ_{B^-}, $\tau_{\Lambda^0_b}/\tau_{\overline{\Lambda}^0_b}$ and $\tau_{B^0 \to J/\psi K^{*0}}/\tau_{\overline{B}^0 \to J/\psi \overline{K}^{*0}}$, no significant deviation from unity is observed. Even if these results are significantly less precise than other measurements performed to test the validity of the *CPT* theorem, see Section 1.2, it is important to test its validity in different systems.

An overview of the current measurements of $\Delta\Gamma_s$ performed at CDF [56], DØ [57], ATLAS [55], CMS [118] and in this work (LHCb) is shown in Figure 11.2. The value of $\Delta\Gamma_s$ presented in this thesis represents the most precise determination of this observable. The updated world average shows a very good agreement with the HQE prediction [1]. This is a very important test since it confirms the convergence of the perturbative expansion developed in the HQE. However, it is possible to see that the experimental results are now more precise than the theoretical predictions.

The measurement of $\Delta\Gamma_d/\Gamma_d$ presented in this thesis represents the first attempt of the LHCb collaboration to measure this quantity. The most precise measurement up-to-date has been performed by the DØ collaboration and it is $\Delta\Gamma_d/\Gamma_d = (0.50 \pm 1.38) \cdot 10^{-2}$ [61]. It represent the major contribution to the current world average value. Nevertheless, the measurement presented in this thesis is still strongly statistically limited and in the near future it can be improved by analysing additionally the LHCb dataset collected in 2012.

To conclude, this analysis is significant due to the impact of the results obtained and at the same time it is an important benchmark of the LHCb detector understanding. The methods and tools developed are of importance for many other lifetime and decay-time dependent analyses.

Part V

Appendices

$\mathcal{A}$

Legend of the analysis step plots

In this Appendix the different analysis steps used in Figure 6.3 and Figure 6.4, representing the measured lifetime in simulated Monte Carlo samples as a function of the different reconstruction, selection and trigger requirements used in the analysis, is explained. Differences in the selection introduced in order to correct a decay-time biasing requirement are highlited in bold.

A.1 $B^+ \to J/\psi K^+$ decay channel

0. All particles within LHCb geometrical acceptance.

1. Muons $p_T > 550\,\text{MeV}/c$, kaon $p_T > 1\,\text{GeV}/c$ and $p > 10\,\text{GeV}/c$. **All final state particles: $2 < \eta < 4.5$, $|z_{\mathbf{PV}}| < 100\,\text{mm}$.**

2. All final state particles tracks are reconstructible as VELO tracks.

3. All final state particles tracks are reconstructible as Long tracks.

4. All final state particles tracks are reconstructed as VELO tracks **(Per-event weight to correct for the VELO inefficiency)**.

5. All final state particles tracks are reconstructed as Long tracks.

6. All final state particles $\chi^2_{\text{track}}/nDoF < 4$.

7. $\chi^2_{\text{vtx}}/\text{nDoF}(J/\psi) < 16$, $m(\mu^+\mu^-) \in [3030,\ 3150]\,\text{MeV}/c^2$, $\Delta\ln\mathcal{L}_{\mu\pi}(\mu^\pm) > 0$.

8. $\Delta\ln\mathcal{L}_{K\pi}(K^\pm) > 0$.

9. -.

10. B^+: $\chi^2_{\text{IP}} < 25$, **new PV reconstruction**.

11. B^+: $\chi^2_{\text{DTF}}/\text{nDoF} < 5$.

12. B^+: $\chi^2_{\text{IP,next PV}} > 50$.

13. L0 triggered.

14. `HLT1DiMuonHighMass`(DEC) **(TOS)** triggered.

15. `HLT2DiMuonJPsi` triggered.

16. $J/\psi \ FDS > 3$ stripping requirement, **Correction for the decay-time dependent inefficiency introduced in the fit**.

17. `HLT2DiMuonDetachedJPsi` triggered, **Correction for the decay-time dependent inefficiency introduced in the fit**.

A.2 $B^0 \to J/\psi K^{*0}$ decay channel

0. All particles within LHCb geometrical acceptance.

1. Muons $p_T > 550\,\mathrm{MeV}/c$, kaon and pion $p_T > 300\,\mathrm{MeV}/c$. **All final state particles: $2 < \eta < 4.5$, $|z_{\mathrm{PV}}| < 100\,\mathrm{mm}$**.

2. All final state particles tracks are reconstructible as VELO tracks.

3. All final state particles tracks are reconstructible as Long tracks.

4. All final state particles tracks are reconstructed as VELO tracks (**Per-event weight to correct for the VELO inefficiency**).

5. All final state particles tracks are reconstructed as Long tracks.

6. All final state particles $\chi^2_{\mathrm{track}}/nDoF < 4$.

7. $\chi^2_{\mathrm{vtx}}/\mathrm{nDoF}(J/\psi) < 16$, $m(\mu^+\mu^-) \in [3030, 3150]\,\mathrm{MeV}/c^2$, $\Delta\ln\mathcal{L}_{\mu\pi}(\mu^\pm) > 0$.

8. $\Delta\ln\mathcal{L}_{K\pi}(K^\pm) > 0$, $\Delta\ln\mathcal{L}_{K\pi}(\pi^\pm) < 0$, $p_T(K^{*0}) > 1.5\,\mathrm{GeV}/c$ and $m(K^+\pi^-) \in [826, 966]\,\mathrm{MeV}/c^2$.

9. $\chi^2_{\mathrm{vtx}}/nDoF(K^{*0}) < 16$ (**removed**).

10. B^0: $\chi^2_{\mathrm{IP}} < 25$, **new PV reconstruction**.

11. B^0: $\chi^2_{\mathrm{DTF}}/\mathrm{nDoF} < 5$ and $\chi^2_{\mathrm{vtx}}/nDoF < 10$ (**removed**).

12. B^0: $\chi^2_{\mathrm{IP,next\ PV}} > 50$.

13. L0 triggered.

14. `HLT1DiMuonHighMass`(DEC) (**TOS**) triggered.

15. `HLT2DiMuonJPsi` triggered.

16. $J/\psi \ FDS > 3$ stripping requirement, **Correction for the decay-time dependent inefficiency introduced in the fit**.

17. `HLT2DiMuonDetachedJPsi` triggered, **Correction for the decay-time dependent inefficiency introduced in the fit**.

A.3 $B_s^0 \to J/\psi\phi$ decay channel

0. All particles within LHCb geometrical acceptance.

1. Muons $p_T > 550\,\mathrm{MeV}/c$, kaon $p_T > 250\,\mathrm{MeV}/c$. **All final state particles: $2 < \eta < 4.5$, $|z_{\mathrm{PV}}| < 100\,\mathrm{mm}$**.

2. All final state particles tracks are reconstructible as VELO tracks.

3. All final state particles tracks are reconstructible as Long tracks.

4. All final state particles tracks are reconstructed as VELO tracks (**Per-event weight to correct for the VELO inefficiency**).

5. All final state particles tracks are reconstructed as Long tracks.

6. All final state particles $\chi^2_{\text{track}}/nDoF < 4$.

7. $\chi^2_{\text{vtx}}/\text{nDoF}(J/\psi) < 16$, $m(\mu^+\mu^-) \in [3030, 3150]\,\text{MeV}/c^2$, $\Delta\ln\mathcal{L}_{\mu\pi}(\mu^\pm) > 0$.

8. $\Delta\ln\mathcal{L}_{K\pi}(K^\pm) > 0$, $p_T(\phi) > 1\,\text{GeV}/c$ and $m(K^+K^-) \in [1008, 1032]\,\text{MeV}/c^2$.

9. $\chi^2_{\text{vtx}}/nDoF(\phi) < 16$ (**removed**).

10. B^0_s: $\chi^2_{\text{IP}} < 25$, **new PV reconstruction**.

11. B^0_s: $\chi^2_{\text{DTF}}/\text{nDoF} < 5$ and $\chi^2_{\text{vtx}}/\text{nDoF} < 10$ (**removed**).

12. B^0_s: $\chi^2_{\text{IP,next PV}} > 50$.

13. L0 triggered.

14. `HLT1DiMuonHighMass`(DEC) (**TOS**) triggered.

15. `HLT2DiMuonJPsi` triggered.

16. $J/\psi\ FDS > 3$ stripping requirement, **Correction for the decay-time dependent inefficiency introduced in the fit**.

17. `HLT2DiMuonDetachedJPsi` triggered, **Correction for the decay-time dependent inefficiency introduced in the fit**.

A.4 $B^0 \to J/\psi K^0_S$ decay channel

0. All particles within LHCb geometrical acceptance.

1. Muons $p_T > 550\,\text{MeV}/c$, pion $p_T > 250\,\text{MeV}/c$ and pions $p > 2\,\text{GeV}/c$. **All particles: $2 < \eta < 4.5$, $|z_{\text{PV}}| < 75\,\text{mm}$**.

2. Muon tracks are reconstructible as VELO tracks.

3. Pion tracks are reconstructible as TT tracks.

4. Muon tracks are reconstructible as Long tracks and pion tracks are reconstructible as Downstream tracks.

5. Muon tracks are reconstructed as VELO tracks (**Per-event weight to correct for the VELO inefficiency**).

6. Muon tracks are reconstructed as Long tracks and pion tracks are reconstructed as Downstream tracks.

7. $\chi^2_{\text{vtx}}/nDoF(K^0_S) < 16$ (**25**).

8. $\chi^2_{\text{vtx}}/nDoF(J/\psi) < 16$.

9. All final state particles $\chi^2_{\text{track}}/nDoF < 4$.

10. FDS wrt B^0 vtx $(K_S^0) > 3$.

11. $p_T(K_S^0) > 1\,\mathrm{GeV}/c$ and $|m(\pi\pi) - m(K_S^0)| < 15\,\mathrm{MeV}/c^2$.

12. $m(\mu^+\mu^-) \in [3030, 3150]\,\mathrm{MeV}/c^2$ and $\Delta\ln\mathcal{L}_{\mu\pi}(\mu^\pm) > 0$.

13. B^0: $\chi^2_{\mathrm{vts}} < 10$ **(25)**.

14. B^0: $\chi^2_{\mathrm{DTF}}/\mathrm{nDoF} < 5$ and $\chi^2_{\mathrm{IP}} < 25$, **new PV reconstruction**.

15. B^0: $\chi^2_{\mathrm{IP,next\ PV}} > 50$.

16. L0 triggered.

17. `HLT1DiMuonHighMass`(TOS).

18. `HLT2DiMuonJPsi` triggered.

19. $J/\psi\ FDS > 3$ stripping requirement, **Correction for the decay-time dependent inefficiency introduced in the fit**.

20. `HLT2DiMuonDetachedJPsi` triggered, **Correction for the decay-time dependent inefficiency introduced in the fit**.

A.5 $\Lambda_b^0 \to J/\psi\Lambda$ decay channel

0. All particles within LHCb geometrical acceptance.

1. Muons $p_T > 550\,\mathrm{MeV}/c$, proton $p_T > 500\,\mathrm{MeV}/c$, pions $p_T > 100\,\mathrm{MeV}/c$ and protons and pions $p > 2\,\mathrm{GeV}/c$. **All particles: $2 < \eta < 4.5$, $|z_{\mathbf{PV}}| < 75\,\mathrm{mm}$**.

2. Muon tracks are reconstructible as VELO tracks.

3. Proton and pions tracks are reconstructible as TT tracks.

4. Muon tracks are reconstructible as Long tracks, proton and pion tracks are reconstructible as Downstream tracks.

5. Muon tracks are reconstructed as VELO tracks **(Per-event weight to correct for the VELO inefficiency)**.

6. Muon tracks are reconstructed as Long tracks, proton and pion tracks are reconstructed as Downstream tracks.

7. $\chi^2_{\mathrm{vtx}}/nDoF(\Lambda) < 16$ **(25)**.

8. $\chi^2_{\mathrm{vtx}}/\mathrm{nDoF}(J/\psi) < 16$.

9. All final state particles $\chi^2_{\mathrm{track}}/nDoF < 4$.

10. FDS wrt Λ_b^0 vtx $(\Lambda) > 3$.

11. $p_T(\Lambda) > 1\,\mathrm{GeV}/c$ and $|m(p\pi) - m(\Lambda)| < 6\,\mathrm{MeV}/c^2$.

12. $m(\mu^+\mu^-) \in [3030, 3150]\,\mathrm{MeV}/c^2$ and $\Delta\ln\mathcal{L}_{\mu\pi}(\mu^\pm) > 0$.

13. Λ_b^0: $\chi^2_{\mathrm{vts}} < 10$ **(25)**.

14. Λ_b^0: $\chi^2_{\mathrm{DTF}}/\mathrm{nDoF} < 5$ and $\chi^2_{\mathrm{IP}} < 25$, **new PV reconstruction**.

15. Λ_b^0: $\chi^2_{\mathrm{IP,next\ PV}} > 50$.

16. L0 triggered.

17. `HLT1DiMuonHighMass`(TOS).

18. `HLT2DiMuonJPsi` triggered.

19. $J/\psi\ FDS > 3$ stripping requirement, **Correction for the decay-time dependent inefficiency introduced in the fit**.

20. `HLT2DiMuonDetachedJPsi` triggered, **Correction for the decay-time dependent inefficiency introduced in the fit**.

Alternative fit technique

The so-called *sPlot* technique [119] is a method that allows to unfold the contributions of signal and background events to the distribution of a given variable, x. To this scope a so-called discriminating variable, y, is used, for which the signal and the background distributions are known. This latter variable must be independent from x. In the context of this thesis, the control variable x is represented by the b-hadron decay time, t, and the discriminating variable is represented by the b-hadron mass, m.

By means of a fit to the b-hadron mass distribution, as explained in Section 5.6, it is possible to obtain estimates of $f_{\mathrm{s}}(m)$ and $f_{\mathrm{b}}(m)$, the normalised functions describing the signal and the background distributions, respectively. Given that N_{s} and N_{b} are the yields of the signal and the background contributions obtained from the fit to the b-hadron mass, a weight function for the signal component, $W_{\mathrm{s}}(m)$, can be defined by

$$W_{\mathrm{s}}(m) = \frac{V_{ss} f_{\mathrm{s}}(m) + V_{sb} f_{\mathrm{b}}(m)}{N_{\mathrm{s}} f_{\mathrm{s}}(m) + N_{\mathrm{b}} f_{\mathrm{b}}(m)} \quad , \tag{B.1}$$

where V_{ss} and V_{sb} are calculated as the inverse of the matrix V_{ij} defined by

$$V_{ij}^{-1} = \sum_{e=1}^{N} \frac{f_{\mathrm{i}}(m_e) f_{\mathrm{j}}(m_e)}{(N_{\mathrm{s}} f_{\mathrm{s}}(m_e) + N_{\mathrm{b}} f_{\mathrm{b}}(m_e))^2} \quad . \tag{B.2}$$

In this way a weight for every event can be calculated. These weights have to satisfy the following conditions

$$\int W_{\mathrm{s}}(m) f_{\mathrm{s}}(m) \, \mathrm{d}m = 1 \,, \tag{B.3}$$

$$\int W_{\mathrm{s}}(m) f_{\mathrm{b}}(m) \, \mathrm{d}m = 0 \,. \tag{B.4}$$

There are many ways to define a weight that satisfies Equation B.3 and Equation B.4. In principle, any function $W_{\mathrm{s}}(m)$ which is orthogonal to $f_{\mathrm{b}}(m)$ but not orthogonal to $f_{\mathrm{s}}(m)$ is allowed. One simple choice for $W_{\mathrm{s}}(m)$ are the weights defined by the sideband subtraction as explained in Section 7.3. In the *sPlot* technique the weights, often called
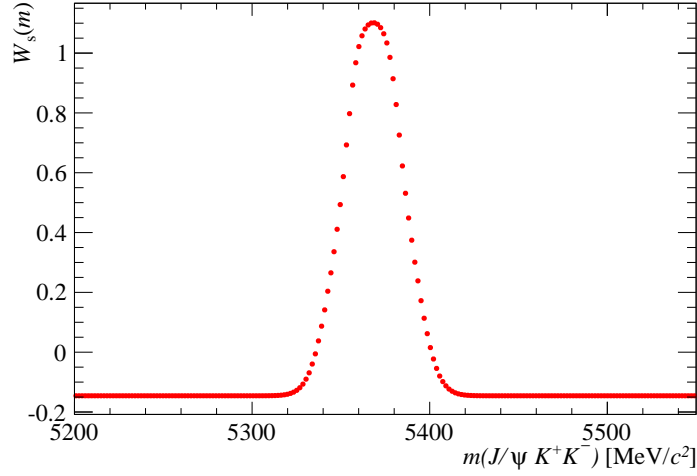
Figure B.1: Distribution of the sWeights, $W_\mathrm{s}(m)$, as a function of the $B_s^0 \to J/\psi K^+ K^-$ invariant mass.

sWeights, are developed in order to minimise the overall statistical uncertainty on the signal component of x. They are calculated by minimising the expression

$$\int W_\mathrm{s}^2(m)\, f_\mathrm{s}(m)\, \mathrm{d}m\, \mathrm{d}t \quad . \tag{B.5}$$

As an example, the sWeights $W_\mathrm{s}(m)$ extracted performing a fit to the mass distribution with the PDF defined in Section 5.6 are shown in Figure B.1 as a function of the $B_s^0 \to J/\psi K^+ K^-$ invariant mass.

The sWeights, as any weight that satisfies Equation B.3 and Equation B.4, are able to statistically extract the signal component of the b-hadron decay-time distribution, $f_\mathrm{s}(t)$, from the overall PDF, $f(m,t)$, without making use of any a priori knowledge on its shape

$$\int W_\mathrm{s}(m) f(m,t)\, \mathrm{d}m = \int W_\mathrm{s}(m)\, [N_\mathrm{s}\, f_\mathrm{s}(m)\, f_\mathrm{s}(t) + N_\mathrm{b}\, f_\mathrm{b}(m)\, f_\mathrm{b}(t)]\, \mathrm{d}m = N_\mathrm{s}\, f_\mathrm{s}(t)\,.$$

In a similar way, a weight function, $W_\mathrm{b}(m)$, can be defined in order to extract the background contribution.

This concept can be further extended defining the following likelihood function

$$\mathcal{L}(\overrightarrow{\vartheta}) = \prod_i^{\text{candidates}} \left[\mathcal{P}_\mathrm{s}(\mathbf{x_i}|\overrightarrow{\vartheta})\right]^{W_\mathrm{s}(m_i)}\,, \tag{B.6}$$

where $\overrightarrow{\vartheta} = \{\vartheta_1, \vartheta_2, ...\}$ is a set of unknown parameters that have to be determined from the fit, see Section 4.4. By including in the likelihood the sWeights, the background contribution cancels on a statistical basis and the signal parameters can be extimated by modelling only the signal PDF, $\mathcal{P}_\mathrm{s}$. This technique is often referred to as sFit method [104].

C

Apollonios function

It is observed that two Gaussian distributions are not enough to describe the invariant mass distribution properly for high MC statistic samples [105]. A common probability density function (PDF) used to fit the mass peak of a resonance in experimental particle physics is the so-called Crystal Ball (CB) function [120]

$$p(m) \propto \begin{cases} e^{-\frac{1}{2}\left(\frac{m-\mu}{\sigma}\right)^2} & \text{, if } \frac{m-\mu}{\sigma} > -a \\ A\left(B - \frac{m-\mu}{\sigma}\right)^n & \text{, otherwise} \end{cases} \tag{C.1}$$

where m is the measured mass, μ is the mean value, σ is the resolution, a is the so-called transition point and n is the power-law exponent. The parameters A and B are calculated by imposing the continuity of the function and its derivative at the transition point a. This function consists of a Gaussian core, that models the detector resolution, with a tail on the left-hand side that parameterises the effect of photon radiation by the final state particles in the decay. In data analysis, one may deal with events which have different uncertainties on the measured mass, therefore distorting the core of the Crystal Ball, which will not be described by a Gaussian distribution any more. This is sometimes modelled by the sum of two or three Crystal Ball functions, which is the equivalent of assuming that the per-event uncertainty is a sum of two or three delta functions. However, per-event uncertainties are usually continuous functions very different from a sum of a small number of delta functions.

An alternative function has been suggested in Ref. [121] in order to deal with continuous per-event uncertainties, so-called double-sided Apollonios function (DSA). It is characterised by an exponential of a hyperbola, $\exp^{\left(-\sqrt{1+\text{x}^2}\right)}$, to describe the core of the invariant mass distribution and two Crystal Ball-like tails for the sides

$$A(m; \mu, b, \delta, a, n_l, n_r) \propto \begin{cases} e^{-b\sqrt{1+a^2}}\left(\frac{\left(n_r\sqrt{1+a^2}-a\right)/(ba)-a}{\left(n_r\sqrt{1+a^2}-a\right)/(ba)-((m-\mu)/\delta)}\right)^{n_r} & \text{, if } \frac{m-\mu}{\delta} > a \\ e^{-b\sqrt{1+(m-\mu)^2/\delta^2}} & \text{, if } \frac{m-\mu}{\delta} \leq -a \\ e^{-b\sqrt{1+a^2}}\left(\frac{\left(n_l\sqrt{1+a^2}-a\right)/(ba)+a}{\left(n_l\sqrt{1+a^2}-a\right)/(ba)-((m-\mu)/\delta)}\right)^{n_l} & \text{, if } \frac{m-\mu}{\delta} < a \end{cases}$$

$$\tag{C.2}$$

where m is the measured mass, μ the mean, b a parameter that controls the shape of the hyperbola, δ a parameter that can be linked to the RMS of the distribution, a the transition point between the core function and the tails and n_l (n_r) the left (right) power-law components of the tails.

D

D.1   Effect on the $B^0 \to J/\psi K_{\mathrm{S}}^0$ lifetime

Assuming no direct CP violation, $\mathcal{A}_{CP}^{\mathrm{dir}} = 0$, the untagged[1] decay rate is obtained summing all the contributions in Equation 1.31. For the $B^0 \to J/\psi K_{\mathrm{S}}^0$ decay and in presence of a B^0 production asymmetry, A_p, it becomes

$$\frac{d\Gamma}{dt}(B^0 \to J/\psi K_{\mathrm{S}}^0) = N_f \, |A_f^{\Delta\Gamma}|^2 \, e^{-\Gamma_d t} \left(1 + A_p \, \mathcal{A}_{CP}^{\mathrm{mix}} \sin \Delta m_d t \right) , \qquad \text{(D.1)}$$

where N_f is a normalisation factor.

The effective lifetime, $\tau_{B^0 \to J/\psi K_{\mathrm{S}}^0}^{\mathrm{eff}}$, is given by

$$\tau_{B^0 \to J/\psi K_{\mathrm{S}}^0}^{\mathrm{eff}} = \frac{\int_0^\infty t \frac{d\Gamma(B^0 \to J/\psi K_{\mathrm{S}}^0)}{dt} dt}{\int_0^\infty \frac{d\Gamma(B^0 \to J/\psi K_{\mathrm{S}}^0)}{dt} dt} = \frac{\int_0^\infty t e^{-\Gamma_d t} \left(1 + A_p \, \mathcal{A}_{CP}^{\mathrm{mix}} \sin \Delta m_d t \right) dt}{\int_0^\infty e^{-\Gamma_d t} \left(1 + A_p \, \mathcal{A}_{CP}^{\mathrm{mix}} \sin \Delta m_d t \right) dt} . \qquad \text{(D.2)}$$

Solving the integrals the expression for the effective lifetime becomes

$$\tau_{B^0 \to J/\psi K_{\mathrm{S}}^0}^{\mathrm{eff}} = \frac{1}{\Gamma_d} \frac{1 + A_p \mathcal{A}_{CP}^{\mathrm{mix}} \frac{2\Gamma_d^3 \Delta m_d}{\left(\Gamma_d^2 + \Delta m_d^2 \right)^2}}{1 + A_p \mathcal{A}_{CP}^{\mathrm{mix}} \frac{\Gamma_d \Delta m_d}{\Gamma_d^2 + \Delta m_d^2}} . \qquad \text{(D.3)}$$

In case of a small production asymmetry $(A_p \ll 1)$ the approximation $1/(1 \pm x) = 1 \mp x + \mathcal{O}(x^2)$ can be used in order to get the final expression of the effetive $B^0 \to J/\psi K_{\mathrm{S}}^0$ lifetime in presence of a production asymmetry

$$\tau_{B^0 \to J/\psi K_{\mathrm{S}}^0}^{\mathrm{eff}} \;\approx\; \frac{1}{\Gamma_d} \left[1 + A_p \mathcal{A}_{CP}^{\mathrm{mix}} \left(\frac{2\Gamma_d^3 \Delta m_d}{\left(\Gamma_d^2 + \Delta m_d^2 \right)^2} - \frac{\Gamma_d \Delta m_d}{\Gamma_d^2 + \Delta m_d^2} \right) \right] \qquad \text{(D.4)}$$

$$\;\approx\; \left(1 + A_p \mathcal{A}_{CP}^{\mathrm{mix}} \frac{\Gamma_d \Delta m_d (\Gamma_d^2 - \Delta m_d^2)}{\left(\Gamma_d^2 + \Delta m_d^2 \right)^2} \right) . \qquad \text{(D.5)}$$

---

[1]With the term untagged is indicated a sample composed of B^0 and $\overline{B}^0$, where one does not distinguish the initial state.

D.2   Effect on the $\tau_{B^0 \to J/\psi\, K^{*0}} \big/ \tau_{\overline{B}^0 \to J/\psi\, \overline{K}^{*0}}$ ratio

The decay $B^0 \to J/\psi\, K^{*0}$ is a flavour specific decay characterised by $\lambda_f = 0$. Thus, $\mathcal{A}_{CP}^{\mathrm{dir}} = 1$, $\mathcal{A}_{CP}^{\mathrm{mix}} = 0$ and $\mathcal{A}_{J/\psi K^{0*}}^{\Delta\Gamma} = 0$. The decay rates for $B^0 \to J/\psi\, K^{*0}$ and $\overline{B}^0 \to J/\psi\, \overline{K}^{*0}$ are obtained summing the contributions in Equation 1.31. In presence of a B^0 production asymmetry, A_p, they become

$$\frac{d\Gamma}{dt}(B^0 \to J/\psi\, K^{*0}) = N_f\, |A_f^{\Delta\Gamma}|^2\, e^{-\Gamma_d t}\, (1 + A_p\, \cos \Delta m_d t)\;, \tag{D.6}$$

$$\frac{d\Gamma}{dt}(\overline{B}^0 \to J/\psi\, \overline{K}^{*0}) = N_{\bar{f}}\, |A_f^{\Delta\Gamma}|^2\, e^{-\Gamma_d t}\, (1 - A_p\, \cos \Delta m_d t)\;, \tag{D.7}$$

where N_f and $N_{\bar{f}}$ are normalisation factors.

Indicating the final states $J/\psi K^{*0}$ and $J/\psi \overline{K}^{*0}$ with f and $\bar{f}$, respectively, the effective lifetime is given by

$$\tau_{f\,(\bar{f})}^{\mathrm{eff}} = \frac{\int_0^\infty t \frac{d\Gamma(f\,(\bar{f}))}{dt} dt}{\int_0^\infty \frac{d\Gamma(f\,(\bar{f}))}{dt} dt} = \frac{\int_0^\infty t e^{-\Gamma_d t}\,(1 \pm A_p\, \cos \Delta m_d t)\, dt}{\int_0^\infty e^{-\Gamma_d t}\,(1 \pm A_p\, \cos \Delta m_d t)\, dt}\;. \tag{D.8}$$

Solving the integrals the expression for the effective lifetime becomes

$$\tau_{f\,(\bar{f})}^{\mathrm{eff}} = \frac{1}{\Gamma_d}\, \frac{1 \pm A_p\, \frac{\Gamma_d^2(\Gamma_d^2 - \Delta m_d^2)}{(\Gamma_d^2 + \Delta m_d^2)^2}}{1 \pm A_p \frac{\Gamma_d \Delta m_d}{\Gamma_d^2 + \Delta m_d^2}}\;. \tag{D.9}$$

In case of a small production asymmetry $(A_p \ll 1)$ the approximation $1/(1 \pm x) = 1 \mp x + \mathcal{O}(x^2)$ can be used in order to get the expression of the effetive $B^0 \to J/\psi\, K^{*0}$ $(\tau_{\overline{B}^0 \to J/\psi\, \overline{K}^{*0}})$ lifetime in presence of a production asymmetry

$$\tau_{f\,(\bar{f})}^{\mathrm{eff}} \;\approx\; \frac{1}{\Gamma_d}\left[1 \pm A_p \left(\frac{\Gamma_d^2\,(\Gamma_d^2 - \Delta m_d^2)}{(\Gamma_d^2 + \Delta m_d^2)^2} - \frac{\Gamma_d^2}{\Gamma_d^2 + \Delta m_d^2} \right) \right] \tag{D.10}$$

$$\approx\; \left(1 \mp 2\, A_p \frac{\Gamma_d^2 \Delta m_d^2}{(\Gamma_d^2 + \Delta m_d^2)^2} \right)\;. \tag{D.11}$$

Thus, the expected shift in the $\tau_{B^0 \to J/\psi\, K^{*0}} \big/ \tau_{\overline{B}^0 \to J/\psi\, \overline{K}^{*0}}$ ratio is

$$\Delta \frac{\tau_{B^0 \to J/\psi\, K^{*0}}}{\tau_{\overline{B}^0 \to J/\psi\, \overline{K}^{*0}}} = \frac{1 - 2\, A_P(B^0)\, \frac{\Gamma_d^2 \Delta m_d^2}{(\Gamma_d^2 + \Delta m_d^2)^2}}{1 + 2\, A_P(B^0)\, \frac{\Gamma_d^2 \Delta m_d^2}{(\Gamma_d^2 + \Delta m_d^2)^2}} \approx 1 - 4\, A_P(B^0)\, \frac{\Gamma_d^2 \Delta m_d^2}{(\Gamma_d^2 + \Delta m_d^2)^2}\;. \tag{D.12}$$

Bibliography

[1] A. Lenz, *Lifetimes and HQE*, IPPP/14/46, DCPT/14/92 (2014) `arXiv:1405.3601`.

[2] Heavy Flavor Averaging Group, Y. Amhis *et al.*, *Averages of b-hadron, c-hadron, and τ-lepton properties as of early 2012*, `arXiv:1207.1158`. updated results and plots available at: `http://www.slac.stanford.edu/xorg/hfag/`.

[3] LHCb collaboration, R. Aaij *et al.*, *Measurements of the B^+, B^0, B_s^0 meson and Λ_b^0 baryon lifetimes*, JHEP **1404** (2014) 114, `arXiv:1402.2554`.

[4] LHCb collaboration, R. Aaij *et al.*, *Prompt charm production in pp collisions at $\sqrt{s} = 7$ TeV*, Nucl. Phys. **B871** (2013) 1–20, `arXiv:1302.2864`.

[5] LHCb collaboration, R. Aaij *et al.*, *Measurement of CP-violation and the B_s^0-meson decay width difference with $B_s^0 \to J/\psi K^+ K^-$ and $B_s^0 \to J/\psi \pi^+ \pi^-$ decays*, Phys. Rev. **D87** (2013) 112010, `arXiv:1304.2600`.

[6] LHCb collaboration, R. Aaij *et al.*, *Precision measurement of CP violation in $B_s^0 \to J/\psi K^+ K^-$ decays*, to be published in Phys. Rev. Lett. (2014) `arXiv:1411.3104`.

[7] G. Altarelli, *The Standard model of particle physics*, `arXiv:hep-ph/0510281`.

[8] G. Altarelli, *The Standard electroweak theory and beyond*, `arXiv:hep-ph/0011078`.

[9] I. Brock and T. Schorner-Sadenius, *Physics at the Terascale*. Wiley-VCH, (2011).

[10] ATLAS collaboration, G. Aad *et al.*, *Observation of a new particle in the search for the Standard Model Higgs boson with the ATLAS detector at the LHC*, Phys. Lett. **B716** (2012) 1–29, `arXiv:1207.7214`.

[11] CMS collaboration, S. Chatrchyan *et al.*, *Observation of a new boson at a mass of 125 GeV with the CMS experiment at the LHC*, Phys. Lett. **B716** (2012) 30–61, `arXiv:1207.7235`.

[12] UA1 collaboration, G. Arnison *et al.*, *Experimental observation of isolated large transverse energy electrons with associated missing energy at $\sqrt{s}$=540 GeV*, Phys. Lett. **B 122** (1983), no. 1, 103–116.

[13] UA1 collaboration, G. Arnison *et al.*, *Experimental observation of lepton pairs of invariant mass around 95 GeV/c^2 at the CERN SPS collider*, Physics Letters **B 126** (1983), no. 5, 398–410.

[14] Particle Data Group, J. Beringer *et al.*, *Review of Particle Physics*, Phys. Rev. D **86** (Jul, 2012) 010001.

[15] LHCb collaboration, R. Aaij *et al.*, *Observation of the resonant character of the $Z(4430)^-$ state*, Phys. Rev. Lett. **112** (2014) 222002, `arXiv:1404.1903`.

[16] L. Wolfenstein, *Parametrization of the Kobayashi-Maskawa Matrix*, Phys. Rev. Lett. **51** (1983) 1945.

[17] U. Nierste, *Three Lectures on Meson Mixing and CKM phenomenology*, `arXiv:0904.1869`.

[18] H1 and ZEUS collaboration, F. Aaron *et al.*, *Combined Measurement and QCD Analysis of the Inclusive e^+- p Scattering Cross Sections at HERA*, JHEP **1001** (2010) 109, `arXiv:0911.0884`.

[19] LHCb web page, *Operations plots*, Available at http://lhcb.web.cern.ch/lhcb/speakersbureau/excel/default.html.

[20] LHCb collaboration, R. Aaij *et al.*, *Measurement of J/ψ production in pp collisions at $\sqrt{s} = 7$ TeV*, Eur. Phys. J. **C71** (2011) 1645, `arXiv:1103.0423`.

[21] LHCb collaboration, T. L. collaboration, *Measurements of the branching fractions and CP asymmetries of $B^+ \to J/\psi\pi^+$ and $B^+ \to \psi(2S)\pi^+$ decays*, Phys. Rev. **D85** (2012) 091105, `arXiv:1203.3592`.

[22] LHCb collaboration, R. Aaij *et al.*, *First observation of CP violation in the decays of B_s^0 mesons*, Phys. Rev. Lett. **110** (2013), no. 22 221601, `arXiv:1304.6173`.

[23] I. Dunietz, R. Fleischer and U. Nierste, *In pursuit of new physics with B_s decays*, Phys. Rev. **D63** (2001) 114015, `arXiv:hep-ph/0012219`.

[24] R. Fleischer and R. Knegjens, *Effective Lifetimes of B_s Decays and their Constraints on the B_s^0-$\bar{B}_s^0$ Mixing Parameters*, Eur. Phys. J. **C71** (2011) 1789, `arXiv:1109.5115`.

[25] T. Gershon, *$\Delta\Gamma_d$: A Forgotten Null Test of the Standard Model*, J. Phys. **G38** (2011) 015007, `arXiv:1007.5135`.

[26] LHCb collaboration, B. Adeva *et al.*, *Roadmap for selected key measurements of LHCb*, `arXiv:0912.4179`.

[27] J. Charles *et al.*, *Predictions of selected flavour observables within the Standard Model*, Phys. Rev. **D84** (2011) 033005, `arXiv:1106.4041`.

[28] C. Linn, *Measurement of the CP-violating phase ϕ_s using $B_s \to J/\psi\phi$ and $B_s^0 \to J/\psi\pi^+\pi^-$ decays with the LHCb experiment.* PhD thesis, Heidelberg U., Apr, 2013. Presented 15 May 2013.

[29] M. Neubert, *B decays and the heavy quark expansion*, Adv. Ser. Direct. High Energy Phys. **15** (1998) 239–293, `arXiv:hep-ph/9702375`.

[30] I. I. Bigi, *The QCD perspective on lifetimes of heavy flavor hadrons*, `arXiv:hep-ph/9508408`.

[31] N. Uraltsev, *Heavy quark expansion in beauty and its decays*, `arXiv:hep-ph/9804275`.

[32] A. J. Buras, *Flavor dynamics: CP violation and rare decays*, `arXiv:hep-ph/0101336`.

[33] R. Feynman and M. Gell-Mann, *Theory of Fermi interaction*, Phys. Rev. **109** (1958) 193–198.

[34] A. S. Kronfeld, *Twenty-first Century Lattice Gauge Theory: Results from the QCD Lagrangian*, Ann. Rev. Nucl. Part. Sci. **62** (2012) 265–284, `arXiv:1203.1204`.

[35] V. A. Khoze and M. A. Shifman, *Heavy quarks*, Sov. Phys. Usp. **26** (1983) 387.

[36] M. A. Shifman and M. Voloshin, *Preasymptotic Effects in Inclusive Weak Decays of Charmed Particles*, Sov. J. Nucl. Phys. **41** (1985) 120.

[37] M. A. Shifman and M. Voloshin, *Hierarchy of Lifetimes of Charmed and Beautiful Hadrons*, Sov. Phys. JETP **64** (1986) 698.

[38] I. I. Bigi, N.G. Uraltsev and A.I. Vainshtein, *Nonperturbative corrections to inclusive beauty and charm decays: QCD versus phenomenological models*, Phys. Lett. **B293** (1992) 430–436, `arXiv:hep-ph/9207214`.

[39] A. Lenz, *Theoretical status of B_s-mixing and lifetimes of heavy hadrons*, Nucl. Phys. Proc. Suppl. **177-178** (2008) 81–86, `arXiv:0705.3802`.

[40] E. Franco, V. Lubicz, F. Mescia, and C. Tarantino, *Lifetime ratios of beauty hadrons at the next-to-leading order in QCD*, Nucl. Phys. **B633** (2002) 212–236, `arXiv:hep-ph/0203089`.

[41] A. Lenz, *Selected Topics in Heavy Flavour Physics*, `arXiv:1404.6197`.

[42] A. Lenz, *B-mixing in and beyond the Standard model*, `arXiv:1409.6963`.

[43] A. Lenz and U. Nierste, *Numerical Updates of Lifetimes and Mixing Parameters of B Mesons*, `arXiv:1102.4274`.

[44] C. Tarantino, *Beauty hadron lifetimes and B meson CP violation parameters from lattice QCD*, Eur. Phys. J. **C33** (2004) S895–S899, `arXiv:hep-ph/0310241`.

[45] M. Battaglia *et al.*, *The CKM matrix and the unitarity triangle. Workshop, CERN, Geneva, Switzerland (2002): Proceedings*, `arXiv:hep-ph/0304132`.

[46] T. Ito, M. Matsuda and Y. Matsui, *New possibility of solving the problem of lifetime ratio $\tau(\Lambda_b^0)/\tau(B^0)$*, Prog. Theor. Phys. **99** (1998) 271–280, `arXiv:hep-ph/9705402`.

[47] F. Gabbiani, A. I. Onishchenko and A. A. Petrov, *Lambda(b) lifetime puzzle in heavy quark expansion*, Phys. Rev. **D68** (2003) 114006, `arXiv:hep-ph/0303235`.

[48] F. Gabbiani, A. I. Onishchenko and A. A. Petrov, *Spectator effects and lifetimes of heavy hadrons*, Phys. Rev. **D70** (2004) 094031, `arXiv:hep-ph/0407004`.

[49] N. Uraltsev, *Topics in the heavy quark expansion*, `arXiv:hep-ph/0010328`.

[50] ATLAS collaboration, G. Aad *et al.*, *Measurement of the Λ_b lifetime and mass in the ATLAS experiment*, Phys. Rev. **D87** (2013), no. 3 032002, `arXiv:1207.2284`.

[51] CMS collaboration, S. Chatrchyan *et al.*, *Measurement of the Λ_b^0 lifetime in pp collisions at $\sqrt{s} = 7$ TeV*, JHEP **07** (2013) 163, `arXiv:1304.7495`.

[52] CDF collaboration, T. Aaltonen *et al.*, *Measurement of b hadron lifetimes in exclusive decays containing a J/ψ in $p\bar{p}$ collisions at $\sqrt{s} = 1.96$ TeV*, Phys. Rev. Lett. **106** (2011) 121804, `arXiv:1012.3138`.

[53] A. Lenz, *B-mixing in and beyond the Standard model*, `arXiv:1409.6963`.

[54] LHCb collaboration, R. Aaij *et al.*, *Measurement of the CP-violating phase ϕ_s in the decay $B_s^0 \to J/\psi\phi$*, Phys. Rev. Lett. **108** (2012) 101803, `arXiv:1112.3183`.

[55] ATLAS collaboration, G. Aad *et al.*, *Time-dependent angular analysis of the decay $B_s^0 \to J/\psi\phi$ and extraction of $\Delta\Gamma_s$ and the CP-violating weak phase ϕ_s by ATLAS*, JHEP **1212** (2012) 072, `arXiv:1208.0572`.

[56] CDF collaboration, T. Aaltonen *et al.*, *Measurement of the Bottom-Strange Meson Mixing Phase in the Full CDF Data Set*, Phys. Rev. Lett. **109** (2012) 171802, `arXiv:1208.2967`.

[57] DØ collaboration, V. M. Abazov *et al.*, *Measurement of the CP-violating phase $\phi_s^{J/\psi\phi}$ using the flavor-tagged decay $B_s^0 \to J/\psi\phi$ in 8 fb^{-1} of $p\bar{p}$ collisions*, Phys. Rev. **D85** (2012) 032006, `arXiv:1109.3166`.

[58] BaBar collaboration, B. Aubert *et al.*, *Limits on the decay-rate difference of neutral B mesons and on CP, T, and CPT violation in $B^0\overline{B}^0$ oscillations*, Phys. Rev. Lett. **92** (2004) 181801, `arXiv:hep-ex/0311037`.

[59] BaBar collaboration, B. Aubert *et al.*, *Limits on the decay rate difference of neutral$-B$ mesons and on CP, T, and CPT violation in $B^0\overline{B}^0$ oscillations*, Phys. Rev. **D70** (2004) 012007, `arXiv:hep-ex/0403002`.

[60] T. Higuchi *et al.*, *Search for Time-Dependent CPT Violation in Hadronic and Semileptonic B Decays*, Phys. Rev. **D85** (2012) 071105, `arXiv:1203.0930`.

[61] DØ collaboration, V. M. Abazov *et al.*, *Study of CP-violating charge asymmetries of single muons and like-sign dimuons in $p\bar{p}$ collisions*, Phys. Rev. **D89** (2014), no. 1 012002, `arXiv:1310.0447`.

[62] N. Uraltsev, *On the problem of boosting nonleptonic b baryon decays*, Phys. Lett. **B376** (1996) 303–308, `arXiv:hep-ph/9602324`.

[63] I. I. Bigi, M. A. Shifman and N. Uraltsev, *Aspects of heavy quark theory*, Ann. Rev. Nucl. Part. Sci. **47** (1997) 591–661, `arXiv:hep-ph/9703290`.

[64] D. Pirjol and N. Uraltsev, *Four fermion heavy quark operators and light current amplitudes in heavy flavor hadrons*, Phys. Rev. **D59** (1999) 034012, `arXiv:hep-ph/9805488`.

[65] M. Voloshin, *Reducing model dependence of spectator effects in inclusive decays of heavy baryons*, Phys. Rev. **D61** (2000) 074026, `arXiv:hep-ph/9908455`.

[66] C. Lefèvre, *The CERN accelerator complex*, 2008.

[67] ALICE collaboration, K. Aamodt *et al.*, *The ALICE experiment at the CERN LHC*, JINST **3** (2008) S08002.

[68] ATLAS collaboration, G. Aad *et al.*, *The ATLAS Experiment at the CERN Large Hadron Collider*, JINST **3** (2008) S08003.

[69] CMS collaboration, S. Chatrchyan *et al.*, *The CMS experiment at the CERN LHC*, JINST **3** (2008) S08004.

[70] LHCb collaboration, J. Alves, A. Augusto *et al.*, *The LHCb Detector at the LHC*, JINST **3** (2008) S08005.

[71] LHCb collaboration, R. Aaij *et al.*, *Prompt K_s^0 production in pp collisions at $\sqrt{s} = 0.9$ TeV*, Phys. Lett. **B693** (2010) 69–80, `arXiv:1008.3105`.

[72] LHCb collaboration, S. Amato *et al.*, *Lhcb magnet: Technical design report*, Available at CERN-LHCC-2000-007 (2000).

[73] LHCb collaboration, P. R. Barbosa-Marinho *et al.*, *LHCb VELO (VErtex LOcator): Technical Design Report*, Available at CERN-LHCC-2001-011 (2001).

[74] J. Gassner, M. Needham, and O. Steinkamp, *Layout and Expected Performance of the LHCb TT Station*, Tech. Rep. LHCb-2003-140, CERN, Geneva, Apr, 2004.

[75] LHCb collaboration, P. R. Barbosa-Marinho *et al.*, *LHCb inner tracker: Technical Design Report*, Available at CERN-LHCC-2002-029 (2002).

[76] LHCb collaboration, P. R. Barbosa-Marinho *et al.*, *LHCb outer tracker: Technical Design Report*, Available at CERN-LHCC-2001-024 (2001).

[77] LHCb collaboration, S. Amato *et al.*, *LHCb RICH: Technical Design Report*, Available at CERN-LHCC-2000-037 (2000).

[78] M. Adinolfi *et al.*, *Performance of the LHCb RICH detector at the LHC*, Eur. Phys. J. **73** no. C5 .

[79] A. Powell *et al.*, *Particle identification at LHCb*, PoS **ICHEP2010** (2010) 020. LHCb-PROC-2011-008.

[80] J. R. Harrison, *Radiation damage studies in the LHCb VELO detector and searches for lepton flavour and baryon number violating tau decays*. PhD thesis, Manchester U., 2014. Presented 16 05 2014.

[81] LHCb collaboration, S. Amato *et al.*, *LHCb muon system: Technical Design Report*, Available at CERN-LHCC-2001-010 (2001).

[82] LHCb collaboration, S. Amato *et al.*, *LHCb calorimeters: Technical Design Report*, Available at CERN-LHCC-2000-036 (2000).

[83] R. Aaij *et al.*, *The LHCb Trigger and its Performance in 2011*, JINST **8** (2013) P04022, `arXiv:1211.3055`.

[84] M. Clemencic *et al.*, *Recent developments in the LHCb software framework gaudi*, Journal of Physics: Conference Series **219** (2010), no. 4 042006 . see also "The Gaudi project".

[85] LHCb collaboration, *The Brunel project*, available at http://lhcb-release-area.web.cern.ch/LHCb-release-area/DOC/brunel/.

[86] LHCb collaboration, *The DaVinci project*, available at http://lhcb-release-area.web.cern.ch/LHCb-release-area/DOC/davinci/.

[87] W. D. Hulsbergen, *Decay chain fitting with a Kalman filter*, Nuclear Instruments and Methods in Physics Research A **552** (Nov., 2005) 566–575, `arXiv:physics/0503191`.

[88] LHCb collaboration, *The Moore project*, available at http://lhcb-release-area.web.cern.ch/LHCb-release-area/DOC/moore/.

[89] LHCb collaboration, *The Gauss project*, available at http://lhcb-release-area.web.cern.ch/LHCb-release-area/DOC/gauss/.

[90] T. Sjöstrand, S. Mrenna and P. Skands, Pythia *6.4 physics and manual*, JHEP **05** (2006) 026, `arXiv:hep-ph/0603175`.

[91] I. Belyaev *et al.*, *Handling of the generation of primary events in* Gauss, *the LHCb simulation framework*, Nuclear Science Symposium Conference Record (NSS/MIC) **IEEE** (2010) 1155.

[92] D. J. Lange, *The* EvtGen *particle decay simulation package*, Nucl. Instrum. Meth. **A462** (2001) 152–155.

[93] P. Golonka and Z. Was, *Photos Monte Carlo: a precision tool for QED corrections in Z and W decays*, Eur. Phys. J. **C45** (2006) 97–107, `arXiv:hep-ph/0506026`.

[94] GEANT4 collaboration, J. Allison *et al.*, GEANT4 *developments and applications*, IEEE Trans. Nucl. Sci. **53** (2006) 270; GEANT4 collaboration, S. Agostinelli *et al.*, GEANT4*: a simulation toolkit*, Nucl. Instrum. Meth. **A506** (2003) 250.

[95] M. Clemencic *et al.*, *The LHCb simulation application,* GAUSS*: design, evolution and experience*, J. Phys: Conf. Ser. **331** (2011) 032023.

[96] LHCb collaboration, *The Boole project*, available at http://lhcb-release-area.web.cern.ch/LHCb-release-area/DOC/boole/.

[97] M. De Cian, U. Straumann, O. Steinkamp, and N. Serra, *Track Reconstruction Efficiency and Analysis of $B^0 \to K^{*0}\mu^+\mu^-$ at the LHCb Experiment.* PhD thesis, Zurich U., Sep, 2013. Presented 14 Mar 2013.

[98] O. Callot and S. Hansmann-Menzemer, *The Forward Tracking: Algorithm and Performance Studies*, Tech. Rep. LHCb-2007-015, CERN-LHCb-2007-015 (2007).

[99] O. Callot, *FastVelo: a fast and efficient pattern recognition package for the Velo*, LHCb-PUB-2011-001 (2011).

[100] W. D. Hulsbergen, *The global covariance matrix of tracks fitted with a Kalman filter and an application in detector alignment*, Nuclear Instruments and Methods in Physics Research A **600** (Mar., 2009) 471–477, `arXiv:0810.2241`.

[101] R. Aaij *et al.*, *Performance of the LHCb Vertex Locator*, JINST **9** (2014) 09007, `arXiv:1405.7808`.

[102] CERN program library, *Minuit: reference manual*, available at http://wwwasdoc.web.cern.ch/wwwasdoc/minuit/minmain.html.

[103] Langenbruc, C., *Measurement of the B_s^0 mixing phase in the decay $B_s^0 \to J/\psi\phi$ with the LHCb experiment*, CERN-THESIS-2011-161 (2011).

[104] Y. Xie, *sFit: a method for background subtraction in maximum likelihood fit*, `arXiv:0905.0724`.

[105] F. G. Dupertuis, *Measurements of b-hadron lifetimes and the calibration and performance of the LHCb tracking system*, CERN-THESIS-2014-059 (2014). Presented 28 03 2014.

[106] Wandernoth, Sebastian, *Measurement of the B_s^0–$\bar{B}_s^0$ Oscillation Frequency at LHCb using 1 fb^{-1} of data taken in 2011*, CERN-THESIS-2013-317 (2013). Presented 04 Feb 2014.

[107] LHCb collaboration, R. Aaij *et al.*, *Measurement of the effective $B_s^0 \to J/\psi K_S^0$ lifetime*, Nucl. Phys. **B873** (2013) 275–292, `arXiv:1304.4500`.

[108] LHCb collaboration, R. Aaij *et al.*, *Amplitude analysis and branching fraction measurement of $\overline{B}_s^0 \to J/\psi K^+ K^-$*, Phys. Rev. **D87** (2013) 072004, `arXiv:1302.1213`.

[109] LHCb collaboration, R. Aaij *et al.*, *First measurement of time-dependent CP violation in $B_s^0 \to K^+K^-$ decays*, JHEP **10** (2013) 183, `arXiv:1308.1428`.

[110] LHCb collaboration, R. Aaij *et al.*, *Precision measurement of the B_s^0-$\bar{B}_s^0$ oscillation frequency with the decay $B_s^0 \to D_s^-\pi^+$*, New J. Phys. **15** (2013) 053021, `arXiv:1304.4741`.

[111] S. Borghi *et al.*, *First spatial alignment of the {LHCb} {VELO} and analysis of beam absorber collision data*, Nuclear Instruments and Methods in Physics Research A **618** (2010), no. 1–3 108 – 120.

[112] G. A. Krocker, *Development and calibration of a same side kaon tagging algorithm and measurement of the B_s^0–$\bar{B}_s^0$ oscillation frequency Δm_s at the LHCb experiment*. PhD thesis, Heidelberg U., Sep, 2013. Presented 20 Nov 2013.

[113] LHCb collaboration, R. Aaij *et al.*, *Precision measurement of CP violation in $B_s^0 \to J/\psi K^+K^-$ decays*, to be published in Phys. Rev. Lett. (2014) `arXiv:1411.3104`.

[114] LHCb collaboration, R. Aaij *et al.*, *Precision measurement of the ratio of the Λ_b^0 to $\overline{B}^0$ lifetimes*, Phys. Lett. **B734** (2014) 122, `arXiv:1402.6242`.

[115] LHCb collaboration, R. Aaij *et al.*, *Precision measurement of the Λ_b^0 baryon lifetime*, Phys. Rev. Lett. **111** (2013) 102003, `arXiv:1307.2476`.

[116] D. Becirevic, *Theoretical progress in describing the B meson lifetimes*, PoS **HEP2001** (2001) 098, `arXiv:hep-ph/0110124`.

[117] UKQCD collaboration, M. Di Pierro, C. T. Sachrajda, and C. Michael, *An Exploratory lattice study of spectator effects in inclusive decays of the Lambda(b) baryon*, Phys. Lett. **B468** (1999) 143, `arXiv:hep-lat/9906031`.

[118] CMS collaboration, S. Chatrchyan *et al.*, *Measurement of the CP-violating weak phase ϕ_s and the decay width difference $\Delta\Gamma_s$ using the $B_s^0 \to J/\psi\phi(1020)$ decay channel*, CMS-PAS-BPH-13-012 (2014).

[119] M. Pivk and F. R. Le Diberder, *sPlot: a statistical tool to unfold data distributions*, Nucl. Instrum. Meth. **A555** (2005) 356–369, `arXiv:physics/0402083`.

[120] M. Oreglia, *A Study of the Reactions $\psi' \to \gamma\gamma\psi$*, Ph.D. thesis (1980).

[121] D. M. Santos and F. Dupertuis, *Mass distributions marginalized over per-event errors*, submitted to Nucl. Instrum. Meth. A (2013) `arXiv:1312.5000`.